A study of radiation-matter interactions for safe operative protocols on paintings in Heritage Science

Maria Amelia Suzuki

A thesis submitted in partial fulfilment

of the requirements of Nottingham Trent University

for the degree of Doctor of Philosophy

This research programme was carried out

in collaboration with the Institute of Heritage Science,

National Research Council of Italy (ISPC-CNR).

September 2024

Copyright statement

To my dearest aunt Maria Grazia Sandrini

Abstract

Many technological improvements in Heritage Science make use of intense radiations, such as optical lasers and synchrotron X-rays, to perform non-invasive analysis and treatment on artworks and historical materials' samples. The radiation damage risk associated with such intense radiation on artworks is insufficiently known and mitigation strategies are still limited. When dealing with highly heterogeneous materials, such as historical paintings, *a priori* knowledge of radiation damage is an ineffective way to prevent damage. The available methods to detect damage are very limited and often fails to detect some type of damage. Therefore, reliable detection methods capable of comprehensively detecting radiation damage are needed.

In this work, a new metric for radiation damage detection is proposed and used for the online monitoring of optical laser and X-ray irradiation of paintings. Any change in VIS-NIR (400-900 nm) reflectance (ΔR) is the result of changes in absorption and/or scattering of a material surface under investigation, hence ΔR can provide an indication of both chemical and physical changes of the surface. Moreover, the intrinsically high sensitivity of VIS-NIR reflectance spectroscopy technique enables the detection of even subtle material changes not detectable by other techniques. Its use in a time and spatially resolved modality, using a VIS-NIR hyperspectral imaging system (HSI), proved to be an efficient, sensitive and robust online radiation damage monitoring set-up capable of detecting early warning signs of damage that can be used to prevent or minimize radiation damage.

The VIS-NIR HSI system was employed for online laser-induced damage monitoring during Raman spectroscopy and proved to be orders of magnitude more sensitive in detecting damage than Raman itself and synchrotron-based micro-X-ray powder diffraction. In case of thermally driven alterations, it can even detect transient/reversible changes as precursors to prevent damage. The study of the effects of the fundamental laser parameters highlighted the importance of including, power, duration and spot size, to define damage, as intensity is not the only parameter that defines the severity of damage.

The VIS-NIR HSI was also used for *operando* X-ray induced damage monitoring during a synchrotron experiment while performing X-ray absorption spectroscopy (XAS) on paintings. The method proved to be able to detect subtle changes at a lower absorbed dose than XAS, permitting early-warning damage threshold detection and can enable prevention of further damage to samples during measurements.

The effect of NIR radiation on plattnerite (lead dioxide) was investigated post-exposure with various complementary techniques, using VIS-NIR HSI, short wave infrared HSI, Raman spectroscopy, synchrotron XRPD and XAS. This was performed to allow further understanding of the fundamental mechanism causing the transformation of plattnerite to recover darkened wall paintings containing the pigment red lead (mixed valence state lead oxide). The primary underlying mechanism of this transformation was determined to be thermally driven, requiring temperatures in the range of 400-500° to be effective without inducing damage to the pigment, with the treatment remaining stable for at least two years. This study of the NIR radiation exposure restoration treatment for red lead pigment contributes to the fundamental knowledge required to determine the suitability and safety of this method for wall paintings.

Overall, this study contributes knowledge towards the development of safe procedures in Heritage Material Science applications when using intense radiation for the analysis and treatment of paintings, which is of paramount importance for the improvement of data collection strategies to reduce the risk of radiation-induced damage to paintings.

Acknowledgements

First, I would like to thank my main supervisor Haida Liang for her great constant support during this project and for the extremely interesting scientific discussions we had in these years. I also want to thank my other supervisors from ISPC-CNR, Cristiano Riminesi for his encouragements, constant support and useful suggestions and feedback during the discussions along the project, and Costanza Miliani for the possibility to access to the BAG 'Historical Materials' at ESRF, for her inputs and suggestions for the thesis and for the funding support. A big thank you also to the rest of my supervisory team from NTU, Sophie Benjamin for her help during the single crystal diffraction trials and for proofreading, and to the former co-supervisor Ian Shuttleworth for his interesting insights into structural defects.

I want to warmly thank Sammy Cheung for his precious help during all the set-ups and measurements (and for his lovely spirit that makes each experiment even more fun!).

I also deeply thank my colleagues Yu Li for the collection and calibration of the remote Raman spectra during the monitoring of laser-induced damage, Patrick S. Atkinson for the acquisition and processing of the OCT data, Alexander Hogg for preparing the codes for data calibration of the VIS-NIR HSI cubes and Florence Liggins for helping me with the SWIR HSI acquisition and calibration of the cubes.

A big thanks also to Francesco di Benedetto from the University of Ferrara for his support in the synchrotron beamtime proposals and for the analysis of the XAS spectra, to Iacopo Osticioli from IFAC-CNR for his help in acquiring the micro-Raman spectra, and to Werner Oberhauser from ICCOM-CNR for his help in the acquisition of the VT-XRPD measurements.

I acknowledge the SOLEIL synchrotron radiation facility for provision of synchrotron radiation facilities, and I would like to thank the beam scientists Sebastian Schoeder and Laurent Tranchant for their great help during the PUMA experiment (proposal number: 20231243). I acknowledge the European Synchrotron Radiation Facility for provision of synchrotron radiation facilities, and I would like to thank Mauro Rovezzi, for his help during the experiment at BM16 at ESRF (proposal HG191), Francesco D'Acapito, for his

support during the BM08 experiment at ESRF (proposal HG175). Marine Cotte and the Rss of the BAG ‘Historical Materials’ of ESRF (HG-172 and HG-213) are also greatly acknowledge for their help, support and training during the many beamtimes at ID13 at ESRF and I thank all the local contacts of each beamtime for their help to run smoothly the experiment: Manfred Burghammer, Alexey Melnikov, Jiliang Liu and Remi Tucoulou.

Thanks to Hartmut Kutzke from the Museum of Cultural History of the University of Oslo for the provision of the materials and preparation of the Prussian blue and lead white sample within the Task 5.1 of IPERION HS.

More generally, I thank the great current and previous team members of ISAAC research group for the extremely supportive environment, the great discussions and the fun inside and outside the lab.

A big thank to my dearest Alex, my beloved family, my special old friends and the great new Nottingham friends for their support, love and patience during this long journey.

I finally thank the Tuscany Region POR-FSE2012-2020 project CNR4C Plas@rt, IPERION HS “Integrating Platform for the European Research Infrastructure” H2020-INFRAIA-2019-1 under Grant No. 871034 and NTU for funding this project.

List of publications

Peer reviewed journals:

A. Suzuki, C.S. Cheung, Y. Li, A. Hogg, P.S. Atkinson, C. Riminesi, C. Miliani, H. Liang. Time and spatially resolved VIS-NIR hyperspectral imaging as a novel monitoring tool for laser-based spectroscopy to mitigate radiation damage on paintings, Analyst, (2024), DOI: 10.1039/d3an02041j

A. Suzuki, I. Osticioli, F. Di Benedetto, W. Oberhauser, H. Liang, F. d'Acapito, C. Riminesi. Experimental evidence of the thermally dominated effect of CW NIR laser irradiation for the restoration of darkened red lead in wall paintings, Microchemical Journal, 2025, DOI: 10.1016/j.microc.2025.113471.

A. Suzuki, C.S. Cheung, F. Di Benedetto, C. Riminesi, S. Schoeder, L. Tranchant, H. Liang. *Operando* VIS-NIR microscopic Hyperspectral imaging for synchrotron X-ray monitoring on paintings. *(in preparation)*

Y. Li, **A. Suzuki**, C.S. Cheung. Y. Gu, S. Kogou, H. Liang. A study of potential laser-induced degradation in remote standoff Raman spectroscopy for wall paintings, Eur. Phys. J. Plus. 2022. DOI: 10.1140/epjp/s13360-022-03305-2

A. Suzuki, C. Riminesi, M. Ricci, S. Vettori, B. Salvadori. Testing of a new Yb:YAG fiber laser system for the removal of graphic vandalism from marble, Heritage Science. 2023 DOI: 10.1186/s40494-023-00966-9

E. Villani, **A. Suzuki,** M**.** Ricci, B. Salvadori, S. Vettori, E. Cantisani. Red stains on heritage marbles: application of micro-scale analyses to assess the presence and distribution of lead compounds. Analyst, 2024. DOI: 10.1039/D4AN00692E

Y. Li, **A. Suzuki**, C.S. Cheung, S. Kogou, H. Liang. Ground-based remote standoff laser spectroscopies and spectral imaging for multimodal analysis of wall painting stratigraphy. Analytical Chemistry, 2024. DOI: 10.1021/acs.analchem.4c05264

Presentations at conferences

A. Suzuki, C.S. Cheung, F. Di Benedetto, C. Riminesi, S. Schoeder, L. Tranchant, H. Liang. Monitoring possible synchrotron X-ray damage on paintings via time and spatially resolved VIS-NIR HSI, European X-ray Spectrometry conference, EXRS, Athens 2024.

A. Suzuki, C.S. Cheung, F. Di Benedetto, C. Riminesi, S. Schoeder, L. Tranchant, H. Liang. *Operando* VIS-NIR microscopic Hyperspectral imaging for synchrotron X-ray monitoring on paintings, Gordon conference on Advances in Heritage Science, Les Diableret, Switzerland, 2024

A. Suzuki, Y. Li, C.S. Cheung, C. Riminesi, H. Liang, VIS-NIR Hyperspectral Imaging as a valuable tool to monitor radiation damage on paintings. SPIE O3A conference, 26-30 June 2023.

A. Suzuki, C. Riminesi, H. Liang, Assessment of synchrotron X-ray alteration on paintings with time and spatially resolved VIS-NIR Hyperspectral imaging. TECHNART2023 - Non-destructive and Microanalytical Techniques in Art and Cultural Heritage: Book of Abstracts. (DOI: 10.34619/ipq7-vuaj)

A. Suzuki, Yu Li, C. S. Cheung, C. Riminesi, H. Liang. Investigation of laser induced damage to historical paint during Raman analysis. STAR conference 2022 The work has been awarded as best animated 3 min presentation.

A. Suzuki, Y. Li, C. S. Cheung, C. Riminesi, and H. Liang "Novel method to characterise laser-induced damage on paintings during Raman spectroscopy with VIS-NIR Hyperspectral Imaging" LACONA (Lasers in the Conservation of Artworks) XIII Conference 2022,Florence, 12-16 September. The work has been granted for Best Poster Award of LACONA XIII.

A. Suzuki, I. Osticioli, W. Oberhauser, S. Siano, C. Riminesi. 2D high lateral resolution XRPD mapping for the in-depth characterization of CW NIR laser irradiation to thermally induce the conversion of plattnerite into red lead pigment. LACONA (Lasers in the Conservation of Artworks) XIII Conference 2022. (oral presentation)

A. Suzuki, W. Oberhauser, I. Osticioli, C. Riminesi. Insight into thermally-induced reduction of Plattnerite into Red Lead pigment, 33rd edition of the European Crystallography Conference (ECM33), 23-27 August 2022, Versailles, France (poster)

A. Suzuki, Y. Li, Y. Gu, C.S. Cheung, C. Riminesi, and H. Liang "Investigation of laser-induced damage to historical paint during Raman analysis", Proc. SPIE 11784, Optics for Arts, Architecture, and Archaeology VIII. June 2021

Y. Li, **A. Suzuki**, S.C. Cheung,S. Kogou, H. Liang, Ground-based remote sensing depth-resolved multimodal material identification of wall paintings at 3-15 m. SPIE O3A conference, 22-25 June 2021.

Contribution in the deliverables of task 5.3 of IPERION HS : mitigation strategies for safe analysis of artwork, April 2024 coordinated by the task leader Mathieu Thoury.

Successful proposals for beamtime:

2021_BM08 at ESRF XAS Pb speciation
2022_ BM16 at ESRF
2023_PUMA beamline at SOLEIL for the X-ray radiation damage monitoring with operando VIS-NIR HSI.
2023_HRPD at ISIS facility for neutron diffraction of lead oxides

List of abbreviations

CH	Cultural Heritage
CW	Continuous Wave
EPR	Electronic Paramagnetic Resonance
EXAFS	Extended X-ray absorption Fine Structure
FOV	Field Of View
FTIR	Fourier-Transformed Infrared spectroscopy
FWHM	Full-Width-Half-Maximum
HSI	Hyperspectral imaging
LIBS	Laser-Induced Breakdown Spectroscopy
LIF	Laser-Induced Fluorescence
MOFs	Metal Organic Frameworks
NLM	Non-Linear Microscopy
OCT	Optical Coherence Tomography
SNR	Signal-to-Noise-Ratio
SR	Synchrotron Radiation
SWIR	Short Wave Infrared
VIS-NIR	Visible-Near Infrared
XANES	X-rays Absorption Near edge structure
XAS	X-ray Absorption Spectroscopy
XPS	X-ray Photoelectron Spectroscopy
XRF	X-Ray Fluorescence
XRPD	X-Ray Powder Diffraction

Table of Contents

1. Introduction

The introduction and advances in mobile non-invasive analytical techniques has been a major contribution to the widespread adoption of scientific analysis for the characterization of artists' materials and their possible degradation products, owing to the ease of application to historical cultural assets *in situ*, especially immovable heritage and fragile artworks [1,2]. At the same time, there is an increased interest in the use of synchrotron radiation (SR) [3], especially for SR X-ray techniques which provide invaluable information on heterogeneous artists' materials, thanks to low detection limits, extremely high lateral resolution and exceptional chemical sensitivity [4,5].

In the last decades, laser- and X-ray-based techniques have been used extensively and developed for a broad variety of methods for analysing and documenting artworks. They are used to study the molecular, structural and elemental composition of artists' materials, as well as enabling 3D reconstruction of surfaces, structural deformation and stratigraphic analysis, etc. Most of these techniques can be performed *in situ* and are considered non-invasive, which are analytical requirements that are becoming increasingly mandatory as the transport or sampling of cultural assets is often impossible and detrimental for their conservation. Moreover, lasers are extensively used for restoration purposes, as laser ablation has overcome important limitations of more traditional cleaning methods for the removal of undesired layers on artworks, nowadays representing one of the established methods in the toolbox of conservators. Some of the most relevant laser-based and X-ray-based techniques used in Heritage Science are discussed in Chapter 2.1 and Chapter 2.2 respectively.

During the early periods of adoption of mobile and "fixed" techniques the measurements were performed as point analysis, however, this raised questions concerning the representativeness of single data points for the analysis of extremely heterogeneous materials, like paintings (organic/inorganic pigments and dyes + organic/inorganic binder + extenders/additives). Therefore, an increasing research effort has been put into the development and widespread use of imaging modalities [6–8].

Moreover, a consensus has been reached that more than just a single technique needs to be employed to obtain all the information required to answer heritage research questions. Thus, more recently, research effort is focusing on the implementation of multi-technique hybrid systems for comprehensive characterization of materials in a more effective and faster way, to gain insights on our Cultural Heritage in a non-invasive way [9,10].

With many mobile non-invasive analytical techniques now being well-established in the Cultural Heritage field, a transition towards democratisation of these scientific tools can be seen, owing to more portable, compact, user-friendly devices and, most importantly, accessible and affordable instruments. This way, even museums, heritage sites and institutions with less resources can expand their knowledge about their collections, to enhance the understanding of our past and its materiality, improve preservation strategies and guarantee the passage to the next generations.

The current trend at synchrotron facilities is the use of increasingly more brilliant light sources and miniaturized beams to rapidly obtain unprecedent high resolution information at the micro and nano scale to gain insights at molecular and atomic level. Although this development paves the way for new research and discoveries about artworks, SR applications in the Cultural Heritage field can be hindered by the higher damage probability caused by the brilliance upgrade [11].

Many technological improvements in Heritage Science make use of intense radiations and the risk associated with such radiation is insufficiently known [11,12]. With such development in advanced analytical techniques, it is necessary to consider and make an effort to assess the safety of analysis and interventions on artworks, as damage is intrinsic in every type of analysis and treatment. Whilst working with unique and precious artists' materials, it is paramount to demonstrate the advantages of analytical technique, as well as being aware of possible associated risks and how to mitigate them. Therefore, research effort is needed to better understand the radiation-matter interaction, identify the critical parameters and develop monitoring methods to better design strategies to reduce the risk associated with the use of intense radiation. A review

of the current understanding of laser and X-ray-damage on paintings is reported in Chapter 2, showing a limited and fragmentary literature. Still little is known regarding the characteristics and reversibility of damage induced on paintings by lasers and X-rays and the methods to evaluate and detect damage are restricted to few cases [12]. The scarcity of relevant literature shows how crucial is the development of such research for the safe analysis of artworks, especially for the aforementioned development of high intensity miniaturized beams and mapping modalities and the widespread use of these techniques, also by non-expert users.

Any alteration of artworks must be minimized as much as possible as the integrity and stability of culturally significant artworks must be preserved and are strict requirements governed by conservation ethics. The samples collected from artworks also need to be preserved to enable future analysis, as they represent invaluable sources of information for scientists, conservators, archaeologists, art historians and curators. Moreover, knowledge about radiation damage and detection strategies are important to avoid misinterpretation of the data collected.

Radiation damage denotes any permanent change in the characteristics of the surface or bulk of a specimen that can be observed by an inspection technique [13] and that can modify the physical, chemical, mechanical, optical functional response of the materials. It strictly depends both on the material properties and the radiation characteristics, and to some extent also on environmental conditions.

The most common inspection technique used to observe radiation damages is visual examination, but some damages are not visible at plain sight [12]. Another common strategy is the control of possible signal modification during consecutive acquisitions in the same area (e.g. changes in the Raman spectra itself or modification of the diffraction pattern with prolonged X-ray exposure), however, at times, monitoring with the primary beam itself is not enough to detect some damages [14–16]. Therefore, independent and more sensitive methods are necessary to comprehensively capture any damage.

The primary aim of this research was to contribute to the development of safe operative protocols in Heritage Science when using intense radiations for analysis and treatment

of painting materials. To do so, an online monitoring method based on time and spatially resolved VIS-NIR reflectance spectroscopy using hyperspectral imaging was developed (Chapter 3.1) [17]. The method was applied in combination with thermal imaging for *in situ* monitoring of possible laser-induced damage during Raman Spectroscopy measurements on painting mock-ups using CW lasers, following the damage evolution from just after laser irradiation (Chapter 4).

The time and spatially resolved reflectance monitoring method provides a direct detection of radiation damage. To better understand the type of damage and mechanisms involved in such damage (whether physical or chemical), further monitoring and complementary analytical methods were used. These methods enabled ascertaining the nature of the damage and identify correlations of specific reflectance spectral changes with the type of damage (Chapter 3.2).

To explore possible applications of the method to other types of radiation, the reflectance monitoring method was adapted for an *operando* set-up at a synchrotron beamline (thanks to a successful proposal at PUMA beamline at SOLEIL synchrotron) to follow the possible occurrence of damage during an X-ray absorption spectroscopy experiment on painting mock-ups. Early-warning signs of damage were identified, showing that the real-time damage detection represents the most effective way to prevent damage (Chapter 5).

A deeper understanding of radiation damage mechanisms is a key factor for preventing damage. Moreover, studying specific radiation-matter interactions may pave the way to new applications. In this context, the possible use of continuous wave (CW) laser irradiation was explored for the possible restoration of darkened wall paintings originally containing the pigment red lead (Chapter 6). The focus of the work was the in-depth characterization of the laser-induced products from macro to micro scale, making use of spectral imaging techniques, point analysis spectroscopic measurements and micro mapping diffraction modality with synchrotron radiation. The combination of these techniques enabled studying the mechanism behind the laser reconversion of darkened red lead on mock-ups and contributed to the improvements in efficiency and safety of such laser treatment for the restoration of wall paintings (Chapter 3.2).

2. Radiation damage of artworks: state of the art, current monitoring methods and mitigation strategies

With the current use and development of increasingly brilliant light sources to obtain extremely high-resolution information from artists' materials, it is important and not possible to further develop such advanced technologies without simultaneously developing systematic assessment of the possible risks associated with those analytical methods.

This chapter aims at collecting and discussing current knowledge regarding the possible damage on artworks induced by both, optical lasers (section 2.1) and X-rays (section 2.2). The discussion focuses on the paintings' materials, and the available methods developed to monitor and mitigate radiation damage when performing laser-based spectroscopic analysis (such as Raman Spectroscopy), laser cleaning and X-ray spectrometry and diffraction. To reflect on the possible development of mitigation strategies at the same time, literature from other fields in which this topic is well studied is also discussed, with particular focus on laser damage of optical materials, laser processing and macromolecular crystallography. This review provides a starting point to open the discussion regarding most appropriate protocols for best practice in Heritage Science.

2.1 Laser-induced damage

An extensive review concerning radiation damage on artworks [12] has brought into attention the importance of developing a common vocabulary concerning the description of damages and the need to study the types and mechanisms of radiation damage to be able to better develop specific mitigation strategies. However, the main focus of the review paper, and even more the recent review update [11], is the evaluation of damages induced by intense ionizing radiations such as proton beams and X-rays, especially the ones from synchrotron sources.

Another example that demonstrates the common necessity to guarantee safe laser-based analysis is the development of a specific sub-task dedicated to radiation damage in the framework of the pan-European projects IPERION CH and IPERION HS [18].

Despite the rising awareness of the possible risks associated with the use of optical lasers, an extensive review on laser-induced damage monitoring methods and mitigation strategies for the analysis and treatment of artworks is yet to be compiled. This is mainly due to lack of literature in which authors also report the risks that can occur when not adjusting the laser parameters properly or defining applications where a specific type of laser cannot be used safely on a certain material. This lack of information in existing literature during the establishment period of analytical techniques is understandable, as it would have promoted the spread of over-alarming messages.

Damages may manifest in different ways and to varying extents, some of which are undetectable by visual inspection. The damage can be related to physical modification at the surface, interface of stratified materials and in the bulk; reversible or permanent molecular structural changes can occur, and they can appear in short term, or it can manifest in a long-time scale. Overall, it can impact on the optical, electrical or magnetic functional response of materials.

The specific meaning of non-invasiveness or the micro-destructive nature of laser-based techniques has to be called into question and revised, to make sure that the principle of conservation is strictly followed. This means that the historical materials must be preserved in its integrity in all aspects, preventing any appearance of damage induced by any investigation or conservation treatment. For this reason, improvement in the assessment of the type and extent of damage is needed. The following paragraph briefly describes the main laser-based techniques in the cultural heritage field.

Intense coherent monochromatic optical radiations are extensively and increasingly used in the field of cultural heritage. Many instruments that make use of laser radiation are now well-established tools in the suite of analytical techniques for characterisation of artists' materials and successful conservation treatments [9,19–22]. A broad variety of lasers are used depending on: i) the wavelength (λ), from UV, VIS to IR spectral range;

ii) the delivering regime, in a continuous wave (CW) or with different pulse width (τ) from ps to μs, with repetition rates from Hz to kHz and with eventual scanning system; iii) beam shape, mainly gaussian or top hat; iv) the laser beam size, from μm to mm spot diameter; v) laser power from μW to kW. The following paragraph briefly describe the main laser-based techniques in the cultural heritage field.

Raman Spectroscopy is a well-established laser-based technique that provides the molecular composition of the investigated material (for details see chapter 3.2.1). The commonly used lasers for Raman are continuous wave (CW) lasers with wavelengths ranging from visible (VIS) to near infrared (NIR) - both, in bench top systems, such as micro-Raman and portable devices [23] with spot sizes ranging from tens to hundreds of μm [22], up to remote Raman systems with spot sizes of a mm [24]. Recently, time-gated pulsed Raman spectroscopy has also been explored to obtain a versatile *in situ* instrument [9,25] and could be further developed using SPAD sensors [26]. Another recent development in heritage science field is the Spatially Offset Raman Spectroscopy (SORS) [27–29] that enable identification of the composition from sub-surface layers in turbid media. Raman measurements are usually carried out as point analysis, but recent interest falls in macro-Raman mapping *in situ* [30,31].

Optical Coherence Tomography (OCT) is an interferometry technique that provides virtual cross sections of transparent and semi-transparent layers (for details see chapter 3.2.3). It makes use of CW lasers mainly from NIR to shortwave infrared (SWIR) in a scanning modality. The technique has a similar intensity compared to micro-Raman spectroscopy systems (of the order of 10^3 W/cm^2), but at least 5 orders of magnitude lower in fluence, due to the fast scan rate (see Table 2 of Liang et al. 2017 where the intensities and fluences of the mentioned laser-based techniques are compared [32].

Laser-induced fluorescence (LIF) is a diagnostic technique based on spontaneous emission of fluorescence photons during the de-excitation process after absorption of incident photons by a molecule. LIF provides molecular information of different types of materials due to delocalized electrons in specific bonds and can be used to identify, for example, organic binders, stones and pigments. Although in paintings the discrimination

of different materials contribution in the mixture may be challenging [21]. The laser wavelength, the delivering regime and fluence used for LIF is highly dependent of the material to analyse, but the most common are UV lasers in ns or µs pulses. Typical fluence values reported for a 248 nm laser of 25 ns are 1-1.5 mJ/cm^2.[21]

Non-linear optical techniques are a relatively recent family of techniques used in the cultural heritage field. These techniques are based on non-linear optical processes observable when using ultra-fast pulsed lasers in the fs and ps regime, where molecules interact simultaneously with two or more photons within the same quantum event. Non-Linear Microscopy (NLM) for second and third harmonic generation and multiphoton excitation fluorescence is used primarily to study the thickness, composition and distribution of materials [33–35]. NLM typically is performed with NIR lasers and the average intensity can reach 3 orders of magnitude higher intensity compared with micro-Raman and 3 orders of magnitude less in fluence.[32]

Another emerging modality is pump-probe microscopy [36] that enables to enhance contrast for the imaging of artists' materials when non-fluorescent materials are imaged (limited paintings materials are fluorescent). Pump-probe experiments make use of 2 synchronized laser source in the fs or ps regime with a specific wavelength selection and time-delay to detect other non-linear effects, such as two-photon absorption (TPA, i.e. electronic transition that occur due to simultaneous absorption of two photons), excited-state absorption (ESA, i.e. the first pulse excites the molecule to an intermediate state and this can increase the absorptivity of the second pulse, exciting to a higher energy state), ground-state depletion (GSD, i.e. the excitation induced by the first pulse reduces the population in the ground state, therefore the second pulse will find fewer molecules to excite from the ground state), and Stimulated Emission (SE, i.e. the first pulse excites to higher energy levels and the second pulse stimulate the emission of a photon). The detections of these transient absorption processes enable to distinguish even between two materials with very similar linear absorption features [37]. The same principles are used in the spectroscopic modality often called Transient Absorption (TA) spectroscopy, that is gaining interest for the characterization of the electronic band structure of pigments [38,39]. The advantage of TA over fluorescence is due to the higher specificity of the detected signal compared to the broad fluorescence features

and the possibility to investigate non-emitting electronic transitions. What is measured is the transmitted signal from the probe with and without the pump signal at different time delay between the pump and the probe pulses.

Laser Induced Breakdown Spectroscopy (LIBS) is a technique that exploits the optical emission of the plasma plume generated by an intense pulsed laser to characterize the elemental composition of the ablated material and has been used for several application in the field of CH [40]. The goal is to confine the ablation to the single irradiated spot without affecting the surrounding area. This technique makes use of intense pulsed lasers, generally in the ns regime often using a Q-Switched Nd:YAG laser 1064 nm or its second and third harmonic. The spot sizes can vary from few tens of microns to a millimetre, the fluence range is generally 1–50 J/cm^2 and the intensity range is ca. 0.1–5 × 10^9 W/cm^2 [21].

Laser ablation is extensively used in restoration as a tool to remove undesired layers from artworks. The objective of laser cleaning is the selective removal of undesired layers without compromising the integrity of the substrate. Laser ablation is performed with intense pulsed lasers from ns to μs [41–43] with wavelengths from UV to SWIR and both in a single point or scanning mode [44,45].

The majority of these laser-based techniques used for the study of historical materials are considered non-invasive, while LIBS is considered micro-destructive. Ideally, the laser radiation used should be low enough in intensity and/or fluence to not induce any damage. In reality, signal-to-noise (SNR) considerations may require higher intensity, longer exposure, accumulation over several pulses, etc. Therefore, damage to the material under investigation induced by photochemical or thermal effects may occur [32,46,47]. An even higher risk of side effects is associated with laser cleaning, as the self-limited interaction solely with the layer to be removed is rare [48].

The next sections aim at reviewing studies related to laser damage in heritage science field, as well as discussing relevant literature from other fields, (laser damage of optics materials and laser processing), and are divided in three categories: i) identification of damage thresholds to determine safe limits; ii) improvements in understanding some

degradation mechanisms thanks to specific analytical methods; iii) recent strategies developed for the on-line monitoring of laser-induced damage. To conclude, available mitigation strategies and the possible future developments are briefly discussed.

2.1.1 Definition of safe-damage limits

One of the main parameters that influence the occurrence of damage when using CW laser sources is the laser intensity, expressed in W/cm^2. When the laser intensity is gradually increased, we can observe on the material the transition from no visible damage to some side-effects of laser-matter interaction, such as increase in temperature and consequent possible expansion and contraction of material and strain. This type of damage can temporarily or permanently change the optical properties of the material, such as scattering, absorption coefficients and refractive index. As the laser intensity is further increased, irreversible changes may occur in the materials, such as colour changes, melting, swelling, combustion, vaporization, phase transition, pitting and cracking.

The laser-induced damage threshold (LIDT) is defined as the level of radiation that initiates any undesired alteration and/or degradation of the material. The concept of LIDT is extremely widespread in the field of optics materials [49] and is used to define the lifetime of optical components based on damage probability [50], and a dedicated ISO 21254:2011 has been developed to standardize the LIDT test procedures and the detection methods. In heritage science, LIDT is often used in laser cleaning studies and is expressed in terms of laser fluence ($mJ/\mu m^2$). Ablation threshold is also identified to set the safe fluence range to operate an effective cleaning intervention on a specific material [20].

The damage detection is often based on visual observation or by optical microscope evaluation. In laser-based techniques, such as Raman spectroscopy, the detection is also based on the changes of the Raman spectra collected consecutively on a single spot. This way, LIDT of micro-Raman measurements, expressed in laser power, has been defined for lead-based pigments [51] and Prussian blue [52]. It should be considered that, depending on pulse width (including a CW regime) and spot size, LIDT can be more

significantly expressed by fluence (energy density, J/cm^2) or intensity (power density W/cm^2) [53].

The identification of tabulated LIDT values for each type of material are well suited for homogeneous and well-defined multi-composite materials, such as coatings of optical components, although even for this type of material the micro-scale difference may modify LIDT. With the extreme heterogeneity of artworks, the identification of safe limits for each material does not provide a successful strategy to prevent damage. Pre-defined LIDT values are rarely directly applicable to a specific case and the comparison with literature is complicated even more by the sometimes-incomplete information regarding the laser source (such as spot size, beam profile, exposure time) and the characteristics of the mock-ups used (such as pigment/binder ratio and thickness). Bearing in mind the extremely high number of variables that can significantly modify LIDT, in the field of heritage science, LIDT should not be used to indicate the safe limits, or it should always be made clear that those values represent only a very general indication of the possible safety thresholds.

Instead, LIDT is useful to better understand the influence of laser and material parameters in the occurrence and extent of damage. Changes in LIDT enabled to objectively study for example the laser wavelength [54–56] and the pulsed duration [57,58] effects, as well as the effect of grain size [59], pigment agglomeration, binding medium, and pigment concentration [60], and the presence of impurities in different pigment batches [61].

2.1.2 The pre/post assessment strategies to understand laser-induced damage mechanisms

There are several types of mechanisms which generate laser-induced damage that may occur simultaneously, or, in some circumstances, one type of damage might prevail. Between the most important mechanisms when dealing with paintings' materials are thermal processes, arising from energy absorption of the incoming laser in the material, and is generally predominant with CW lasers, long pulse widths and high frequency repetition rates. Photochemical processes are also relevant due to possible phase

transition of pigments induced at specific wavelength, such as realgar to pararealgar [62], and the interaction of UV lasers with polymers of the binding media and varnishes [63].

Pigment discoloration has often been observed upon laser irradiation [48,64–67]. The origin and detection of the pigment alteration products represents a well-known challenge, being highly superficial and resulting from a complex set of different phenomena. Many methods have been used to identify the mechanisms, and several analytical techniques were explored to characterize the alteration products of specific colour changes.

Early studies of pulsed lasers effects on pigments attempted to understand the mechanisms of discoloration by comparison with purely heating effects [64,66]. X-ray photoelectron spectroscopy (XPS) was proven useful in the characterization of discolouration effects on some pigment paint mock-ups [68]. In the case of the reversible darkening of lead white induced by low-intensity pulsed lasers, XPS was found not exhaustive to characterize the black deposit. The atomization effect of the ablation induced on lead white produces unstable metallic lead particles [69]. This metallic lead, also produced by high intensity pulses for LIBS [70], very quickly reacts with oxygen in the atmosphere to produce lead monoxide (massicot) and produces a brown yellowish near crater discoloration around the ablated spot. Some ochres were shown to be highly susceptible to laser irradiation. Raman spectroscopy identified dehydration and changes in the iron oxidation state of some iron hydroxides/oxides [71,72]. Photothermal damage has been identified to be the main cause of alteration of iron oxides when irradiated with CW laser used for Raman spectroscopy. A demonstration of such a purely thermal mechanism was proposed by monitoring and comparing the Raman bandwidth change of specific peaks of maghemite during a heating treatment and by gradually increasing laser power during irradiation tests, obtaining a linear correlation between temperature and the Raman spectral change [73]. Prussian blue laser-induced degradation was proven to be a thermally driven effect and its alteration product upon CW irradiation was identified as hematite [14]. Other reduction reactions of pigments were identified with Raman spectroscopy and XRPD for the transformation of plattnerite into red lead with CW lasers [74] and with XPS analysis on chrome yellow discoloration with pulsed lasers [58]. The by-product of vermilion laser-induced blackening has been

highly debated as to whether metallic mercury or the black meta-cinnabar is formed [58,68,75–78]. The debate arises from the complex reactivity of the pigment, the difficult differentiations of the by-products with the analytical techniques mentioned up to now (both due to peak overlaps and lack of spatial resolution, such as for bench-top XRPD systems), and the analytical difficulty in detecting metallic mercury. An emerging technique to study pigments and their degradation products is pump probe microscopy and it was used to assess the possible laser-induced discoloration product of vermilion [79], suggesting evidence for the formation of meta-cinnabar via an unidentified intermediate.

Due to the extremely different phenomena behind colour changes, there is clearly not a specific technique that can solve the problem; therefore, a suite of complementary methods is needed. Sometimes a similar darkening may be the result of different by-products when induced by different irradiation conditions. Therefore, it is impossible to define systematic damage detection protocols, and other analytical techniques should be further explored.

2.1.3 Online Monitoring methods

While irradiating a surface of interest with a laser, the online monitoring of signals, such as acoustic wave, plasma optical emission and thermal radiation, can be helpful for detecting possible damage. If prediction markers or early warning signs of damage are identified, the online monitoring methods represent powerful tools to mitigate the risk of damage.

The majority of the online monitoring methods developed up to now are provided by laser cleaning research studies, both for industrial applications [80] and for restoration [81], probably due to the micro-destructive nature of the ablation and the extreme control required for an effective process.

In this context, LIBS has been sporadically used for monitoring during laser cleaning of artworks, mainly on metals and stones, with the objective to identify marker elements of the substrate in the spectra, which indicate when to stop the laser treatment [[82–

84]. Such LIBS application has not been extensively explored in the cultural heritage field probably because of the complex analysis of emission spectra. Moreover, this technique does not provide information on the state of conservation of the surface. In laser processing field, LIBS has been extensively studied with large effort in data processing improvements, such as the use of convolution neural networks in cases where the elemental composition between the layer to remove and the material to preserve are similar [85], which is often the case in artworks.

Photoacoustic is another method studied in laser processing for at least 3 decades [86]. It is based on the monitoring of the acoustic wave generated by the pressure wave induced by instantaneous thermal expansion of the surface material that absorbed the laser pulse and is particularly strong in the ns regime. Some first attempts to apply such technique were carried out to monitor laser cleaning of stones and metals, such as [87,88], demonstrating a correlation between acoustic wave amplitude and the thickness of the layer to remove. More recently, a statistical method based on amplitude measurements to define the critical onsets for effective or damaging cleaning was developed [89], paving the way for a more systematic use of such technology, as the monitoring of varnish removal [90]. Compared to the LIBS monitoring method, acoustic signal monitoring works on a wider laser fluence range and can be applied also when a laser scanning cleaning procedure is used [91]. However, the signal acquired is not material-specific and clear-cut changes in the acoustic wave response between the layer to remove and the substrate are needed, therefore the interpretation may be challenging. For this reason, a combined photoacoustic and optical monitoring system has been developed and used to assist the removal of black crusts from marble [92].

LIF has also been used to monitor the ablative photo-oxidative process of polymer removal by doping a varnish layer with a photoluminescent compound of known emission [93], which can be a useful method to study the removal mechanisms but not applicable as a monitoring method on real objects. LIF has also been used to monitor the composition of the plume produced during ablation with UV laser. This monitoring is done by exiting the plume with a second laser with an appropriate time-delay [94]. Alternatively, the evaluation of the cleaning progress has been done quantifying the

fluorescence emission signal loss in ablated areas compared to the non-irradiated areas after each pulse [95]. The technique can be useful to quantify some types of cleaning but is limited to fluorescent materials.

Another investigated monitoring method is OCT, especially for its application for the online monitoring of laser varnish cleaning evolution with Spectral Domain OCT [96–98]. The method results useful to quantify the thickness of the material removed, and at the same time gain information on the morphological state of conservation of the subsurface (i.e. the paint layer to preserve). As for other cleaning cases where highly scattering layers need to be removed, this technique would only enable to evaluate the thinning. Moreover, the imaging speed of Spectral Domain OCT, normally in the order of μs, is not suitable for real-time detection of fast ablative events that are generally in the ns regime.

Evaluation of laser cleaning with VIS-NIR spectral imaging was also explored [99], by following the changes in reflectance at a specific wavelength range representative of the layer to remove after each step of cleaning. As for all the aforementioned online monitoring techniques (except OCT), the method can be applied when clear signal differences exist between the undesired layer and the surface to preserve.

With laser-based techniques, apart from visual and microscopic observation, the most widespread radiation damage monitoring method, is the evaluation of possible modifications of the signal recorded upon repetitive measurements in the same spot, as the case of NLM [100] and Raman spectroscopy [51,52,101]. The evaluation of damage through changes in the Raman spectra is based on the detection of peaks shifts, broadening and intensity drop due to enhanced anharmonic components related to bond expansion with heat [102], or the formation of new peaks [103]. However, sometimes this method fails to detect some damages in pigments [14,104]. Therefore, alternative methods are needed to comprehensively detect any damage.

Only very sporadic attempts in developing complementary methods have been investigated and are related to the monitoring of surface temperature induced by a CW laser during a Raman spectroscopy measurement.

One case is the use of Raman thermometry for the laser-induced darkening of azurite [59]. The method consists of collecting both the Stokes and anti-Stokes Raman spectra, and their ratio is directly related to surface temperature. Unfortunately, this method is challenging to apply (for details see chapter 3.2.1), not suitable for a real-time modality and expensive because of the need for notch filters.

Another important contribution is the implementation of a thermoelectric sensor in a portable Raman system for simultaneous surface thermal monitoring of the irradiated area and possible modulation of the laser power to maintain the temperature below a certain critical value [105]. Thermally-controlled Raman spectroscopy is reported to be useful, not only to safely perform measurements, but also to enhance signal collection efficiency, as power modulation enables reducing the background induced by heat for IR lasers [106]. Such device was further implemented with two thermopile sensors to perform simultaneous adjustment of emissivity of the material case by case [107].

2.1.4 Mitigation strategies

The fundamental base of mitigation strategy is the principle of “as little radiation as possible”, therefore any test should start with the lowest laser intensity and/or fluence and assess the safety step by step. Besides that, based on the above review of current studies regarding laser damage during analysis and treatment of painting materials, it is clear that we are still far from having well developed mitigation strategies to define best practices.

The only clear mitigation strategies actively implemented to prevent damage are the efforts dedicated to Raman spectroscopy instruments. A helium jet has been incorporated in a Raman system to actively prevent thermal damages while performing the measurement [108]. For some pigment irradiation tests the helium jet prevented the occurrence of visible damage by eye but in other cases it only reduced the extent, and the helium flux required is quite high (up to 9 l/min). Another important achievement is the aforementioned temperature-controlled Raman device that enable the laser power tunability based on pre-set thermal threshold.

And, although indirect, the very recent development of a portable prototype micro-SORS that makes use of an optical fibre bundle [109], enabling the simultaneous collection of micro-SORS sequences in a single shot, considerably reducing the duration of irradiation.

In light of the many laser-based techniques now well established in the field, there is rising interest and obvious need to study laser damage to investigate how to prevent it in an era of increasingly brilliant light sources especially in the pulsed regime. More effort should be dedicated in the implementations of damage control protocols for laser-based techniques to guarantee the safety operation.

Studies providing sound, clear and detailed evidence need to be developed to facilitate the literature comparison, and to avoid misleading or over-alarming information on potential laser damage to guarantee the future development of advanced laser-based methodologies for the conservation and study of cultural assets.

2.2 X-ray induced damage

In the last decades, X-ray radiation is increasingly used in the cultural heritage field for atomic, molecular and structural analyses of historical materials, owing primarily to the non-destructive nature of these techniques. The most widespread methods are X-ray fluorescence (XRF) and absorption (XAS) spectroscopy and powder diffraction (XRPD). Computed Tomography CT is also often used but is not covered here. These techniques can be performed with X-ray tubes in a laboratory or in the field, or they can be undertaken with synchrotron radiation (SR) in large-scale facilities.

XRF is a well-established elemental analysis in heritage science and commonly used for identification of the elemental composition of paintings' materials. Its extremely broad application in the field is demonstrated by the very large and still rising literature [110]. The widespread use of XRF is due to some important technological developments: the first historical turning point was the development of portable and hand-held XRF instruments that have revolutionized archaeological science and diagnostic campaigns

in situ. Secondly, the development of macro XRF (MA-XRF) systems [111] enabled the acquisition of elemental maps of whole paintings or objects. MA-XRF mapping has also contributed significantly to the democratization of the technique, delivering scientific outcomes in a way easily understandable also by non-expert users. SR XRF is not as much widespread in the field, mainly because heritage samples can be effectively analysed with SEM-EDS with high lateral resolution and very similar elemental quality data, with no substantial benefits to compete and wait for beamtime.

X-ray Absorption Spectroscopy (XAS), namely X-ray Absorption Near Edge Structure (XANES) and Extended X-ray Absorption Fine Structure (EXAFS) provide information on the electronic structure and short-range arrangement of materials respectively (for details see section 3.2.5). Until very recently it was mainly performed at synchrotron facilities due to extremely inefficient data collection time, poor energy resolution and no sensitivity to trace elements of laboratory set-ups. Recent advances in X-ray optics and spectrometer technology re-focussed attention to the development of bench-top systems [112]. Inverse Compton scattering effect is also the base of the most recent development of extremely brilliant X-ray laboratory sources similar to a second-generation synchrotron and a dedicated end station for cultural heritage material analysis is under construction [113]. The brilliance of synchrotron radiation has been extensively improved over the years, with the most recent 4^{th} generation synchrotrons having approximately 14 times higher brilliance than conventional X-ray tubes (Fig. 2.1) [114]. One of the main benefits of such improvement is the efficiency in data collection that enables the evolution of mapping modalities for techniques otherwise too time-intensive, such as XANES.

X-ray powder diffraction (XRPD) is a unique technique that provides information on long-range order and symmetry of solid-state materials (see details in chapter 3.2.4). It is extensively used both in conservation science and archaeometry mainly for qualitative phase identification, quantitative analysis and structural and microstructural analysis [115]. In the fields of heritage science, XRPD has historically been performed in a laboratory setting for many decades. In the last 10 years, an extensive effort for the development of portable devices has enabled the identification of crystalline structure

of paintings' materials *in situ*. At the same time, synchrotron facilities have seen a significant increase of users from the cultural heritage field for SR-XRPD analysis, with access even more facilitated by a Block Allocation Group (joint access proposal shared between many institutions) dedicated to the analysis of historical materials [116]. In both, portable devices and SR-XRPD, recent research efforts are focused on developing mapping modalities [117] with unprecedent access to crystalline information of highly superficial and heterogeneous alteration products and insights into ancient manufacturing technologies. However, the quantification and structural analysis of XRPD maps remains challenging.

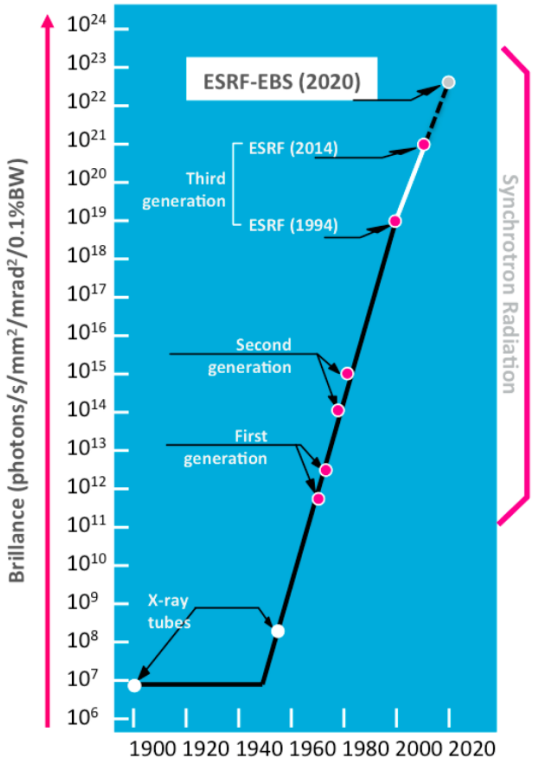

Fig. 2. 1 An example of SR brilliance development over the years from the European Synchrotron Radiation Facility ESRF of Grenoble.

Within the framework of potential ionizing radiation damage, a project is being developed since 2017 at the Netherlands Institute for Conservation, Art and Science, which demonstrates the importance of radiation damage in conservation communities. The project, called IRRADIATION PASSPORT FOR ART [118], aims to create an open platform where records of irradiation history of single artefacts are stored. The irradiation history of a material (an entire object or a sample of it) is important, as

exposure to intense ionizing radiation can cause a cumulative damage effect, which means that past exposures may have altered or changed the sensitivity of the object or sample. In addition to the detrimental loss of irreplaceable cultural heritage materials, such damage can cause alteration and misinterpretation of analytical results. For example, the erroneous optical stimulated luminescence dating of archaeological objects exposed to just low brilliance radiation from X-ray tubes [119], or the alteration/destruction of genetic information for the study of ancient DNA [120].

To better understand the possible future developments of mitigation strategies, the next sections aim at reviewing literature concerning X-ray irradiation of painting materials. A more general review of radiation damage on cultural heritage materials is reported in [12] for metals, glass, fossils, manuscripts etc. In order to reflect on the possible transfer of knowledge and experience, inputs from macromolecular crystallography are reported. Research on radiation damage is also performed in other fields (e.g. environmental science) but the topic is more mature in macromolecular crystallography and stronger similarities are found with cultural heritage field, as for the energy range commonly used (~6-20 keV) and for the high susceptibility to X-ray radiation of similar materials, like proteins and metal-organic-frameworks (MOFs, for example Prussian blue).
The sections are divided as follow: i) the current knowledge regarding the mechanisms of X-ray induced damage on paintings materials and the long-term damage evolution; ii) the online monitoring methods currently available; and iii) the possible mitigation strategies based on data collection optimization.

2.2.1 The mechanisms of X-ray radiation damage

The higher the brilliance of an X-ray source, the higher the probability to cause radiation damage. Not all X-ray damages are necessarily visible by naked eye and some side-effects may appear long after X-ray exposure. One example is the delayed yellowing effect due to cellulose depolymerisation which appears several weeks or months after X-ray exposure of different paper samples [121].

When a material is exposed to a high X-ray incident flux, the absorbed dose generates the emission of a significant amount of photoelectrons, which can produce reduction of the pigments, like in the case of Prussian blue [15] and chrome yellow [122]. This type of mechanism can be extremely challenging for *operando* photochemistry experiments, such as time-resolved XANES [123], as the UV/VIS photo-induced reaction can be considerably enhanced by the highly energetic contribution from the X-ray beam. X-ray induced amorphization has also been reported, like the case of lead white pigment exposed for a prolonged time to a micro X-ray beam at 12.9 keV and detected by monitoring changes in the diffraction pattern of consecutive measurements [116]. In other cases, no changes in the oxidation state are reported, but the formation of crystal defects, for example in the case of Egyptian green where oxygen-holes and aluminium centres were detected with Electron Paramagnetic resonance (EPR) [124]. The emitted photoelectrons can also recombine with the molecules producing radicals, leading to radical reactions that can change the degree of polymerisation of organic materials and create reactive ion species.

X-ray damage in macromolecular crystallography is a very well-known issue and significant resources have been invested to understand and minimise X-ray damage [125]. Specific terminology has been developed to describe the damage phenomena, distinguishing global radiation damage, when disorder is produced due to long-range breakdown of a crystal structure (visible from changes in the XRD patterns), from local damage that occurs when particular ion or bond is damaged, such as disulfide bond breaking in proteins or the reduction of occupancy of metal atoms in metal-organic frameworks (MOFs) [126].

In contrast, X-ray radiation damage on artworks is clearly under-reported based on the scarce literature [11]. Different analytical methods are necessary to probe the vast variety of alteration products that can be produced upon X-ray irradiation. Long-term monitoring is fairly unexplored, with only one study that reports a 3-year assessment of the polymerization state of cellulosic material after X-ray exposure [121]. This type of study is an essential, and somewhat unique, requirement for the heritage science field. The resource investments required for long-term studies, however, represents a limitation of its development.

2.2.2 The online monitoring methods

The very common online monitoring method consists in checking any possible changes in the signal collected upon repeated measurement on the same spot. However, some damages are not detectable by signal changes obtained from the primary beam, like the case of XANES analysis of ultramarine: at the Al K-edge no XANES changes were detected, although microscopic assessment suggested a subtle colour fading [16], while XANES at the S K-edge enabled to assess the transformation of the sulphur speciation induced by X-rays [127,128]. Another example is the damage to zinc white at the Zn K-edge, that is not detectable by any XANES changes but detectable by changes in the photoluminescence signal [15]. Another example is the assessment of damage from modifications of diffraction patterns during the analysis of metal organic framework MOFs, where insidious local damages, related to induced disorder of heavy atoms sites in MOFs, and not clearly visible by eye, can occur well before sufficient anomalous signal is measured during diffraction studies (damage assessed with XANES or UV-VIS spectroscopy) [129]. Therefore, independent methods need to be developed to comprehensively detect damage during X-ray analysis.

In structural biology, online monitoring methods are increasingly explored for at least 2 decades. The main method makes use of UV-VIS spectrophotometers to capture protein alterations in real time and are now available on many macromolecular diffraction beamlines [130,131]. X-ray irradiation of proteins often induced formation of disulfide radical anions and trapped electrons [132]. By monitoring the changes in the UV-VIS absorption spectra, researchers have been able to identify specific features (absorption peaks) around 400 nm and 600 nm, attributable to disulfide radical anions and trapped electrons respectively [130,133]. X-ray-excited optical luminescence (XEOL) has also been explored to monitor damage, but in some works the decay rate of XEOL do not correlate to decay in diffraction signal [134], raising doubts on its reliability as a damage metric method. But photoluminescence is more sensitive to local changes (i.e. around a specific atom and the neighbouring atoms) that do not necessarily correlate to modifications to the long-range (i.e. repetitive ordered arrangement of atoms within a

crystal). In fact, XEOL is becoming an interesting monitoring method to assess the X-ray damage to fossil teeth during XAS experiments [135]. Both methods are extremely interesting for the field of heritage science and more work in this direction is expected in the next future.

Another recent research effort focused on the development of real-time radiation damage monitoring for the analysis of paintings, combining fast Energy dispersive XAS (ED-XAS) spectroscopy and FT-IR analysis in transmission [136]. With this method, the authors were able to assess the possible damage to the binding media and the pigment of a paint mock-up at the same time.

The scarcity of relevant literature shows the urgency of developing complementary online monitoring methods for the safe analysis of artworks, as real-time damage detection represents the most effective way to prevent damage if reliable early warning signs of damage are identified.

2.2.3 The data collection optimization to minimize damage risk

In order to reduce the amount of damage accumulated upon X-ray radiation, several strategies for efficient and safe data collection can be applied once the effect of the main parameters is understood (flux, fluence, flux density, absorbed dose, dose rate, photon energy and spot size). Another interesting mitigation strategy to reduce radiation dosage is the determination of the minimum dose required on a specific material to still obtain a significant analytical result. Lastly, environment conditioning during sample irradiation is also useful to minimize damage. Some of these mitigation strategies are described hereafter.

2.2.3.1 The absorbed dose and the dose-rate

X-ray damage is considered a cumulative effect that depends on the absorbed photons rather than the incident photon flux (number of photons per seconds ph/s), and it is

strongly dependent on the material. Fluence is the amount of incident photons per unit area (ph/mm^2) and the flux density is the rate of incident photons per unit area (ph/mm^{2}s). These 2 parameters can vary considerably between beamlines due to the broad availability of fluxes (from 10^8 to 10^{14} ph/s) and spot sizes (from nm to cm). The absorbed dose is the energy absorbed by a target per unit of mass, called Gray Gy (J/Kg). A heavy atom sample will have more energy deposited on the surface and exponentially decay within the volume, a light element sample would absorb energy within a larger volume, hence with the same number of incident photon flux the absorbed dose will be higher for the former. This demonstrates why it is more appropriate to describe damage and compare different experimental conditions based on the dose.

Very few works report the absorbed dose for specific heritage materials, such as X-ray damage studies on chrome yellow [122], and Egyptian blue [137]. More often the fluence or the flux density are used to compare different damage effects.

The calculation of the absorbed dose, which is not measurable, is complicated by the heterogeneous systems (such as sample geometry and composition) of heritage materials and the beam parameters (like beam profile and flux density) which can vary significantly for each experiment set-up, even in the same beamline.

In some cases, the damage extent is also dependent on how fast the energy is provided and absorbed, therefore the dose rate is also an important parameter to consider. In radiation damage studies for protein X-ray crystallography, both dose-rate-dependent and dose-rate-independent X-ray damage is reported, and the rate-dependent damage is often attributed to heat contribution [138]. The effect of the dose rate is still fairly unexplored in cultural heritage applications.

2.2.3.2 The photon energy selection

All electrons in an atom can absorb X-rays, and the photoelectric cross-section increases with Z^n, where Z is the atomic number and n ca. 2.7. Therefore, it is commonly thought that the damage extent can be reduced by increasing the X-ray photon energy (when

applicable), especially when dealing with organic molecules [139]. On the same material, a low energy beam will deposit most of the dose on the surface of the sample, while higher energy photons will distribute the energy into deeper layers. In a recent study, the effect of X-ray photon energy (specifically 7.7, 9.6 and 13 keV) has been investigated by irradiating a sample of animal glue binder alone and a paint mock-up containing animal glue and zinc white [136]. The estimated percentage of absorption from the two samples shows that the binder alone absorbs only 1% at 7.7 keV and just 0.16% at 13 keV. The zinc white paint mock-up instead absorbs 9% and 5% at 7.7 keV and 13 keV, respectively, while near the Zn K-edge (9.6 keV) the absorption increases to 25%. The damage evaluation, performed by time-resolved FTIR following the binder protein bands distortions, showed that the binder of the zinc white sample is more damaged than the binder alone, and especially near the Zn K-edge. On the binder sample it was observed that the lower the photon energy, the higher the damage.

In protein crystallography the photon energy effect is controversial as some papers demonstrated that between 6 keV and 33 keV there is no significant difference in damage extent [126,140,141]. But care must be taken when comparing results. In the work on animal glue and zinc white the damage extent of the mock-ups irradiated with different photon energy was very similar when the irradiation was kept below 5 min, while it became very different only over prolonged exposure [136]. In addition, it must be taken into account that the specific damage evaluation method is sensitive to different characteristics of the material, and this may contribute to the apparent contradictory results. More experiments are needed to clarify the photon energy effect.

2.2.3.3 The spot size

It is commonly considered that small X-ray beams tend to be more dangerous, as a focused beam concentrates all the energy in a smaller area, hence increasing the flux density considerably. In fact, it is usually suggested to defocus the beam to reduce the intensity (at the expenses of lateral resolution) for a safer measurement when the sample is homogeneous [11,122]. However, if we provide the same flux density, the spot

size effect may be very different. As the main X-ray damage is due to photoelectrons, the mean free path of photoelectrons in a specific matrix can be considered to assess the damaged volume and extent. If the X-ray spot size is smaller than the path length of photoelectrons in a specific matrix, these can escape from the irradiated volume, thus reducing the damage within the illuminated volume [141]. If the primary goal is to obtain reliable data, then it is of interest to spread the photoelectrons to a larger volume, but this strategy may not guarantee a safer operation to maintain the integrity of the material.

From the thermal point of view, if some of the X-ray energy is transformed into thermal energy then some reactions may be enhanced and therefore contribute to the increase of damage. If the heat is induced in a small volume, it will be better dissipated compared to a larger volume, hence where thermal contribution is important, smaller beam spots can reduce the damage risk.

Such considerations, both on the photoelectrons free path and the thermal contribution, need systematic experiments on artists' materials, as the spot size effect may be extremely useful to guide some mitigation strategies.

2.2.3.4 Pre-estimation of minimum dose for quality data

In order to facilitate the estimation of dose within a sample volume and in time, a dedicated software, RADDOSE-3D [142], has been developed in the field of structural biology. The software enables modelling of the X-ray diffraction experiment to estimate the minimum dose required to obtain meaningful analytical data while avoiding signal distortion induced by X-ray damage. In cultural heritage field, based on the same concept of calculating the minimum dose for significant results, statistical methods are under development to pre-define the minimum number of points and dwell time needed to obtain a statistically significant result from X-ray Raman Scattering measurements on painting materials [143].

2.2.3.5 Sample environment

In structural biology, many X-ray measurements of proteins are performed under cryogenic condition to minimize or slow down radical diffusion [144] and also to minimize thermal damage. A similar strategy was tested to minimize damage on chrome yellow paint mock-ups resulting in a significant decrease of the photoreduction of chromium species [122]. Cryocooling is a useful strategy to collect reliable data because it reduces the damage. However, long-term monitoring is necessary to ascertain the safety for the material once the sample is heated up again to room temperature after the measurement, as this may produce radicals' mobilization and damaging mechanisms may propagate Moreover, many historical materials may suffer considerably under cryo-cooling. Alternatively, vacuum can be adopted as environment conditioning strategy [122]. This is mainly done to minimize the oxidative processes with atmospheric oxygen, but potential reductive process and thermal effects may be enhanced in vacuum. To avoid the side-effects of vacuum, a possible unexplored alternative strategy can be the use of inert gas environment for the analysis of heritage materials.

2.3 Conclusions

Based on the review literature regarding both X-ray and optical laser radiation damage on painting materials, some considerations can be made:

- More details are needed in the published papers regarding the irradiation conditions and samples characteristics to facilitate comparison of literature studies.
- It is still difficult to determine what is damage and what can be considered an acceptable material alteration and common vocabulary is still scarce.
- It is important to define the right analytical techniques to probe damage, although this is complicated by the vast possible type of damage but there is still space to explore new methods for damage characterisation.

- The development of long-term monitoring to assess the damage evolution over years is a unique requirement of the CH field and is very important to better address the possible reversibility of some damage or the time increase of others.
- There are still some parameters fairly unexplored to better optimize data collection for safer analysis, such as spot size and photon energy.
- It is desirable that instruments will soon incorporate online damage control protocols as part of the advances in data collection strategies, as online damage detection is not based on a-priori knowledge of damage and may result in the best strategy when analysing heterogeneous heritage materials.

3. Methods

Based on the analysis of the literature concerning radiation damage, it is clear that one of the most effective ways to prevent damage is the possibility to capture early-warning signs of damage during the measurement to promptly stop the irradiation to avoid/minimize the possible damage.

The complementary monitoring method developed in this thesis makes use of time and spatially resolved UV-VIS reflectance spectroscopy and it represents a novel application in the field of cultural heritage (Chapter 3.1). Here below are reported the specifications of the system used and the details of the set-ups for the *in situ* monitoring of laser-induced damage (section 3.1.1) and for real-time X-ray radiation damage detection (section 3.1.2).

To better understand the types of radiation damage induced on the paint mock-ups used within the experiments, several complementary techniques have been used and described in Chapter 3.2.

3.1. VIS-NIR reflectance spectral imaging for radiation damage monitoring

Reflectance Spectral imaging (RSI or RIS, for Reflectance Imaging Spectroscopy), combines the advantages of both point-based spectroscopy and imaging techniques, providing simultaneously spectral and spatial information of a material. The technique is widespread in cultural heritage for many applications, such as pigment identification, study of the state of conservation and detailed and accurate documentation of artworks [145,146]. The measurement consists of acquiring images of an object in contiguous narrow spectral windows from Visible-Near Infrared (VIS-NIR .4-1 μm) to Short Wave Infrared (SWIR 0.9 - 2.5 μm), with more recent developments up to mid-IR (2.5 - 16.5

μm) [147]. The obtained data cube is generally composed of 2 spatial dimensions and the spectral dimension. There are several methods for acquiring RSI based on the different wavelength selection and scanning strategies [145]. The most common ones in cultural heritage applications are the ones based on wavelength selection in the reflected light: filter-based systems and grating-based systems. The former consists in filtering the reflected light in front of the detector and acquiring the entire image at a specific wavelength range to record multiple sequential images at different spectral windows [148]. The grating-based system makes use of a slit and disperses the entire reflected light through a diffraction grating and a 2D detector enables the simultaneous acquisition of the spectra from the spatial pixels aligned with the slit (Fig.3.1.1). The spectral cube is obtained by scanning in space in perpendicular direction with respect to the slit, either moving the object or the system.

The grating-based (or "push broom") technique is well suited for time-resolved imaging studies, thanks to the simultaneous acquisition of the entire spectrum from a single spatial slit that enable kinetic measurements in the timescale of milliseconds. RSI performed with a grating-based system is commonly called hyperspectral imaging (HSI), its acronym will be used from now on. Here we present the two developed methods for time-resolved reflectance VIS-NIR HSI to monitor radiation damage: from telescopic to microscopic applications. The first method for *in situ* monitoring of laser-induced damage on paintings makes use of an in-house built remote HSI system (section 3.1.1). The second one for *operando* monitoring of synchrotron X-ray radiation damage on paintings (section 3.1.2), makes use of an adapted microscopic set-up of the HSI system, specifically developed for this study.

3.1.1. Development of the remote HSI monitoring method for *in situ* laser induced damage assessment

During the development of the remote Raman system at the ISAAC laboratory at NTU [24], a series of experiments were conducted to assess the safety of the laser system by using fiber optic reflectance spectroscopy (FORS)[32]. The method has been successfully applied for an extensive survey on artists' pigments and some short term (within few seconds) reversible changes in reflectance were detected [149]. Performing reflectance spectroscopy with optical fibers is made difficult due to the extreme sensitivity of the set-up to subtle perturbations and being a point analysis, the spatial extent of the possible damage is missing. To improve the stability and spatial resolution compared to our previous study using FORS, a grating-based hyperspectral imaging system was chosen which allows simultaneous monitoring of the changes within the laser spot and the surrounding area. The simultaneous acquisition of the spectra from the laser spot surrounding area provides an internal control for the assessment of the data quality for each acquisition.

3.1.1.1 The remote HSI system

The instrument used is an in-house built line-scan grating-based imaging system developed at the ISAAC laboratory at NTU (Fig.3.1.1). The system consists of an Andor Zyla 5.2 sCMOS camera combined with a Specim ImSpector V10E spectrograph. A Meade ETX90 telescope (focal length 1250 mm and aperture diameter 90 mm) is attached to the spectrograph-camera system, enabling a minimum working distance of 3 m. The spectral range analyzed is from 400 nm to 900 nm. The wavelength calibration was performed by imaging a Neon and a Mercury-Argon lamp that provides very narrow peaks corresponding to known transitions, whose position can be used to fit a 3rd order polynomial to get a match between pixel position and wavelength. The spectrograph provides an optical spectral resolution of about 2.8 nm over the spectral range 400-1000

nm. The spectra were binned to a spectral sampling resolution of 4.53 nm for data compression without losing significant spectral information. After binning the resolution no longer depends on wavelength even though the optical spectral resolution is linearly proportional to wavelength.

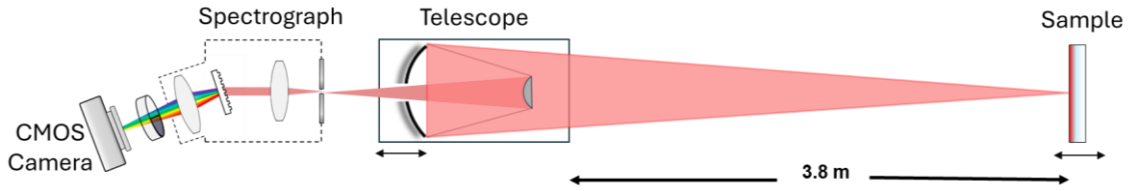

Fig.3.1. 1 Schematic of the in-house built remote VIS-NIR HSI system.

The measurements were performed in a stationary modality with the vertical slit centered on the laser spot. An integration time of 0.2 s was used to detect the evolution of the fast reversible reflectance changes. Calibration of the spectra was achieved using a 99% Spectralon© diffuse reflectance target larger than the FOV to perform at the same time flat fielding to correct for spatial inhomogeneity of the illumination and for spectral reflectance calibration on a reference material with the same exposure time as the data collection. To perform dark correction for thermal noise of the CCD camera and possible stray light contribution from the laboratory, the ambient dark was collected at the beginning and at the end of each set of measurements with the same exposure time as the data collection and with the cap off and illumination light off. The calibrated reflectance *R* of the raw intensity signal (*Is*) was performed with the following equation, where *i* stands for pixel index and *Iw* the intensity of the white standard:

$$\mathrm{R}(i,\lambda) = \frac{\mathrm{Is}(i,\lambda) - \overline{\mathrm{D}}(\lambda)}{\overline{\mathrm{I_W}}(\lambda) - \overline{\mathrm{D}}(\lambda)}$$

3.1.1.2 Set-up testing, focusing and alignment

Several illumination lights were tested for stability in order to identify the most suitable one to have the lower noise fluctuation to increase our sensitivity to subtle changes in reflectance. The light illumination was also selected to have the most uniform illumination (tungsten) with lower IR contribution and placed at a specific distance to keep the broadband light induced surface temperature rise to a maximum of 1-2 C° (evaluation performed by thermal imaging). A tungsten DC-950 Fiber-Lite® light source was chosen and placed at ~1 m and 45° to the target surface. Light stability test (Fig. 3.1.2) was performed after a 20-30 min of light warming up on a white standard reference to check the stability over 1 h and 40 min (the duration of the longest laser experiment is 15 min). The noise fluctuation of the reflectance is generally below 0.5% in the central part of the spectrum, while near 400 nm and close to 900 nm the noise is higher due to lower efficiency of the detector at the two edges of the spectral range and the spectrum of the light. The optical spatial resolution and field-of-view (FOV) were estimated by scanning a 1951 USAF resolution test chart. At 3.8 m working distance used for these experiments, a spatial resolution of ~30 μm was estimated, and the vertical slit provides an area of 30 μm × 15000 μm with 15 μm pixel size. The geometry of illumination-sample-spectrometer is crucial to minimize or enhance the specular contributions, as the diffuse light would give more chemical information (higher SNR for chemical changes), while the specular part could give some indication to surface changes, i.e. melting of the surface. In our case, the optical axis of the HSI was 60° with respect to the surface of the mock-up and the light at 45° on the same side.

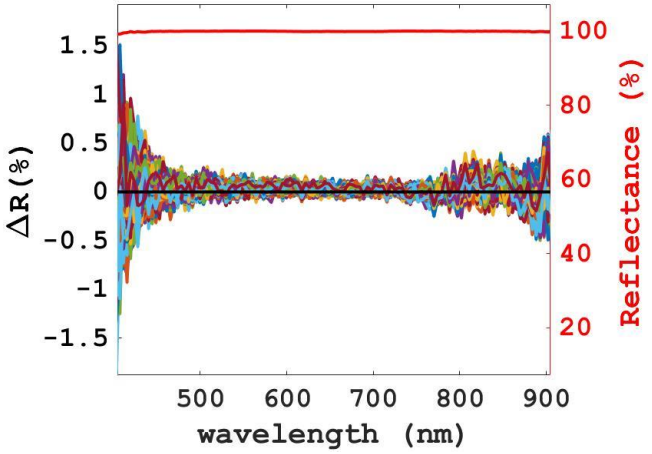

Fig.3.1. 2 The reflectance changes (ΔR) over 6000 s of the DC-950 Fiber-Lite light source. The red curve in the right Y-axis is the reference reflectance of the white Spectralon used for this stability test.

The samples were placed on a bidirectional motorized stage to focus the HSI on the paint target and translate the sample perpendicular to the HSI to perform the set of experiments in contiguous spots but with enough space to avoid contribution from the previously irradiated spot. We also performed some experiments where the entire surface of the spot was scanned before and after the laser irradiation by moving the stage at a speed of 0.05 mm/s and the exposure time fixed at 0.2 s.

The details of the procedure for focusing and alignment are reported in Appendix A. In summary, at first the laser is positioned on the area of interest of the sample, then the HSI system is focused on the sample and then the HSI is aligned with the laser beam.

The reflectance spectra were recorded for the whole duration of the experiment at the exact same position, without scanning and keeping the illumination constantly on. A series of reference spectra of the paint layer prior to irradiation were first recorded for 120 s. Then, during the laser irradiation, a manual shutter was placed in front of the telescope to avoid damage to the CCD camera. Just when turning off the laser, the shutter was removed, and the reflectance post irradiation was recorded for 300 s. Control experiments were also conducted by operating the whole procedure but

without the laser source such that any perturbation during the procedure could be minimized.

3.1.1.3 The damage evaluation

The damage is evaluated in terms of percentage of reflectance changes (ΔR) by subtracting the average pre-irradiation spectrum from the post reflectance cube for each *t* time frame:

$$\Delta R(\lambda, t) = (R_{Post}(\lambda, t) - \overline{R_{Pre}}(\lambda)) \cdot 100$$

Internal control on the system stability was possible using areas along the slit of the HSI far from the position of the laser irradiation. Any ΔR above the level of system stability and noise fluctuation were identified either as permanent or transient damage within the 300 s monitoring post irradiation. The reflectance spectra of the three main pigments analysed for the laser-induced damage experiments (vermilion, realgar and red lead) all show the typical "S" shape of a semiconductor material. Examples of ΔR internal control on these paint mock-ups are shown in (Fig.3.1.3a, b, c) and an example of subtle damage of ca. 1% ΔR detected on realgar paint mock-up is shown in Fig.3.1.3 d, with Fig.3.1.3 c as its internal control. The extent of random noise fluctuation in the internal controls is different between the short and long wavelength region, especially for vermilion and red lead. This is due to the contribution of photon noise in the highly reflective part of the spectrum (for these pigments in the 600-900 nm spectral region).

Three measurements were performed on the vermilion paint mock-up in order to check the reproducibility of the measurement (Fig. 3.1.4), at the maximum ΔR change around 600 nm a ΔR variation of 0.5% was detected.

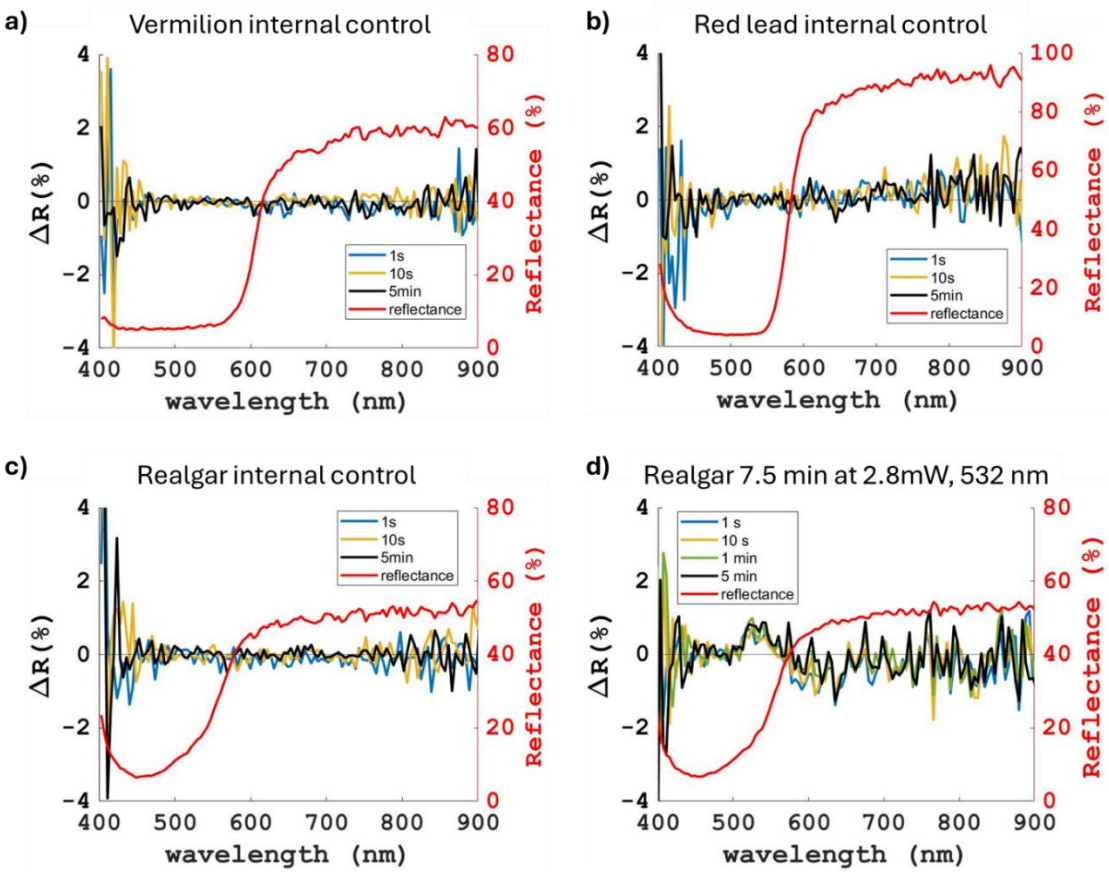

Fig.3.1. 3 a) example of ΔR plot on the vermilion paint layer far from the irradiation spot as internal control during the post monitoring of an irradiation test, b) the same for red lead paint mock-up and c) for realgar. The latter is the internal control of the irradiation test in d) where is shown the ΔR monitoring on realgar irradiated with a 532 nm laser at 2.8 mW for 7.5 min. The red curve in the right Y-axis is the reference reflectance of each mock-up.

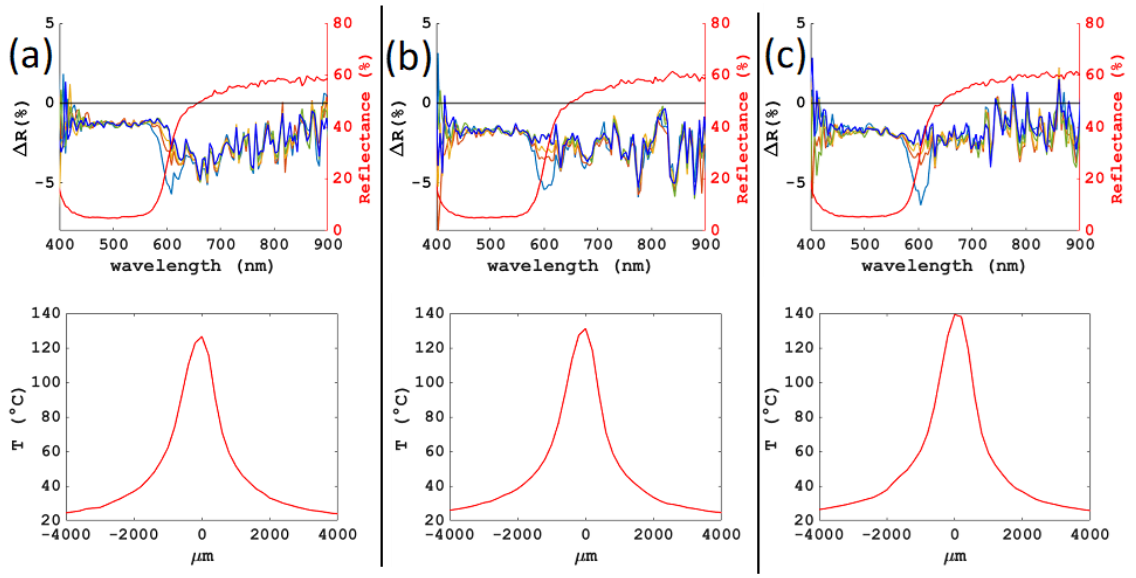

Fig.3.1. 4 Reproducibility test: vermilion paint mock-up irradiated with high power at 100 mW (power measured at the sample surface) for 10 s with a spot size of 900 µm repeated 3 times (a, b, c) to check the reproducibility. Top row: ΔR VIS-NIR changes (1 s light blue, 5 s orange, 10 s yellow, 60 s green, 300 s dark blue post irradiation, in red the reference spectrum before irradiation). Bottom row: temperature profiles around the laser spot.

3.1.1.4 The laser sources investigated

The three laser sources investigated are a 532 nm fiber laser (L1C-MPA_532 Oxxius) with maximum output of 100 mW, the 785 nm matchbox laser (0785L-21A-NI-NT-CF) integrated in the remote Raman system with a maximum output of 126 mW, the diode 780 nm laser[1] (TLB-7100) with a maximum power of 46 mW, and a 1064 nm Wasatch demo unit (WP1064L) with 445 mW maximum output. All these lasers have a Gaussian collimated beam of ca 1 mm at the target (3.5 m distance). When spot size tests were performed, the laser was focused using different lenses at a close range (30/20 cm) from the target. This way we achieved spot sizes from 450 to 40 µm. On each occasion, the spot size was measured (FWHM) by imaging directly onto a detector (UI-2250SE-M-GL) with a pixel size of 4.4 µm and the reflected beam profile was captured with the HSI. The laser power on the target was measured prior to each test with a standard Thorlabs photodiode power sensor S120C with a neutral density filter of 10%.

[1] This second 780 nm laser was used as a replacement of the previous laser due to a failure of the 785 nm.

3.1.2. The development of the microscopic VIS-NIR HSI system for *operando* monitoring of SR X ray damage

The monitoring of synchrotron X-ray radiation damage was carried out at the PUMA beamline at SOLEIL synchrotron. Due to dimension constrains of PUMA beamline, it was necessary to adapt the HSI system to work at a close range to fit our instrument in the position usually occupied by their optical microscope used for alignment and focusing. Moreover, due to the micro-X-ray beam dimension (usually 5 x 7 μm^2) higher spatial resolution was needed to resolve the spectral changes within the X-ray beam. The best compromise between minimum working distance, low chromatic aberration and high spatial resolution was achieved using a Mitutoyo WE 697599820 MY5X-802 - 5X Plan Apochromat Objective, 0.14 NA, with a working distance of 34 mm. A tube lens with f = 200 mm (ITL200, external M38 x 0.5 Threads) was used to focus and to enable a 5x magnification. The resulting overall length of the system is 77 cm, with a WD of 3.4 cm, a spatial resolution of around 2.7 µm, a pixel size of 1.2 µm and a vertical slit to the target of ca. 1 mm (Fig. 3.1.5).

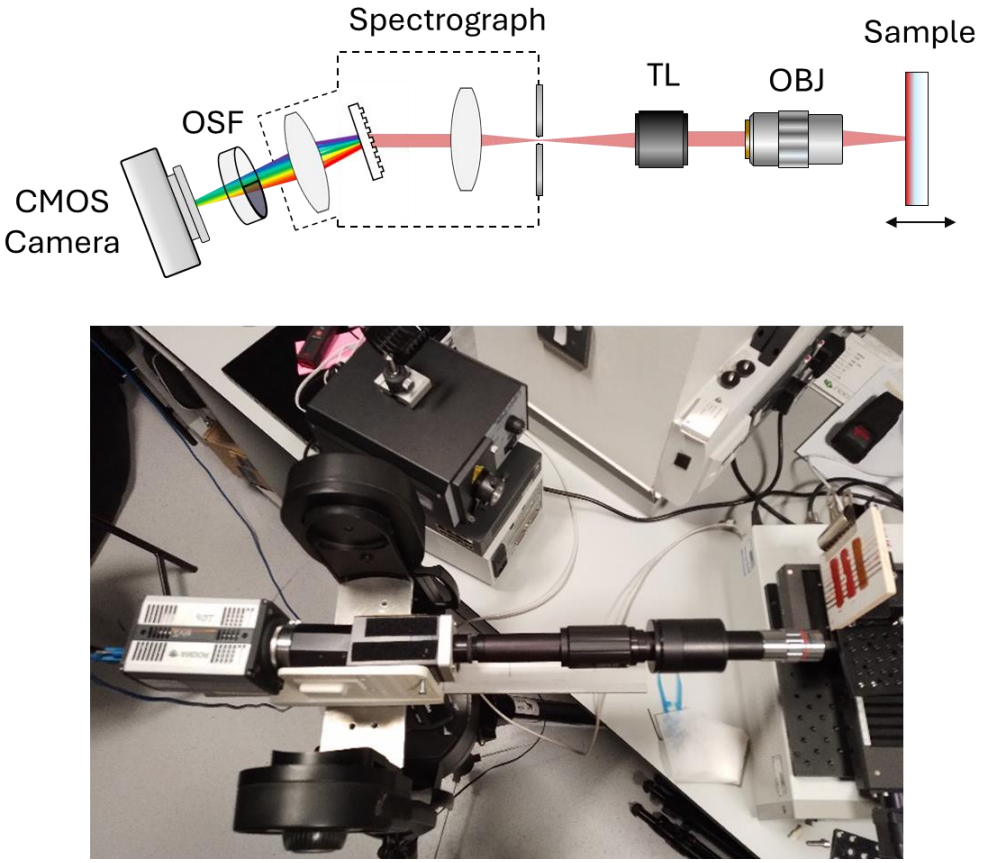

Fig.3.1. 5 Schematic of the VIS-NIR microscopic set up and below a picture of the system during the laboratory set-up tests in preparation for the beamtime.

3.1.2.1 X-ray beam measurements and alignment strategy

The microbeam set-up at PUMA beamline usually provides a focal X-ray spot of 5 x 7 μm^2. Due to the dimension of the HSI system and the limited space in the end-station, the sample stage was placed further away from the focal position to be able to align the X-ray beam and the HSI slit (see Fig.3.1.6 and the schematic in Fig. 5.1). The resulted X-ray beam is 15 x 60 μm^2 (vertical x horizontal) and was measured by recording the fluorescence signal of a chrome deposit on a Thorlabs resolution chart which acts as a knife edge. The beam size is estimated from the width of the first derivative of the intensity versus the spatial position of the knife edge.

The flux of the X-ray beam was measured with a calibrated photodiode, and it varies based on the energy used. Passing from 13 keV to 7 keV (energy range investigated in this experiment) the flux is two orders of magnitude lower, and part of this flux reduction is due to the absorption of the X-ray photons by air. To gain 10 times more flux at 7 keV, the chamber of the KB Mirror, used for focusing the beam, was filled with helium. This way the maximum flux measured was: 1.6×10^{10} ph/s at 13 keV and 1.7×10^{9} ph/s at 7 keV. To perform irradiation tests with different flux, we attenuated the beam by small misalignments of the mirrors, maintaining the same spot size.

The alignment of the X-ray beam and the vertical slit of the HSI system was performed by positioning a fluorescent paper on the sample stage and moving up and down in the direction of the optical path of the X-ray beam, until capturing the green fluorescence signal from the HSI system. This way, the exact spatial position of the X-ray beam on the HSI vertical slit was also recorded, and the FWHM of the fluorescence beam profile was 12 pixels. The pixel size of the HSI slit is ca. 1.2 µm. The damage has been evaluated based on the average ΔR changes extracted from 16 pixels (very similar in extent to collecting it from 12 pixels only), monitoring during and after irradiation.

A first dataset (lead white in linseed oil sample) was recorded with 0.2 s exposure time, while all the rest were recorded with 1 s, except for 2 datasets where 3 s and 5 s were used.

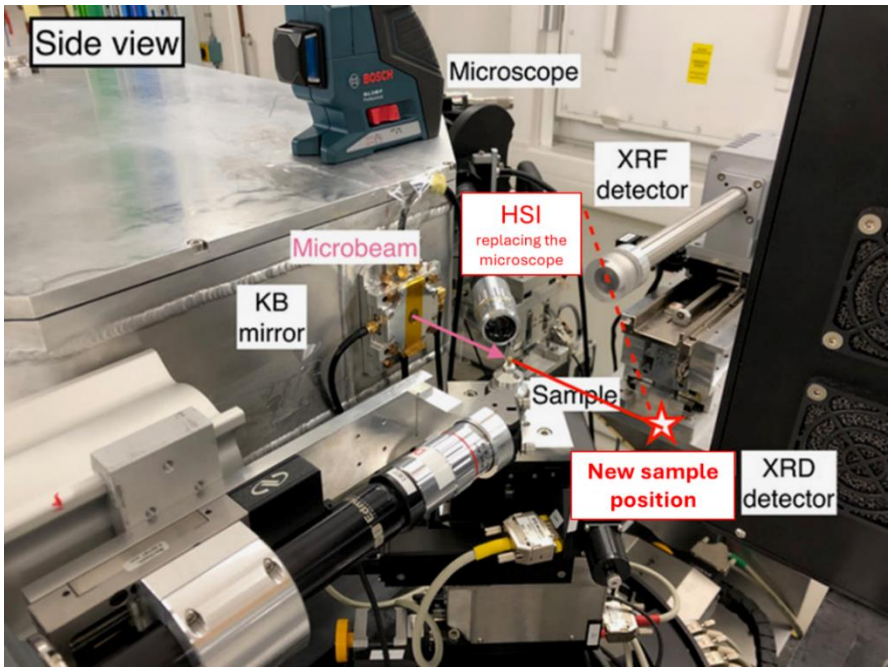

Fig.3.1. 6 The side view of the modified set-up at PUMA beamline to allocate our HSI system at the place of the microscope, due to dimensions constrains of the HSI the sample position has been moved to enable alignment.

An example of ΔR internal control for each sample is reported in Fig. 3.1.7. The lead white samples (Fig. 3.1.7a,b) show a higher random fluctuation amplitude around 0 compared to the ones containing Prussian blue. This can mainly be attributed to the higher reflectance of the lead white, and associated higher photon noise contribution, compared to the highly absorbing Prussian blue. The control on the mixture of Prussian blue and lead white sample (Fig. 3.1.7c) has been collected for a long-term experiment and after 5 hours it shows a small ΔR increase of 0.5% at around 400-450 nm. Prussian blue is well known to bleach upon visible illumination [150]. Due to the increase of reflectance at this specific spectral range, the control ΔR change is likely related to the fading of the pigment induced by the broadband light used as illumination source for the HSI acquisition (during the experiment the illumination light is kept constantly on for light stability purpose).

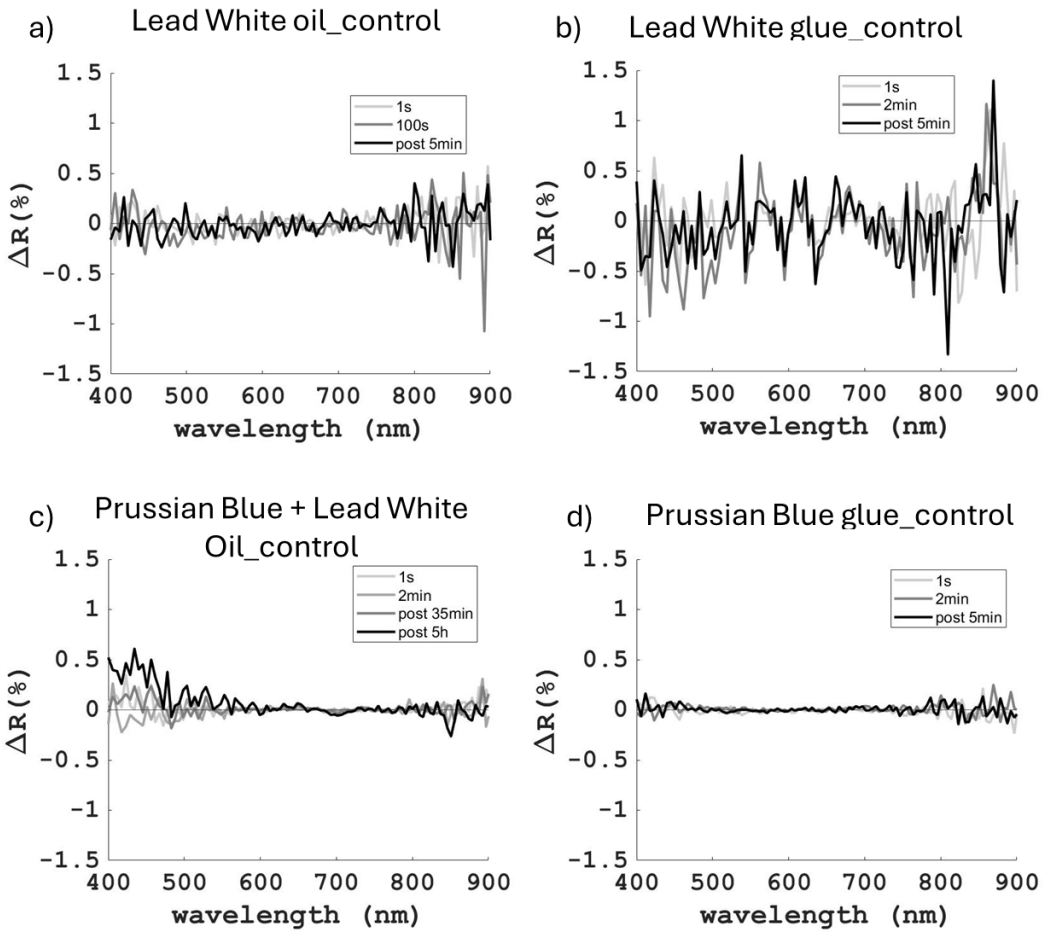

Fig.3.1. 7 The ΔR controls of the 2 min irradiation tests at 7.4 keV and 12.95 keV for a) lead white I linseed oil, b) lead white in animal glue, c) Prussian blue mixed with lead white in linseed oil and d) Prussian blue alone in animal glue.

The intensification of fluctuations observed in the animal glue sample (Fig. 3.1.7b) compared to the linseed oil one (Fig. 3.1.7a) seems to be related to the higher roughness of the glue sample and the associated speckle effect. In fact, the reflectance spectrum of the glue sample has higher fluctuations compared to the reflectance of the linseed oil sample (black and blue curves of Fig. 3.1.8). This fluctuation speckle effect is more pronounced when observed by the higher resolution microscopic set-up compared to the telescopic set-up of section 3.1.1 (red curve in Fig. 3.1.8), resulting in the ΔR being more sensitive to small environmental perturbations

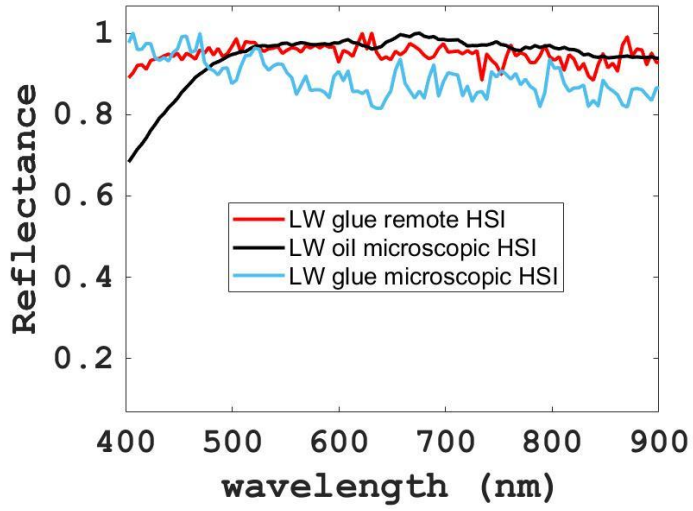

Fig.3.1. 8 The comparison of the normalized reflectance spectra of lead white in linseed oil (LW oil) and in animal glue (LW glue) collected with the remote HSI set-up of section 3.1.1 and the microscopic set-up.

The minimum irradiation time for the X-ray tests was set to 1 s and was performed using an internal command to automatically close the fast shutter. Later, performing some duration measurements of the command used (Fig.3.1.9), we realized that such fast irradiation was not achieved. The minimum irradiation time is 2.256 s. This delay corresponds to the time that the beamline commands are blocked due to the safety system check on the shutter position. As we can see by the spread of the points at low irradiation command times, this time can vary by a few 100 ms. At this fast irradiation condition, we repeated twice a 1 s irradiation tests to check the reproducibility of the experiment (Fig. 3.1.10). The repeated experiment shows a small difference of 1% at the 4^{th} second of irradiation, this could be related to a small difference in exposure between the first and the second repetition. The ΔR difference becomes irrelevant when irradiating in the order of minutes and hours.

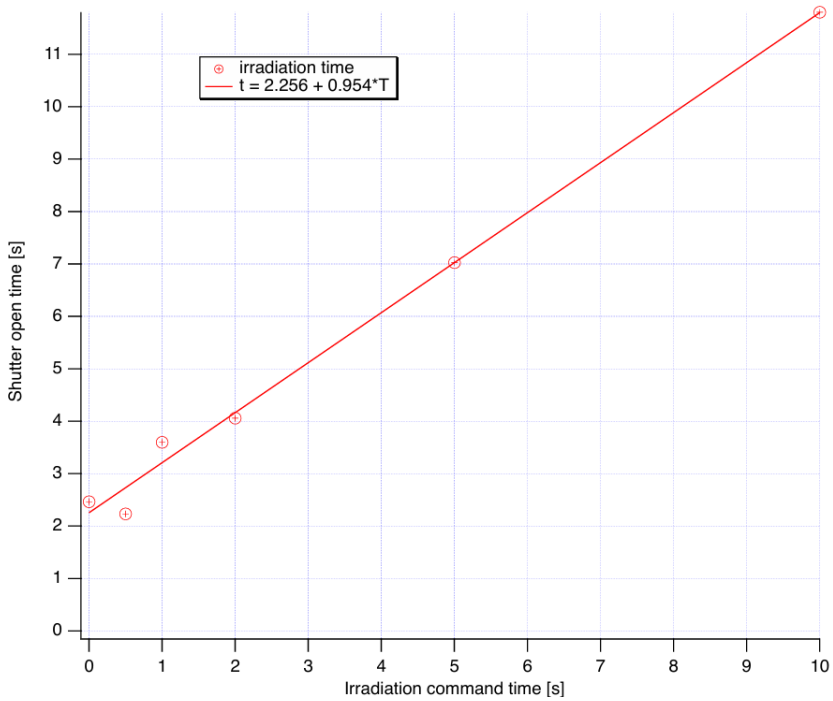

Fig.3.1. 9 The measurements of the effective shutter opening time at each irradiation time command.

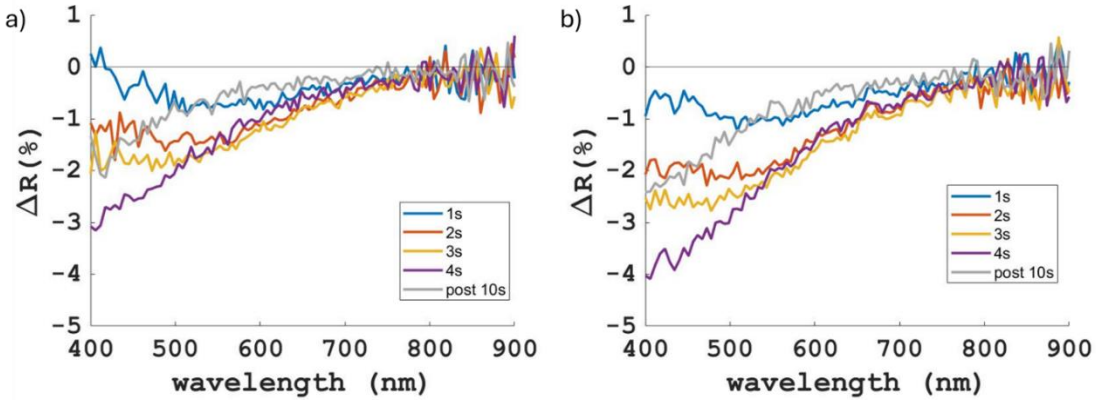

Fig.3.1. 10 Reproducibility test: ΔR plots of the 2 repeated irradiation tests, a) and b), on lead white in linseed oil for 1s at 12.95 keV.

3.2 Complementary methods for the characterization of radiation damage on paintings

In order to further monitor and characterize radiation-induced modifications, due to damage (induced both by laser and X-ray) or an intentional modification (later treatment of plattnerite to recover red lead), several complementary techniques have been used. Raman spectroscopy was used to assess whether it is possible to monitor laser-induced damage directly from the Raman spectral changes and to characterize the by-products of the laser treatment of plattnerite. Thermal imaging monitoring during laser irradiation allowed to ascertain when a predominant thermal effect takes place. Optical coherence tomography (OCT) was used to detect possible changes in the surface and subsurface microstructure and optical properties of the irradiated paint mock-ups. X-ray powder diffraction (XRPD) was used to ascertain any crystal structural modifications by laser or X-rays and was complemented by X-ray absorption spectroscopy (XAS) to quantify the laser treated plattnerite mock-up. XAS spectral changes were also monitored over consecutive measurements to ascertain its X-ray damage detection sensitivity and characterise the type of damage.

The general principles of each technique are reported in appendix C, while details of its use in the present work, and specification of the instrument and acquisition settings, are briefly described here below.

3.2.1 Raman spectroscopy

In this work, Raman spectroscopy has been used to:

1. Evaluate the possible Raman spectral changes upon different laser irradiation conditions on paint mock-ups and pigment powders.
2. Characterize the products formed upon different CW laser treatments of the plattnerite wall painting mock-up to convert plattnerite into red lead.

For the monitoring of laser-induced damage, it was also considered to acquire at the same time the anti-Stokes to measure the surface temperature directly from the Raman spectra instead of using thermal imaging. But after evaluation of the current literature, we realized the inapplicability of Raman thermometry for our purpose due to:

- the difficulty in selecting the peak (case by case) as it has to be intense enough to detect the anti-Stokes and clear from interference from other compounds and as much as possible unaffected by fluorescence background (more intense at lower frequency).
- Selecting a peak at high or low frequency impacts significantly on the temperature range sensitivity (Fig. 3.2.1a), especially in the case of room temperature applications and for the frequencies of pigments that are generally below 1000 cm^{-1};
- the indispensable step of fluorescence background subtraction prior to the calculation of the Stokes and anti-Stokes ratio that has a significant impact on the resultant temperature (with examples of temperature accuracy changing from 1% to more than 5% in [151]);
- the poor sensitivity of the technique to small changes of temperature (few degrees} (Fig.3.2.1).

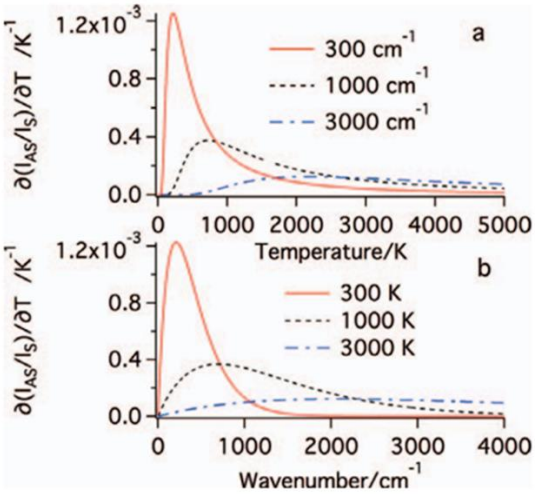

Fig.3.2.1 The temperature sensitivity measured as the partial derivative of the anti-Stokes to Stokes intensity ratio a) versus temperature expressed in Kelvin for different frequency (300, 1000 and 3000 cm^{-1}) and b) versus frequency at different temperature (300, 1000 and 3000 K) (figure from [152]**).**

For the monitoring of laser-induced damage on paintings, a remote standoff 785 nm Raman system developed by ISAAC lab (for details of the system refer to [24]) was used with a 500 l/mm diffraction grating, resulting in a spectral resolution of 8.5 cm^{-1}. The measurements were performed with a spot size of 900 µm using a power ranging from 0.005 mW to 126 mW. The wavelength calibration was performed using Argon and Mercury lamp and Neon lamp.

The changes in Raman spectra were evaluated in terms of changes in net peak counts above the fluorescence continuum spectrum and peak positions. Raman spectra were recorded simultaneously while irradiating with the 785 nm laser. The same 785 nm Raman system was employed to monitor the effects of the 1064 nm and 532 nm lasers, for consistent comparison. In these cases, several Raman spectra were recorded pre and post irradiation with the 785 nm laser at 2.8 mW over a 900 µm spot (the safety of this setting was previously checked with the same monitoring procedure described in Chapter 3.1).

For the analysis of the laser treated plattnerite mock-ups, an XPlora Horiba micro-Raman instrument was used with a laser excitation wavelength at 785 nm, with a diffraction grating of 1200 g/mm (spectral resolution of 4 cm^{-1}) and a 100× objective. The laser spot

size at the focal point was around 1.5 µm and the power on the sample around 0.4 mW. Raman spectra were acquired using 300 s acquisition time. Wavelength calibration was performed on a standard silicon wafer.

3.2.2 Infrared thermal imaging

Thermal imaging was used to monitor the surface temperature before, during and after laser irradiation to correlate the temperature rise with specific irradiation conditions on different paint materials.

The thermo-camera used for the monitoring of laser-induced effects on painting mock-ups is a FLIR T620. This camera works in the 7.5-14 µm spectral window with a temperature range of -40°C – 650°C. The field of view (FOV) is 25° × 19° and the radiometric images are acquired with a frame rate of 30 Hz. The recording was performed at 45° and at a distance of 25 cm, providing a spatial resolution of ~200 µm. Temperature was monitored for the whole duration of the experiment (before, during and after the laser irradiation) with emissivity set at 0.95 based on preliminary test on the 3 specific mock-ups. Assuming a black paper as a black body, on the thermal camera the emissivity was set to 1 and the correspondent temperature was read, then moving to the mock-up, that is in thermal equilibrium with the ambient, the emissivity was changed such that the temperature read was the same as the one measured on the black paper. This rough estimation is enough as the primary aim of using thermal imaging is the assessment of the temperature difference and not the absolute values.

For the monitoring of the temperature rise induced by laser spots smaller than 200 µm, an A700 FLIR was used with a microscope lens that provides a spatial resolution of 70 µm at a distance of 8 cm from the target.

3.2.3 Optical coherence tomography

OCT was primarily used to assess the surface changes induced by laser irradiation, such as possible crater formation or change in subsurface structure (Fig.3.2.2) or modification of optical properties and roughness changes. It was also used to measure the thickness of the paint layer of the prepared paint mock-ups.

To characterize the surface and sub surface structure of the irradiated region, an in-house built ultra-high resolution Spectral Domain OCT developed by ISAAC lab [153] was used. The system has a central wavelength of 810 nm and produces a 5 x 5 x 2 mm^3 virtual volume cube with depth (axial) resolution of ~2 µm in air and a transverse resolution of 7 µm. The paint surface position is extracted from the OCT cube and a root-mean-squared surface roughness map (RMS roughness) is calculated with a 50 µm window [154]

A 1300 nm OCT (TELESTO-II Spectral Domain OCT Imaging System) with an axial resolution in air of 7 µm was only used for paint thickness measurements.

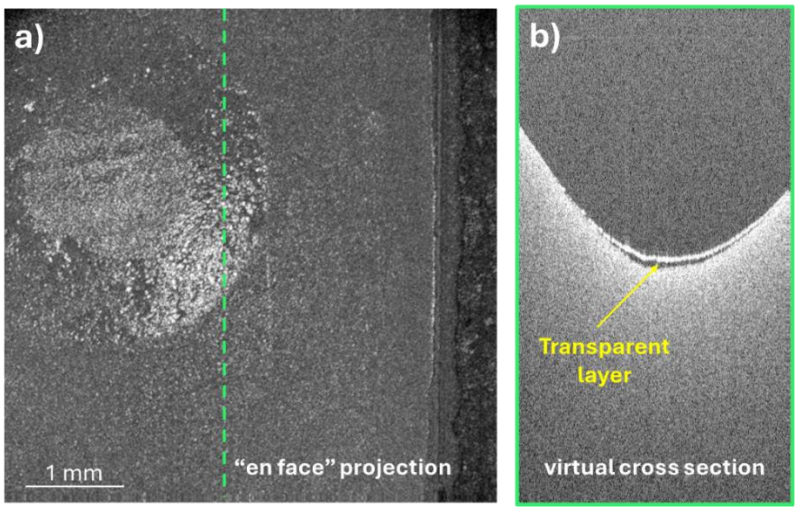

Fig.3.2.2. An example of the use of UH-OCT for the evaluation of surface and sub-surface modifications induced with a CW 532 nm laser with 100 mW over a spot of 900 µm on a vermilion in linseed oil paint mock-up. a) the "en face" average projection of the entire scanned surface, and b) the vertical virtual cross section of the dashed green line in a). The virtual cross section in b) is not corrected for field curvature.

3.2.4 X-ray powder diffraction

In this work, XRPD was performed to:

1. identify the crystalline composition of the altered paint surface after laser irradiation in order to correlate specific ΔR changes to a possible phase transition or formation of new compounds.
2. characterize the X-ray induced damage spots on the surface of paint thin sections, again to correlate possible crystal modification with specific ΔR changes.
3. follow and characterize the phase transitions during a purely thermal treatment of a plattnerite powder with different heating rates and environmental conditions (inert nitrogen or air) to obtain red lead.

The experiments at point 1. and 2. were performed in transmission with synchrotron radiation (SR) micro-XRPD mapping (SR μ-XRPD mapping). The measurements of point 3. were performed in a bench-top XRPD in Bragg-Brentano geometry with a conditioning chamber to induce the heating ramp. Further characterization of non-stoichiometric lead compounds was carried out in transmission with a 2D areal detector of a single crystal instrument. All the details of the 3 specific methods are briefly described below.

3.2.4.1. SR high lateral resolution μ-XRPD

To assess the possible changes in the crystal structure of the pigments, SR μ-XRPD mapping was performed at the μ-brunch of ID13 at the European Synchrotron Facility (ESRF, Grenoble, Heritage Historical Materials BAG access HG172 and HG312 [116,155] (Fig. 3.2.3a). Thin sections from small fragments of the oil paint mock-ups were prepared with a microtome with the support of an adhesive tape to obtain slices of 10 μm thickness (Fig. 3.2.3c). For the plattnerite wall painting mock-ups, due to the hard nature of the mortar substrate, petrographic thin sections were prepared with a support in polycarbonate instead of the standard glass (Fig. 3.2.3b). With this technique thin

sections between 30 and 50 µm thickness were obtained. Raster scanning maps were performed on areas of 400 x 100 μm^2 with a beam size of ca. 2.5 x 2.5 μm^2, a step size of 2 µm in both horizontal and vertical directions, an acquisition time per point of 10 ms at 12.92 keV (0.95967 Å) and a flux of ~ 1.9 x 10^{11} ph/s (at I= 34 mA electron beam current). The two-dimensional diffraction patterns collected in transmission were azimuthally integrated using dedicated Jupyter notebooks, based on the PyFAI software package [156] and were then analysed with PyMCA software to perform ROI imaging [157]. This way, RGB false colour correlation maps are generated based on the intensity of a diagnostic reflection peak of a specific crystal generated by defining a ROI in the 2θ range. Average diffraction patterns were then extracted from the heat map generated by a single 2θ ROI or by selecting a specific area of the sample from the map of the sum pattern acquired. The identification of the crystalline compounds was then performed with Match! software using COD inorganics database.

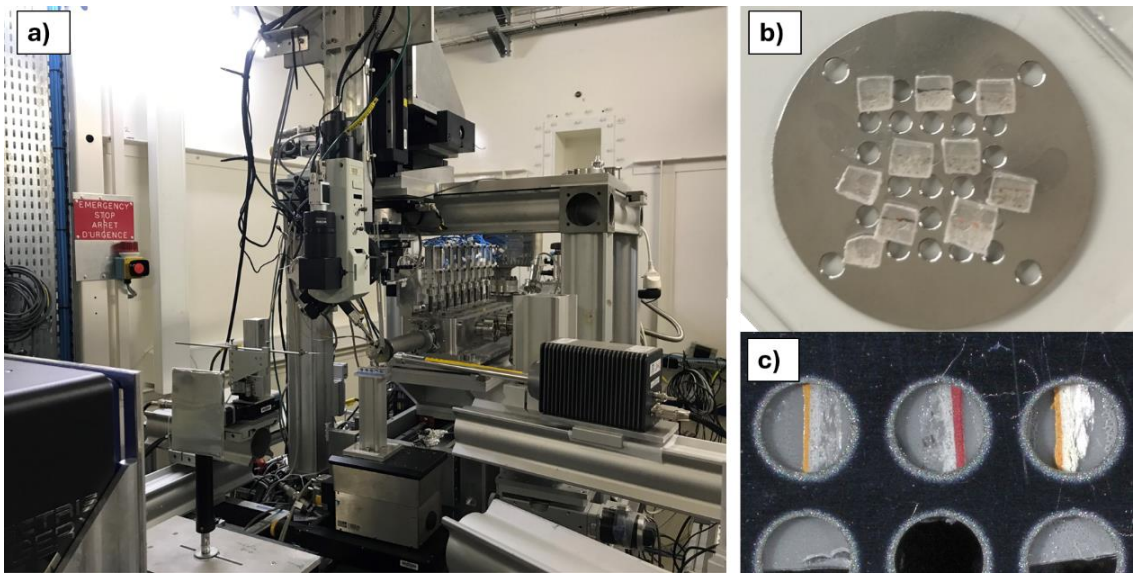

Fig.3.2. 3 a) the end-station at ID13 at ESRF with the eiger areal 2D detector on the left corner, the SDD detector for XRF on the right and on the top of the sample stage, the optical microscope for focusing on the target. b) one of the sample plates with 2 mm diameter holes were many petrographic thin sections were allocated and c) a microscope image of the mounted thin sections made with a microtome and adhesive tape of vermilion and realgar oil mock-ups before measurement.

3.2.4.2 Variable temperature XRPD

The chemical grade plattnerite powder was heated up in an Anton Parr variable temperature X-ray diffraction cell in inert nitrogen environment or in air. The diffraction patterns were collected at each step after a temperature increase of 25 C° in a Bragg-Brentano geometry with a Cu anode PanAlytical X'Pert Pro diffractometer and the acquisitions were performed at a scan speed of 0.14°/s and step size of 0.013°. The heating test was repeated also with different rates between 20°/min up to 150°/min with a cooling rate of 50°/min.

3.*2.4.3 Powder diffraction on a single crystal diffractometer*

Modern single-crystal diffraction systems with 2D detectors can be considered very useful for low to medium angular resolution XRPD applications, especially when a very small amount of material is available (micro to nano grams) or when we want to separate the patterns coming from different particles (agglomerate of crystal) in a powder.
In the case of the byproduct of the thermal treatment of plattnerite powder, XRPD measurements were conducted on single particles of different colours separated from the non-stoichiometric lead oxides powder produced with the thermal treatment. Each single particle was mounted with a needle on a single crystal Rigaku Synergy DW diffractometer (Fig. 3.2.4) with a Cu anode and measured in transmission with a 2D arial detector positioned at 37 cm from the target. The sample was cooled down by a nitrogen jet. The 2D patterns were integrated to obtain the 1D pattern.

Fig.3.2 .4 A picture of the single crystal Rigaku Synergy DW diffractometer during the measurement.

3.2.5 X-ray absorption spectroscopy

In this work, XAS was used to:

1. analyse the speciation of Pb at the LIII edge (13042 eV) on the plattnerite wall painting mock-up irradiated with CW 1064 nm laser to identify and quantify, upon deconvolution of the spectra, the lead compounds present on the treated volume and possibly obtain indirect depth information combining the signal coming from XANES acquired in the 3 different modalities.
2. Perform irradiations at different energies (7-13 keV) on some painting mock-ups to follow the possible damage induced during a XAS experiment and monitor the ΔR changes.

The experiments of point 1. were conducted at beamlines BM08 (proposal HG 175) and BM16 (proposal HG191) at the European synchrotron radiation facility in Grenoble (ESRF) after successful proposals. The experiments of point 2. were carried out at PUMA beamline at the French synchrotron facility of SOLEIL after successful proposal (number 20231243). The details of the 3 set-ups and beamlines are briefly described below.

3.2.5.1 The set-up at BM08-LISA beamline at ESRF

At the Italian BM08-LISA beamline [158] (Fig. 3.2.5a) of ESRF, XANES at the Pb LIII edge were performed with a beam spot of ~70 × 100 μm^2 with a flux of ~10^9 ph/s under He atmosphere (0.5 atm) with a Si(3 1 1) crystal monochromator. A reference spectrum of metallic lead placed in a second experimental chamber after the sample was measured simultaneously for energy calibration (position of the first inflection point taken at 13035 eV). A specific sample holder [159] (Fig. 3.2.5b) was used to enable simultaneous recording of TEY as well as fluorescence yield and transmission (with a Pb foil at the end of the station for transmission calibration of energy). The wall painting mock-up fragments of plattnerite were positioned vertically and attached to the holder with carbon tape to guarantee conductivity, and a collecting anode polarized at ~20 V was placed at about 10 mm from the sample. The samples were measured rotated 20° with respect to the incoming beam. All the acquisitions were repeated 3 times on each spot and data processing was performed with the open-source software ATHENA program to merge, normalize and background subtract each set of XANES. To be able to perform deconvolution of the XANES spectra by linear combination-least squares fitting (LCF), standards of the main lead compounds were prepared in pressed pellets of 10 mm diameter at 15% wt in cellulose and measured in fluorescence mode. The standards of red lead (Pb_3O_4) and plattnerite (β-PbO_2) are chemical grades, while litharge (α-PbO) and massicot (β-PbO) were previously synthesized in the laboratory based on the procedure described in [160], and the non-stoichiometric lead oxides (called Pb_xO_y) was prepared upon heat treatment based on the experiment described in Chapter 6. All the standards were previously characterized with XRPD to check the purity of the compound. The total amount of associated phases in each compound, if present, resulted approximately below 5 wt% that correspond to the conventionally assumed detection limit of secondary phases in the XANES analysis.

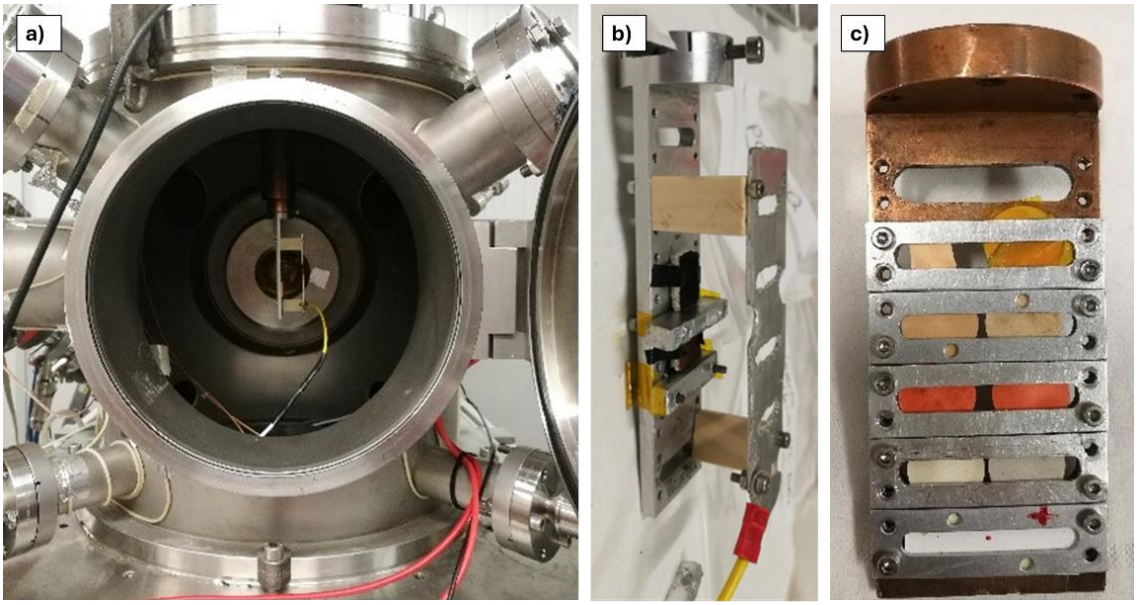

Fig.3.2.5 a) the end-station sample chamber at BM08 during sample mount for the simultaneous recording of TEY, fluorescence and transmission. b) the TEY sample holder. The plattnerite wall painting mock-up fragments are attached with carbon tape to the holder to guarantee conductivity and checked prior each measurement. c) the standard compounds in pressed pellets in cellulose.

3.2.5.2 The set-up at BM16-FAME-UHD beamline at ESRF

At the French Ultra-High Dilution BM16-FAME-UHD beamline of ESRF, high energy resolution fluorescence detected x-ray absorption spectroscopy (HERFD-XAS) was performed at the Pb LIII edge with a multi bunch beam of 200 x 100 μm^2 (horizontal x vertical) with a flux of ca. 10^{11} ph/s in ambient condition using a Si(220) double crystal monochromator with energy calibration performed on a Pb foil in transmission. The samples were positioned 45° with respect to the fluorescence detection system composed of a 14-crystal analyser spectrometer that provides an energy resolution of 1 eV (Fig. 3.2.6). Relevant standards lead-based phases (the same compounds as described for BM08) were measured in fluorescence mode prior preparation in pressed pellets of 5 mm diameter at 15% wt in cellulose and boron nitride. The XANES spectra were background subtracted and normalized, using the IFEFFIT software package [161]. Linear Combination Fitting (LCF) of the experimental XANES spectra using the adopted set of reference compounds spectra was also performed using the dedicated module included

in the IFEFFIT software package. The number of reference spectra to be included in the final LCF was chosen as the minimum number able to introduce a significant reduction of the overall χ2 value (i.e. change by more than 20%). The final accepted number of reference compounds was set to 4. The same set of standards was then used to fit all experimental XANES spectra of laser treated and untreated areas of the plattnerite mock-up.

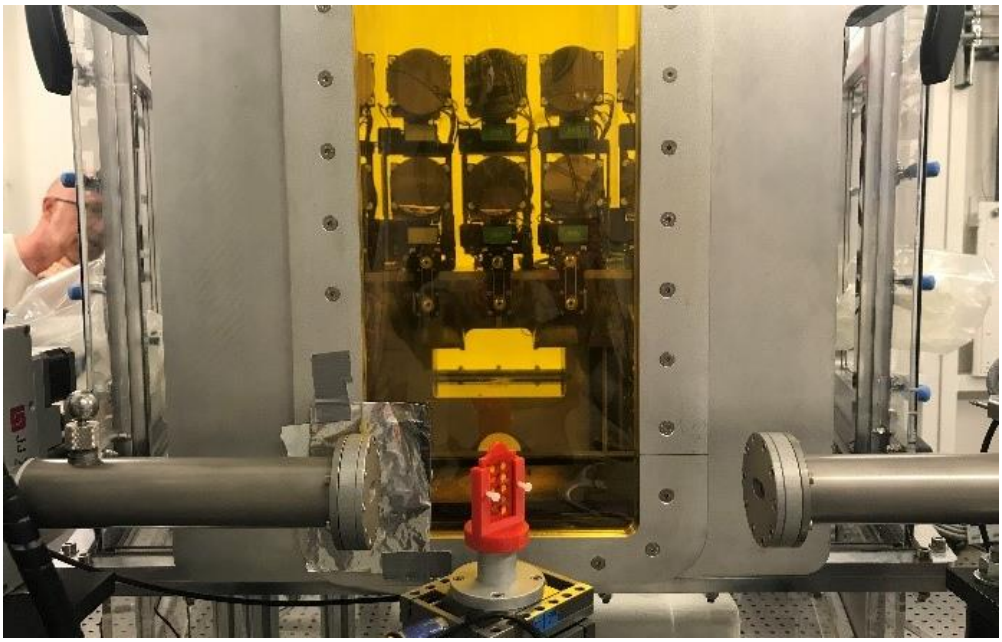

Fig.3.2.6 The end station at BM16 with the sample holder (red) and on the back, the 14-crystals analyser spectrometer separated from the environment with a Kapton foil.

3.2.5.3 The set-up at PUMA beamline at SOLEIL

At PUMA beamline of the French synchrotron facility of SOLEIL (Fig. 3.2.7), XANES experiments were conducted at 4 different energies: Fe K-edge (7112 eV), As K-edge (11864 eV), Hg LIII edge (12284 eV) and Pb LIII edge (13035 eV). The experiment was conducted with the *operando* VIS-NIR hyperspectral imaging monitoring method (Chapter 5) and consecutive XANES were acquired on the same spot of a painting mock-up to assess any XAS spectral changes, especially the possible shift of the energy edge

that could determine oxidation or reduction of the analysed chemical element induced by the X-ray beam. The measurements were carried out in fluorescence mode by means of a Rayspec Silicon drift detector (SDD) with an active area of 100 mm^2 (80 mm^2 collimated), a crystal thickness of 450 µm and a beryllium window of 25 µm. The collimator is made of aluminium with a hole of 8 mm diameter and 10 mm length. Signal readout is done using a FalconX (company: XIA) signal processor. The energy resolution of the SDD is around 150 meV. The energy bandwidth of the monochromator, which determines the resolution of the XAS spectra, is around 1 eV at 10 keV. The X-ray beam spot size was 15 x 60 μm^2 and the maximum flux, being energy dependent, was: 1.6 x 10^{10} ph/s around 13 keV; and 1.7 x 10^9 ph/s at 7keV. To reduce the flux for the experiment, the mirrors of the monochromator were misaligned such that part of the beam was cut off at the source, still providing the same beam spot on the target. The energy calibration was performed on a metal lead and metal iron foils.

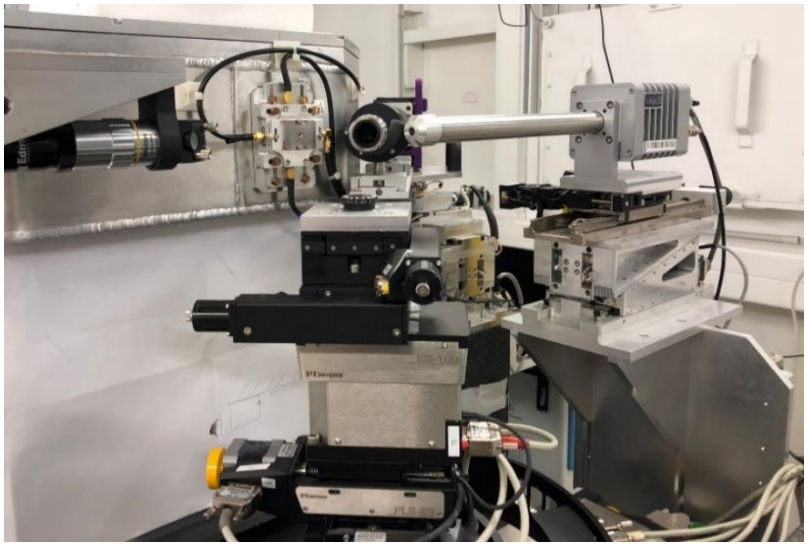

Fig.3.2.7 The end-station at PUMA beamline for X-ray absorption spectroscopy in fluorescence modality with the SDD detector on the right.

3.2.6 Short Wave InfraRed (SWIR) hyperspectral imaging

SWIR (930–2500 nm) reflectance spectroscopy enables the measurement of the combination bands and broad overtones of some of the fundamental vibrations, the ones with higher frequency. Performing it in a hyperspectral imaging modality enables to map the spatial distribution of the specific features.

In this work SWIR hyperspectral imaging was used to scan the surface of the plattnerite paint mock-up after laser treatment to follow possible features characteristic of plattnerite and red lead.

The system is a NEO HySpex SWIR-384 hyperspectral camera operating in the range 930–2500 nm with a spectral resolution of 5.45 nm and a total of 288 channels. This instrument is a line-scan (or 'pushbroom') providing 384 spatial pixels from a 16 bit cooled HgCdTe (MCT) sensor. The spatial resolution is ca. 70 µm at a working distance of 10 cm in a microscopic mode of operation. The imaging of the sample was performed by mounting the sample on a motorized stage at a speed of 1.2 mm/s. At 45° and at a distance of 40 cm from the target a tungsten halogen light was placed for illumination. The data were calibrated over a 5" × 5" standard white diffuse reflectance Spectralon© 99%.

4. Time resolved VIS-NIR hyperspectral imaging as a novel monitoring tool for radiation damage on paintings

As reviewed in Chapter 2, the methods to assess the occurrence of radiation-induced alteration on paintings are very limited and none of them can predict damage. In this chapter is presented the application of the developed VIS-NIR hyperspectral imaging (HSI) monitoring method (detailed in sections 3.1.1) to detect the time and spatial evolution of laser-induced damage due to the interaction between continuous wave (CW) lasers commonly employed in Raman spectroscopy and artists' paint materials. To correlate specific reflectance spectral changes with damage mechanisms, a multimodal monitoring approach was used by simultaneously recording the surface temperature with thermal imaging and consecutively acquiring multiple Raman spectra. The resultant physical and chemical changes were then examined in detail by optical coherence tomography (OCT) and synchrotron based micro-X-ray powder diffraction (SR μ-XRPD).

4.1 Introduction

Within laser-based techniques, Raman spectroscopy is one of the most well-established techniques thanks to its high specificity for molecular characterization [162] especially used for pigment analysis [56]. Its increased use in recent years has challenged conventional assumption of non-invasiveness, especially for the development of macro-Raman mapping which can affect a significant area of the artwork [30,31]. When dealing with pigments, some damage may occur upon laser irradiation [52,56,163], and if laser-induced transformation occurs, the reliability of the data acquired, and the materials identified can be questioned [46].

Visual observation or assessment under optical microscopes are the most frequent inspection techniques adopted, even though some damages are difficult to see in plain sight [12,108]. When performing Raman spectroscopy, a common monitoring strategy consists of detecting changes in the Raman spectra itself, such as peak broadening, shifting [52,164], a decrease of the peak intensities [101], or new peaks emerging due to phase transformation [163]. The use of Raman spectral changes for the detection of damage is convenient as it is integrated in the measurement itself. However, this monitoring often fails in the detection of damage, e.g., no Raman spectral changes were detected despite discoloration observed in phthalocyanine [164], indigo [14] or chrome yellow [104]. Our recent studies found that the two commonly employed inspection techniques, visual observation and Raman monitoring, are also not sensitive enough to detect some short-term alterations on paints that can be detected only with visible and near infrared (VIS-NIR) reflectance spectroscopy [30,165,166]. Although visual inspection and Raman spectroscopy can offer useful guidance for the detection of certain laser-induced damages, they can be blind to physical changes (e.g., partial melting of the surface) and inter and intra molecular scale damage below the detection limit. In some cases, the alteration may not correspond to damage of the pigment (e.g., alteration in the binding medium). Laser-induced damage threshold (LIDT) expressed in terms of the minimum laser intensity (power per unit area) at which a damage is observed, is usually determined on mock-ups to avoid causing damage to the real paintings by gradually increasing laser power. This method is often unrepresentative of real cases because of numerous material parameters that can vary the damage probability on real artists' materials. One example is the particle size, reported to affect the phase transformation of iron oxide nanoparticles [167] and blackening of azurite [59]. The degree of crystallinity can also modify the laser damage susceptibility of a material [103]. Another key factor is the presence of impurities as highlighted in Ciofini et al. [61], where different batches of lead white heated up differently upon the same irradiation condition as a result of varying concentration of impurities of iron oxides. Therefore, the identification of LIDT on artificial samples does not represent a successful strategy to avoid radiation damage. Instead, research effort should aim at developing on-line monitoring methods to prevent damage.

A very useful monitoring method has been designed by Mencaglia et al. [105,107] that enables adjustment of the Raman laser power based on simultaneous thermal monitoring of the irradiated surface. However, the fundamental limitations are that thermal damage thresholds of materials are not always known *a priori*, and laser-induced alterations may not always result in a significant increase of surface temperature, e.g., photochemically dominated reactions. Therefore, the development of alternative monitoring methods for comprehensive damage detection is still in demand.

The multimodal imaging set-up developed in this thesis consists of time resolved hyperspectral imaging (HSI) for VIS-NIR (400-900 nm) reflectance spectroscopy and IR-thermography. To verify the sensitivity to damage detection of this new method, the HSI detection sensitivity is compared to the sensitivity to capture radiation damage from the Raman spectral changes. OCT is used to confirm morphological surface changes, and SR µ-XRPD mapping is performed to assess the possible crystal structure changes of the pigments induced by the lasers. The proof of concept of the method is demonstrated through the detection of physical and/or chemical damages while irradiating oil paint containing 3 red-orange pigments that show similar absorption and scattering properties in the visible regime but different behaviour upon laser irradiation. Simultaneous monitoring of the spectral changes in the laser spot surrounding area provides an internal control to evaluate the quality of each single measurement on the same pigment (see Chapter 3.1.1). Moreover, most thermal related damages will dissipate heat from the irradiated area, which makes it possible to evaluate the extent of the damage as a function of temperature away from the laser spot, where no photons are directly involved allowing differentiation of changes caused by heat alone compared to those that involved photons. The data obtained by this multi-modal approach allow the distinction between thermal or non-thermal effects thanks to specific changes in spectral reflectance. Of particular interest is the possibility to objectively define safety thresholds based on transient and reversible reflectance spectral changes that are precursors to the occurrence of more permanent damage. Based on the survey of the main laser and material parameters that are relevant to the risk of damage, experimental strategies for damage prevention are discussed.

4.2. Experimental design

4.2.1 Mock-up samples

Irradiation tests were performed on mock-ups designed to simulate a naturally aged oil painting on panel (Fig. 4.1): 15-year-old oil paint mock-ups [145] with pigments reported as unstable to laser irradiation (vermilion, realgar and red lead) [30,56,163]. The selection of the oil painting mock-ups was made to assess potential damage in realistic examples representing a real painting. The studies performed up to now concerning laser-induced damage were performed on pressed pigment powders [52,101,163]. For comparison with literature, irradiation tests were also performed on vermilion pigment powder. The pigments were mixed with linseed oil and applied on a preparation layer of chalk in rabbit skin glue on a plywood substrate. The paint thickness is ca. 200 µm (measured with OCT). The pigments were selected to have similar reflectance spectra: all three pigments absorb at 532 nm while they are all strong scatterers at 785 and 1064 nm. Moreover, the pigments show different light and thermal stability, which are key material parameters that influence the occurrence of radiation damage. Realgar (As_4S_4) represents one of the most light-sensitive [168] and thermally unstable pigments (up to 200 °C) [169], while vermilion (α-HgS) represents a relatively light-stable pigment [170] with a low thermal stability (300 °C) [171]; red lead (Pb_3O_4) is considered a relatively light-stable pigment with a high thermal stability (up to 600°C).

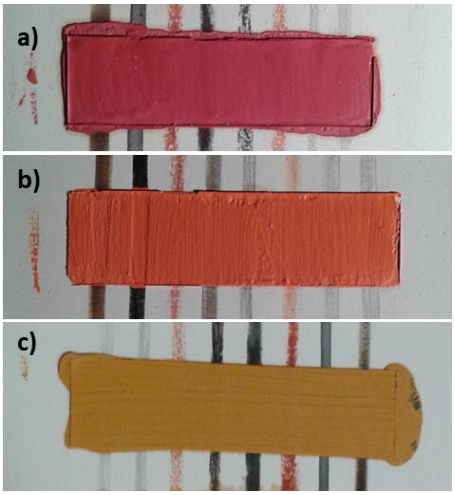

Fig.4. 1 Pictures of the three 15 years old paint mock-ups of a) vermilion (light from Kremer), b) red lead, c) realgar (grade 3 Beijing) mixed with linseed oil and applied on a wooden board with a white preparation layer.

4.2.2. Multi-modal imaging set up for damage monitoring

The monitoring strategy was developed based on the combination of previous experiences: with reflectance specroscopy used to evaluate laser-induced damage on pigments at the ISAAC lab [32,166], and the temperature monitoring while performing laser cleaning to correlate surface temperature with specific laser effects at ISPC-CNR [44]. The combination of these 2 techniques eneables to identify the thermal contribution of a specific laser irradiation, and correlate the relative reflectance spectral change.

The set up for the multi-modal monitoring of laser irradiation is shown in Fig. 4.2. The monitoring consists of recording the VIS-NIR reflectance spectra of the mock-up paint pre-irradiation (120 s) and post-irradiation (300 s). To correlate the reflectance changes with the effects of heat, a thermal imaging device (details in section 3.2.2) was used to monitor the relative trend of the surface temperature during the experiments. Raman spectroscopy, performed with the remote Raman system described in section 3.2.1, was used to assess the spectral modification induced by the laser irradiation. The interrogating laser source is normal to the mock-up, at 3.5 m. Three different CW lasers commonly used for Raman spectroscopy were tested, 532 nm, 785 nm and 1064 nm, at

different spot sizes (from tens of µm to 900 µm), power and exposure times in order to verify the most damaging combination of parameters. The overall range of power investigated varies between 0.015 mW and a maximum of 100 mW. As the investigated pigments are strong Raman scatterers the standard laser irradiation time was set to 10 s, which represents more than a typical integration time to collect a high signal-to-noise-ratio (SNR) Raman spectrum of these pigments. The effect of irradiation time was assessed between 10 s and 450 s. Several irradiation tests were performed on each of the mock-ups. All the tests were performed on previously un-irradiated zones of the mock-up. Some tests were first repeated to check the reproducibility of the measurements (see section 3.1.1), and the results show small variation in the detected temperature over a range of 7% and a variation in the spectral reflectance change ΔR over a range of 0.5%.

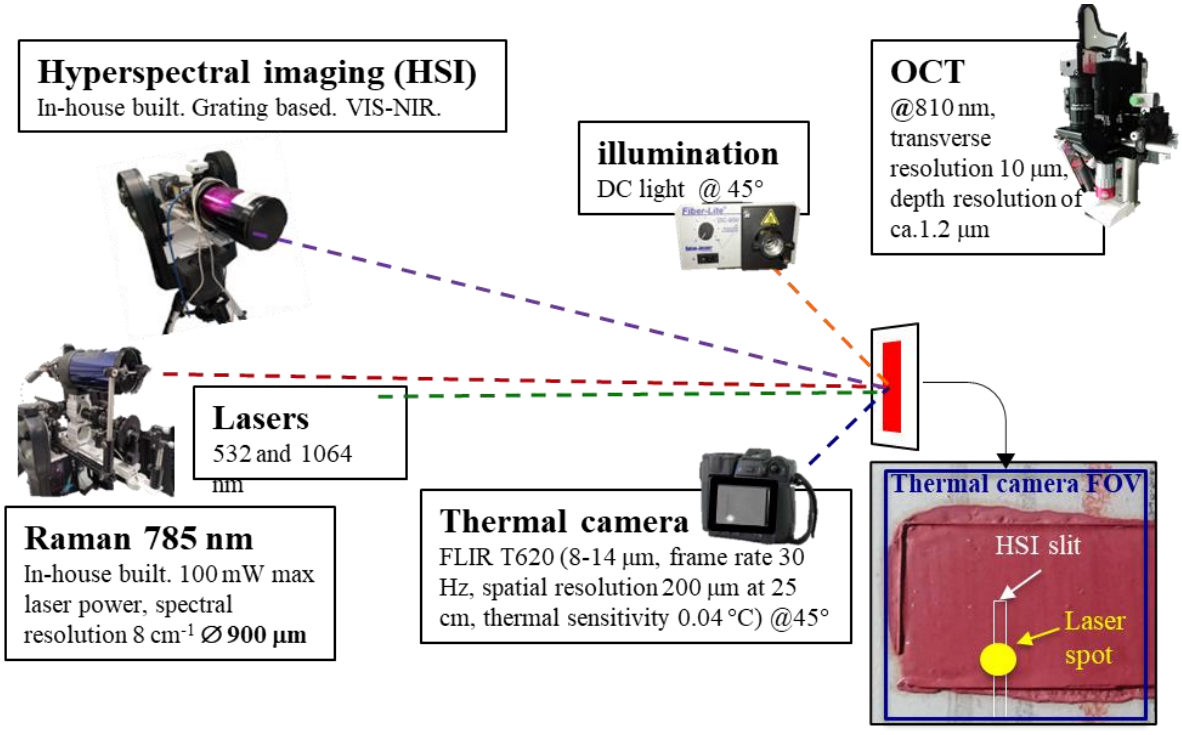

Fig.4. 2 The set-up for monitoring laser induced alterations and a brief description of instrument specifications. The enlarged picture of the sample shows the probing area for each technique: thermal imaging (dark blue box), hyperspectral imaging (HSI) slit

(white rectangle) and the laser irradiation spot for Raman spectroscopy (yellow solid circle).

The damage was evaluated based on the difference spectra between post and pre-irradiation (ΔR) plots. Internal checks on the system stability were enabled using areas along the slit of the HSI far from the position of the laser irradiation where no temperature increase is detected by the thermal camera (see section 3.1.1.3 on damage evaluation). Any ΔR above the level of system stability and noise fluctuation were identified either as permanent or transient damage within the 300 s monitoring post irradiation.

4. 3. Results

4.3.1. Thermally dominant effects

Fig. 4.3 shows the results of the monitoring while irradiating the vermilion oil mock-up with 785 nm and 532 nm lasers at a high laser power of 100 mW. The 785 nm laser produced a spot with a milky appearance and the surface temperature reached 80°C (Fig. 4.3a). The 532 nm laser, strongly absorbed by the pigment, caused a surface darkening, and reached an elevated temperature of 180°C. The VIS-NIR percentage reflectance changes (ΔR) extracted from the hyperspectral images at a single slit position monitored over time are reported in ΔR plots by subtracting the pre irradiation spectra from the post irradiation spectra. The evolution of the ΔR plots is shown at various times immediately after the laser was turned off (from 1 to 300 s) and at different spatial offset from the centre of the laser spot. A short-term ΔR change at 600 nm was detected within the first few seconds post irradiation and this corresponds to a temporary shift towards longer wavelengths at the point of inflection in the typical “S-shaped” reflectance spectrum of semiconductors. The short-term reversion of ΔR at the same wavelength was also detected outside the laser spot and gradually disappeared further out from the laser spot as the surface temperature decreased. The same ΔR and temperature were

detected at the laser spot, when irradiated with the 785 nm laser (Fig. 4.3a, column 3), as at 1 mm away from the laser spot, when irradiated with the 532 nm laser (Fig. 4.3b, column 4), suggesting that the alteration induced by the 785 nm laser at the laser spot is thermally driven. We obtained similar results for realgar (Fig. 4.4) and red lead when irradiating with 785 nm laser, suggesting a thermally dominated effect on all three pigments. The results obtained from irradiation with 785 nm and 1064 nm lasers have no significant differences in terms of changes in reflectance, Raman spectra and surface temperature for all three pigments.

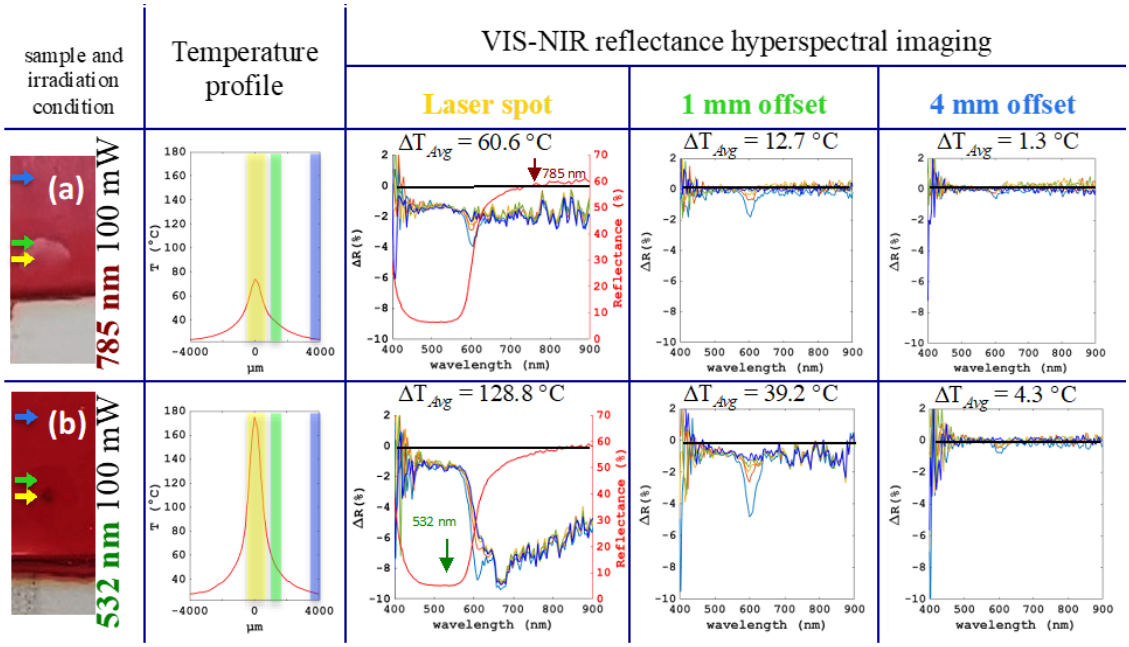

Fig.4. 3 Laser induced alteration dominated by thermal effects: vermilion oil paint mock-up irradiated at 100 mW with a spot size of 900 µm for 10 s with (a) 785 nm laser, and (b) 532 nm laser. Column 1: images of the sample around the irradiated areas (the yellow arrow indicates the position of the laser spot, green arrow is 1 mm offset and blue arrow is 4 mm offset from the laser spot); Column 2: temperature profile just before turning off the laser (yellow, green and blue bands indicate the position of the laser spot, 1 mm and 4 mm offset from the laser spot); Column 3: evolution of ΔR difference spectra measured with the HSI post irradiation at different times compared with pre-irradiation (1 s post irradiation shown in light blue, 5 s orange, 10 s yellow, 60 s green, 300 s dark blue) at the laser spot, and reflectance spectrum of the mock-up prior to irradiation (red curve) is also shown. Column 4: evolution of ΔR spectra 1 mm away from the centre of the laser spot; Column 5: 4 mm away from the laser spot. The average temperature change (ΔT_{Avg}) is indicated in each case.

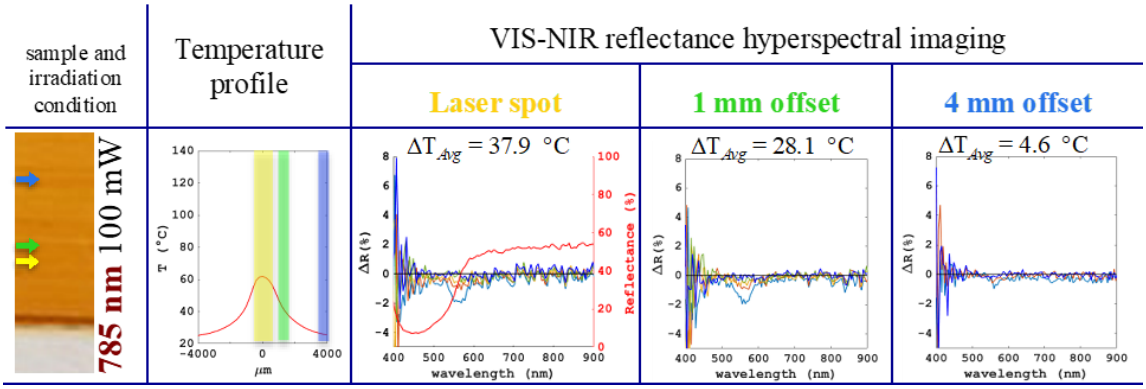

Fig.4. 4 The thermal effect of 785 nm on realgar mock-up irradiated with 785 nm laser with a spot size of 900 µm at 100 mW for 10 s. Column 1: images of the irradiated areas (the yellow arrow indicates the position of the laser spot, green arrow is 1mm offset and blue arrow is 4mm offset from the laser spot); Column 2: temperature profile just before turning off the laser (yellow, green and blue bands indicate the position cantered at the laser spot, 1 mm and 4 mm offset from the laser spot); Column 3: ΔR difference reflectance spectra (1 s light blue, 5 s orange, 10 s yellow, 60 s green, 300 s dark blue) at the position of the laser irradiation, and the reflectance spectrum of the mock-up prior to irradiation (red curve). Column 4: evolution of ΔR spectra 1 mm away from the centre of the laser spot; Column 5: 4 mm away from the laser spot. The average temperature change (ΔT_{Avg}) is indicated in each case.

Further information can be extracted by comparing the hyperspectral cube and the thermal data cube in time and spatial extent as shown in Fig. 4.5. The time evolution of ΔR at 600 nm (Fig. 4.5a) gradually tends to a plateau as the temperature approaches room temperature. As ΔR at all wavelengths plateaus at a non-zero value (-2%) within the laser spot, there is an additional permanent change to the reversible change (Fig. 4.3a). Fig. 4.5b shows the intensity profile of the beam, the ΔT profile, and the reversible ΔR profile across the laser spot and its surrounding. Within the laser spot, the temperature and reversible ΔR profiles show a similar spatial trend; outside of the laser spot, the reversible ΔR profile show a deviation from the ΔT spatial trend, with a more gradual decrease in ΔR from the laser spot and an abrupt decrease occurring when the edge of the substrate was reached (Fig. 4.5b). The Ultra high-resolution OCT was used to image the damaged area to obtain the RMS surface roughness map (see details in section 3.2.3), showing a reduction in surface roughness, which is double the diameter of the laser spot (Fig. 4.5c). It is important to note that permanent damage detectable by reflectance changes correlated with significant temperature rise (Fig. 4.3), are visible by eye but not by any Raman spectral changes (Fig.4.6). Moreover, no amorphization or

phase transition was found when analysing thin sections obtained from the two irradiated spots with SR µ-XRPD mapping. Spectral reflectance monitoring allows a much more sensitive detection of permanent surface changes compared to Raman and even SR µ-XRPD.

The milky appearance of the damaged spot obtained with 785 nm laser is due to changes in the scattering properties of the pain layer. The temperature rise induced by the laser irradiation caused the partial melting of the binder and after cooling a reduction of surface roughness was induced. Chemical structural changes of the pigment do not seem to contribute to this damage, while chemical or morphological changes on the binder have not been ascertained yet.

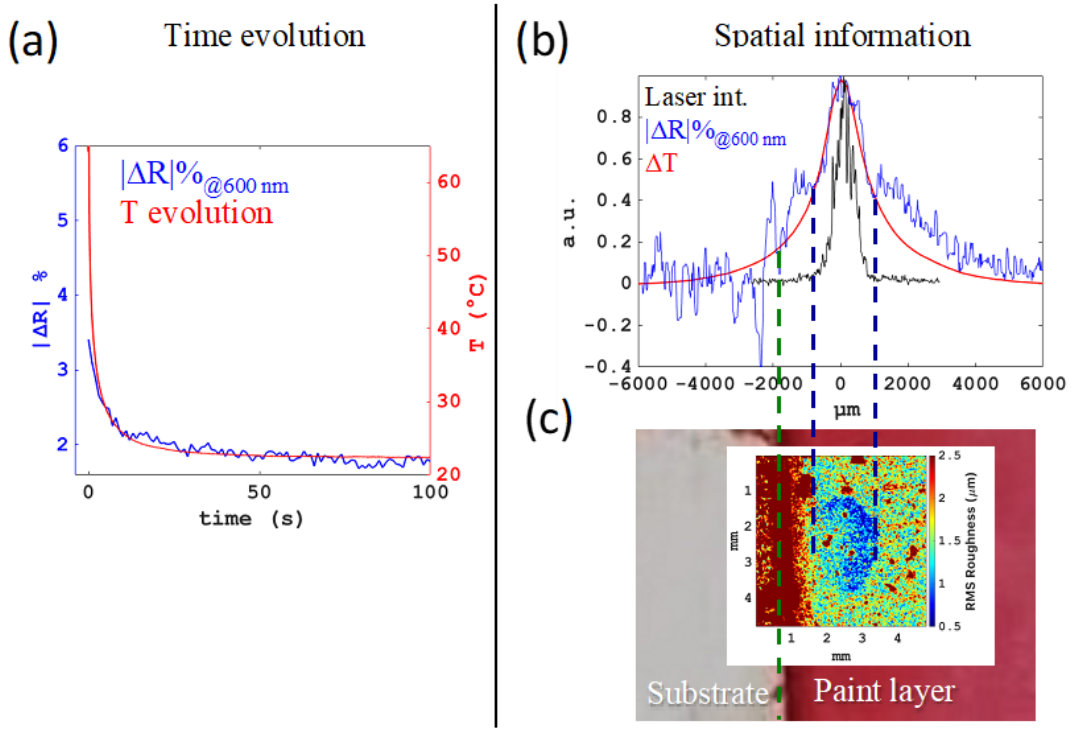

Fig.4. 5 Time and spatial evolution of the alteration. The same irradiation test of Fig. 4.3a on vermilion mock-up with 785 nm: (a) the time evolution of the reversible ΔR at 600 nm (blue curve) and the temperature evolution (red curve); (b) the spatial profile of the change in temperature ΔT (red), the reversible ΔR at 600 nm (blue) and the laser intensity (black). The spatial resolution of thermal camera (T), HSI (ΔR) and measurement of laser beam profile are 200 µm, 15 µm and 4.4 µm respectively. The curves are normalized to the peak value. (c) The RMS surface roughness map obtained within a 50 µm window from the ultra-high resolution OCT cube. The dark blue dashed lines define the edge of the damage. The green dashed line delineates the edge between the paint layer and the substrate.

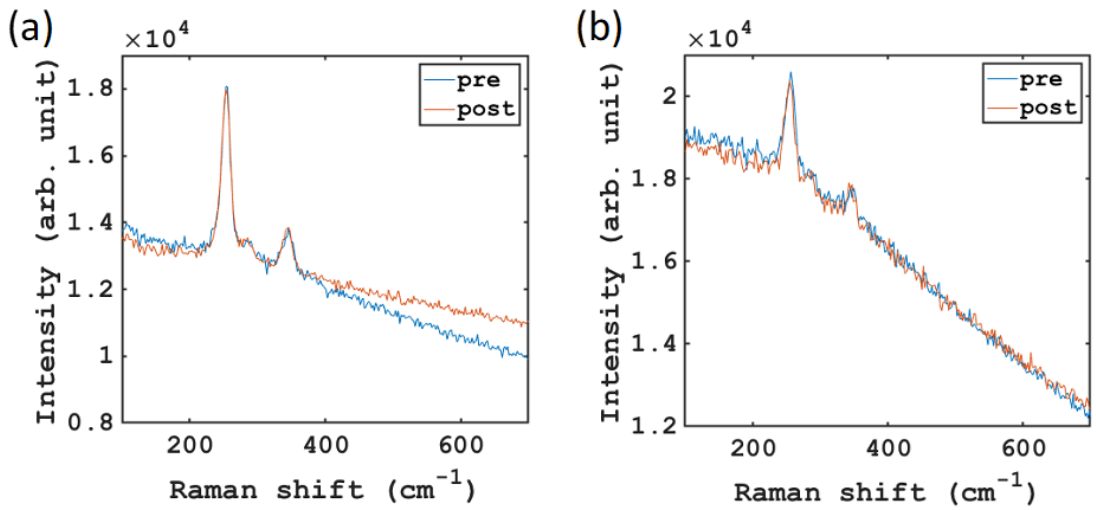

Fig.4. 6 Raman spectra collected with 785 nm laser for the irradiations test a) during the 785 nm irradiation with 900 µm spot, 100 mW for 10s; and b) before and after irradiation with 532 nm laser at 100 mW, 10 s with a 900 µm spot size. The background was shifted vertically to better visualize the differences in the Raman peaks.

A decrease of the net peak counts of the main Raman bands of vermilion were detected only when irradiating with 532 nm at a much higher laser intensity, achieved by reducing the spot size from 900 to 180 µm while keeping the laser power and exposure time fixed. In this case a more severe darkening was observed (Fig. 4.7a). Vermilion darkening has been reported both as a natural degradation occurring in paintings [79,172–174] and induced by laser irradiation [75,101]. The mechanisms and the compounds that impart this darkening are still of open debate and due to the difficulty in identifying the degradation products and the highly superficial nature of the degradation. The laser-induced darkening has mainly been attributed to the formation of the black metacinnabar (β-HgS) [58,79]. In the field of laser processing, a recent method has been proposed to produce the beta phase from the alpha phase using a pulsed 1064 nm laser [175]. Other recent studies explain the darkening as also due to a progressive amorphization of the alpha phase and possible defected alpha phase due to sulfur deficiencies [39,176]. In our experiments, the SR µ-XRPD mapping (details of the technique in section 3.2.4) of the thin section of the most severely darkened area (Fig. 4.7)[155] revealed a reduction of the peaks ascribed to cinnabar on the surface and a slight asymmetric broadening of some cinnabar peaks. Extracting diffraction patterns from the cross-sectional layers (the top 5 µm, the sub-surface layer 5-10 µm in depth,

and the bulk of the paint layer 10 to 20 µm in depth) (Fig. 4.7d), it is possible to observe also a weak peak appearing as a shoulder at a smaller angle next to the most intense peak of cinnabar, which can indicate the presence of metacinnabar (the 200 Bragg peak, 9008849 COD inorganics [177]). All these features could indicate the possible formation of very small particles of metacinnabar produced on the top few microns of the irradiated area, as shown by the Red-Green false colour combination map in Fig. 4.7c. Thus, a surface darkening detected by HSI was produced on the vermilion oil mock-up at 100 mW both with a spot size of 900 µm (Fig. 4.3b) and with a spot of 180 µm (Fig. 4.7). However, only in the latter case, where the intensity is 20 times higher, a subtle crystal transformation in µ-XRPD was detected and a reduction of the main Raman peaks of vermilion was observed (Fig.4.8). The darker surface of the high intensity test absorbs many more incident photons, leaving significantly less photons for Raman scattering of the unaltered vermilion below the surface, and hence a reduced Raman signal of vermilion. The predominant thermal contribution to this darkening effect is clear as each darkening were associated with a significant temperature rise, nevertheless the possible additional contribution of photochemical effect cannot be excluded.

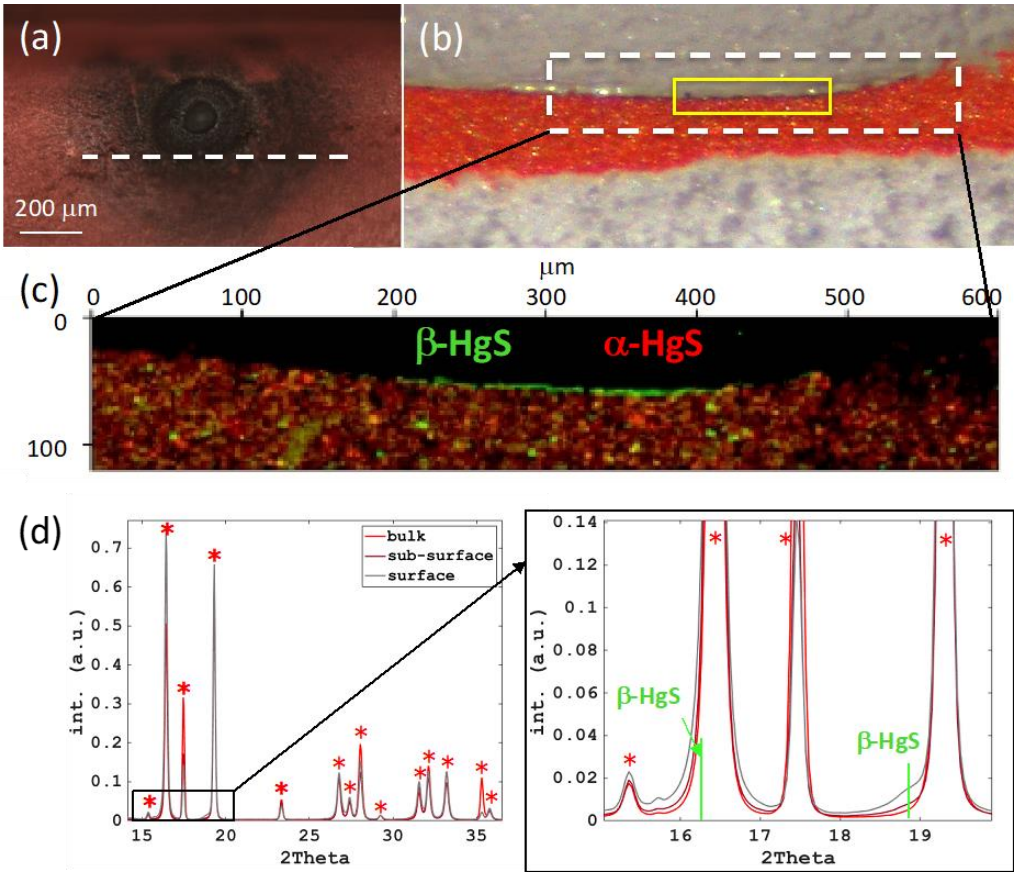

Fig.4. 7 Laser induced crystal structural change of vermilion. Results of vermilion oil mock-up irradiation with the 532 nm laser for 10 s at 100 mW and a spot size of 180 µm. (a) the optical microscope image of the darkened surface; (b) the thin section of 10 µm obtained from the sample (yellow area corresponds to laser spot, dashed white rectangle is the analysed area); (c) the Red/Green composite SR µ-XRPD map of respectively α-HgS/β-HgS; (d) the average XRD patterns from the first 5 µm of the surface (grey curve), from sub-surface 5 to 10 µm (dark red curve) and from the bulk 10-20 µm (red curve), with * indicating the Bragg peaks of α-HgS and vertical green lines indicating the β-HgS Bragg peaks.

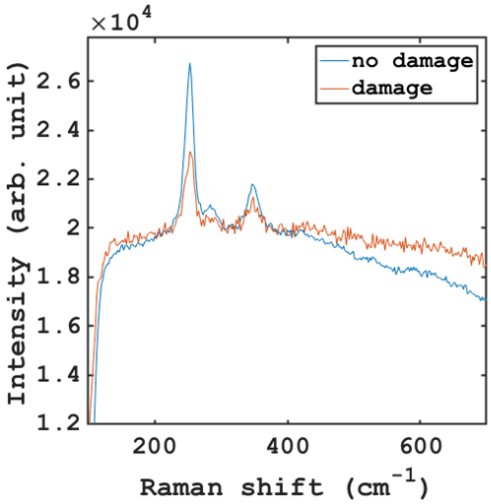

Fig.4. 8 Raman spectra collected with the micro-Raman 785 set-up collected on non-damaged area (light blue line) and the damaged area (orange line) after irradiation of vermilion oil mock-up with 532 nm laser at 100 mW for 10 s and a spot size of 180 µm. The background was shifted vertically to better visualize the differences in the Raman peaks.

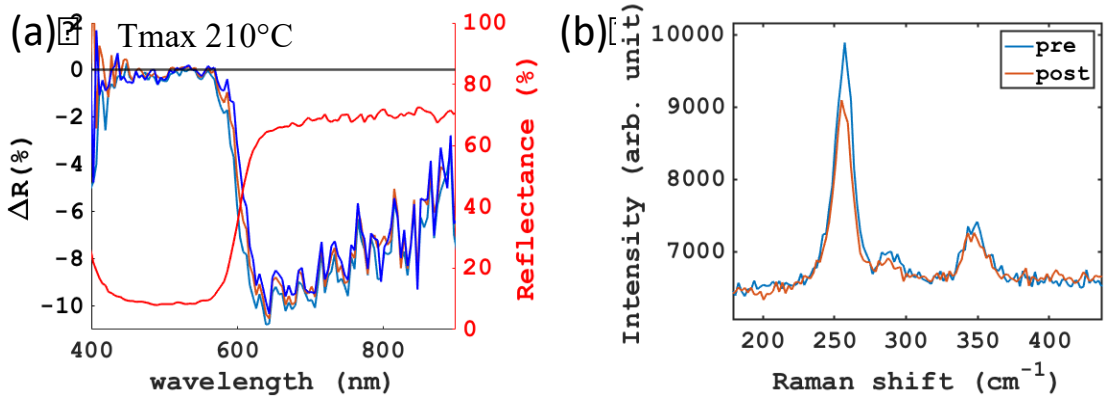

Fig.4. 9 The irradiation of vermilion pigment powder with 532 nm laser at 100 mW, 10 s and a spot size of 900 µm, reaching a maximum temperature of 210°C. (a) ΔR VIS-NIR spectral changes (1 s light blue, 5 s orange, 10 s yellow, 60 s green, 300 s dark blue post irradiation, in red the reference spectrum before irradiation); (b) the Raman spectra before (light blue) and after (orange) 532 nm laser irradiation collected with the 785 nm Raman system. The background was shifted vertically to better visualize the differences in the Raman peaks.

To assess the effect of the binding medium, the irradiation test at 100 mW using the 532 nm laser was replicated on the vermilion powder. In this case, the temperature rose to 210 °C, a more severe darkening occurred, and the main Raman peak of vermilion reduced in intensity (Fig. 4.9). The different behaviour of the pigment powder and the oil paint of the same pigment may suggest a better heat dissipation of the oil binder, which was suggested also in another study [107]. This comparison highlights how important it is to study the laser interaction of the pigments in the specific binding medium of interest, to avoid misleading conclusions on the potential damage.

Intensity is known to be one of the key parameters that increase damage risk, but a prolonged exposure (increase of fluence or total energy per unit area irradiated) may also have its impact that needs to be investigated. At a laser intensity where a short irradiation time (10 s) did not cause permanent damage with the 785 nm laser, the prolonged exposure (up to 450 s) did not cause further damage for any of the three pigments either (see Fig. 4.10 for an example on red lead). In these cases, a temperature plateau is reached after a few seconds of irradiation. This data suggests that for safe operation at 785 nm where thermal effects dominate with these pigments, it is preferable to operate at low laser intensity with increased exposure time to obtain the same SNR Raman signal.

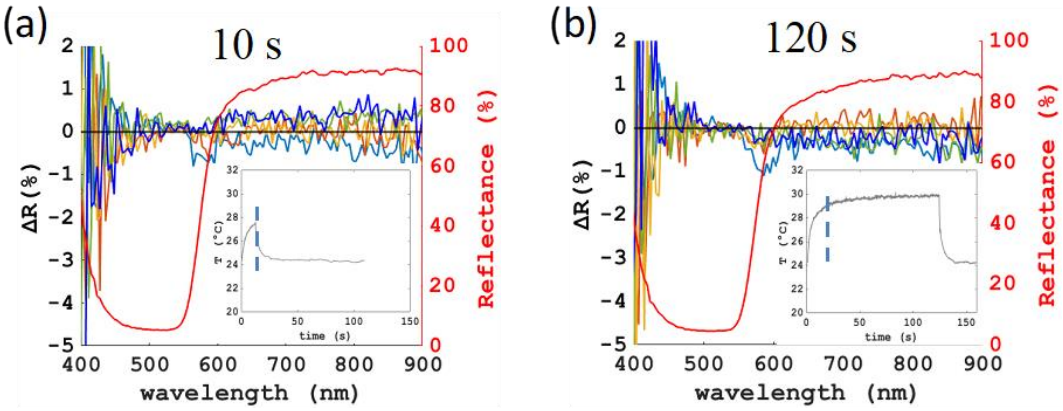

Fig.4. 10 The effect of prolonged exposure of red lead paint mock-up with 785 nm laser at 100 mW with a spot size of 900 µm for (a) 10 s irradiation time and (b) 120 s. The ΔR VIS-NIR spectral changes (1 s light blue, 5 s orange, 10 s yellow, 60 s green, 300 s dark blue post irradiation, in red the reference spectrum before irradiation). In the insets, the temperature evolution. The dashed light blue line indicates in both graphs the 10 s time stamp.

4.3.2. Contribution of photochemical effects

Fig. 4.11 shows the results of a realgar oil paint mock-up irradiated with the 532 nm laser, where different types and extents of damage occurred depending on the intensity and exposure time. The high-power test (100 mW) induced a permanent increase of percentage reflectance around 540 nm (up to 7%) and a significant temperature rise to 128°C (Fig. 4.11a). The heat dissipation away from the irradiated spot resulted in the detection of only a reversible ΔR at around 565 nm, which gradually disappeared away from the laser spot. With a reduced power of 2.8 mW, the temperature rise was minimal (2-3°C) and only the permanent damage at around 540 nm was present though considerably reduced within the laser spot (Fig. 4.11b). In comparison, a similar temperature rise of 2-3°C was detected 4 mm away from the laser spot in the high-power test (Fig. 4.11a), where only the reversible ΔR at 565 nm was detected, indicating that a purely thermal contribution of 2-3°C without photon irradiation does not cause permanent damage. Therefore, the permanent damage seen in the low-power test at the laser spot is likely to be of non-thermal origin. The effect of a prolonged exposure time was tested at low power (2.8 mW) irradiating for 450 s (Fig. 4.11c). The temperature rise (2-3°C) is comparable to the 10 s exposure but a permanent reflectance change of -11% (c.f. 7% for 10 s) appeared at a different wavelength of 580 nm (c.f. 540 nm for 10 s). The damage is visible by eye as an orange spot with dimensions comparable to the laser spot size (900 μm). In this non-thermal dominated effect, the prolonged exposure resulted in increased damage, in contrast to the thermally dominated case observed with 785 nm laser.

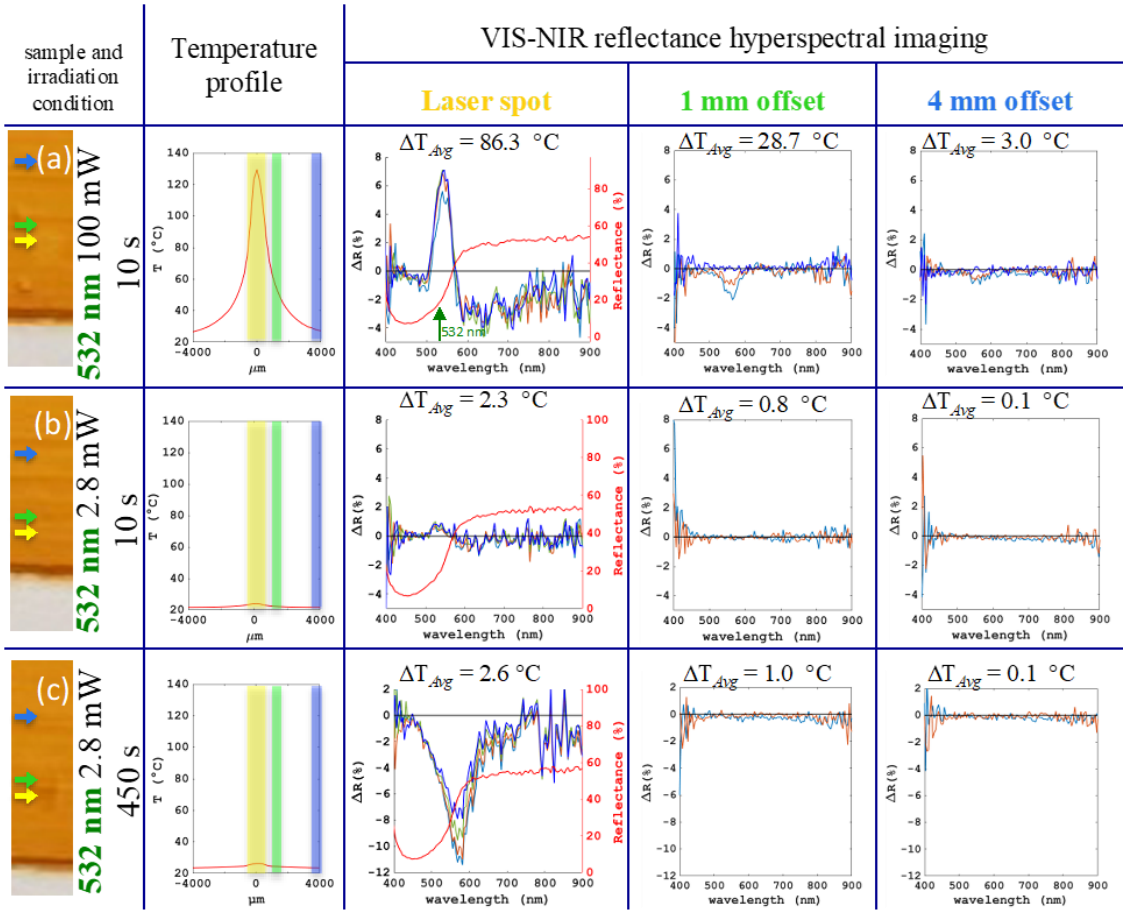

Fig.4. 11 The thermal and photochemical effects on realgar paint mock-up irradiated with 532 nm laser with a spot size of 900 µm (a) at 100 mW for 10 s; (b) at 2.8 mW for 10 s; (c) at 2.8 mW for 450 s. Column 1: images of the irradiated areas (the yellow arrow indicates the position of the laser spot, green arrow is 1 mm offset and blue arrow is 4 mm offset from the laser spot); Column 2: temperature profile just before turning off the laser (yellow, green and blue bands indicate the position centred at the laser spot, 1 mm and 4 mm offset from the laser spot); Column 3: ΔR difference reflectance spectra (1 s light blue, 5 s orange, 10 s yellow, 60 s green, 300 s dark blue) at the position of the laser irradiation, and the reflectance spectrum of the mock-up prior to irradiation (red curve). Column 4: evolution of ΔR spectra 1 mm away from the centre of the laser spot; Column 5: 4 mm away from the laser spot. The average temperature change (ΔT_{Avg}) is indicated in each case.

The capability of hyperspectral imaging to distinguish the spatial extent of different reflectance changes within the same dataset is highlighted in Fig. 4.12. We can see that under high power (100 mW) at 532 nm, the permanent reflectance change ΔR at 540 nm

appeared only within the laser spot where photons were incident on the sample (Fig. 4.12a), while the reversible ΔR at 565 nm steadily decreased away from the laser spot and showed a similar trend to the temperature profile (Fig. 4.12b). This data suggests the presence of two competing effects, thermal and non-thermal, when irradiating the realgar paint mock-up with 532 nm laser at high intensity.

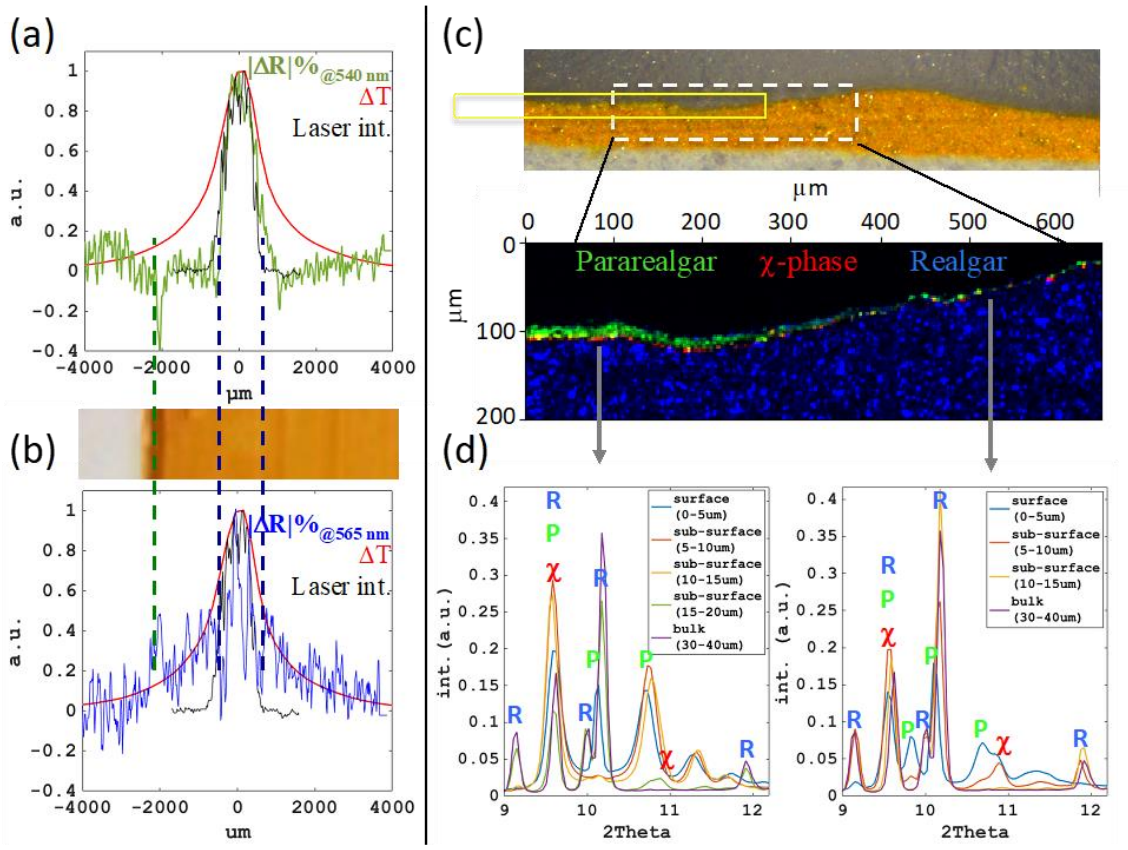

Fig.4. 12 Photochemical and thermal contributions in the alteration of realgar paint sample irradiated for 10 s with 532 nm laser at 100 mW and spot size of 900 μm. (a) spatial variation of the permanent reflectance change ΔR at 540 nm compared with the temperature and the laser intensity profile; (b) the reversible reflectance change ΔR at 565 nm; (c) the thin section (10 μm) of the sample (yellow area corresponds to laser spot, dashed white rectangle is the analysed area) and the Red/Green/Blue composite SR μ-XRPD map of χ phase/pararealgar/realgar respectively; (d) the averaged diffraction patterns from each 5 μm in depth of the thin section from the area irradiated by the laser and from an area out of the laser spot. Realgar (R), pararealgar (P) and the χ phase (χ) were identified.

It is well known that realgar is particularly susceptible when irradiated at around 500–670 nm as a photochemical transformation to pararealgar occurs [62]. Several studies show that the process undergoes several intermediate steps related to a progressive, randomly distributed change of the As_4S_4 into As_4S_5 cages [178–180], also called χ phase in early literature [62]. In our experiments, the possible crystal structure change of realgar to pararealgar induced by 532 nm laser can be seen in the changes observed in the Raman spectra collected before and after the irradiation. However, no peaks ascribed to pararealgar were detected and only a decrease of intensity of the main realgar peaks after irradiation was observed for the high-power short-exposure test and the low-power long-exposure test (Table 4.1, Fig.4.13). To further assess the possible formation of pararealgar, a thin section of these two tests subjected to the same total energy of radiation, high-power short-exposure and the low-power long-exposure, were analysed with SR μ-XRPD mapping. Extracting diffraction patterns from every 5 μm going from surface to bulk shows that in the irradiated area of the high-power test (Fig. 4.12c and d), a 10-15 μm layer of pararealgar was produced followed by a thin intermediate layer with a small quantity of the χ phase with pararealgar before reaching the unreacted bulk. Peaks ascribed to the presence of a discontinuous thin layer (ca. 5 μm) of pararealgar with a higher amount of the intermediate χ phase are already present due to the age of the mock-up (15 years old) as shown in an area outside the laser spot (Fig. 4.12d, diffractogram on the right). A similar composition to the pristine paint is detected in the SR μ-XRPD map of the low-power long-exposure test (Fig. 4.14), suggesting that this type of irradiation did not clearly produce a pararealgar layer. It is known that for some pigments, and in specific intensity range, reciprocity can fail, meaning that the amount of degradation depends not only on the total energy that the sample is exposed to, but also the light intensity. It has been found that in the case of broadband light-induced alteration of realgar, reciprocity does not hold even within one order of magnitude in intensity [181]. In our case, reciprocity do not hold over one order of magnitude in power and the failure of the reciprocity principle may be attributed to a high contribution of thermal effects at high power and dominance of non-thermal effects (photochemical) at low power.

Table 4. 1 Raman monitoring of realgar paint mock-up irradiated with 532 nm laser.

532 nm on realgar *	Δ Raman shift (cm^{-1}) †	Δ net peak counts ‡
2.8 mW, 10 s	-0.3 ± 0.8	-12.6 ± 13.5
2.8 mW, 450 s	-0.7 ± 0.8	**-40.7** ± 11.1
100 mW, 10 s	-0.3 ± 1.0	**-47.3** ± 12.6

* Irradiation of the paint mock-up with a spot size of 900 µm.

† Raman spectral difference in peak position between pre and post irradiation of the main characteristic peak of realgar (354 cm^{-1}). Raman spectra collected with 785 nm.

‡ Raman spectral difference in neat peak counts between pre and post irradiation of the main characteristic peak of realgar (354 cm^{-1}).

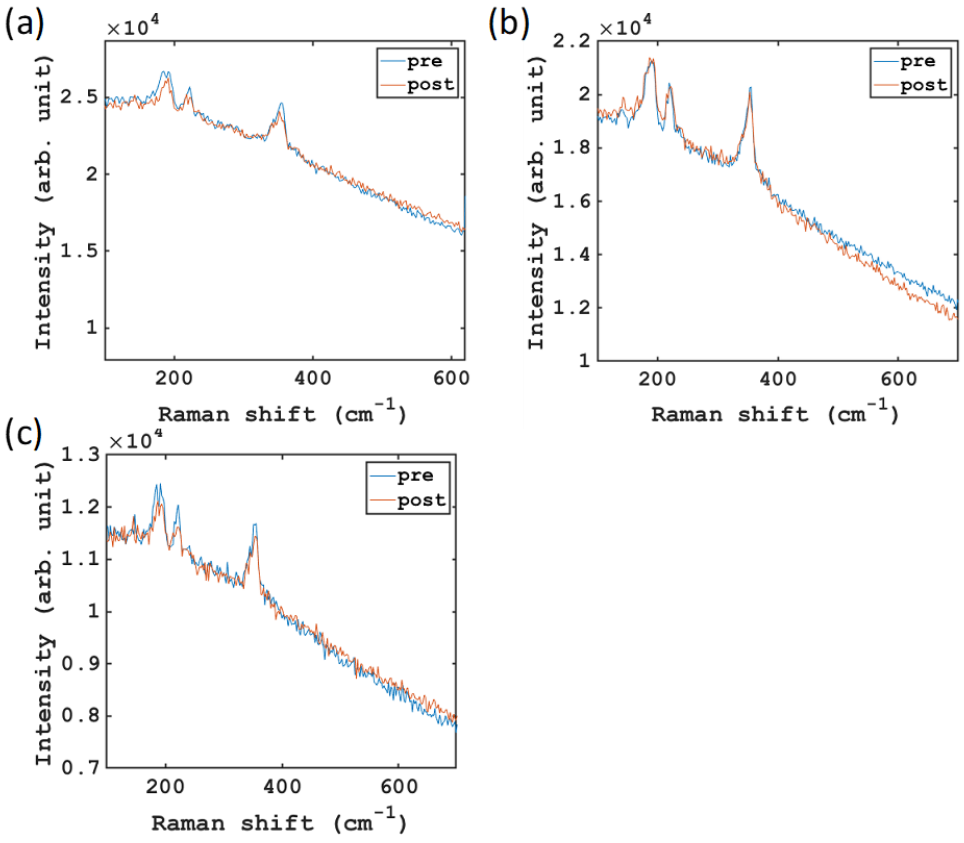

Fig.4. 13 Raman spectra collected with 785 nm laser before (light blue) and after (orange line) irradiation of realgar oil mock-up with the 532 nm laser and a spot size of 900 µm with a) 100 mW for 10 s; b) 2.8 mW for 10 s; c) 2.8 mW for 450 s. The background was shifted vertically to better visualize the differences in the Raman peaks.

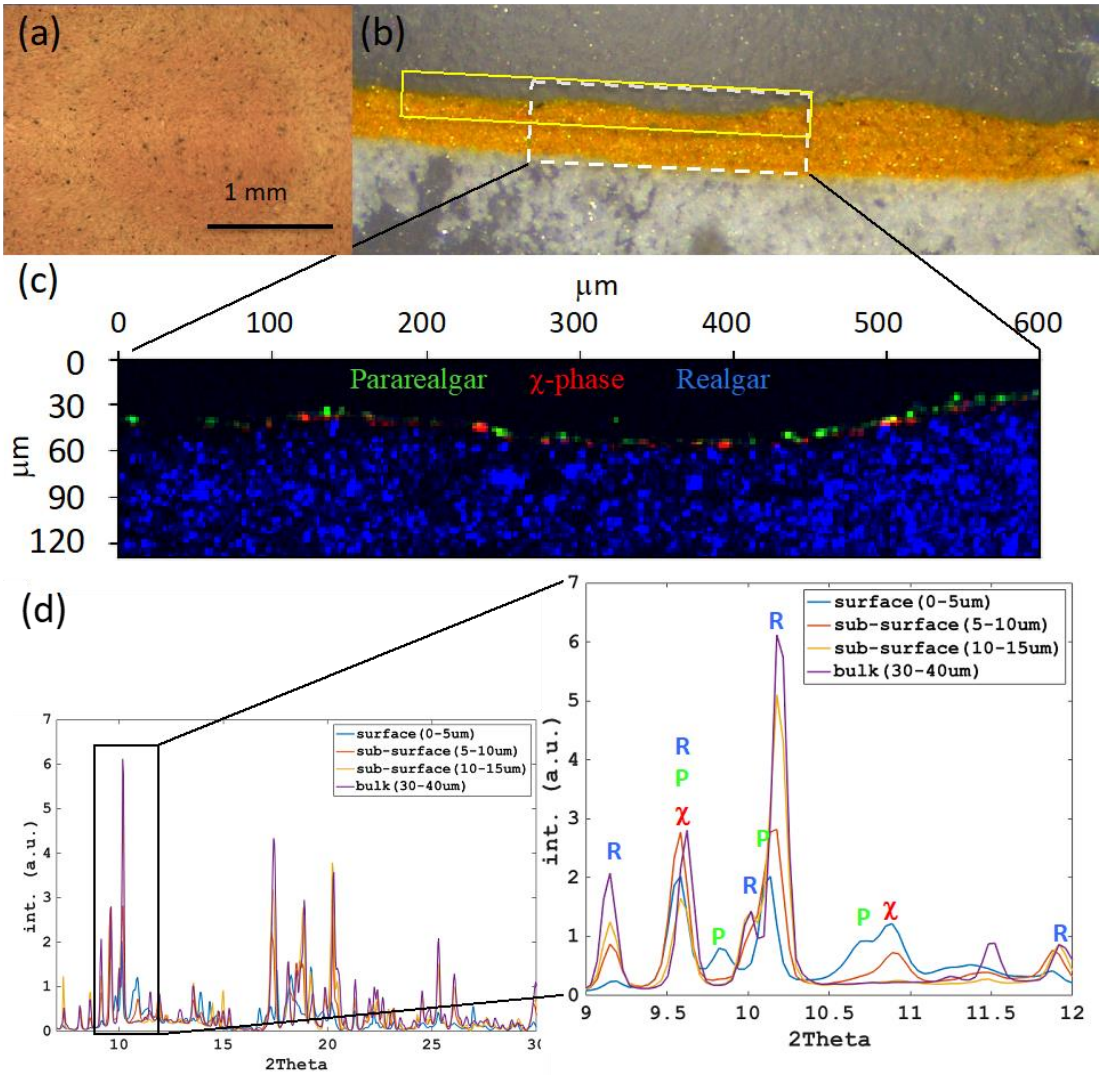

Fig.4. 14 The structural changes of realgar irradiated with a prolonged exposure with 532 nm laser at 2.8 mW for 450 s with a spot size of 900 µm. (a) optical microscope image, (b) the thin section of 10 µm of the same sample examined by synchrotron (SR) µ-XRPD (yellow box corresponds to laser spot, dashed white rectangle is the analysed area) and (c) the Red/Green/Blue composite SR µ-XRPD map of respectively χ phase/pararealgar/realgar; (d) the average diffraction pattern at different depth of the thin section from the area irradiated by the laser. Realgar (R), pararealgar (P) and the χ phase (χ) were identified.

4.3.3. Identification of damage prediction marker

The interaction between the 785 nm laser and the investigated pigments has shown a predominant thermal effect. In this regime, by increasing the laser power (Fig. 4.15) we observed that the first alteration detected is a reversible spectral reflectance change ΔR (Fig. 4.15b), and permanent damage eventually appeared only when the laser power was increased further (Fig. 4.15c and 4.15d). The occurrence of a reversible ΔR prior to permanent damage has been observed in all three pigments irradiated with the 785 nm laser. This data suggests that reversible ΔR can be identified as a damage prediction marker. In the predominantly photochemical effect that occurred in the case of realgar with 532 nm laser at low powers, a prediction marker was not detected. Nevertheless, the very high sensitivity of the HSI allows detecting even subtle changes (Fig. 4.11b) not detected by Raman or SR μ-XRPD, nor by the naked eye.

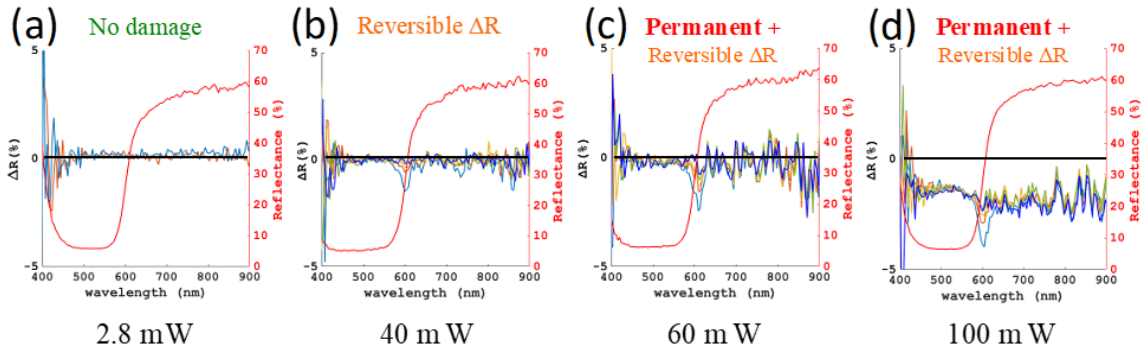

Fig.4. 15 The reversible ΔR as prediction marker: the ΔR VIS-NIR changes (1 s light blue, 5 s orange, 10 s yellow, 60 s green, 300 s dark blue) and initial reflectance spectrum (in red) of vermilion oil mock-up irradiated with the 785 nm laser with a laser spot of 900 μm for 10 s at increasing laser power: (a) 2.8mW, (b) 40 mW; (c) 60 mW; (d) 100 mW.

4.3.4. Safety threshold

The identification of LIDT is generally performed by varying laser power for a given setup and is expressed in terms of the minimum laser intensity at which damage is observed. When dealing with Raman spectroscopy for sensitive materials, such as heritage objects, a balance must be struck between efficiency in collecting Raman photons and safe limits to avoid damage. Thanks to the reversible reflectance changes (ΔR) appearing prior to thermally dominated permanent damage, we can use this prediction marker to objectively define the safety threshold.

As shown in the earlier sections, apart from intensity, the duration of irradiation can contribute to the damage. Only recently, it was found that the laser spot size has an effect as well, independent from intensity [101,166]. It is quite common to refer to micro-Raman as a riskier technique compared to portable Raman, due to the smaller spot size exploited in micro-Raman (from hundreds of μm for portable devices to just few μm for micro-Raman) that increases considerably the intensity for a given laser power [71]. This consideration assumes that the intensity damage threshold is independent of other laser parameters. However, by plotting safety threshold (i.e., laser intensity when only reversible ΔR is observed) and the LIDT (i.e., at the threshold of permanent ΔR appearing) at fixed exposure time for various spot sizes between 40 μm and 900 μm (Fig. 4.16a), it is clear that spot size has a considerable effect. If we compare spot sizes of 40 μm and 900 μm, the safety threshold in laser intensity is at least 90 times lower for the larger spot size than that for the smaller one, while in contrast, the safety threshold in laser energy (or power at the same irradiation time) is around 5 times higher for the larger spot size (Fig. 4.16b). This means that in this example, under safe operation, the larger spot size can be up to 5 times more time efficient in collecting Raman photons than the smaller spot size, assuming the total laser energy incident at the sample is proportional to the Raman photons generated. Delivering the same 532 nm high laser intensity (20.8 W/cm^2) with different spot sizes on vermilion mock-up, shows that the bigger the spot the more severe the damage and the higher the surface temperature (Fig. 4.16c). Therefore, for a comprehensive assessment of damage and safety threshold,

not only intensity has to be considered but instead the 3 experimental parameters: power, duration of irradiation, and spot size in combination.

The spot size effect can clearly be the result of better heat dissipation in smaller volume than those of larger spot and volume as already hypothesized in previous works [101,166]. However, it is interesting to note that this trend is observed not only on vermilion oil paint with a high intensity laser, but also on realgar at a low intensity (0.5 W/cm^2) where there is no significant temperature rise detected (Fig. 4.16d).

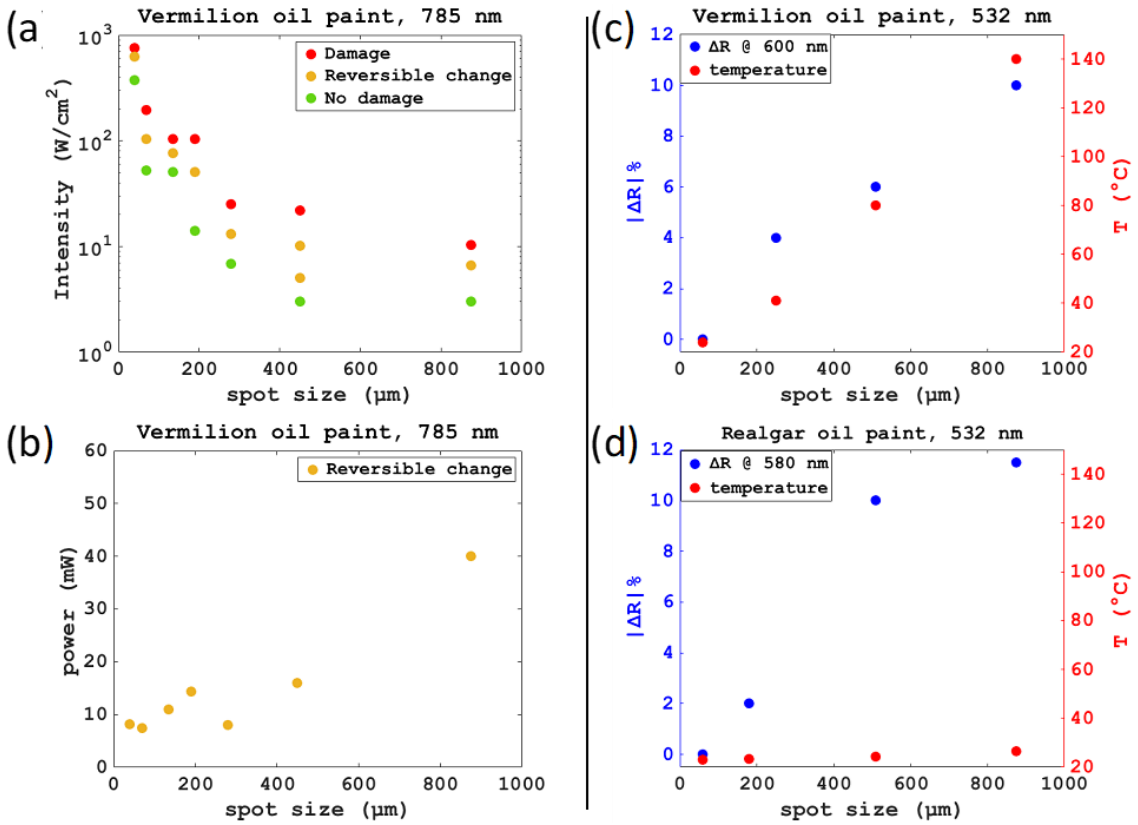

Fig.4. 16 The safety threshold and the effect of spot size. (a) intensity damage threshold (red, corresponding to permanent reflectance changes, ΔR), safety threshold (orange, corresponding to only reversible reflectance changes) and no alteration (green, no reflectance changes) for different spot sizes of 785 nm laser irradiation for 10 s on vermilion oil paint mock-up and in (b) the corresponding incident power at each spot size for safe operation. (c) the maximum absolute spectral reflectance changes |ΔR| after 1 s of 532 nm laser irradiation with different spot sizes at the same intensity of 20 W/cm2 for 10 s for vermilion mock-up (|ΔR| at 600nm) and (d) at 0.5 W/cm2 for 450 s for realgar mock-up (|ΔR| at 580 nm).

A possible explanation for the spot size on the realgar mock-up, would be the contribution of a surface effect in the damage, like the interaction with the oxygen in the environment. Therefore, some tests were repeated irradiating the realgar paint mock-up while flowing nitrogen gas directly on the target to simulate an anoxia environment (Fig. 4.17). The results show that the ΔR between the irradiation in air and under nitrogen environment are similar in extent, even repeating the same measurement twice (Fig. 4.17a,b,d,e). The only small difference can be observed in the short (10 s) irradiation tests between air and nitrogen atmosphere, as in the latter a small increase at 550 nm of ca. 0.4% is detected. Therefore, still unclear is the origin of the spot size effect in absence of thermal contribution.

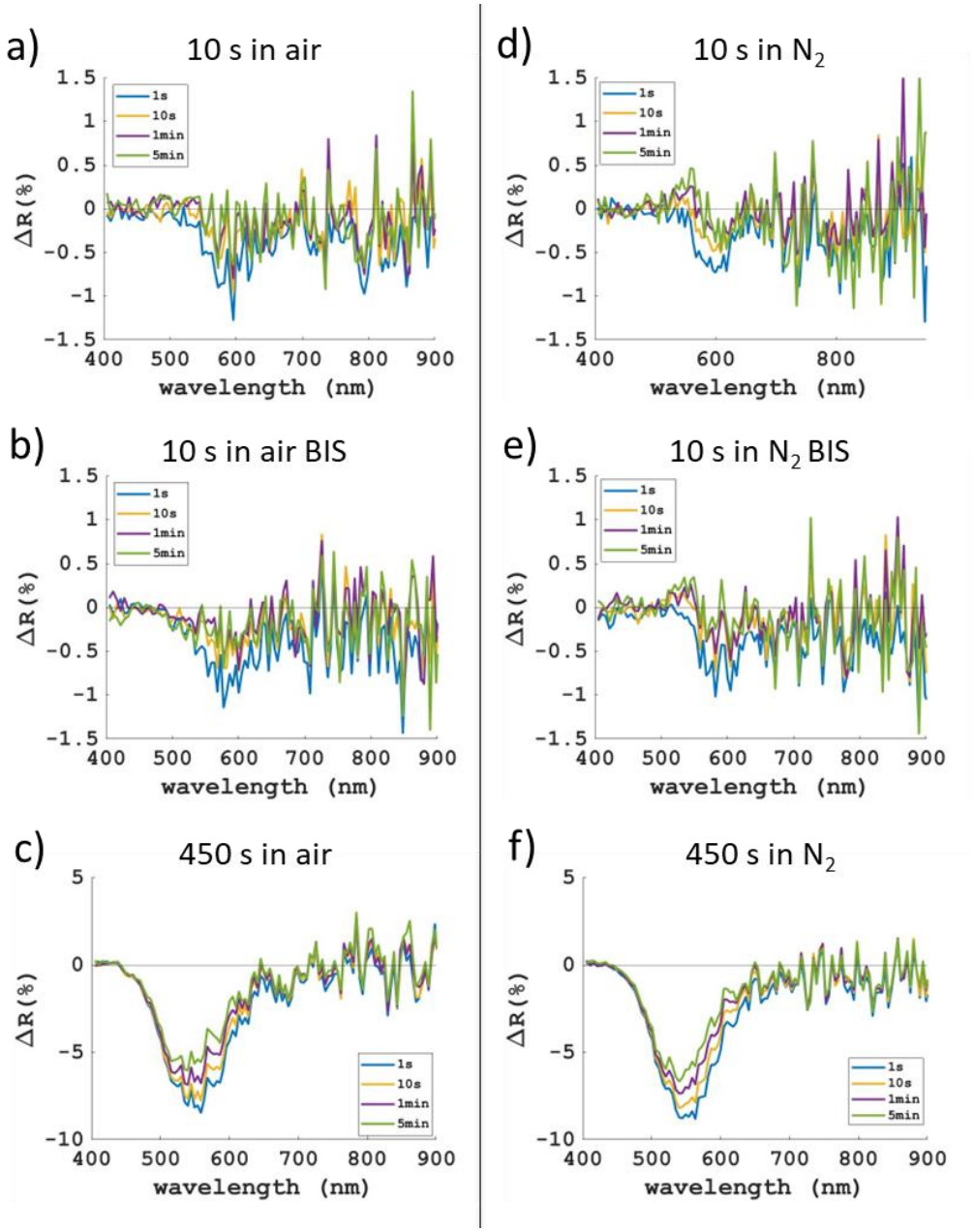

Fig.4. 17 The ΔR plots of the irradiation tests on realgar paint mock-up with 532 nm laser with 1 mW and a spot size of 440 µm; a) and b) in air for 10 s and c) for 450 s. d), e) and f) are the same tests but with nitrogen (N_2) gas purging in front of the target.

4.3.5 Survey of radiation damage on different pigments with 780 nm laser

Up to now only semiconductor pigments were tested and a reversible ΔR has been detected at the point of inflection of the typical “S shape” reflectance of these pigments. The reversible ΔR change has been associated to a measured surface heating but the origin is unclear. The plausible hypothesis are mainly 2: it occurs at the point of inflection, as it represents the sharpest reflectance feature in this case, or it is directly related to a temporary shift of the band gap induced by heat that reduces the energy level between the valence and conduction bands, known to occur at high temperature for example for semiconductor photocatalysts [182]. To expand the survey to more common pigments having different reflectance spectral shape and different composition (including dielectrics), the 780 nm laser was used to perform irradiation tests on the following pigments applied in animal glue on a polycarbonate substrate: lead white (lead carbonates), zinc white (zinc oxide), titanium white (titanium dioxide, rutile polymorph), Prussian blue (hydrated iron hexacyanoferrate complex), malachite (hydrated copper carbonate), chrome green (chrome oxide), brown ochre (iron hydroxide), and orpiment (arsenic sulphide). The irradiations were performed on all mock-ups with the same parameters: 10 s of irradiation at 35 mW with a spot size of 450 µm. These tests intend to be a preliminary survey to identify the materials which show interesting reflectance changes for further investigation in the near future.

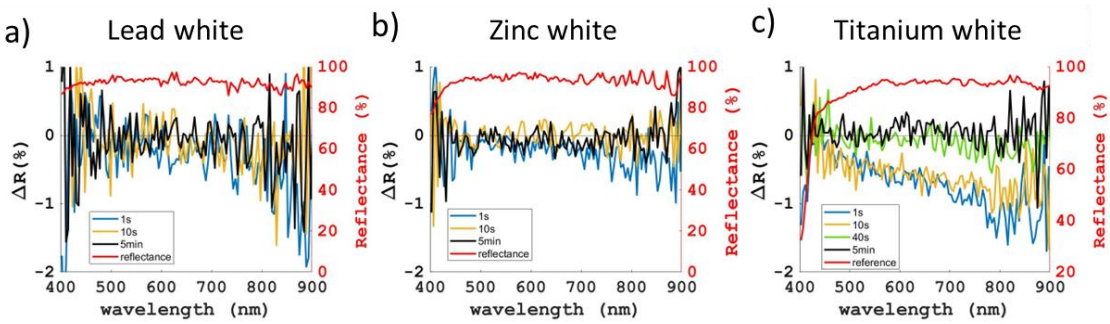

Fig.4. 18 ΔR plots of a) lead white, b) zinc white and c) titanium white in animal glue mock-ups irradiated with the 780 nm laser for 10 s at 35 mW with a spot size of 450 µm. The red curve is the reference spectrum prior to the laser irradiation.

The lead white and zinc white pigments did not show any significant ΔR change and the temperature did not increase more than 1 °C. Instead, titanium white heated up of 6 °C and a reversible change mainly towards 800 nm occurred in the first few tens of seconds post irradiation (Fig. 4.18). Prussian blue, malachite and brown ochre (Fig. 4.19 a and b) are the mock-ups that heated up the most with an increase of temperature of 93, 81 and 83 °C respectively. On these irradiation tests the maximum ΔR appeared at the peaks of the corresponding reflectance spectra and in the surrounding of the laser spot, where the heat dissipates, no clear signs of a reversible change was detected. Chrome green (Fig.4.20), another semiconductor pigment, had a smaller increase of temperature (ΔT_{avg} of 35 °C) followed by a reversible ΔR change in two distinct spectral regions corresponding to 2 points of inflection, at 525 nm and 780 nm, even more visible out of the laser spot (Fig.4.20 b and c). Finally, orpiment did not heat up and no ΔR changes were detected.

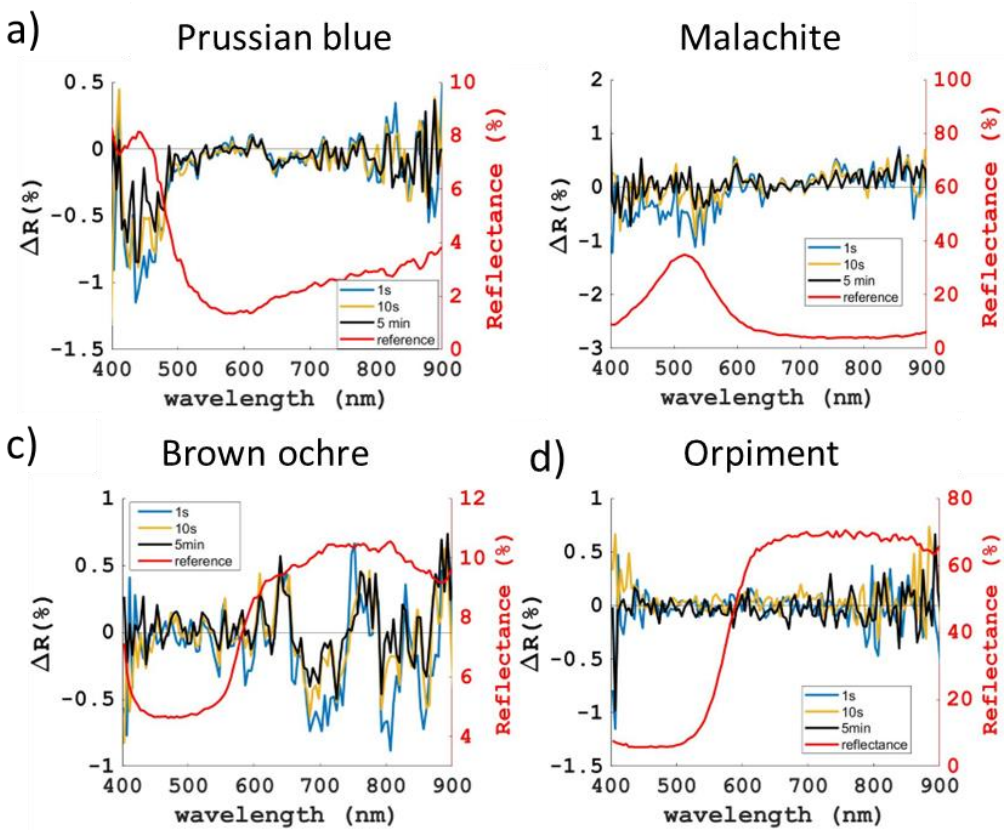

Fig.4. 19 ΔR plots of a) Prussian blue, b) malachite, c) brown ochre and d) orpiment in animal glue mock-ups irradiated with the 780 nm laser for 10 s at 35 mW with a spot size of 450 µm. The red curve is the reference spectrum prior to the laser irradiation.

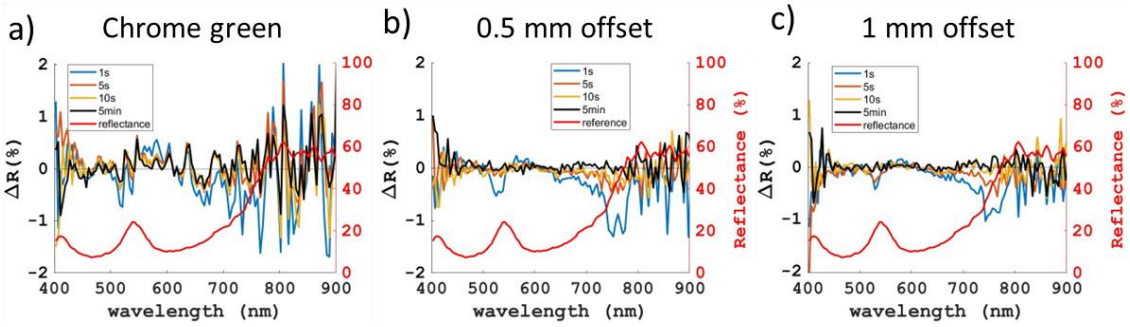

Fig.4. 20 chrome green irradiated with the 780 nm laser for 10 s at 35 mW with a spot size of 450 µm. a) ΔR plots of the irradiated area, b) 0.5 mm off set from the laser spot, and c) 1 mm offset. The red curve is the reference spectrum prior to the laser irradiation.

4.4. Discussion

The identification of LIDT on mock-ups is intrinsically an unreliable method owing to the highly heterogeneous nature of artists' materials. Research effort should focus on developing monitoring strategies to prevent damage while measuring with laser-based techniques. The inspection technique used to detect damage must also measure directly material alterations and be sensitive to low level alterations to mitigate damage. In this work, we have demonstrated the effectiveness of VIS-NIR HSI in detecting a broad variety of laser-induced alterations on representative artist materials, providing information both on the spatial extent and the evolution over time of the possible damage. We have shown that the very high sensitivity of reflectance spectroscopy allowed us to detect subtle changes not detectable visually, even under a microscope. The minimum laser intensity at which we can see permanent alteration with HSI is at least a factor 20 lower than that detectable by Raman spectroscopy (Fig. 4.3b and Fig. 4.7). The HSI monitoring over time enabled us to identify a transient change in reflectance that appears prior to permanent damage (Fig. 4.15), when the effect is thermally driven. Owing to the intrinsic sensitivity of reflectance spectroscopy to laser induced alterations, damage can be effectively mitigated. Moreover, in the case of photo-thermal damage, this prediction marker can be used to prevent damage. Hence the method can objectively define the safety threshold and is suitable for safe Raman measurements directly on real historical materials without the need to perform unreliable preliminary tests on mock-ups to define LIDT. Monitoring of radiation damage during Raman measurements *in situ* may be more convenient with a simpler system using reflectance spectroscopy, similar to the setup in our previous work [166].

A deeper understanding of the laser-material interaction allows the design of a better damage mitigation strategy when measuring real artists' materials. Thanks to the lateral resolution and field of view of the HSI, it is possible to detect alterations not only in areas directly irradiated with photons but also in regions away from that, where the dissipated heat from the laser spot has an effect. The multi-modal set-up with time and spatially

resolved thermal and spectral reflectance monitoring allowed the distinction between spectral changes associated with photochemical and thermal effects (Fig. 4.14a and b). The heat accumulation induced by increased laser intensity is well known, but here we demonstrated that it is necessary to consider the combined effect of the 3 parameters, power, spot size, and exposure time, to define safety thresholds. Through this, some not so commonly known effects were found. The laser induced damage threshold in intensity considerably decreases when using a larger spot size, that is, it is less safe to use a larger spot size for the same laser intensity. Prolonging the irradiation time does not necessarily increase the extent of damage. While prolonged exposure caused a significant increase in the extent of damage in a case where photochemical effect dominated (Fig. 4.11b and c), it did not increase the extent of damage in another case where the thermal effect dominated (Fig. 4.8). We aim to explore further the spot size effect on the damage threshold. In particular, to identify the optimum combination of power, spot size and exposure time for the highest SNR Raman signal within safe operation limits.

The three selected pigments present similar absorption and scattering properties in the VIS-NIR regime (absorbing at 532 nm and highly scattering at 785 and 1064 nm) but demonstrated different responses to laser irradiation. Red lead paint mock-up proved to be very resistant to the three lasers (532, 785 and 1064 nm) investigated, with no permanent damage detected in the survey (maximum laser power 100 mW). The vermilion oil paint mock-up appeared to be damaged mainly by thermal effects, with 532 nm laser causing the highest temperature rise. The vermilion oil paint was heated up less than the vermilion powder and resulted in less damage under the same irradiation conditions. In the most severely darkened case, a very thin layer of black meta-cinnabar was formed (Fig. 4.7). To a higher or lower extent, a superficial layer of pararealgar and intermediate phases were produced when realgar was irradiated with 532 nm laser (Fig. 4.12c and d, Fig. 4.14). With the predominant thermal effect induced by the 785 nm and 1064 nm lasers, realgar exhibited a relative stability to temperature rises. Overall, when irradiating with 785 nm and 1064 nm laser, the resultant temperature rise is highest on the vermilion mock-up, followed by realgar and then red lead (Fig. 4.3a, Fig. 4.4 and Fig.

4.10 respectively). The surface temperature rises due to both absorption and scattering, and the kinetics of cooling are mainly related to the heat capacity of the irradiated materials. The lowest reported heat capacity is the one of vermilion (48.4 J/K mol), followed by realgar (82.9 J/K mol) and then red lead with the highest heat capacity (130 J/K mol) [183,184]. These results indicate that both light stability and thermal stability are important in determining how sensitive a pigment is to laser irradiation. A survey on different common pigments, both dielectric and semiconductor materials, has been started with the 780 nm laser, showing that the most absorbing pigments reported a significant increase of temperature but with still small changes in ΔR. More systematic measurements on a larger set of pigments will better help identifying other specific ΔR changes that may be used as prediction marker or as early warning sign of damage. Further work will also be related to exploring the reflectance changes when the pigments are mixed in a paint layer.

4.5. Conclusions

The multimodal imaging set-up is valuable for understanding and studying different damage mechanisms and contributes to the development of a safe analytical protocol for Raman spectroscopy on paintings. Owing to the extremely high sensitivity of VIS-NIR reflectance spectroscopy in detecting even subtle changes, it is an effective monitoring technique to be used in tandem during laser-based analyses. It could also be applied to the monitoring of other types of radiation, such as X-ray, for safe analysis of paintings. Furthermore, its application could also be extended to other fields, such as laser processing where a high control of intentional laser induced modifications are required.

5. *Operando* VIS-NIR microscopic Hyperspectral imaging for synchrotron X-ray monitoring on paintings

The microscopic VIS-NIR hyperspectral imaging (HSI) system, described in section 3.1.2, was aligned with the X-ray micro beam at the PUMA beamline at Soleil synchrotron. The HSI measurements were performed o*perando* during a synchrotron experiment to assess the possible beam damage while performing XAS for the speciation of painting's materials. Common artists' pigments that are known to be sensitive to radiation damage were selected for painting mock-ups (lead white, vermilion, Prussian blue and realgar) with different binders (linseed oil and animal glue). In section 5.3 specific irradiation conditions (flux density, beam spot, photon energy and fluence) and materials characteristics (thickness and binder) are explored to identify possible improvements in data collection for safer analysis. The results of the monitoring method during XAS at specific X-ray photon energies, between 7 keV and 13 keV, are discussed in section 5.4. Finally, a comparison between laser-induced damage and X-ray damage is discussed in section 5.5.

5.1. Introduction

When analysing historical samples with X-ray synchrotron radiation, the probability to cause beam damage is much higher than conventional laboratory sources due to the orders of magnitude more intense source at synchrotron facility compared to X-ray tubes [12]. The available methods proposed by synchrotron beam scientists to mitigate damage consist of using: i) a cryogenic environment, primarily to slow down radical reactions [144]; ii) under vacuum, mainly to avoid oxidative reactions; or, when applicable, iii) the spinning of the sample or consecutive measurements in "fresh spots" if the sample is homogeneous. But sometimes these strategies failed to minimize

radiation damage, like the case of helium cooling during the crystal structure analysis of enzymes [185]. Moreover, all these strategies are aiming at guaranteeing the significance and reliability of the data collected but are not necessarily suitable to guarantee the preservation of the integrity of the analysed materials. The safeguard of the analysed sample is a quite unique request of the specific Heritage Science community. It is of primary importance the preservation of all aspects of heritage materials due to their unique nature and it's a moral duty to conserve such materials also for future research as the sampling is more and more a practice to minimize.

For this reason, it is important to identify alternative control and mitigation strategies suitable for the cultural heritage community needs. One strategy is to study the possible modifications of the materials under intense radiation to identify safe operative conditions, but due to the extreme heterogeneity of artworks, it is impossible to identify such best operative conditions. Another strategy is based on the monitoring of damage, which is often performed by visual observation by eye or under the microscope and by assessing spectral changes over consecutive measurements on the same spot. Sometimes the damage is not clearly visible by eye or may not be detectable by the primary inspection technique (see Chapter 2.2). These methods do not allow to prevent the occurrence of damage (i.e. providing and "alert") as they are based on a post irradiation assessment. Therefore, independent and highly sensitive techniques are required to comprehensively detected any type of damage.

The focus of this work has been the development of an *operando* monitoring method that enables the identification of early warning signs of damage that can be set as our threshold to stop the irradiation during the measurement, when such early warning alteration is detected. This method aims to contribute to the design of a safe protocol for the analysis of artworks with SR X-rays.

5.2. Experimental design

A microscopic VIS-NIR hyperspectral imaging set-up was specifically designed to be incorporated at a synchrotron beamline (see details in section 3.1.2). The experiment was performed at the PUMA beamline at SOLEIL synchrotron thanks to a successful proposal [186].

The spatial resolution obtained is 2.7 µm with a pixel size of ca. 1 µm at a working distance of 3.4 cm. The spectra are collected from a vertical slit of ca. 1 mm on the target surface. The spectral range is 400 to 900 nm, and the exposure time was set between 0.2 s and 5 s. A DC tungsten light was used at 45 degrees relative to the sample surface and the HSI was set normal to the sample (Fig. 5.1). The monitoring has been performed recording few minutes prior X-ray irradiation, during the X-ray measurement (X-ray absorption spectroscopy, XAS) and after X-ray exposure for a minimum of 5 min and up to few hours post irradiation.

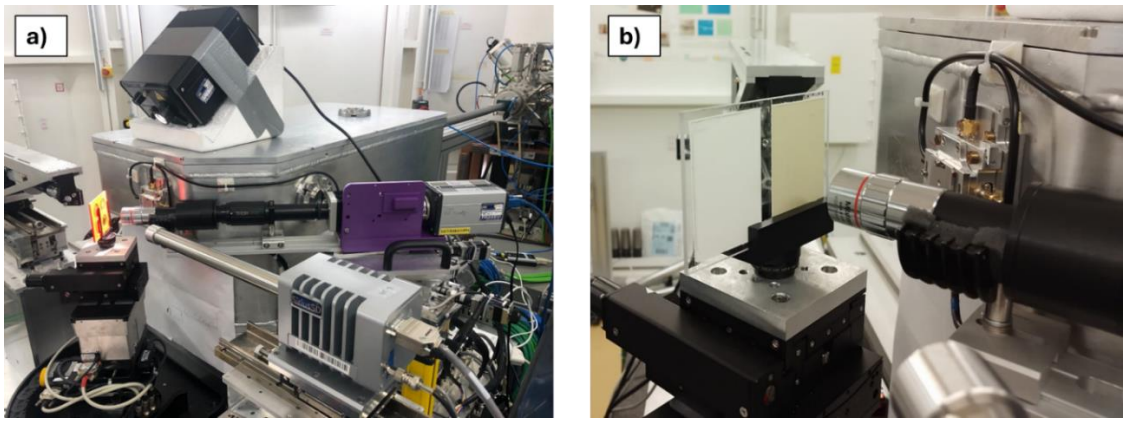

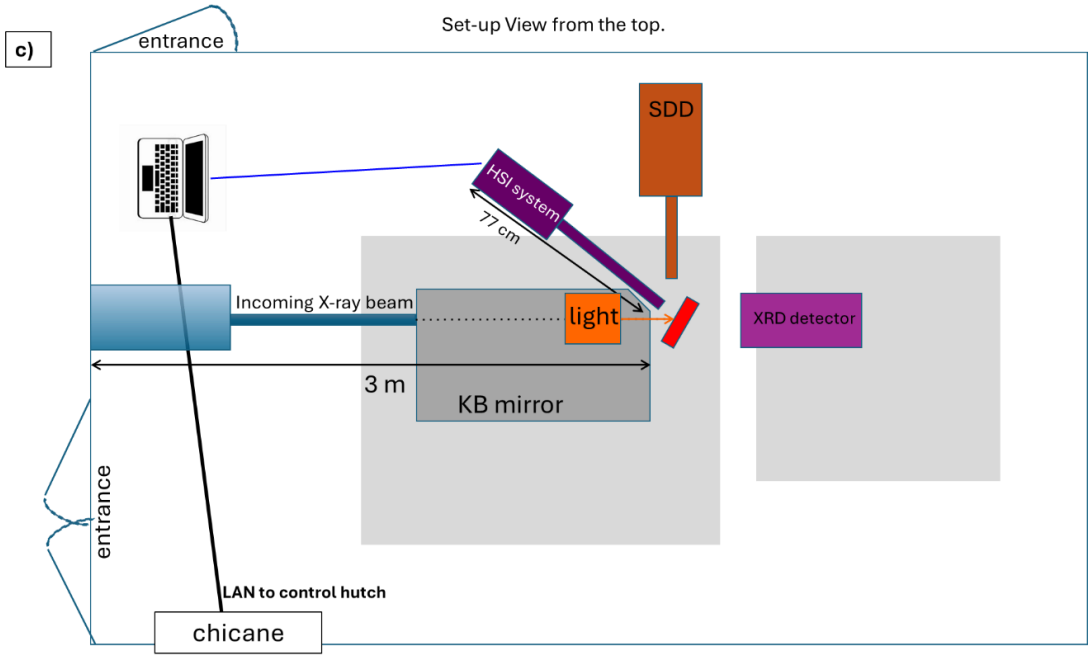

Fig.5. 1 a) The experimental set-up at PUMA beamline with the in-house built VIS-NIR microscopic hyperspectral imaging system and b) an image of one of the samples mounted on the sample stage prior analysis. c) a schematic view of the experimental hutch and the set-up from the top.

To assess the occurrence of damage in the VIS-NIR reflectance spectra, ΔR spectral cubes (Fig. 5.2a) were generated by subtracting the pre-irradiation average spectrum to each spectrum acquired during and after irradiation. At several time interval, ΔR are extracted from the irradiated area over 16 pixels from the ΔR cube (Fig.5.2b) and any change above the level of system stability and noise fluctuation are considered a damage. Thanks to the simultaneous collection of the spectrum over a 1 mm slit, it is also possible to check the reliability of the dataset, by extracting the ΔR plots from a region far away from the irradiation area (Fig. 5.2c). This enables to have an internal control to check system stability and noise fluctuation (generally ±0.5%), which makes the method very robust and highly sensitive to subtle changes.

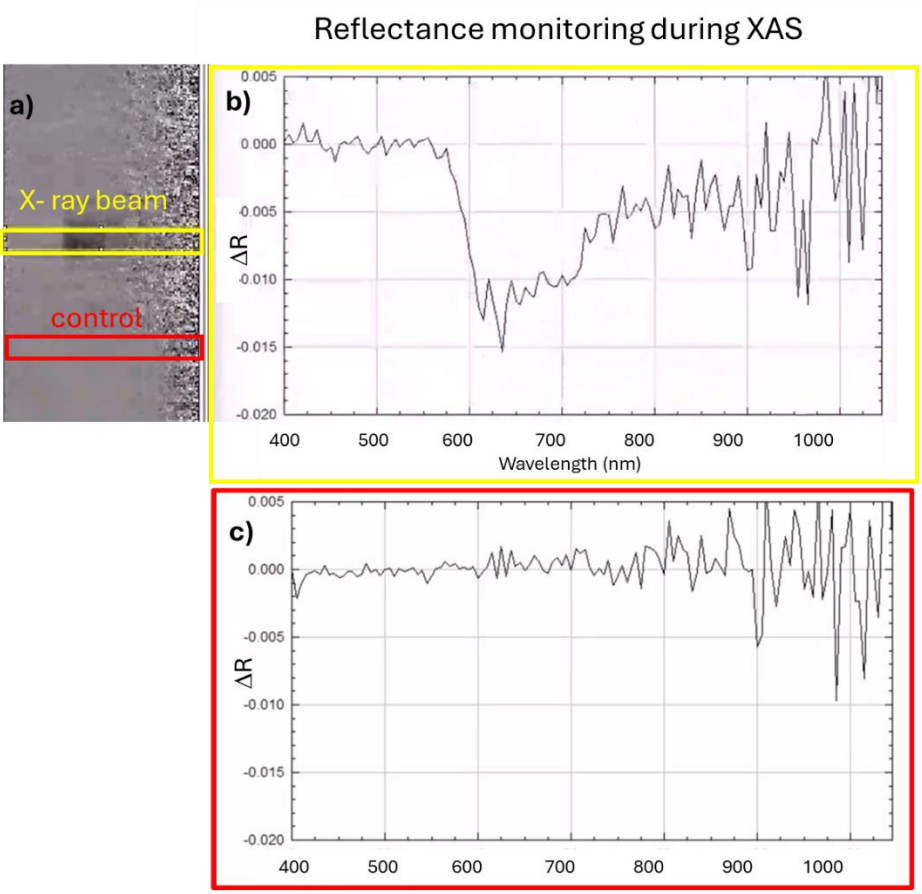

Fig.5. 2 a) The ΔR cube of the monitoring, b) the ΔR spectrum from the irradiated sample and c) the ΔR from an area of the paint far from the irradiation area that works as internal control.

The VIS-NIR hyperspectral imaging monitoring was carried out during a XAS experiment at energies commonly used for the analysis of historical materials, in the energy range between 7 and 13 keV, namely Fe K-edge (7112 eV), As K-edge (11864 eV), Hg LIII edge (12284 eV) and Pb LIII edge (13035 eV).

The samples used in this experiment are listed in Table 5.1. For the Fe and Pb speciation, Prussian blue (hydrated iron(III) hexacyanoferrate(II) complex) and lead white (lead carbonates, namely cerussite/hydrocerussite ratio of ca. 90/10) in different binging media (animal glue and linseed oil) and in mixture, were analysed. For As and Hg speciation, linseed oil paint mock-ups respectively with realgar (As_4S_4) and vermilion (a-HgS) were analysed in thin sections. The XAS spectra were collected in fluorescence mode by means of a SD detector at 45 degrees to the target. The energy scan steps to perform XAS were varied, resulting in different duration (minimum 5 min, to a maximum

of 26 min) and acquiring multiple consecutive spectra on the same spot (minimum 3 to a maximum of 12 consecutive spectra). The energy resolution of the XAS spectra is around 1 eV at the energy range explored (7-13 keV). The beam footprint on the target sample is 15 x 60 μm^2 (horizontal x vertical). When not specified, the flux of the X-ray beam was set to the maximum: 1.6 x 10^{10} ph/s at the As K-edge, Hg LIII edge and Pb LIII edge; and 1.7 x 10^9 ph/s at the Fe K-edge.

Each XAS experiment was monitored with the HSI system, and several microscope images were collected at certain time interval. Apart from the *operando* monitoring during XAS, some tests were carried out at fixed energies, each time varying one X-ray parameter (photon energy, incident flux, exposure time) and on different materials (different pigments, binders and different thicknesses), to better understand the effect of these parameters on the occurrence and extent of radiation damage on paint materials.

Table 5. 1 The list of samples used in this experiment. All the samples were prepared on a polycarbonate substrate, except for the realgar and vermilion that were originally on a plywood substrate and the binders on glass slides. The thickness was measured with the 1300 nm OCT.

Pigments	Binder	Paint thickness	Age of the sample
Prussian blue	Animal glue	~80 µm	Freshly prepared
Prussian blue + Lead white	Linseed oil	~180 µm	1 year old
Lead white	Linseed oil	~150 µm	2 years old
Lead white	Linseed oil	Thin section ~15 µm	2 years old
Lead white	Animal glue	~80 µm	2 years old
Vermilion	Linseed oil	Thin section ~15 µm	15 years old
Realgar	Linseed oil	Thin section ~15 µm	15 years old
--	Animal glue	~15 µm	Freshly prepared
--	Linseed oil	~10 µm	2 years old

5.3. The influence of instrument parameters and materials characteristics on the occurrence of damage

To better understand the X-ray parameters and the materials characteristics that have a considerable impact on the occurrence of damage, a set of irradiation tests were designed and performed to assess the effect of photon energy, the flux density (ph/s μm^2), total fluence (ph/μm^2) and the spot size. Some materials are more susceptible to X-ray radiation damage than others and this is highly specific to the material's composition and properties. Thanks to the selection of samples, some considerations concerning the materials' properties can be drawn, such as the effect of material thickness and the binders.

5.3.1. The effect of photon energy

5.3.1.1 Pre-edge vs edge vs post edge

If we assume that the key factor of radiation damage is absorption, it can be expected that the effect of photon energy may impact significantly the damage extent when close to an absorption edge of a specific element present in the irradiated material. It can be expected that the absorption edge and post-edge energies are more damaging than pre-edge energy. To assess this, at both Fe and Pb edges, short irradiation tests of 2 min were performed at fixed energies: pre-edge (6.96 keV and 12.95keV), edge (7.112 keV and 13.0422 keV) and post edge (7.4 keV and 13.5 keV). This test has been performed for all the Prussian blue and lead white samples and no significant difference between pre-edge, edge and post edge after 2 min of irradiation was detected (Fig.5. 3).

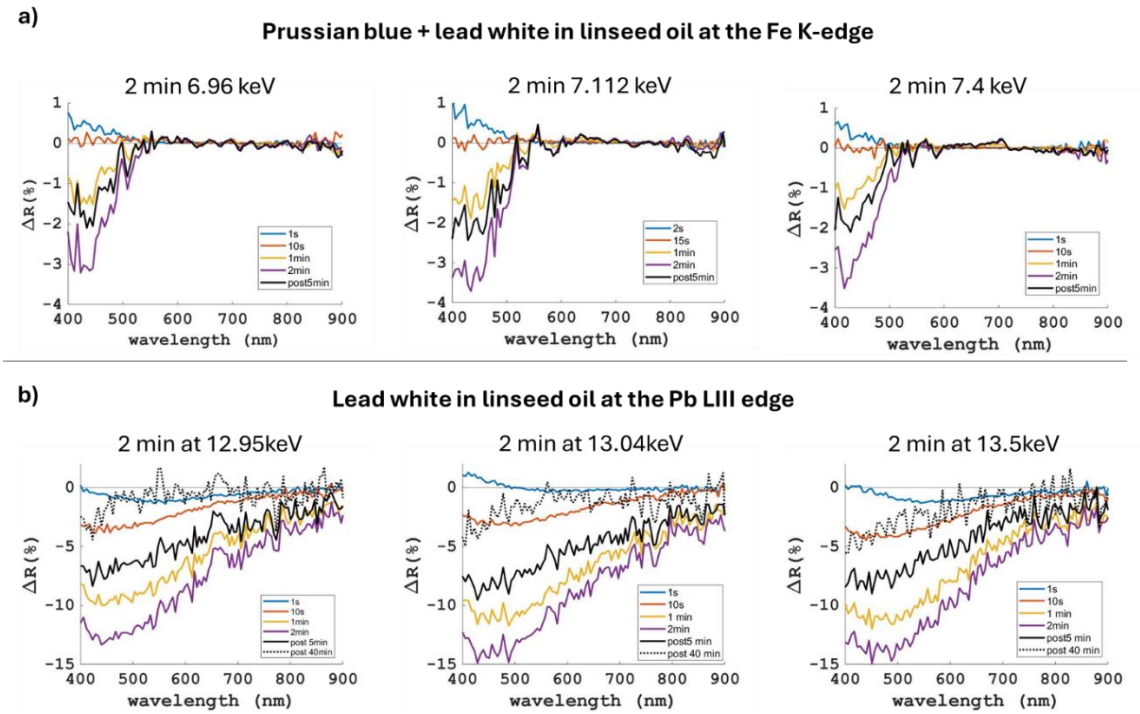

Fig.5. 3 The ΔR plots of the pre-edge, edge, post-edge energy tests of 2 min on a) the Prussian blue and lead white in linseed oil sample at the Fe K-edge and b) on the lead white in linseed oil sample at the Pb LIII edge. The coloured lines correspond to the ΔR during the irradiation (1s light blue, orange 10s, yellow 1 min, purple 2 min) and the black lines post irradiation.

5.3.1.2 7 keV vs 13 keV

It is common sense in some communities to think that the higher the energy, the more damaging the X-ray irradiation can be but, in some cases, especially for organic materials it is said and reported that the softer the energy, the more severe is the damage due to higher absorbed dose (see discussion of section 2.2.3). To assess this, some tests were done to ascertain the severity of damage at the two extreme energies of the range investigated, namely 7 and 13 keV. On Prussian blue and lead white oil sample the irradiation at the Pb edge imparted more severe damage compared to 7 keV at the same irradiation duration. This could be related to the fact that in this sample, the amount of lead white compared to the amount of Prussian blue, is very high. Similar comparison can be done by looking at the lead white in animal glue sample exposed for ca. 3h at the

Pb edge and Fe edge (Fig. 5.4). The ΔR changes are similar in shape, but the Pb edge imparted more severe damage up to -50% at 400 nm compared to -30% with the irradiation at the Fe edge. In both cases the 13 keV is highly absorbed by the lead pigment contained in the paint but it also must be considered that the flux at 7 keV is 1 order of magnitude lower than at 13 keV (see section 3.2.4).

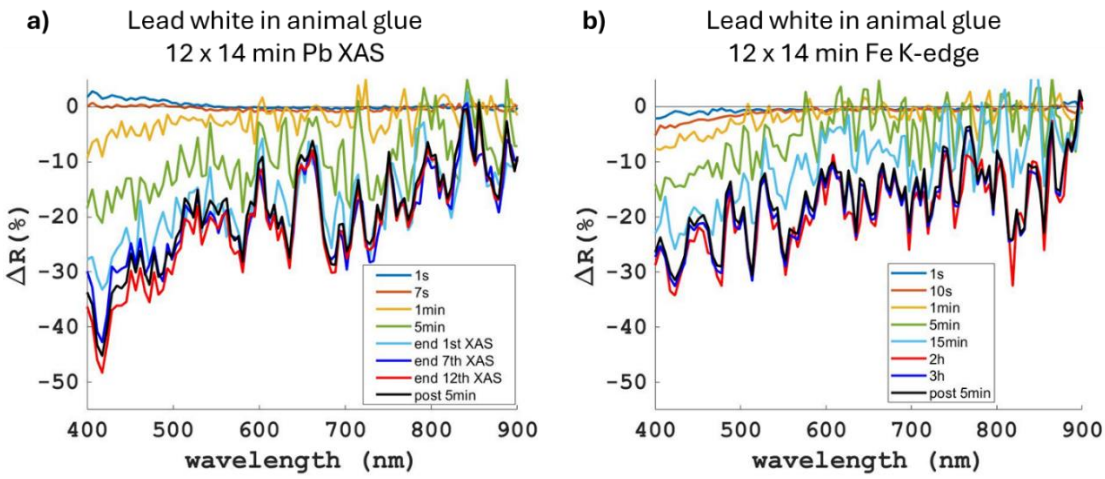

Fig.5. 4 The ΔR changes during ca. 3 h of irradiation of the lead white in animal glue sample a) at the Pb LIII edge during XAS and b) at the Fe K-edge. The coloured lines correspond to the ΔR during the irradiation (1s light blue, orange 10s, yellow 1 min, green 5 min, cyan 15 min, red 2h and blue 3h) and the black one post irradiation.

Based on this evidence, it is not possible to extract a clear conclusion. The short irradiation tests of 2 min may indicate the absence of correlation of damage with photon energy, like already observed in previous works [187]. Alternatively, it may be possible that the energy difference is not large enough to appreciate such effect. But the duration of the irradiation may also be too short to observe significant effect of the photon energy. Indeed, in a recent work [136] the effect of photon energy to the extent of damage on an animal glue binder sample was monitored with FTIR in transmission. The authors found that at a short irradiation time (below 5 min) the 7.7 keV and the 13 keV

imparted similar damage to the binder, while after prolonged exposure the 7.7 keV irradiation gradually induced more severe damage.

5.3.2. The fluence and flux density effect

Some of the most important parameters to obtain meaningful XAS spectra and X-ray diffraction patterns are the incident flux, the beam spot and the duration of irradiation, thus the fluence (ph/µm^2) and flux density (ph/µm^{2}s). A general approach to mitigate damage can consist in attenuating the incident X-ray beam and thus reducing the flux density, but to have the same data quality (or meaningful data) it is often required to increase the exposure time, resulting in the same total fluence. X-ray radiation damage is considered a cumulative effect, but it is not clear whether it is flux density-dependent or if it depends on the total fluence (or irradiance). To assess the effect of these two parameters for the irradiation of our paint materials, some tests were performed by reducing the output flux (ph/s) and increasing the exposure time. The tests were performed to mimic a typical setting to obtain reasonable XRPD patterns from a highly scattering material (1 s at 10^{10} ph/s), like when analysing lead white or vermilion; and a longer acquisition time to mimic the analysis of a paint sample with unknown materials that possibly contains also less scattering materials (10 s at 10^{10} ph/s). These tests were performed at a fixed energy of 12.95 keV with 10^{10} ph/s, then the flux was lowered by a factor 10 and the exposure was increased of the same factor 10. This test was performed for 10^9 ph/s, 10^8 ph/s and 10^7 ph/s, therefore the damage extent is explored in a flux density range of 2.2 x 10^7 to 2.2 x 10^4 ph/µm^{2}s and of total fluence between 2.2 x 10^8 to 2.2 x 10^7 ph/µm^2. The irradiation tests were performed on the oil samples with Prussian blue and lead white (Fig.5.5), the lead white alone (Fig.5.6), and on the realgar (Fig.5.7) and vermilion (Fig.5.8) thin sections. For each test the internal control on the paint area far away from the irradiated spot is also shown to assess the sensitivity at each acquisition.

In the range of flux investigated (10^{10} to 10^7 ph/s) on the Prussian blue and lead white sample the reciprocity seems to be followed, meaning that the damage depends on the

total fluence only and irrespective of the flux density used. Therefore, in this case it is not necessarily useful to acquire for longer time at lower flux to really guarantee a safer analytical condition. For realgar, no trend of ΔR change is detected varying the flux and integration time. While for lead white and vermilion oil samples reciprocity is not followed, resulting in a quite clear dependence on flux density. In the latter case, there is a substantial benefit in reducing the flux of just a factor 10 to be safer while still keeping reasonable integration times that are feasible during a beamtime (10 s and 100 s) to obtain the same quality XRPD patterns.

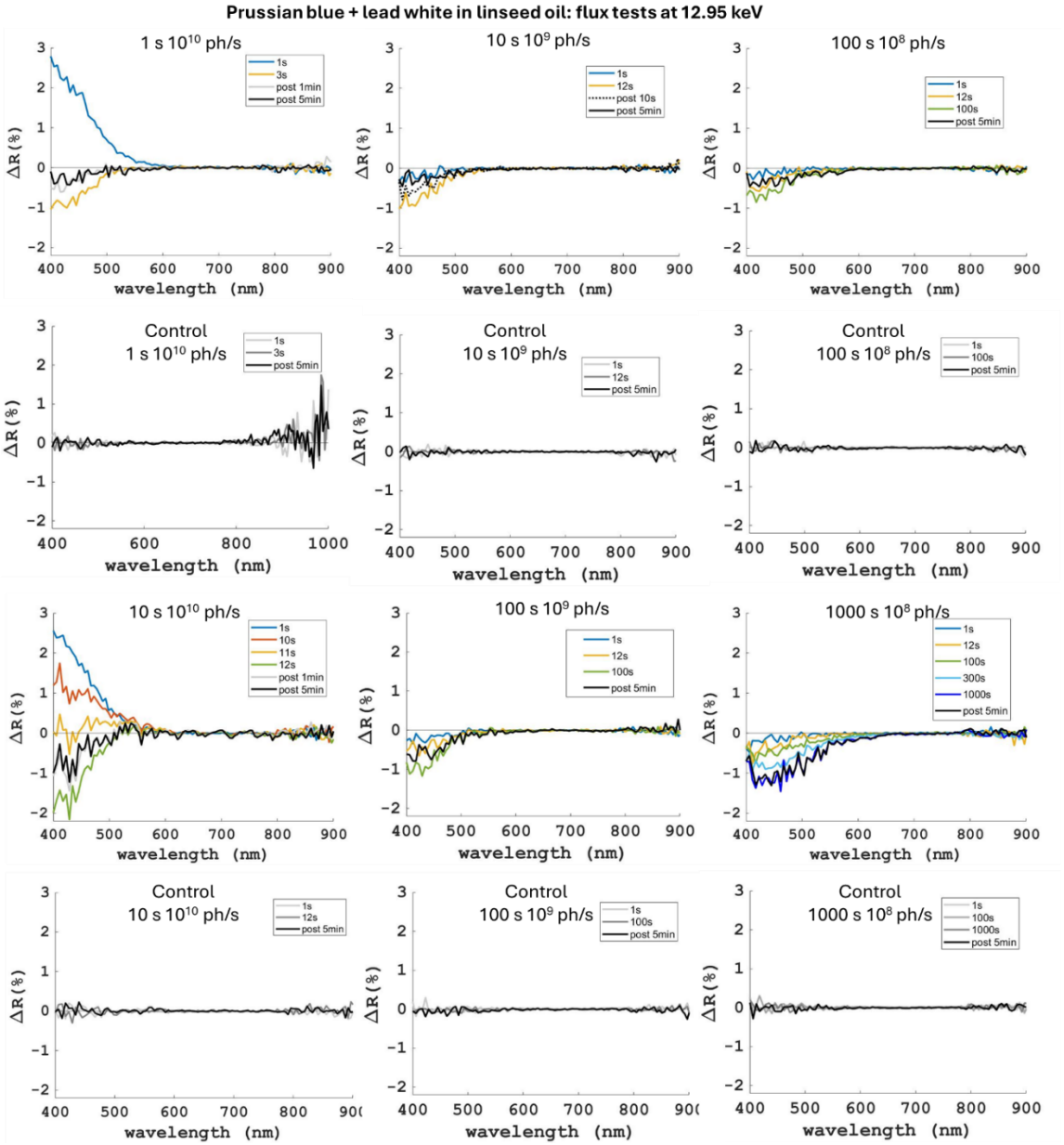

Fig.5. 5 The ΔR plots of the irradiation tests varying flux density and total fluence on Prussian blue and lead white in linseed oil at a fixed energy of 12.95 keV. The coloured curves are the ΔR during the X-ray irradiation, white the post monitoring is shown in grey and black lines. For each dataset the internal control ΔR plot is provided with lines in grey and black. The figures are to read as follow: in horizontal the flux density is changing, while the total fluence is constant; in vertical the opposite,

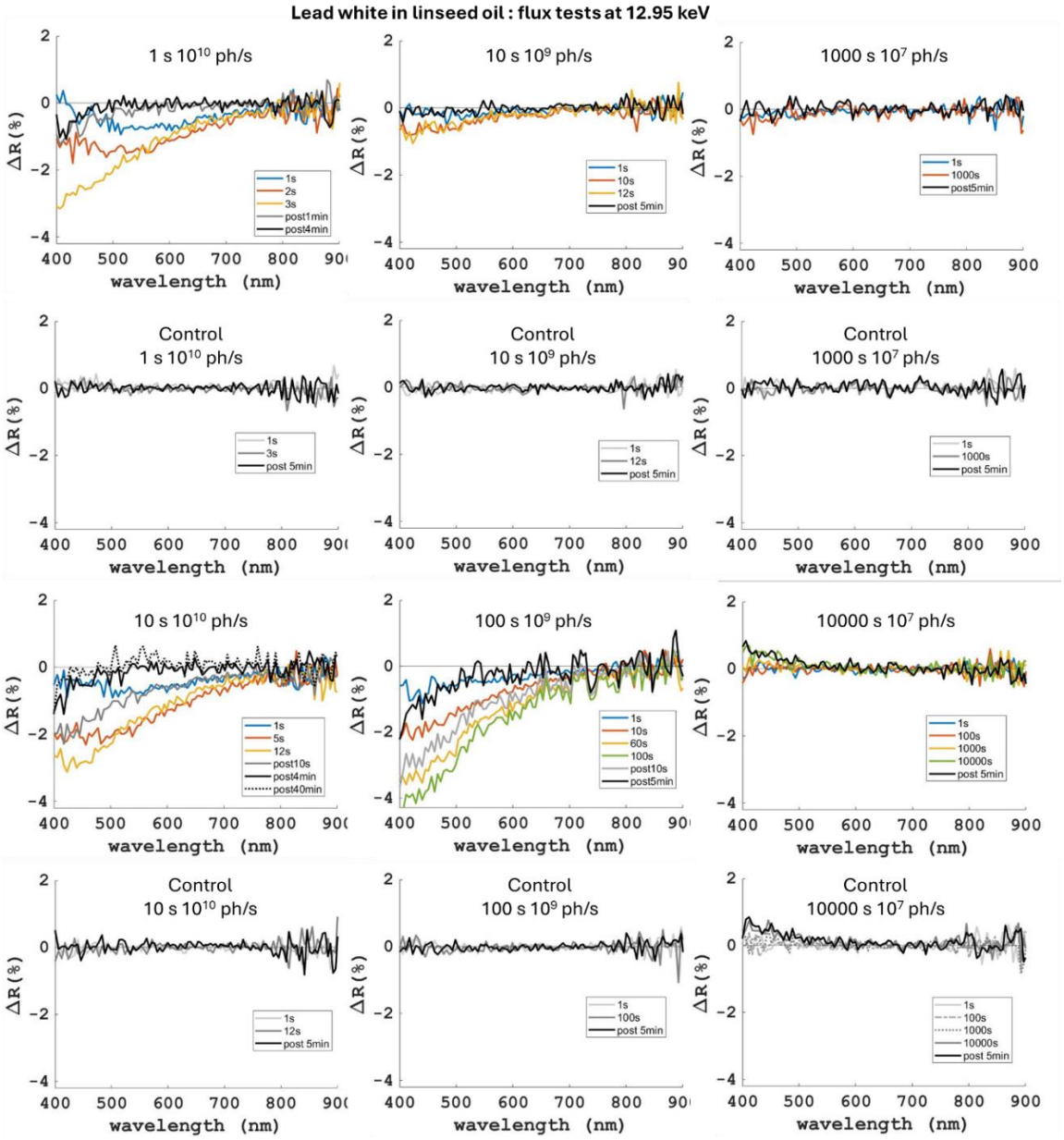

Fig.5. 6. The ΔR plots of the irradiation tests varying flux density and total fluence on lead white in linseed oil at a fixed energy of 12.95 keV. The coloured curves are the ΔR during the X-ray irradiation, white the post monitoring is shown in grey and black lines. For each dataset the internal control ΔR plot is provided with lines in grey and black. The figures are to read as follow: in horizontal the flux density is changing, while the total fluence is constant; in vertical the opposite.

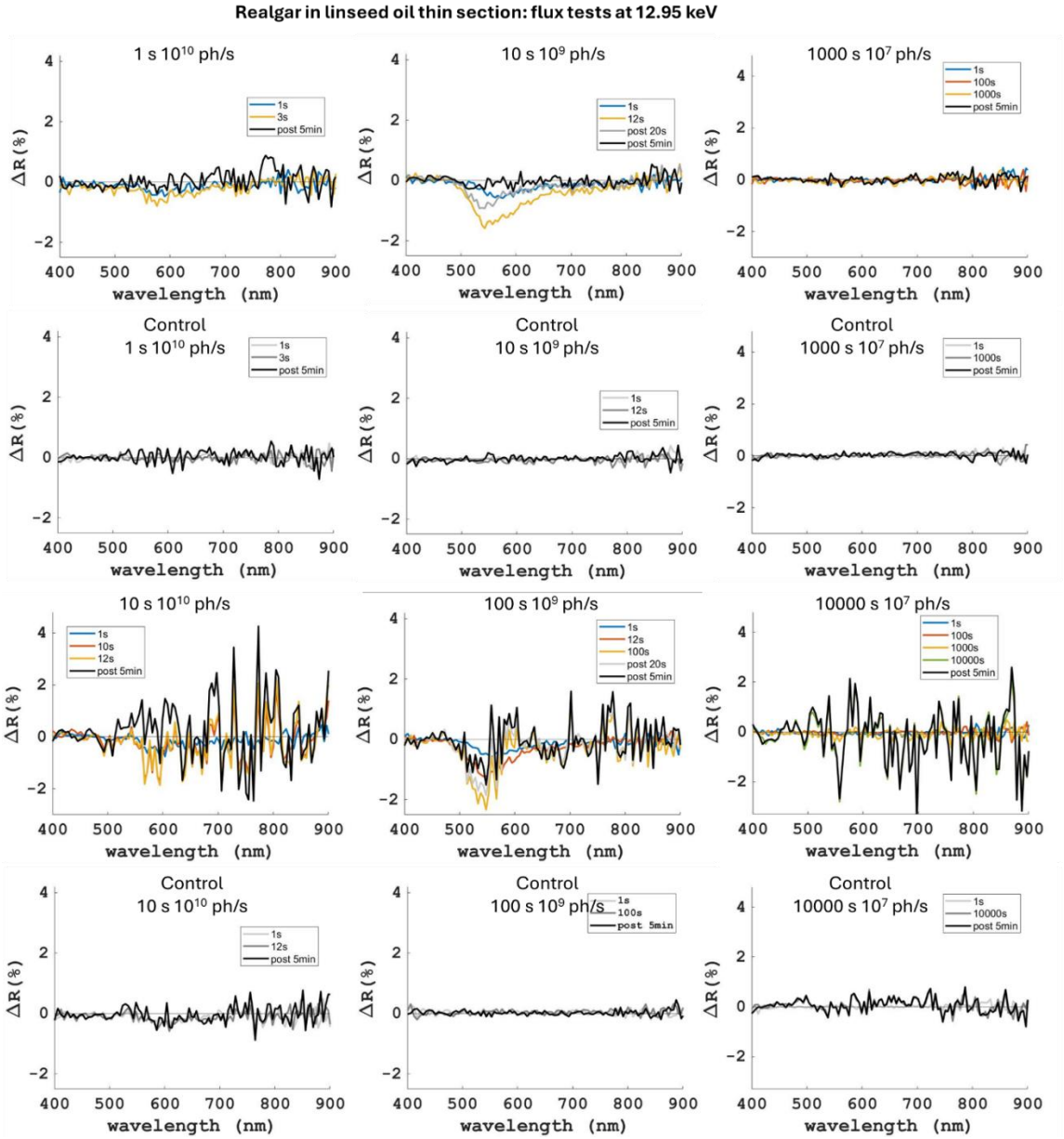

Fig.5. 7 The ΔR plots of the irradiation tests varying flux density and total fluence on realgar in linseed oil thin section at a fixed energy of 12.95 keV. The coloured curves are the ΔR during the X-ray irradiation, white the post monitoring is shown in grey and black lines. For each dataset the internal control ΔR plot is provided with lines in grey and black. The figures are to read as follow: in horizontal the flux density is changing, while the total fluence is constant; in vertical the opposite.

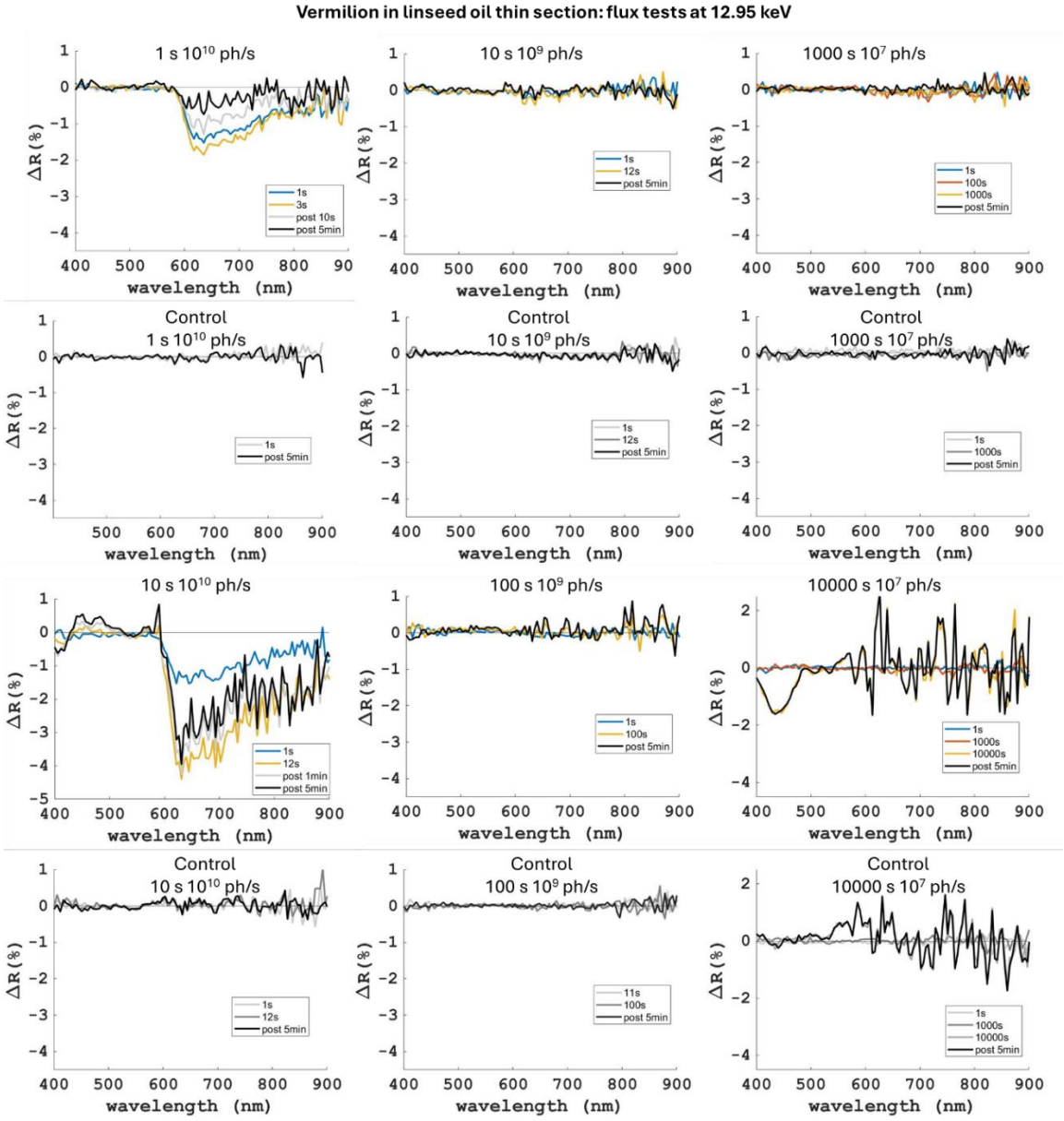

Fig.5. 8 The ΔR plots of the irradiation tests varying flux density and total fluence on Vermilion in linseed oil thin section at a fixed energy of 12.95 keV. The coloured curves are the ΔR during the X-ray irradiation, white the post monitoring is shown in grey and black lines. For each dataset the internal control ΔR plot is provided with lines in grey and black. The figures are to read as follow: in horizontal the flux density is changing, while the total fluence is constant; in vertical the opposite.

5.3.3. The spot size effect

Very often the reduced spot size is reported to be more damaging [188], and this is true when considering the same flux, thus a smaller spot size increases the flux density. At the same time, it is normally considered that the same intensity provided on a small spot compared to a big spot should not affect the resulted damage effect, as the intensity provided is the main parameter that governs the type of effect. With laser-induced damage it was observed that using the same intensity but different spot size has a significant effect on the occurrence of damage (see Chapter 4, section 4.3.4), and this is quite clearly understandable if is considered the thermal effect and the fact that with a small spot, a smaller volume will quickly dissipate the heat, compared to a larger volume that would dissipate more slowly the heat.

To ascertain the spot size effect upon X-ray radiation, some tests were performed by delivering the same intensity, while varying the amount of sample surface under the X-ray beam spot, thus indirectly reducing the spot size (instrumental constrains did not allow a feasible modulation of the spot size). The ΔR results are shown in Fig. 5.9 for the lead white oil thin section sample irradiated for 2 min at 13.5 keV in the middle of the thin section (Fig. 5.9a) and at the tip of the paint section, resulting effectively in an irradiated surface of 20 x 60 μm^2 and 20 x 15 μm^2 (Fig. 5.9b) respectively. The smaller irradiated area clearly shows a smaller extent of ΔR change of -1 % compared to a -3% of the bigger irradiated area. Therefore, with the same flux density, a smaller spot seems to be safer than a big spot. To ascertain if the effect is due to the different heat dissipation, temperature measurements are required. But it should also be considered the mean free path of photoelectrons, which is the primary cause of X-ray damage. If the X-ray spot size is smaller than the path length of photoelectrons in a specific matrix, these can escape from the irradiated volume, thus reducing the damage within the illuminated volume [141].

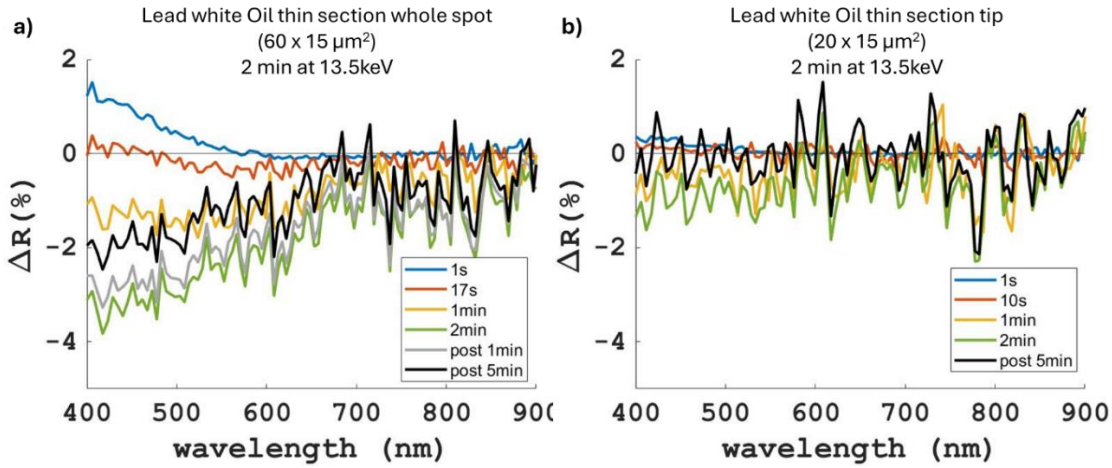

Fig.5. 9 The ΔR plots during and after 2 min of irradiation at 13.5 keV on the lead white in oil thin section a) irradiating the sample with the whole X-ray spot, and b) irradiating only a surface of 20 x 15 µm² at the tip of the paint fragment. The coloured curves are the ΔR during the X-ray irradiation, white the post monitoring is shown in black and grey lines.

5.3.4. The paint thickness

The effect of thickness is investigated by comparing the same irradiation on a bulk material (with an infinite thickness that do not allow any transmission of the incoming X-rays) and on a thin section of few microns. This test has been performed on the lead white in linseed oil which has a thickness of 200 µm and on a thin section of 15 µm obtained by microtome from the same paint mock-up (Fig. 5.10). The reflectance changes of the bulk samples resulted in a severe -15% ΔR change mainly towards 400 nm while the thin section showed a ΔR change of only -3% upon the same irradiation condition. A similar test was performed on a larger surface by scanning the paint sample in consecutive spots, each one irradiated at 13.5 keV for 7 min. The HSI RGB images of the 2 irradiated areas reveals a clear difference, with the bulk paint sample much darker than the thin section (Fig. 5.11). This is likely related to a similar concept as the one of the spot size, for the fact that in the thick paint layer all the energy is deposited within the material, while in the thin section a high amount is transmitted.

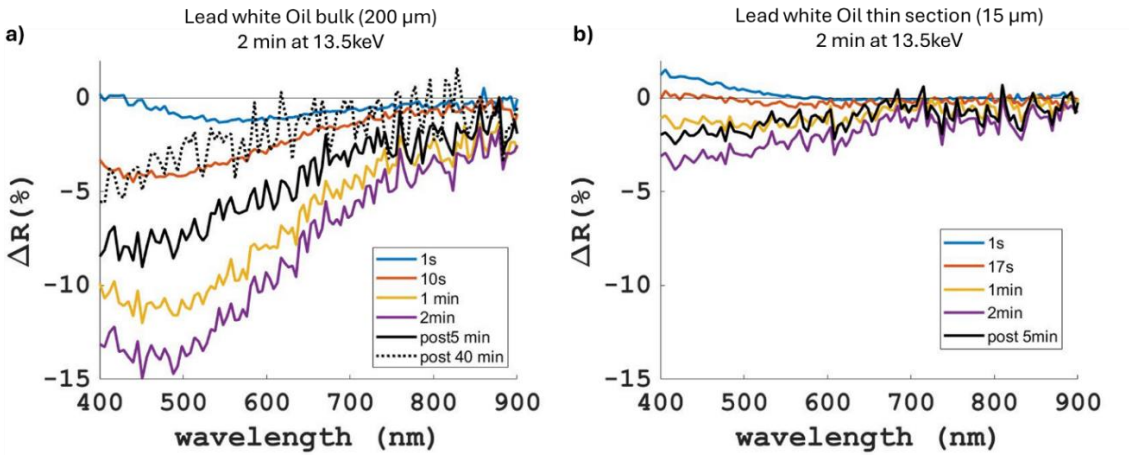

Fig.5. 10 The ΔR plots of lead white in linseed oil a) irradiated from the paint surface (total thickness 200 µm), and b) irradiating a thin section of 15 µm for 2 min at 13.5 keV. The coloured curves are the ΔR during the X-ray irradiation (1s light blue, orange 10s, yellow 1 min, purple 2 min), white the post monitoring is shown in black lines.

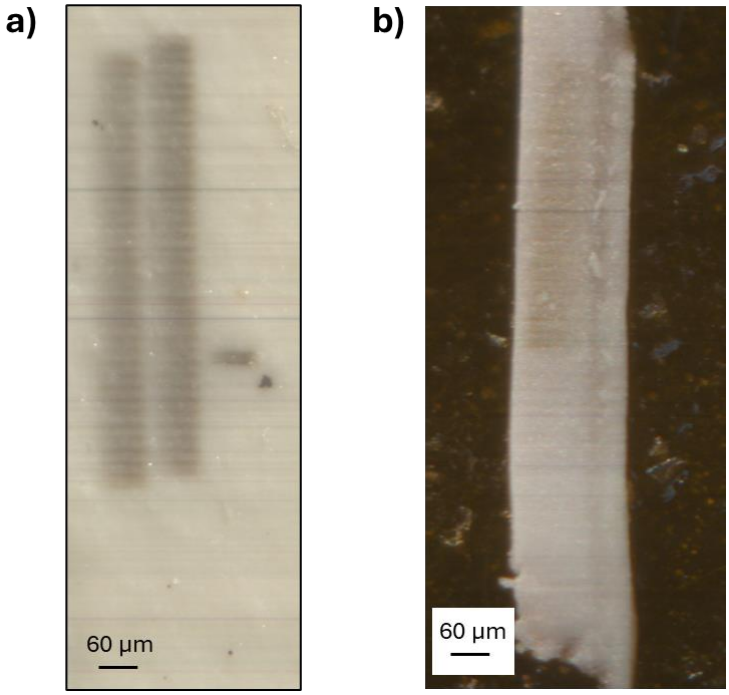

Fig.5. 11 The RGB images obtained from the calibrated HSI scans of the X-ray scanned areas irradiated at 13.5 keV, each spot irradiated for a duration of 7 min. a) on the bulk sample in 2 contiguous lines for a total area of 150 x 750 µm^2 and b) one line on the thin section for a total area of 60 x 450 µm^2.

5.3.5. The binders

When irradiating lead white in linseed oil for 2 min at the Pb LIII pre-edge (12.95 keV), the ΔR shows a decrease of ca. -13% mainly towards 400 nm (Fig. 5.12a). The same irradiation test on the animal glue sample showed a similar ΔR decrease reaching -20% at 400 nm (Fig. 5.12b). Looking at the spatial distribution of the damage, the ΔR of the animal glue sample seems to spread wider than the irradiated area compared to the linseed oil sample (Fig. 5.12c). This could be related to a difference in heat transport or related to a different mean free path of the electrons in the two different binders. Both hypotheses need verifications.

The irradiation at 12.95 keV for 2 min of the sample of animal glue binder alone, without pigment, shows a similar ΔR both in shape and extent compared to the sample containing the pigment. The similar ΔR between the animal glue with and without pigment, clearly shows that the damage, at this energy and duration, can be ascribed to the binder[2]. Indeed, proteins are well known to be frequently affected by radiation damage and prone to reduction by photo-electrons [132,139] and several degradations can be induced such as decarboxylation of acidic residues and disulfide bond breakage [188]. In protein crystallography it has been studied the X-ray induced damage with UV-VIS absorption. In particular, a broad absorption peak at 400 nm has been detected upon X-ray irradiation and was associated to the disruption of disulphide bonds, while a broad peak at 600 nm was associated to electron traps [130,133]. This type of studies shows that with an in-depth characterization of the specific damage it is possible to correlate it to a distinctive ΔR change, demonstrating the material specificity of reflectance spectroscopy in some cases.

The Prussian blue in glue and in oil are from different batches and potentially of different type. For this reason, it is not possible to compare the effect of the binder in this set of samples.

[2] The same test was performed also on the linseed oil binder sample but unfortunately the focusing was challenging and the data is invalid.

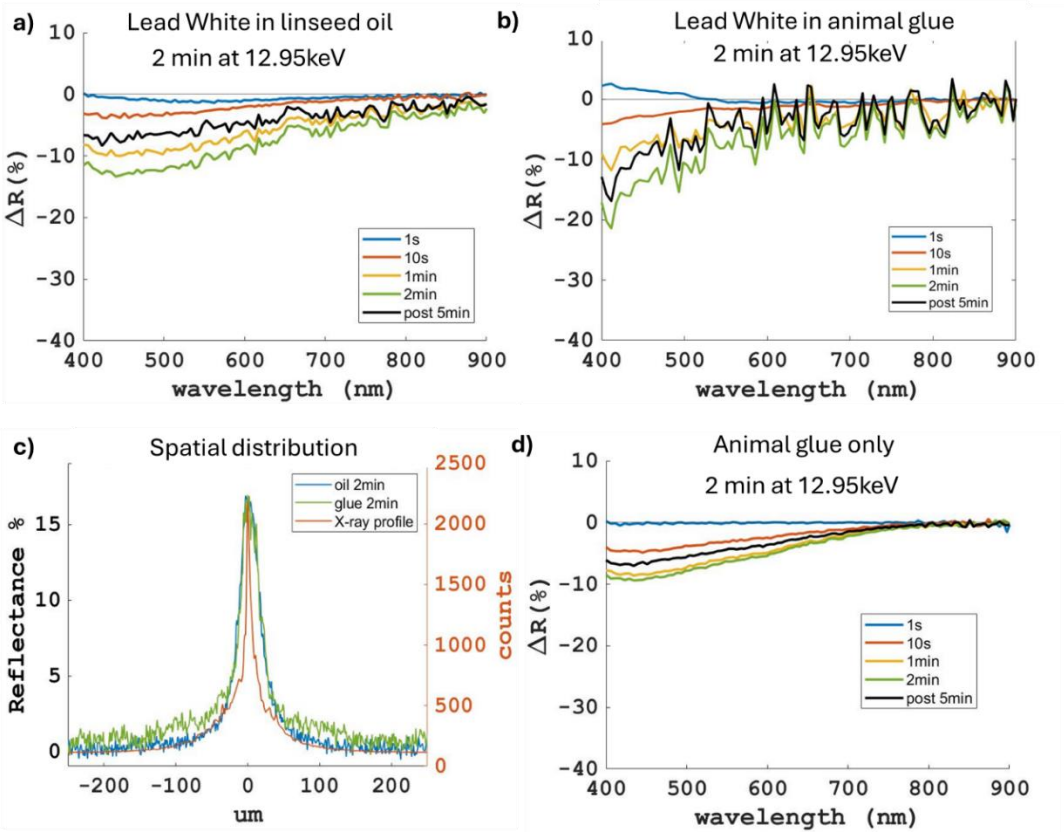

Fig.5. 12 The ΔR changes during the irradiation of lead white in a) linseed oil and b) in animal glue for 2 min at 12.95 keV. c) the spatial evolution of the damage, extracted from the wavelength range 400-480 nm of a) and b) compared to the X-ray beam profile. d) the ΔR changes upon irradiation of animal glue alone for 2 min at 12.95 keV.

5.4. The results of the *operando* microscopic HSI monitoring during XAS measurements

5.4.1. Pb LIII edge

XAS at the Pb LIII edge (13035 eV) was performed on the lead white containing samples. When performing 3 consecutive XAS spectra of 5 min each on the lead white samples, the ΔR change varies based on the paint mock-up: in the linseed oil sample the ΔR

becomes more prominent in the central wavelength range (500-700 nm) up to -35% and the damage results in a severe darkening (Fig.5.13a); in the animal glue sample the ΔR remains mainly close to 400 nm up to -28%, resulting in a more brownish spot, and a consistent increase of fluctuation is observed (Fig. 5.13b). The 3 consecutive XAS collected during these irradiation tests do not show any relevant spectral change. This could possibly indicate that the damage is still occurring in the binding media.

Increasing the irradiation time by collecting 12 XAS spectra, which corresponds to ca. 3 h of irradiation, the XAS spectra collected on the lead white in animal glue still show no changes (Fig. 5.13d), while the reflectance change becomes severe, reaching a ΔR of -50% with a similar shape (Fig. 5.13c).

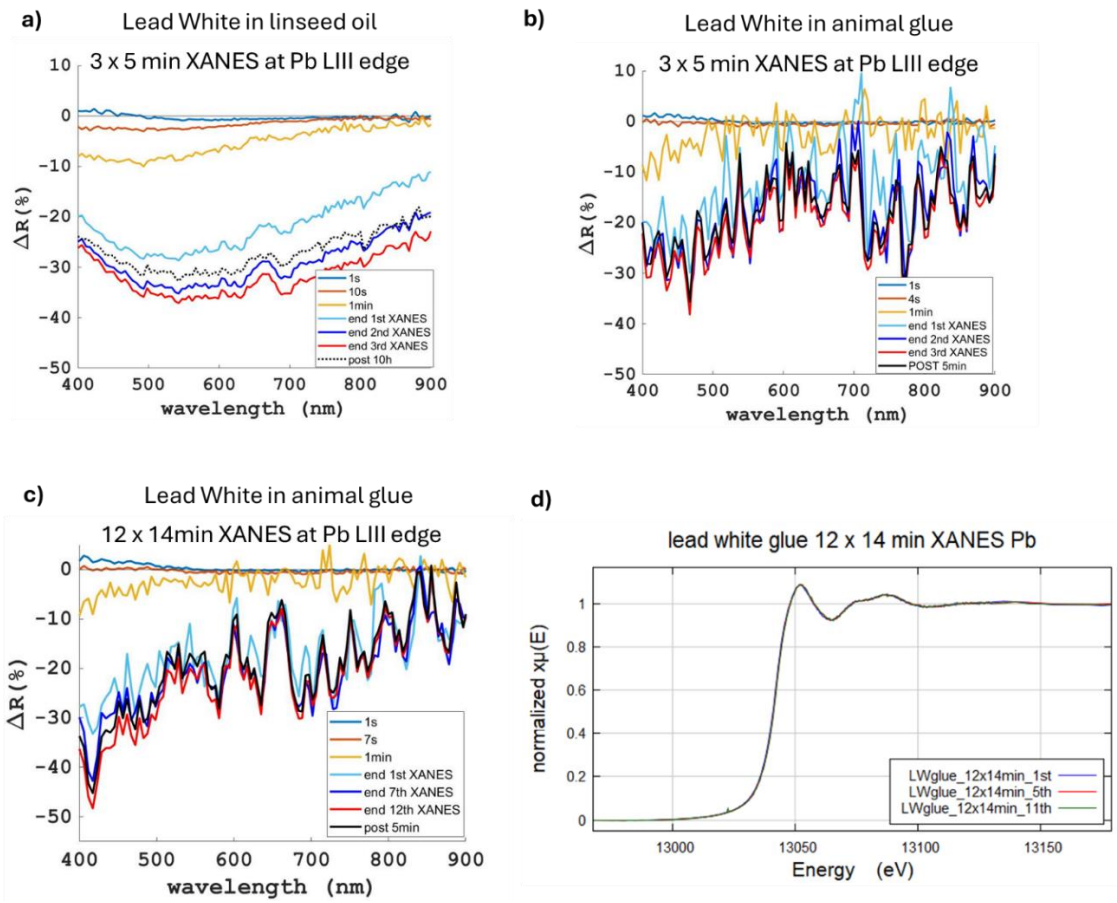

Fig.5. 13 ΔR changes during a) 3 x 5 min XAS at the Pb LIII edge on lead white in linseed oil, b) the same test on lead white in animal glue, c) 12 x 14 min XAS at the Pb LIII edge on lead white in animal glue, and d) the 1st, 5th and 11th XAS collected during the experiment in c).

As none of these darkening are detectable by XAS spectral changes, this could indicate that: i) only the binder is damaged or ii) that any possible electronic change of the lead atoms is below the XAS sensitivity, or iii) an amorphization of the structure is taking place, or iv) that the damage is localized on the other atoms in the lead white molecules (lead carbonates). It has to be taken into account that the XAS collected in fluorescence mode, at the Pb LIII edge of these very thick and highly concentrated paint layers, suffers considerably from self-absorption. This means that a non-linear relationship is present between the fluorescence and the absorption coefficient, resulting in XAS spectra highly distorted, mainly with strong attenuation of the small oscillations of the EXAFS region (Fig. 5.13d), losing any information of the local geometry around the Pb atom. Complementary techniques, such as XRPD, Fourier Transformed Infrared spectroscopy (FTIR) and Electron Paramagnetic Resonance (EPR) will help to address some of the hypothesis. A first attempt with EPR was conducted 3 days after irradiation on the scanned X-ray irradiation test of the raster scan damaged areas of Fig. 5.11 to assess the presence of radicals, but no radicals' signals were obtained either because they were below detection limit or because of their decay after 3 days post irradiation.

In literature lead white is often reported to blacken upon intense 1064 nm CW laser [61], temporarily blackens with pulsed lasers [68], as well as ion beams [189], and with X-rays [116]. In the latter work the damage evolution of lead white in linseed oil was followed with FTIR and XRPD and the damage effect was investigated in a flux density range of 2 x 10^{11}-10^{10} ph/µm^{2}s and a fluence of 2 x 10^{8}-10^{12} ph/µm^2. The authors detected first signs of damage at the expenses of the binder (formation of C=O acids) with a fluence of 2 x 10^{9} ph/µm^2. Only when increasing considerably the fluence to 4 x 10^{11} ph/µm^2 an amorphization of lead white was detected, and by increasing the fluence even more (2 x 10^{12} ph/µm^2) metallic lead was formed, showing a clear correlation of pigment damage with fluence. This damage to the pigment was noticed only with an extremely high fluence, while in the present work the fluence range investigated is even below the binder damage detection of the mentioned study (i.e. 2 x 10^{8}-10^{7} ph/µm^2). Therefore, it is likely that the detected damage in our work is still related to the binding medium. In

any case, the monitoring of ΔR enabled the detection of damage on these paint mock-ups even in cases where the damage is subtle and not visible by eye.

Concerning the evolution of damage post irradiation of the lead white samples, all the detected damages present a small reversion in the minutes time scale. In the long-term scale (days) a reduction of darkening and a more brownish tint of the damage is observed on a large X-ray irradiated test area on the oil mock-up using a raster scan (Fig. 5.14).

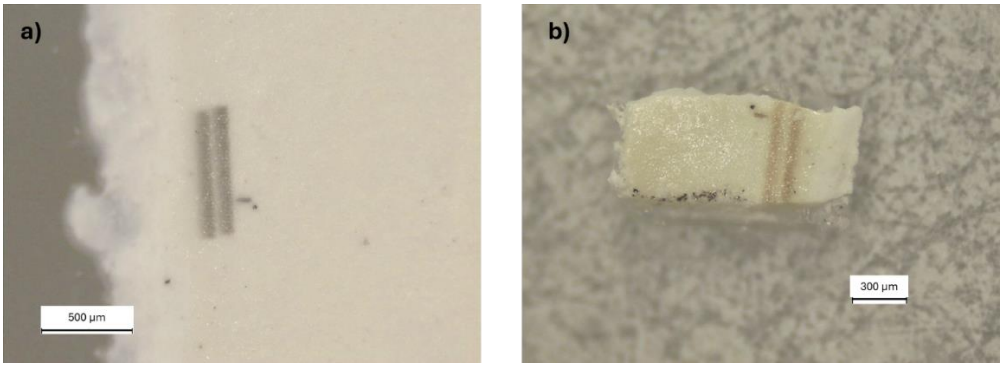

Fig.5. 14 OM image (5.5X) a) just after irradiation, and b) after 2 and a half days since the X-ray irradiation raster scan of 150 x 750 µm^2 (each point irradiated for 7 min) of lead white in linseed oil paint at 13.5 keV.

Some tests of ΔR long term monitoring (post 4 and 11 days) were performed before and after a previous beamtime at BM16 at ESRF synchrotron in Grenoble (proposal number HG191) on lead white in animal glue and in linseed oil (Fig. 5.15). A 15 min XAS was acquired on each sample, in this case the beam spot (FWHM) was 200 x 100 µm^2 with a photon flux of 10^{11} ph/s. The damage extent and shape of these tests, even if performed with different flux and beam size, are consistent with the ones detected in Fig. 5.13. Between 4- and 11-days post irradiation the damage on the linseed oil mock-up shows a small reversion mainly towards the red part of the spectrum, while on the animal glue the damage remains constant (Fig. 5.15), this could indicate either a slower reversion or a permanent nature of the damage induced on the animal glue sample.

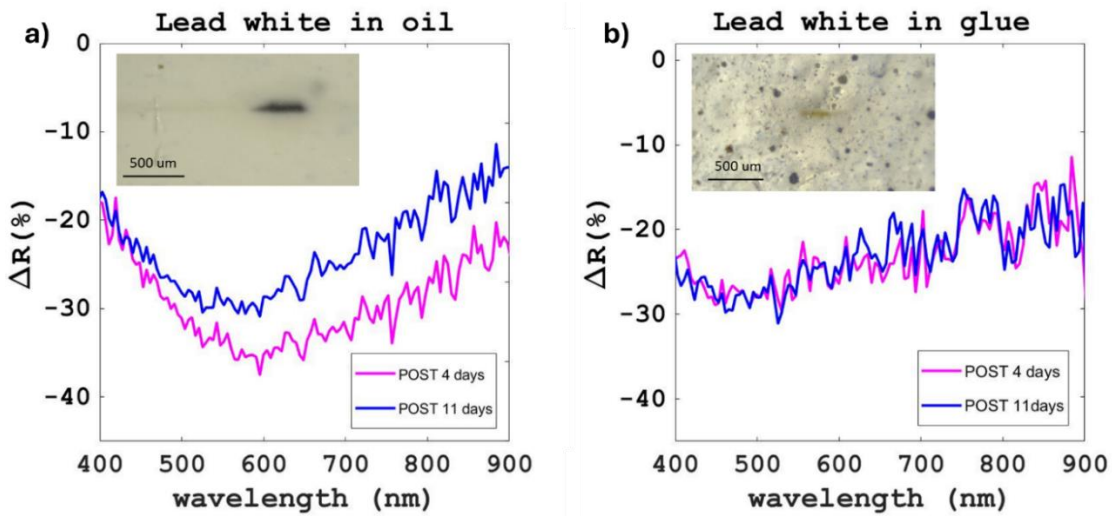

Fig.5. 15 The ΔR plots of the post irradiation long term monitoring (after 4 in pink and 11 days in blue) of lead white in a) linseed oil and b) in animal glue after a XAS at Pb LIII edge of 15 min at BM16 beamline at the ERSF, Grenoble. The beam spot on the sample is 200 x 100 µm^2 with a photon flux of 10^{11} ph/s. In the 2 insets, the optical microscope images (5x) of the damage just after the X-ray irradiation.

The long-term monitoring on the Prussian blue with lead white in animal glue sample irradiated for 2 min at 13.5 keV (Fig. 5.16) shows that a ΔR change after irradiation of -6% towards 400 nm is reduced to -3% after 5 hours. A very short 3 s irradiation of the vermilion in oil thin section at 12.95 keV resulted in a ΔR change of 1.8% (Fig. 5.17). The damage gradually reverted back and is almost completely reverted to 0 after 35 minutes post irradiation.

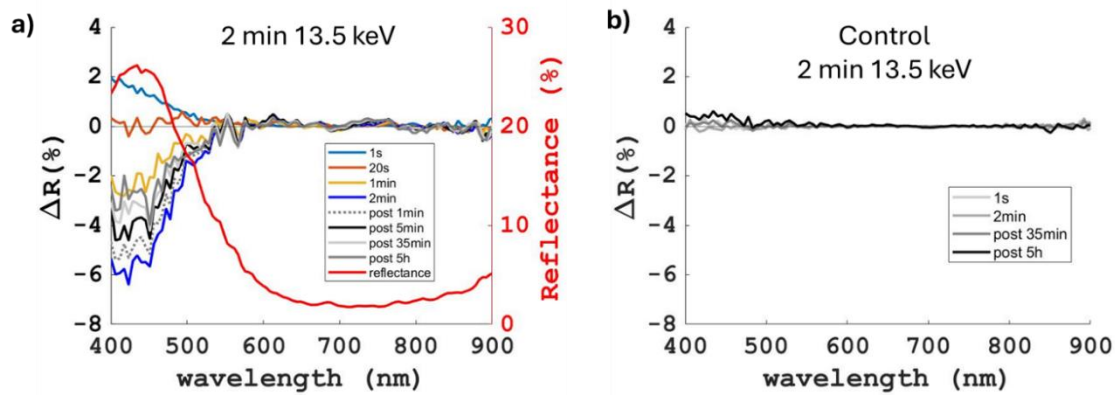

Fig.5. 16 a) the ΔR monitoring during 2 min irradiation at 13.5 keV of the Prussian blue and lead white sample in oil with a long monitoring of the damage within 5 h after irradiation. The red curve corresponds to the reflectance of the paint sample prior to

irradiation, b) the internal control obtained from an area of the paint far from the X-ray spot.

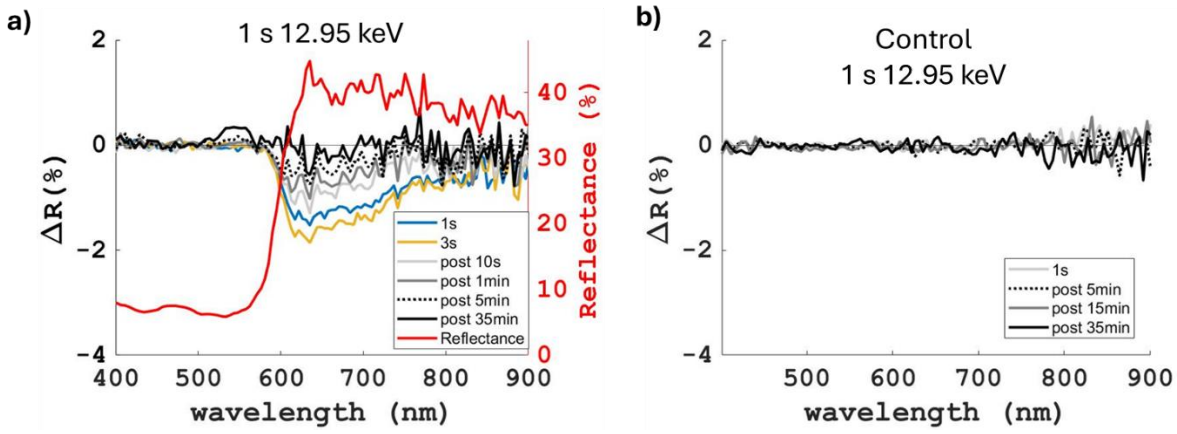

Fig.5. 17 a) ΔR long term monitoring of vermilion irradiated for 1 s at 12.95 keV, with a reference of the reflectance of the paint sample prior to irradiation (red curve); b) the internal control obtained from an area of the paint far from the X-ray spot.

5.4.2. Fe K-edge

At the Fe K-edge (7112 eV) Prussian blue-containing samples were analysed, performing XAS scans at different duration (minimum 5 min, to a maximum of 26 min) and acquiring multiple consecutive spectra on the same spot (minimum 3 to a maximum of 12 consecutive spectra).

During a XAS of 14 min at the Fe K edge on the Prussian blue in animal glue sample, the ΔR show at the beginning a change of -0.5/-1% at around 400 nm and after a couple of minutes, a drop of reflectance starts to appear around 700-750 nm (Fig. 5.18). The latter ΔR change start to occur when in the XAS energy scan the Fe K-edge of Prussian blue at 7126 eV is reached (Fig. 5.18c). It is possible to hypothesize that the spectral change towards 400 nm is due to a damage to the proteinaceous binder, that appears immediately due to the higher susceptibility of organic matter to X ray damage, especially upon irradiation with low energy X-rays [136]. While the Prussian blue, whose intense colour originates from the broad absorption feature around 700 nm related to

the intervalence electron transfer between Fe(II) and Fe(III) ions [190], may starts to be damaged later in the irradiation. In fact, the pigment is well known to be susceptible to X-ray radiation damage, being prone to photoreduction [191]. The observed ΔR change at 700-750 nm may be ascribed to a damage to the Prussian blue, as it appears during the energy scan only when the Fe K-edge is reached and being at the wavelength region that corresponds to the absorption that gives the colour to the pigment.

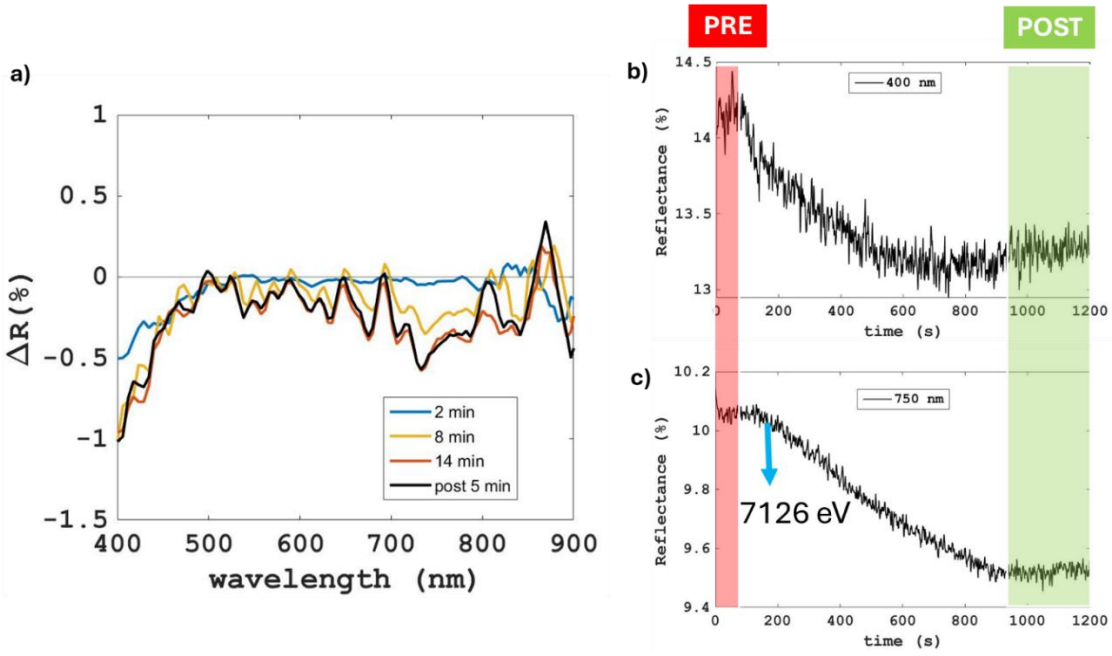

Fig.5. 18 The monitoring of one XAS at the Fe K edge of 14 min on the Prussian blue in animal glue sample: a) the ΔR during (light blue 2 min, yellow 8 min, orange 14 min) and after the XAS measurement (black lines); and b) the evolution in time of the reflectance at 400 nm and c) at 750 nm

.

With an overall irradiation of 14 min performing 3 consecutive shorter XAS of ca. 5 min each (Fig. 5.19.), the XAS spectra do not change while the ΔR is comparable in extent and in wavelength range with the previous test of 14 min of Fig. 5.18. This comparison shows that a slow scan of 14 min in energy has a similar reflectance change as when, in the same amount of time, the energy scan is performed 3 times.

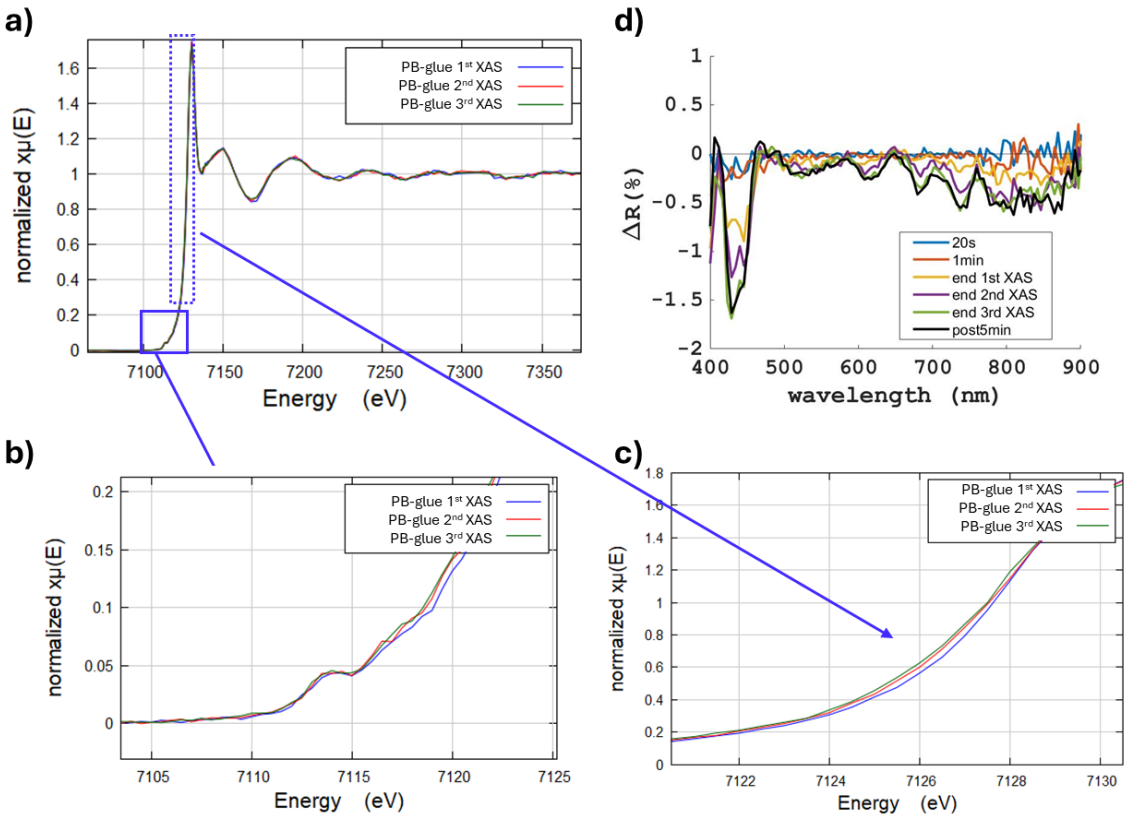

Fig.5. 19 a) the 3 consecutive Fe K-edge XAS of Prussian blue in animal glue with details in the b) pre-edge region and c) edge and d) the ΔR changes during (light blue 20 s, orange 1 min, yellow-purple-green end of 1st-2nd-3rd XAS respectively) and after the XAS acquisitions (black line).

By increasing the number of cumulative spectra (12, of 14 min each), for a total of ca. 3 h of irradiation, the ΔR at 400 nm remain constant at -1%, while the decrease of reflectance at around 700-750 nm gradually decreases up to -4% (Fig. 5.20b). At the iron K-edge, the pre-edge region is characteristic of the contributions of Fe^{2+} and Fe^{3+} [192]. By comparing the 1st, the 6th and the 12th spectra of the series of 12 XAS, a clear change of the pre-edge is detected. The shift of the pre-edge indicates an enrichment of Fe^{2+} species, suggesting that a photoreduction of iron is taking place. The shift of the point of inflection towards lower energy would also indicate the reduction, but is below 1 eV, smaller than the energy resolution. This is a clear example of a questionable dataset as only one part of the XAS spectrum is suggesting beam modifications. In this case, one

would have doubts whether the dataset is reliable to carry on averaging the 12 spectra or if the dataset should be considered invalid.

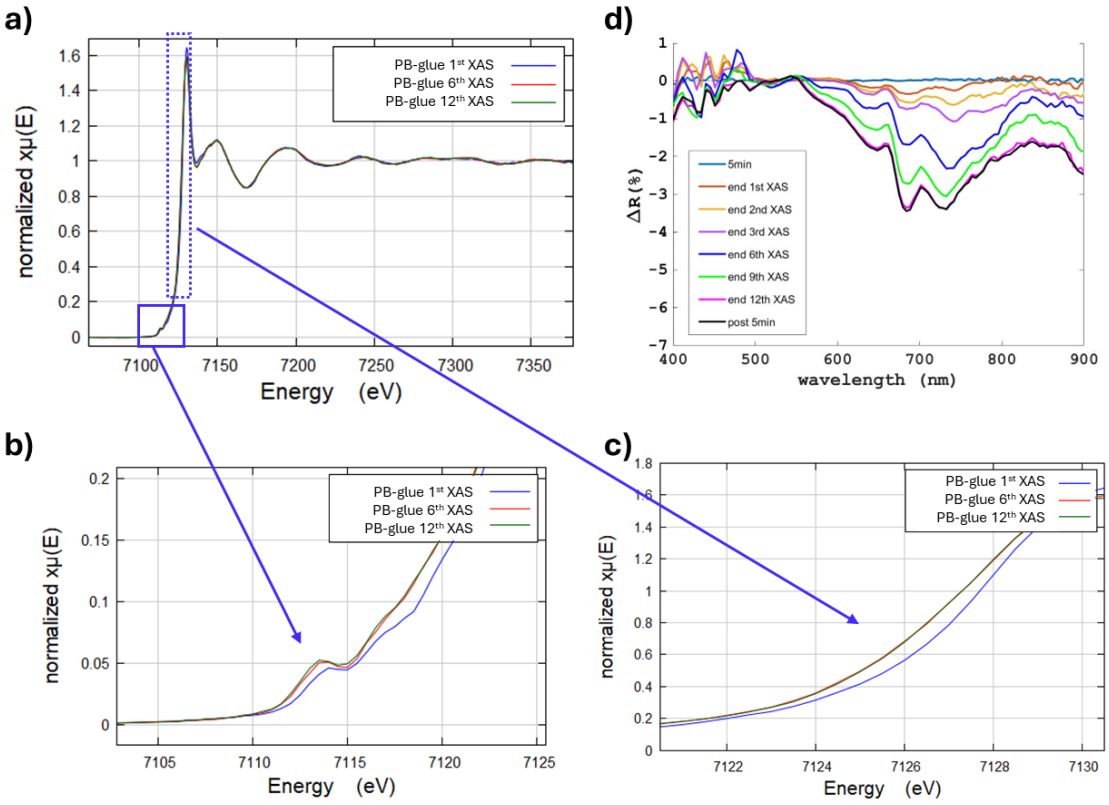

Fig.5. 20 The 12 XAS spectra of 14 min each on Prussian blue in animal glue: a) the 1st, 6th and 12th XAS, b) the detail on the pre-edge region, c) the detail on the edge, d) the ΔR plots during (light blue 5 min, orange-yellow-purple-blue-green-magenta end of 1st-2nd-3rd-6th-9th-12th XAS respectively) and after the XAS acquisitions (black line).

When analysing the same Prussian blue, but in a different environment, e.g. in linseed oil and mixed with lead white, the consecutive 3 XAS spectra of 5 minutes each do not show significant changes, while the reflectance ΔR shows a small decrease of -0.5% towards 450 nm and an increase of 0.3% at 700-750 nm (Fig. 5.21).

When collecting 12 consecutive XAS on this Prussian blue and lead white sample, the changes in ΔR around 450 nm gradually become more severe, increasing to -8%, while at 700-750 nm it remains quite constant at +2% (Fig. 5.22b). Comparing the 1st, the 6th and the 12th spectra of the series of XAS, a clear shift of the point of inflection (above

the energy resolution of 1 eV) clearly shows that a photoreduction of Fe^{3+} to Fe^{2+} is induced by the X-ray irradiation (Fig. 5.22a).

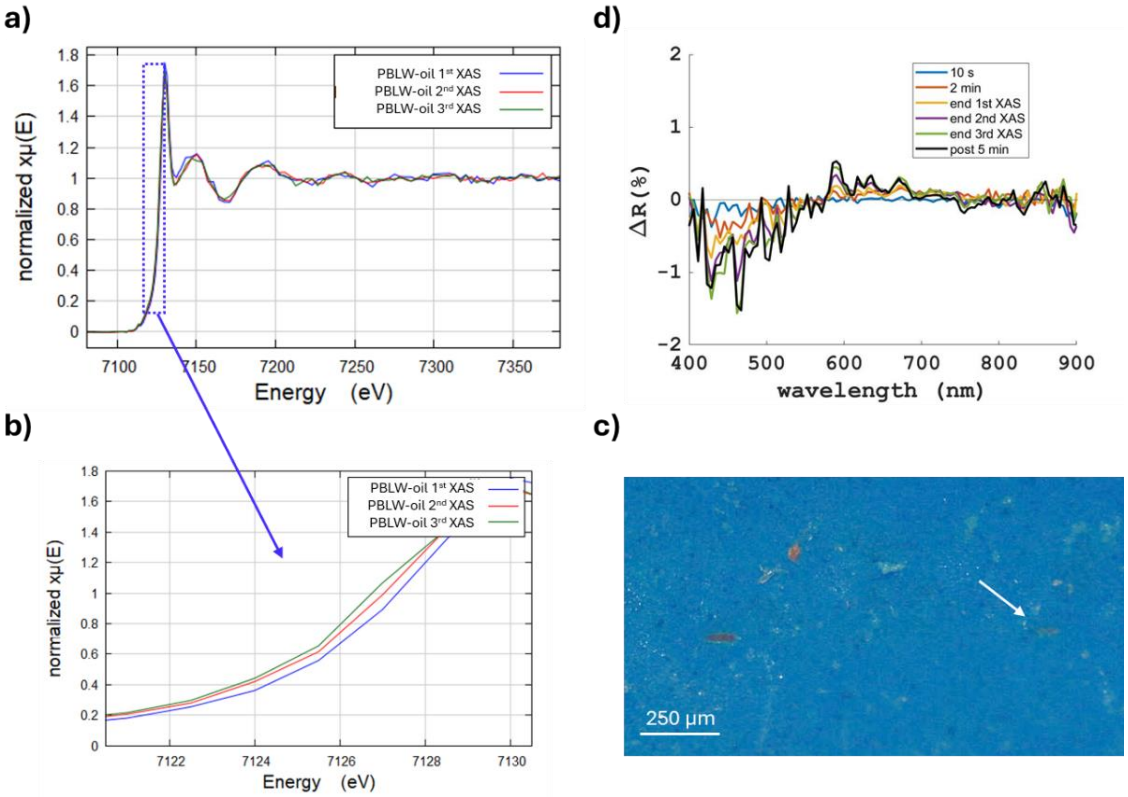

Fig.5. 21 The 3 XAS spectra of 5 min each on the Prussian blue and lead white in linseed oil paint sample: a) the 1st 2nd and 3rd XAS, b) the detail on the edge, c) the optical microscope image of the irradiated area of the sample (white arrow). d) the ΔR changes during (light blue 10 s, orange 2 min, yellow-purple-green end of 1st-2nd-3rd XAS respectively) and after the XAS acquisitions (black line).

Any modification of the electron transfer Fe^{III}–N–C–Fe^{II} bonding pathway, that is the origin of the colour, can result in a fading or a shift in colour. With all these results the photoreduction of iron in the Prussian blue pigment seems clearly correlated to the simultaneous detection of the ΔR change at 700-750 nm. The fact that Prussian blue in animal glue sample and Prussian blue with lead white in linseed oil sample have a very different ΔR but similar shift of the edge of the XANES part of the spectrum must be further investigated, as different degradation mechanisms may occur. With the damage

detection provided by the monitoring of reflectance changes, it is not possible to ascertain the nature of the damage, and complementary techniques would be necessary to characterize the type of damage. For this, the detailed analysis of the EXAFS part of the absorption spectrum may help ascertain the changes in the Fe speciation (e.g. if iron reduces producing a change in the coordination number or if part of the iron escapes the lattice and produces new compounds).

Nevertheless, these data are showing the high material-damage specificity of HSI monitoring and that the technique is very sensitive in detecting early warning signs of damage (only 1% ΔR changes) that are not visible by eye and not detectable by XAS spectral changes (Fig. 5.21). It also proves to be a useful technique to assess the reliability of the XAS data collected on sensitive materials.

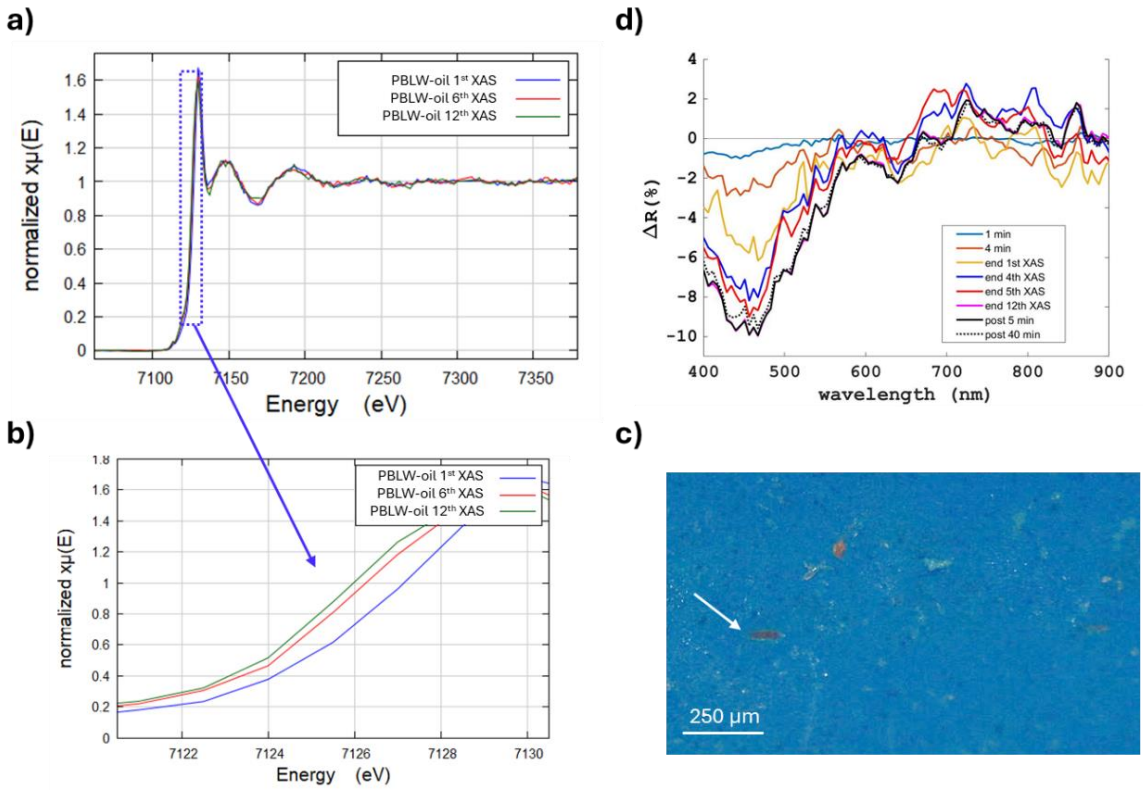

Fig.5. 22 The 12 XAS spectra of 14 min each on the Prussian blue and lead white in linseed oil: a) the 1st, 6th and 12th XAS, b) the detail on the edge, c) the optical microscope image of the irradiated area of the sample (white arrow). d) the ΔR changes during (light blue 1 min, orange 4 min, yellow-blue-red-magenta end of 1st-4th-5th-12th XAS respectively) and after the XAS acquisitions (black lines).

5.4.3. Hg LIII edge

At the Hg LIII edge (12284 eV) a thin section of ca. 15 µm of a 15-year-old vermilion paint mock-up in linseed oil was irradiated. One 14 min long XAS, 2 spectra of 14 min each and 6 spectra of 14 min each were performed (Fig. 5.23). The ΔR of the 3 tests show a severe decrease of reflectance from 600 nm onwards of -32% for the single XAS spectrum and up to -39% for the 6 consecutive spectra (Fig. 5.23). In all 3 cases, after 5 min post irradiation the damage remain constant. All the irradiated areas appear severely blackened just after irradiation (Fig. 5.23a) and after 3 months the damaged spots are still visible (Fig. 5.24a) with the single 14 min XAS spectrum irradiation spot appearing slightly fainter.

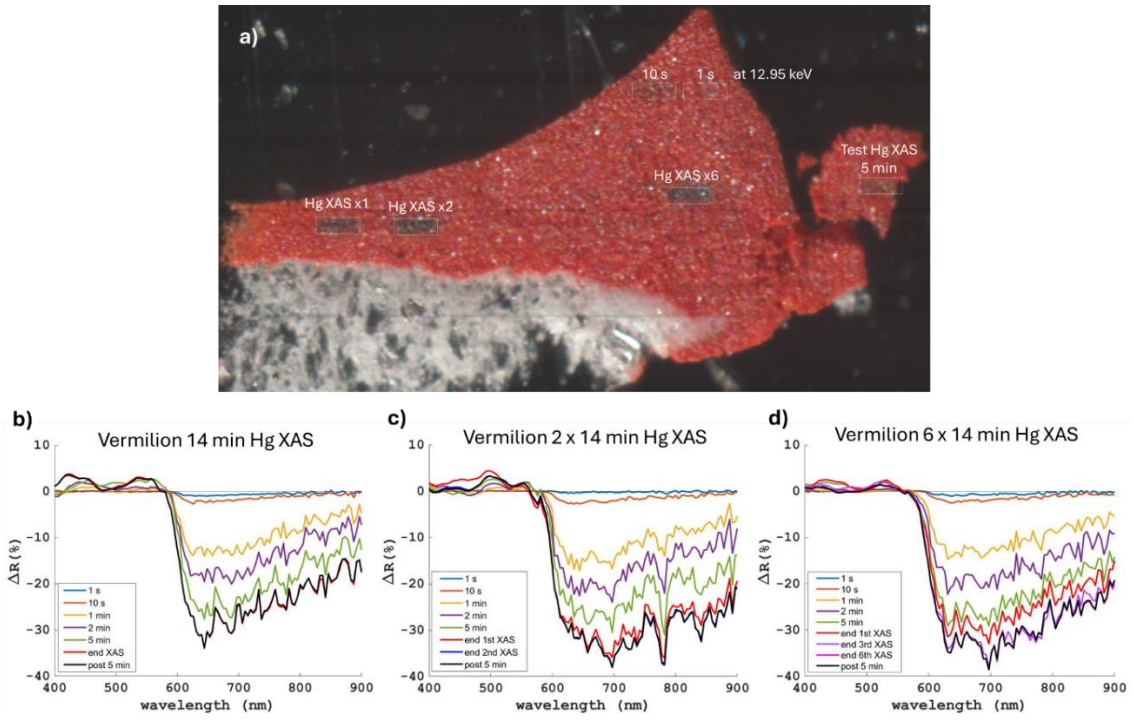

Fig.5. 23 a) The RGB image of the HSI spatial scanning of the vermilion thin section sample after the irradiation tests. Below, b) the ΔR spectra collected during (coloured lines) and after (black line post 5 min) one XAS at the Hg LIII edge. c) the same for 2 XAS of 14 min each and d) 6 XAS of 14 min each.

As for the laser-induced blackening of vermilion (see Chapter 4), to ascertain the nature of the blackening, micro-XRPD mapping was performed at ID13 (details in section 3.2.5). The analysis of the XRPD maps reveal no significant differences between the irradiation spot and the surrounding in terms of changes in the intensity of the diffraction pattern of vermilion. Only a small reflection at 18.76 2Theta (2.92 Å), that can be ascribed to metacinnabar (β-HgS), is present around the thin section, but again with no clear spatial correlation with the X-ray beam spots (Fig. 5. 24). No clear XAS spectral changes are observed in the consecutive tests.

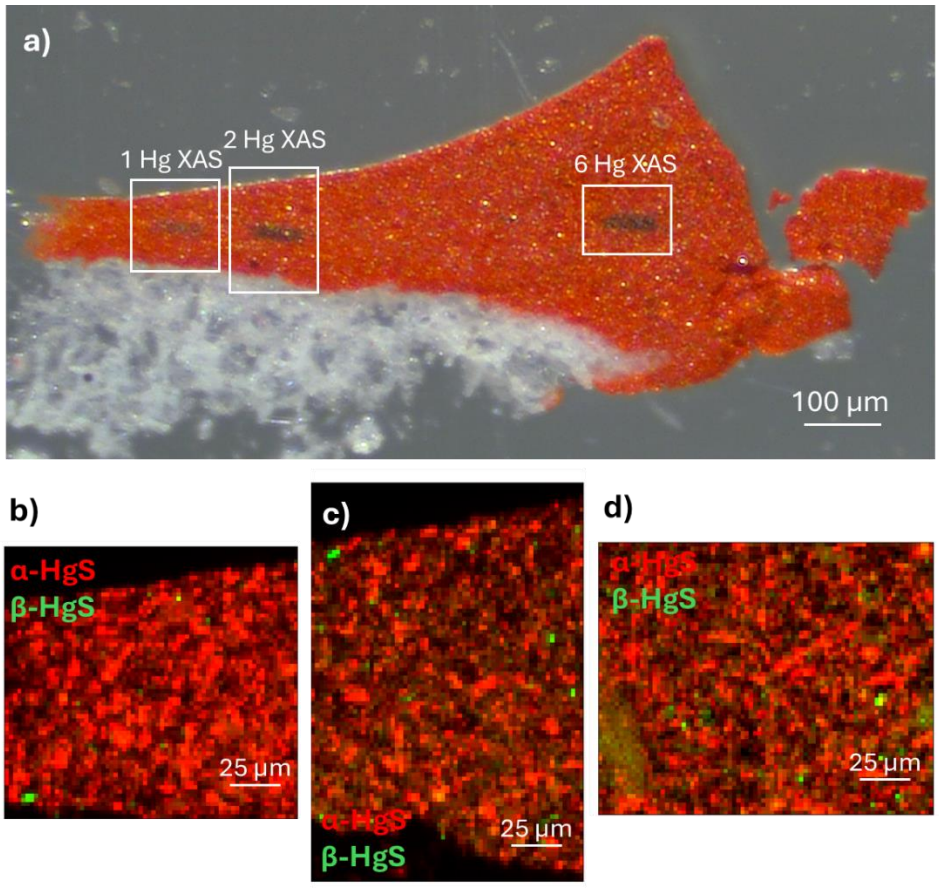

Fig.5. 24 a) the OM image of the thin section after 3 months since the X-ray irradiations. b) the ROI imaging RGB correlation map (Red for vermilion α-HgS, Green for metacinnabar β-HgS) of the area irradiated to acquire one Hg LIII edge XAS spectrum of 14 min, c) 2 XAS spectra of 14 min each and d) 6 XAS spectra of 14 min each.

5.4.4. As K-edge

At the As K-edge (11864 eV) a thin section of ca. 15 µm of a 15-year-old realgar paint mock-up in linseed oil was prepared and used for the X-ray irradiation tests after 2 years since preparation. Due to natural aging, the thin section is mainly formed of pararealgar. One 14 min long XAS, 2 spectra of 14 min each and 6 spectra of 14 min each were performed (Fig. 5.25). The ΔR of the single XAS shows a decrease of reflectance centred at 550 nm of -15% that slightly revert to -11% in the post 5 min irradiation monitoring. The 2 times XAS test shows a similar ΔR, but the damage did not revert much after 5 min post irradiation and it appears orange in colour. The 6 times XAS test shows a decrease of reflectance centred around 560 nm of -22% with a slight reversion after 5 min to -20%. Apart from the ΔR change around 560 nm, also an overall -2% in the rest of the spectral range occurred and remained constant. The spot appears clearly orange just after irradiation (Fig.5.25a).

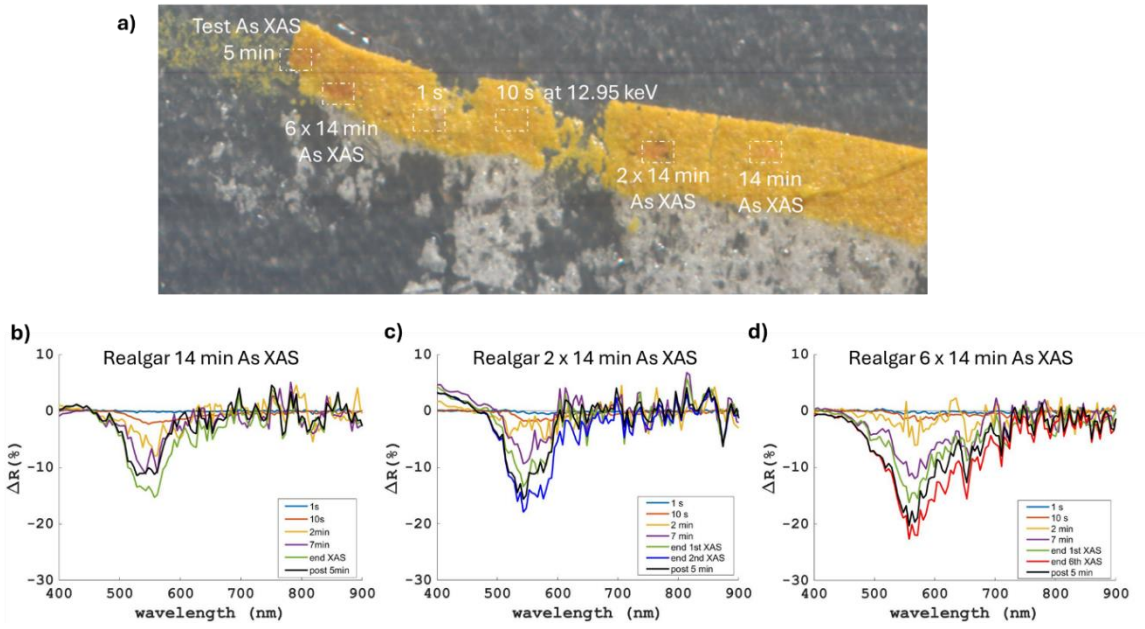

Fig.5. 25 a) The RGB image obtained from the HSI scanning of the realgar thin section sample after the irradiation tests. Below, b) the ΔR spectra collected during (coloured lines) and after (black line post 5 min) one XAS at the Hg K-edge. c) the same for 2 XAS of 14 min each and d) 6 XAS of 14 min each.

All three tests still look orange under the microscope after 3 months since X-ray irradiation (Fig. 5.26a). To ascertain the origin of the colour change, µ-XRPD mapping was performed on the three areas (Fig.5.26). In this case, a clear spatial correlation of the diffraction pattern of the X-ray spot compared to the surrounding is observed. In the single 14 min XAS test (Fig. 5.26 d), the irradiated area shows a small increase of background around 10 2Theta (5.55 Å) and a decrease of contribution of the pararealgar peaks. Within the paint layer, alacranite (As_8S_9) is also found and it is mainly localized in the X-ray damaged. By increasing the number of consecutive XAS, the background around 10 2Theta keeps gradually increasing (Fig. 5.26f). After 2 XAS a slight increase of contribution of alacranite is observed, while in the consecutive 6 spectra test an overall decrease of crystallinity is detected (Fig. 5.26b). No clear XAS spectral changes are observed in these tests.

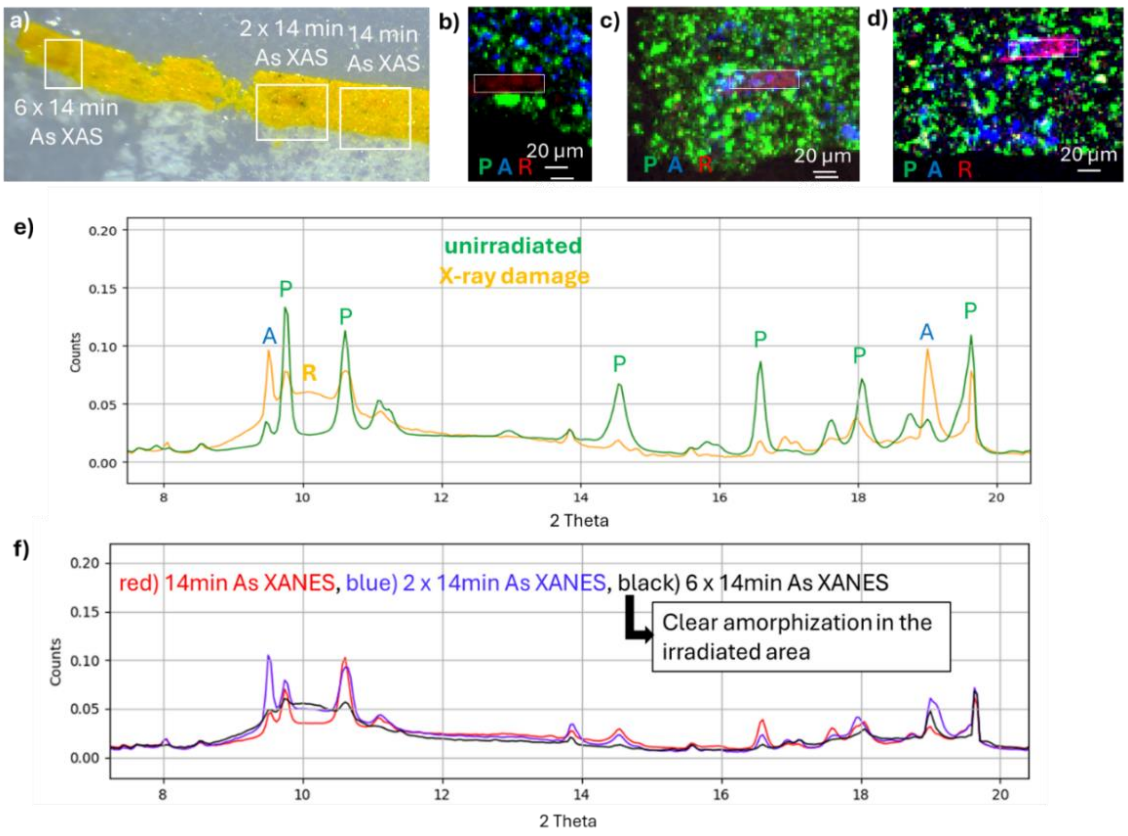

Fig.5. 26 a) the OM image of the realgar thin section after 3 months since X-ray irradiation. b) the RGB false colour correlation maps (Red ROI at 10 2Theta, Green pararealgar, Blue Alacranite) of the area irradiated to collect 6 times a 14 min As K-edge XAS spectra, c) 2 x 14 min and d) one spectrum of 14 min. e) the normalized

average diffraction patterns from the unirradiated area of the map (green curve) and from the X-ray spot of the test c), were pararealgar (P) and alacranite (A) are found as well as a very broad peak around 10 2Theta (R). f) the comparison of the normalized average diffraction patterns from the three X-ray damaged spots of b) in black, c) in blue and d) in red.

5.5. Comparison of X-ray and laser radiation damage

The pigments used for the experiments were selected for their sensitivity both to optical laser radiation and X-rays and the comparison gives useful insights on the two types of radiation damage that are often seen as totally different types of mechanisms but that actually show interesting similarities.

The X-ray irradiation of the realgar paint sample was carried out on a 2-year-old thin section. This thin section resulted to be already transformed into pararealgar (Fig. 5.26), since the slice was cut from the realgar paint mock-up 2 years ago. While, the laser irradiation was carried out on the surface of the paint mock-up, that presented at the surface a thin layer of pararealgar (see Chapter 4, Fig. 4.12). So, although the X-ray and laser irradiation were performed on a different paint thickness, namely 15 µm and 200 µm, in both tests the photons impinged on a surface rich of pararealgar. In both cases a colour change from pale yellow, typical of pararealgar, to orange under X-rays around 11.8 keV (Fig. 5.25) and with a low power 532 nm laser (Fig. 4.14) was noticed. The ΔR changes are also similar (Fig. 5.27). From the µ-XRPD maps it is not clear if a phase change or a modification of crystallinity is taking place in the laser irradiated spot, while in the X-ray spot clear signs of amorphization are found. This could also be due to the different amount of damaged material analysed with XRPD. In fact, the diffraction map was carried out on the whole X-ray spot, while for the laser irradiation only a thin section from the irradiated spot was measured.

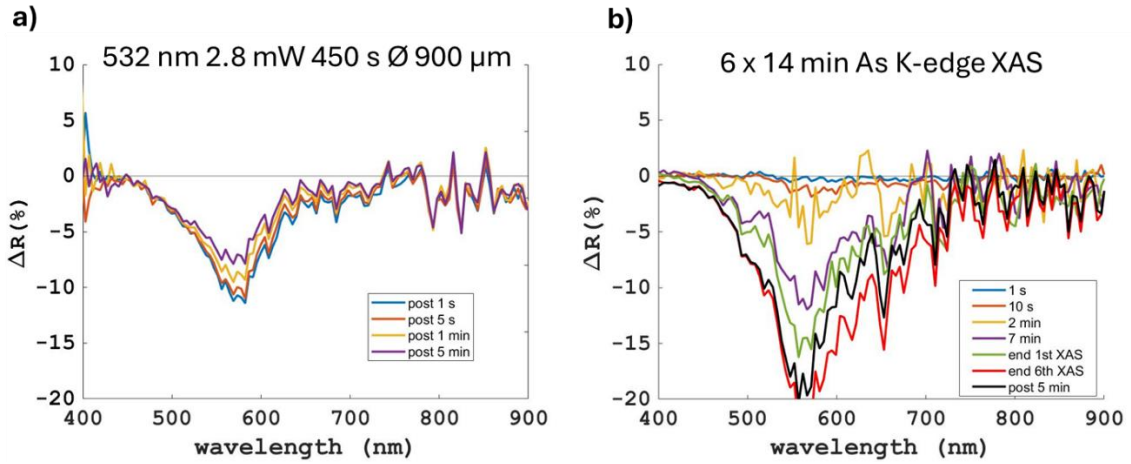

Fig.5. 27 The irradiation tests on realgar paint sample: a) ΔR plots of the post irradiation monitoring of 532 nm laser irradiation of the surface with a spot of 900 µm, at 2.8 mW for 450 s; b) ΔR plots during (coloured lines) and after (black line) the 6 XAS spectra acquired at the As K-edge for a total duration of 84 min on a thin section of 15 µm obtained from the paint mock-up.

Even the irradiation tests on vermilion paint mock-up were performed on the bulk with the lasers and on thin sections with X-rays, therefore the comparison is qualitative. Nevertheless, the X-rays around 12.2 keV and the 532 nm laser irradiations produced a similar darkening effect by eye but the crystal modification and ΔR changes are different. With the 532 nm laser, the ΔR is an overall reduction of -2% in the whole spectral range (400-900nm) and above 600 nm a constant severe reduction of ΔR of -10% was detected (Fig.5.28). With X-rays, the ΔR change consists of a much more severe decrease of reflectance in the range above 600 nm, up to -30/-38% mainly at 600 nm and reducing to -20% at 900 nm; while below 600 nm, in the absorption range of vermilion, an increase of reflectance of 2/4% is observed (Fig. 5. 23). From the micro-XRPD maps, on the laser irradiated spot a crystal modification on a very thin surface layer (below 10 µm thickness, see Chapter 4, Fig. 4.7) ascribable to the formation of a thin layer of metacinnabar was detected. While no clear signs of metacinnabar were detected in the X-ray irradiation spot compared to the surrounding area of the paint.

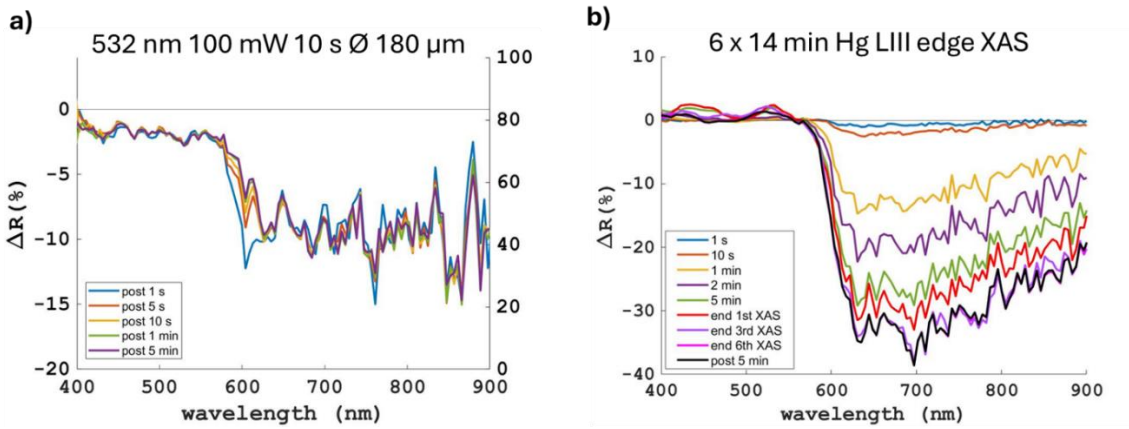

Fig.5. 28 a) The ΔR change after the 532 nm laser irradiation with 100 mW with a spot size of 180 µm for 10s on the vermilion oil paint mock-up. b) The ΔR during (coloured lines) and after (black line) the 6 XAS at the Hg LIII edge on the vermilion in oil thin section.

Prussian blue is well known to be damaged under broad band light [150,193], optical lasers [52] and upon X-ray radiation [15]. The pigment tends to bleach under visible light resulting in an increase of reflectance at 450 nm [181]. The damage seems to be mainly caused by the radiation at the wavelength range of the least absorbed part of the visible spectrum, i.e. 400-450 nm [194]. While with X-rays, Prussian blue is known to photo-reduce and it appears darker [191].

In the present study, with 780 nm laser irradiation of Prussian blue, a decrease at the 400-450 nm range was detected (Fig. 5. 29a). On the same sample, upon XAS acquisitions at the Fe K-edge, at least two ΔR changes were detected at different time scale (Fig. 5.29b): the decrease at 400 nm can be ascribed to the binder damage as suggested by the same change observed when irradiating the binder alone. While a second change around 700 nm (negative ΔR on the Prussian blue in animal glue and positive ΔR in the Prussian blue mixed with lead wite) can be associated to the photoreduction of the Fe species, as it correlates with the XAS spectral changes (Fig. 5.20).

Therefore, while the ΔR change on Prussian blue irradiated with X-ray is similar to the 780 nm laser damage (Fig. 5.29), it is very different with respect to broadband light fading reported in literature [181]. Nevertheless, the XAS analysis at the Fe K-edge of X-

ray induced damage and broad band light fading suggests a photoreduction of the pigment in both cases. The presence of competing effects that produce a reduction of iron in the Prussian blue degraded pigment is still an open question, both with X-ray and visible radiations [195], and the comparative study of these radiation damages may help to shed light on the reactivity of the pigment.

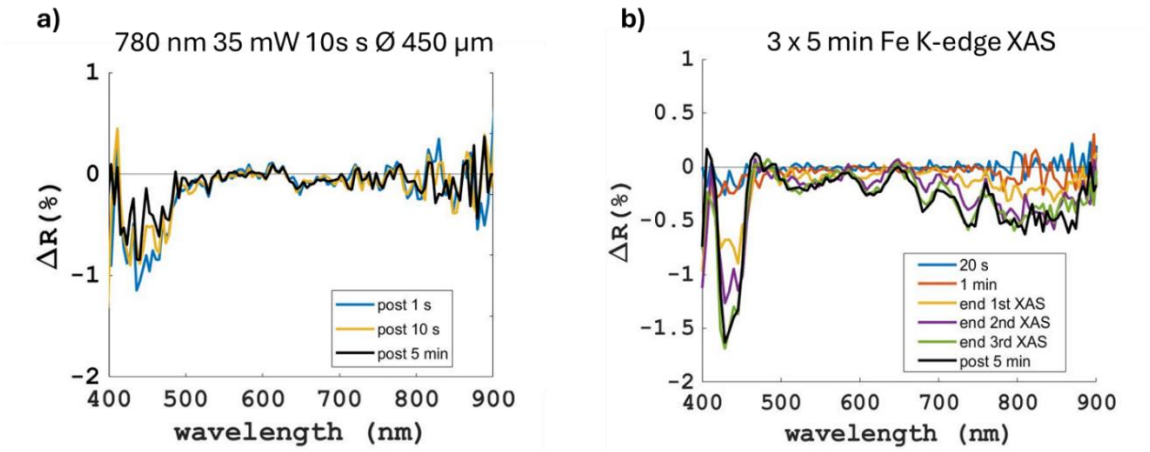

Fig.5. 29 a) The ΔR change after the 780 nm laser irradiation with 35 mW with a spot size of 450 µm for 10 s on the Prussian blue in animal glue paint mock-up. b) the ΔR plots during (coloured lines) and after (black line) the acquisition of a 3 consecutive Fe K-edge XAS of 5 min each on the same Prussian blue in animal glue sample.

5.6. Conclusions

The *operando* VIS-NIR microscopic HSI monitoring method effectively allowed to follow the evolution of specific radiation effects on paint materials while performing XAS and at fixed energy with typical durations used for XRPD. The effects of irradiation at specific energies commonly used to analyse historical materials were explored, namely the K-edge of Fe and As, and the LIII edge of Hg and Pb. This energy range (7-13 keV) falls in the broader range of energy commonly used for multiple X-ray spectroscopic techniques and diffraction measurements in Heritage Material Science (from few keV to 30 keV).

Some paint mock-ups containing lead white, Prussian blue, realgar and vermilion were irradiated.

The method enables the investigation of radiation damage in multiple ways: the diffusion in space, the evolution over time and the spectral changes that can be indicative of specific mechanisms of damage (both physical and/or chemical).

Some ΔR changes upon irradiation were partially or almost completely reverting in the post monitoring (from 5 min to few hours and days). Many ΔR changes were not correlated by any XAS spectral change (i.e. all the irradiation of the lead white containing samples at the Pb LIII edge; the vermilion and realgar at Hg and As edges, respectively; and the short irradiations of Prussian blue samples at the Fe K edge), and for some of them the damage was not visible by eye (i.e. Prussian blue in animal glue). In part, this is because XAS provides information only regarding the speciation of a particular element, that may not be necessarily the one affected by beam damage, e.g. binder damage. Indeed, some changes observed upon irradiation are ascribable to the binder damage, although complementary techniques are needed to corroborate such hypothesis and to better characterize the mechanism.

It is not possible to simply rely on the XAS changes to demonstrate the material safety of a specific measurement. In the case of Prussian blue, it was possible to identify changes to the chemical speciation of the Fe present in the pigment and associate it to specific ΔR change at 700 nm, which corresponds to the wavelength range of the absorption feature that impart the blue colour of the pigment. To better understand the mechanisms of X-ray induced damage on our specific mock-ups, a more thorough study of the XAS spectra, both in the pre-edge region and in the extended region (EXAFS), is needed. In some Prussian blue irradiation tests the ΔR changes at 700 nm were not followed by significant XAS spectral change, demonstrating the higher sensitivity of the reflectance spectroscopy technique in identifying even subtle modifications of the surface. This can easily be explained by the intrinsic low detection limit conventionally assumed for secondary phases in XAS technique, that is 5% wt.

The evaluation of damage based on ΔR reflectance changes varying different instrumental parameters and irradiating several materials, showed that:

- The pre-edge energy does not seem to be less damaging than edge and post edge energies of an element present in the sample with the irradiation conditions used;
- In the energy range and irradiation time investigated it is not clear on our samples whether a low energy is generally more damaging than a high one;
- The reciprocity principle is not followed in all the investigated samples; therefore, it is not possible to always recommend a longer acquisition at lower flux for a safer analysis;
- The spot size seems to have an important role even in X-ray radiation damage mechanisms. Further studies are needed to better understand the reason.
- The thicker paint layer, absorbing a significantly higher amount of energy, seems to be more damaged than the thin section, suggesting safer analysis with the latter;
- The proteinaceous binder (animal glue) seems to be more damaged than the oil binder in the long term and it affects a larger part of the surface than the lipidic binder (linseed oil).

The thermal contribution has not been verified and focused tests in this direction are crucial to assess its contribution in X-ray radiation damage.

Overall, with almost all the irradiation tests carried out on the painting mock-ups, damage has always been detected to some extent, sometimes extremely subtle and partially or almost completely reverting in the post monitoring. Therefore, in line with the basic principle of “as less radiation as possible”, energy dispersive XAS should be considered more for the future of analysis of cultural heritage materials to significantly minimize the absorbed dose (when applicable and meaningful for the specific information required from a XAS experiment). Finally, the method contributes to the development of mitigation strategies necessary to reassure the SR users community from the cultural heritage field and it could be implemented in a routine manner for the analysis of historical materials at a synchrotron facility.

6. In-depth characterization of CW NIR laser irradiation to recover darkened red lead for wall painting restoration

In mural paintings the widely used red lead pigment (Pb_3O_4) may darken due to its transformation to plattnerite (β-PbO_2) and no well-established conversion methods to restore darkened red lead in wall paintings have been reported yet. Only in recent research the Near Infrared (NIR) Continuous Wave (CW) laser irradiation has been proposed and tested on mock-ups and on a mural painting to recover darkened red lead. Although very promising, the method still needs to be fully characterized (penetration depth, stability, by-products etc.) and the understanding of the main mechanism is crucial for the identification of the best operative conditions and to assess the possible risks associated to this method. To identify the laser-induced products and their distribution in the paint layer a combination of synchrotron based (SR) micro X-ray powder diffraction mapping (μ-XRPD), micro-Raman spectroscopy, Near-edge X-ray absorption spectroscopy (XANES) and VIS-NIR and short wave infrared (SWIR) hyperspectral imaging has been used to characterize the bulk, the surface and the stratigraphy of a plattnerite wall painting mock-up irradiated with a CW 1064 nm laser. A comparison of the laser induced products with a purely thermally-induced reduction of plattnerite into red lead showed experimental evidence of a predominant thermally driven effect of a 1064 nm CW irradiation. Apart from the formation of red lead, non-stoichiometric lead oxides where found and specific spectral features of these intermediate phases were identified both with Raman and VIS-NIR reflectance spectroscopy and the compounds are surprisingly stable (up to 2 years).

6.1 Introduction

Red lead, also called Minium, is a bright red pigment particularly appreciated and widely used since antiquity. It is one of the earliest manufactured pigments traditionally produced by calcinating (thermal treatment) for several hours lead white (lead carbonates often a mixture of hycrocerussite and cerussite) [196]. The pigment is a mixed valence state lead oxide (Pb_3O_4), with both Pb(IV) in distorted octahedral and Pb(II) at the vertices of irregular pyramids [197]. Due to the high proximity of the temperature at which also the lead monoxides (massicot and litharge, β- and α-PbO, respectively) are produced [198] and the low control on the effective temperature of the furnaces, lead monoxide impurities are often present even in high concentrations, like 15% in weight [199]. Various types of red lead discoloration have been reported in the literature, mainly referred to as darkening and bleaching [196,200]. The identification of the alteration products of red lead and the understanding of the main mechanisms is an open challenge. On several wall paintings it has been reported to be a darkening phenomenon, often ascribed to the transformation of red lead into the beta form of lead dioxide [201–205], called plattnerite, β-PbO_2, which is a brown-black compound. Only in few cases the α-PbO_2 phase, called scrutinyite (also dark in colour), has also been reported on wall paintings [204,206,207]. The very similar calculated potentials for the formation of plattnerite and scrutinyite suggest a small change in the precipitation conditions in order to obtain these polymorphs [208]. The darkening is mainly reported as a phenomenon starting from the surface like in [209], although also cases of overall darkened stratigraphy or darkening starting from the substrate have been observed [210,211]. The presence of lead monoxides impurities seems to enhance the reactivity of the red lead pigment towards discoloration [210,212]. The main analytical methods used to identify plattnerite are XRPD and Raman spectroscopy [213]. But the latter, although extensively used, does not represent a very reliable identification method for this specific compound. The laser wavelengths conventionally used in the VIS-NIR regime for Raman spectroscopy are 532, 632, 785 and 1064 nm. Plattnerite, being a poor scatterer, highly absorbs both the incident and Raman photons resulting in a very low Raman signal. The spectral features of plattnerite are characterized by a main, very broad

band around 515 cm^{-1}. Moreover, careful control on the laser power must be applied to avoid laser-induced degradation into red lead and the lead monoxides [163].

Several experiments have been conducted to try reproducing the red lead darkening based on environmental factors [210], like light irradiation [214] and microbial activity [207], but many of these artificial experiments did not effectively reproduce the formation of plattnerite [199]. The presence of salts and humidity gave the best artificial ageing results [207]. The authors demonstrated that in presence of water the darkening of red lead is induced by light, but when $NaHCO_3$ is added red lead transforms to plattnerite even in darkness. In acidic solution, red lead was proven to undergo a disproportionation reaction, resulting in the formation of plattnerite and Pb^{2+} in solution [215] which can then form PbO or directly precipitate as a carbonate or sulphate in contact with carbonate or sulphate ions [203]. Hence, although both red lead and lead white degradation can produce the formation of plattnerite, the co-presence of cerussite and plattnerite does not necessarily indicate lead white as the original pigment.

In some cases, the red lead darkening is so pronounced that the wall painting totally lose the readability and extensive research has recently focused to virtually reconstruct the original colour scheme of a wall painting [216]. Up to now, no methods to effectively recover the darkened red lead in wall paintings have been established yet as a restoration procedure and their development are crucial to safeguard the integrity and enhance the readability of artworks. Only in the last two decades, a method based on CW laser irradiation has been tested on mural painting mock-ups and in one real wall painting [74,217]. The authors showed that with VIS-NIR CW lasers the transformation of plattnerite into red lead occurs at different intensity threshold using 514, 811 and 1064 nm lasers. Undesired formation of lead monoxides was obtained mainly with the 514 nm laser and was ascribed to the higher absorption at this wavelength. Although very promising, the method still needs to be understood and fully characterized. Little is known regarding the treatment penetration depth, the efficacy and level of control of the method, and the stability over time. It has been assumed that the main laser-induced effect is thermal but has not yet been correlated to experimental evidence. The understanding of the main mechanism is very important to improve the laser operative

conditions and to better evaluate the risks associated with such restoration treatment. Finally, it is important to identify suitable analytical techniques that could be used *in situ* for the assessment and control of the laser treatment.

To answer these questions, we performed an in-depth characterization of a plattnerite wall painting mock-up irradiated with a 1064 nm CW laser with different laser operative conditions. The multi-analytical investigation was conducted both on the bulk and on the cross section of the paint layer using micro-Raman spectroscopy, VIS-NIR and SWIR hyperspectral imaging, X-ray absorption spectroscopy with near edge fine structure (XANES) and SR micro X-ray Powder Diffractometry mapping (μ-XRPD). To better understand the laser-driven mechanism, the results of the laser treatment were compared to the ones of a purely thermal treatment performed on a variable temperature X-ray powder diffractometer.

The study gave valuable insights on the laser treatment with unexpected identification of stable (up to 2 years) non-stoichiometric lead oxides on the sub-surface. Characteristic features in the VIS-NIR-SWIR spectral range enable the monitoring of the overall laser treatment. The vibrational characteristic Raman bands of the non-stoichiometric lead oxides was identified, enabling a point analysis assessment of the laser treatment. The understanding of the main laser-induced effect allows discussion of the pros and cons of this possible restoration method to recover darkened wall painting containing red lead pigment.

6.2 Samples and experimental design

A chemical grade plattnerite powder (ACROS 97% purity grade) was used for the variable temperature XRPD measurements (see details in section 3.2.4). A first PbO_2 powder sample was heated up from room temperature to 600°C with a heating rate of 20°C/min and collecting the diffractogram every 20°C from 350°C to 450°C and then every 50°C up to 600°C. After cooling at a rate of -50°C/min, the sample was measured again at room temperature. A second PbO_2 powder sample was heated up to 410°C at a heating rate of 150°C/min and immediately cooled down with -50°C/min. The black solid product

formed by this heat treatment was re-measured after 1 day, 2 weeks, and after few months to check the stability both with XRPD and micro-Raman spectroscopy.

A wall painting mock-up was made applying the same chemical grade plattnerite in animal glue on a lime mortar substrate composed of a coarse layer of lime and sand (B/A ratio 1:3) and a smooth thin “intonachino” layer (B/A ratio 1:1) with finer sand.

For the laser irradiation tests, a Nd: YAG CW 1064 nm Spectrum Stabilized Single-Mode laser with > 300 mW of fiber coupled output power was used, providing a gaussian beam that was used with a spot size of 450 and 200 µm. The surface temperature of the tests performed with the 450 µm laser spot was monitored with the thermally controlled Raman system (for details [105]) which allows to monitor the surface temperature during the laser irradiation, the temperature reading represents an average value from an area slightly bigger then the spot size (the ratio between the laser spot area and the sensor area is about 0.64 [106]). Several tests were carried out varying the laser power to identify the suitable intensity threshold for an effective transformation. When a certain effect was observed under the microscope, micro-Raman spectroscopy (details in section 3.2.1), VIS-NIR and SWIR hyperspectral imaging (details in sections 3.1.1 and 3.2.6 respectively) were performed on the surface of the sample fragments. Once identified the best intensity (250 W/cm^2) with a 200 µm spot size (FWHM), a treatment area of 10 x 3 mm^2 was made by continuous scan irradiation in consecutive lines. The treated area of the sample was analysed from the surface with VIS-NIR and SWIR hyperspectral imaging, micro-Raman, and XANES (details in section 3.2.5). Then, a thin section of the stratigraphy was prepared and extensively analysed with micro-Raman and SR 2D high lateral resolution µ-XRPD mapping (details in section 3.2.4).

To compare a purely thermal treatment to the laser irradiation, the chemical grade powder of plattnerite was heated up in a conditioning chamber mounted inside an XRPD bench system (details in section 3.2.4). Isolated products of each thermal treatment were characterized by XRPD and micro-Raman spectroscopy and re-measured over time to check the stability.

6.3 Results

6.3.1 Characterization of the thermal treatment

Two variable temperature XRPD experiments at a heating rate of 20°C/min were carried out in nitrogen environment, one up to 500°C (Fig. 6.1) and one up to 600°C (Table 6.1), showing consistent results regarding the crystallization of several lead oxide phases.

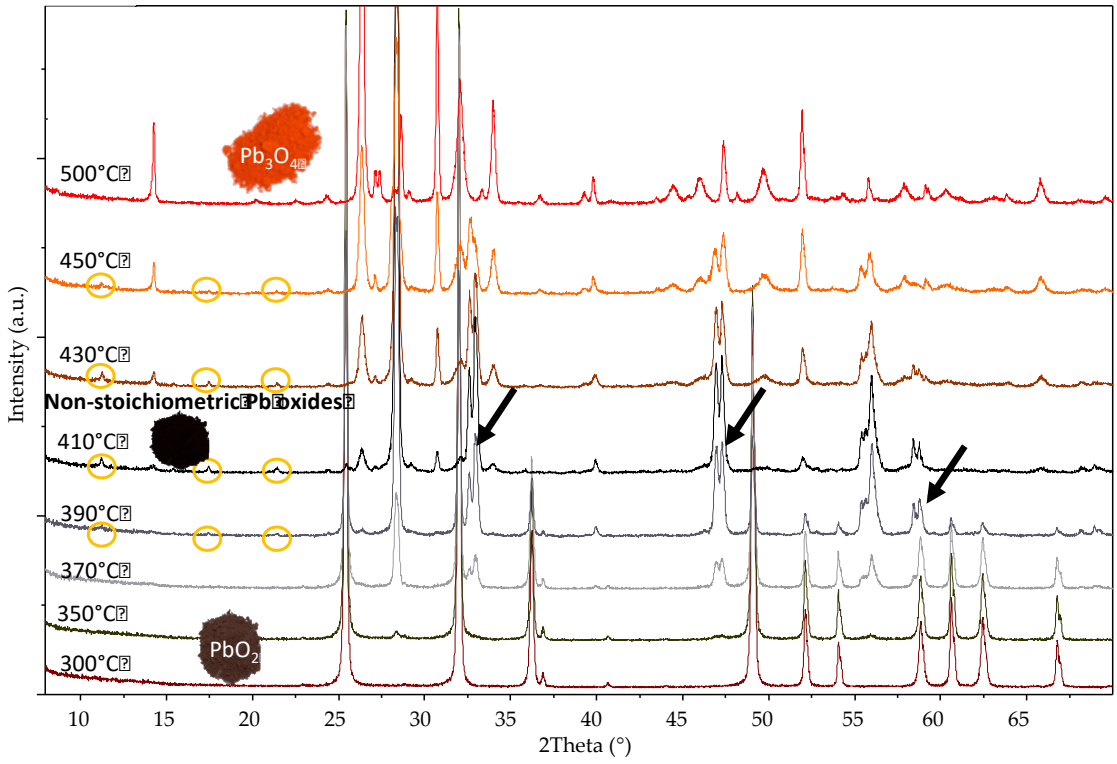

Fig.6. 1 Variable temperature XRPD of plattnerite powder heated up to 500°C at 20°C/min in nitrogen environment. The black arrows indicate the double peaks appearing between 350°C and 450°C and the yellow circles indicate the small diffraction peaks appearing during the transformation from PbO_2 to Pb_3O_4.

Between room temperature and 350°C the diffraction pattern of plattnerite remained unchanged. Above 350°C, new double peaks start to form, and they become very intense at 410°C, when almost all the plattnerite diffraction peaks disappeared. These double peaks can be ascribed to non-stoichiometric lead oxides [218–220], that are

intermediated states in the thermal transformation from plattnerite into red lead and that from now on will be indicated with the formula Pb_xO_y. At 410°C, small diffraction peaks ascribed to red lead start to appear and the quasi-complete transformation to red lead is obtained at 500°C. Above 500°C, both polymorphs of PbO are formed. After cooling no further structural modifications are detected (Table 6.1).

Table 6. 1 The summary of the lead phases identified during variable temperature XRPD of a plattnerite powder sample from room temperature to 600°C in nitrogen environment. From 300°C to 450°C with a step of 20°C and then with a step of 50°C. Heating rate 20°C/min.

Temperature C°	25 - 300	350 - 390	410 – 450	500	550	600	25 after cooling
Phases identified with XRPD	β-PbO_2	Pb_xO_y , β-PbO_2	Pb_xO_y , Pb_3O_4	Pb_3O_4	Pb_3O_4 , α-PbO,β-PbO	β-PbO	β-PbO

Another thermal experiment was conducted by fast heating (150°C/min) plattnerite powder up to 410°C and then cool it down. The powder produced by this fast heating appears black in colour and is composed of the intermediate non-stoichiometric lead oxides (Pb_xO_y). By observing the powder under high magnification, at least 2 optically distinctive particles are visible, bright red and black-grey particles (see inset in Fig.6.2a). The micro-Raman spectra collected from these two distinctive coloured particles show specific spectral features (Fig. 6.2 a): on the red grains all the characteristic peaks of red lead are present but all red-shifted; on the black grains the spectrum is characterized by a main broad band at 418 cm^{-1} and a weak band at 122 cm^{-1}. The red shift of the frequencies of the red grains, that varies between 6 and 10 cm^{-1} compared to red lead, could indicate an increase of the bond length of the structure.

To gain more insights on the specific composition of the two crystals, further XRPD measurements were conducted with a focused beam in transmission on a single red and single black particle. The signal obtained shows a typical pattern from powder, therefore it was not possible to separate a single crystal, but the powder pattern from separate

agglomerate of crystals were measured. The diffraction peaks resulted quite broad due to poor angular resolution caused by experimental constrains. Nevertheless, the patterns collected on the red aggregate is ascribable to red lead, while the black aggregate shows a very similar pattern to the one obtained for the non-stoichiometric lead oxides with still some small diffraction peaks of plattnerite (Fig. 6.2b).

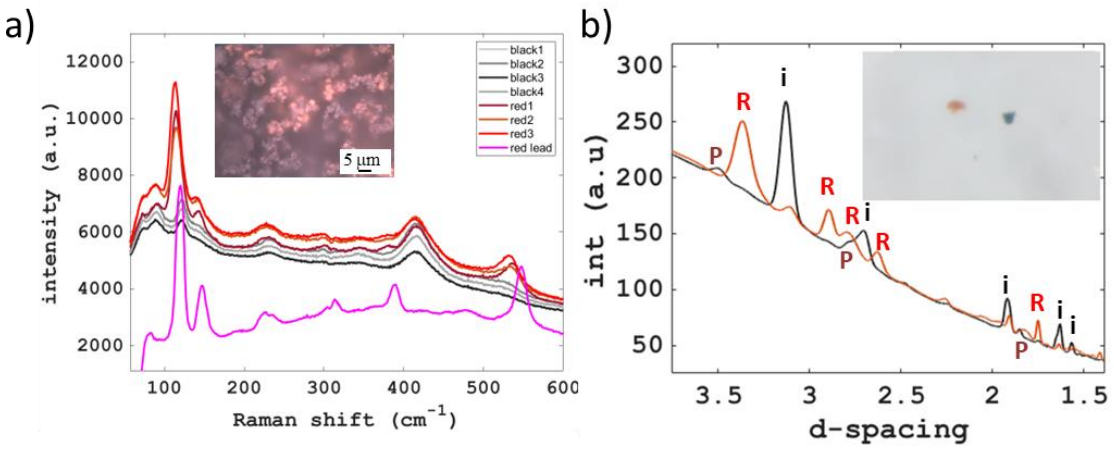

Fig.6. 2 a) Raman spectra collected on the red and black grains of the non-stoichiometric lead oxide produced by heating up plattnerite powder up to 410°C with a fast 150°C/min heating rate. In magenta a reference spectrum of red lead. Inset OM image of the powder. b) powder diffraction obtained in transmission from separated aggregates of the red and black crystals in the inset image. Red lead (R), plattnerite (P) and non-stoichiometric reflection peaks (i) were identified.

6.3.2 The irradiation tests and the bulk analysis

The first visual effect on the plattnerite mock-up surface was noticed when applying an intensity of 220 W/cm^2 with a spot size of 450 µm for 1 min (Fig. 6.3). With this operative condition an average surface temperature of 330°C was reached after few seconds and the irradiated spot appears slight darkened within the laser spot and few red grains formed at the centre of the spot (Fig. 6.3a). Multiple micro-Raman spectra acquired on the black area reveal a consistent spectrum characterized by a main band at 424 cm^{-1} and weak bands at 129 cm^{-1}, 239 cm^{-1} and 355 cm^{-1}, while on the red grains the spectra

show main characteristic peaks of red lead and the bands contribution found on the black area (Fig. 6.3b). In the VIS-NIR regime (400-1000 nm range) the plattnerite surface is characterized by a specific reflection peak at around 760 nm (Fig. 6.3c), this feature gradually shifts towards longer wavelength and increases in reflectance when extracting reflectance spectra from the inside of the irradiated area. The SWIR imaging of the irradiated area shows different reflectance spectra between the treated spot and the pristine surface around it (Fig. 6.3d). In particular, an absorption peak at around 1250 nm and a reflection peak at 1450 nm characterize the plattnerite pristine surface. The absorption peak gradually disappears when extracting the spectra from the inside of the irradiated spot (Fig. 6.3d).

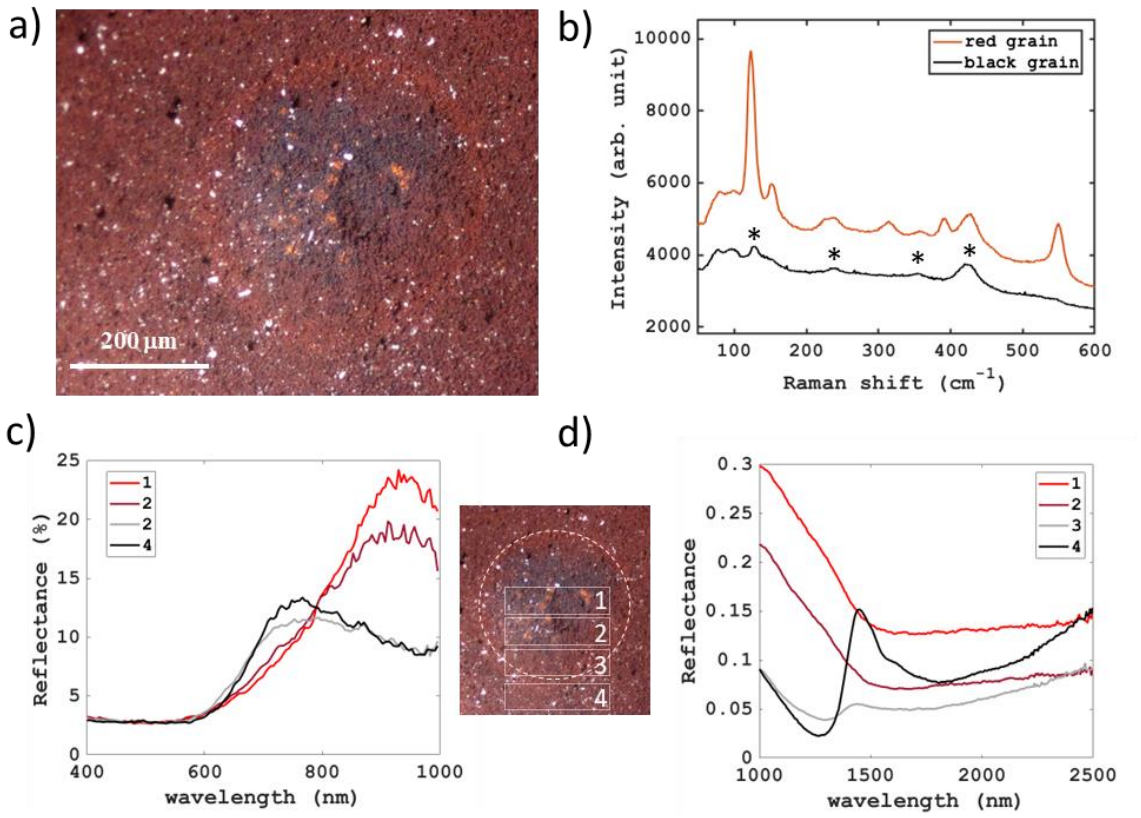

Fig.6. 3 a) the stereomicroscope image of the plattnerite mock-up irradiated on a single spot with a 1064 nm CW laser for 5 s with a spot size of 450 µm and an intensity of 220 W/cm^2. b) the Raman spectra collected on the black and red grains in the irradiated area with * the new bands identified in the black region. c) the VIS-NIR and d) the SWIR spectra, extracted from different areas (1-4) of the irradiated spot as indicated in the image inset.

To identify the most effective operative condition, multiple irradiation tests were carried out by performing line scans using a 200 µm spot size and varying the laser power (Fig. 6.4), with a maximum duration per point of 5 s. With 250 W/cm^2 a very homogeneous red layer was produced upon irradiation (Fig. 6.4b) and the micro-Raman spectra collected on the red stripe reveal a clear presence of red lead characteristic peaks (Fig.6.4c). By further increasing the laser power, the shift from black/brown to red is also followed by the formation of sporadic craters (Fig. 6.4d), and with even higher laser power more severe damage occurred (Fig. 6.4e). The edges of the craters appear yellow in colour and, based on the micro-Raman spectra (Fig. 6.4f), they are composed of massicot, the beta form of the lead monoxide. This indicates an excessive reduction of the lead dioxide.

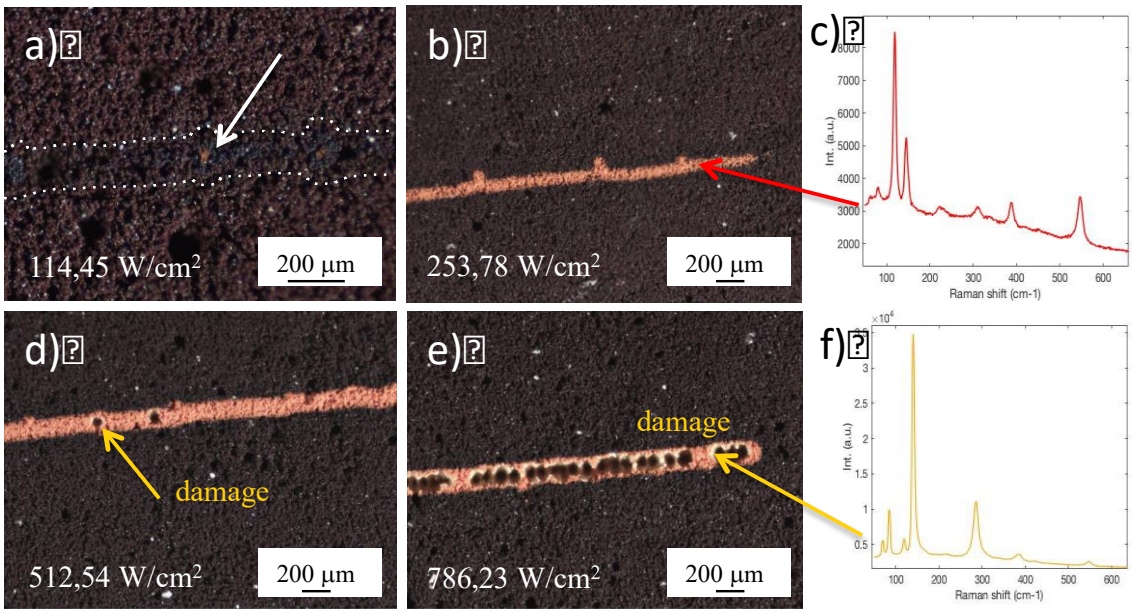

Fig.6. 4 The line irradiation tests with the 1064 nm CW laser with a spot of 200 µm at increasing intensity. c) and f) are the Raman spectra collected on the irradiation tests at 250 W/cm^2 and 786 W/cm^2 respectively.

With 250 W/cm^2 and a spot size of 200 µm, even by prolonging the exposure up to 30 s no clear damage was obtained, therefore this operative condition was used to scan a wide treatment area of 10 x 3 mm^2 for further characterization (Fig. 6.5a). From the surface of this mock-up, VIS-NIR and SWIR hyperspectral imaging were carried out. Even in this case the reflection peak at 750 nm shifts towards longer wavelength, while a clear point of inflection of red lead appears at around 550 nm (Fig. 6.5b), while the absorption feature of the pristine plattnerite surface around 1250 nm disappears in the irradiated area (Fig. 6.5c).

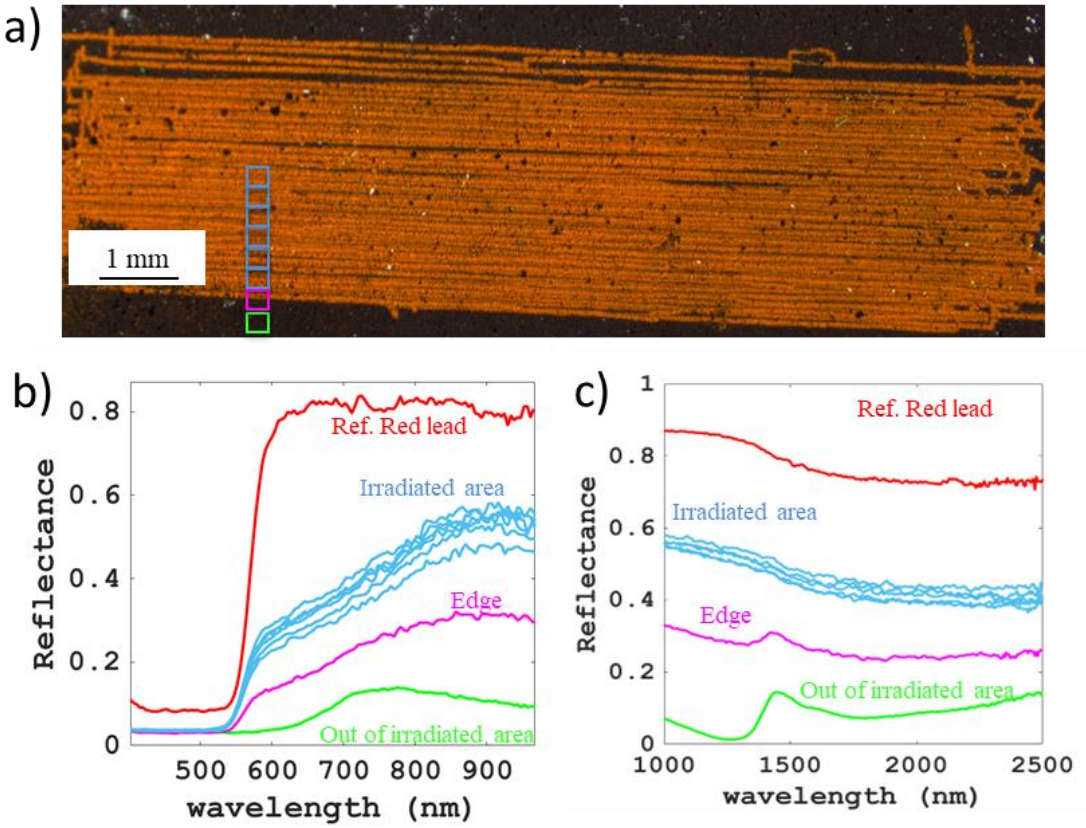

Fig.6. 5 a) the irradiated area of the plattnerite mock-up scanning with the 1064 nm laser with a spot size of 200 µm and 250 W/cm^2. b) the VIS-NIR spectra extracted from the pristine mock-up (in green), from the edge between treated and untreated (magenta) and from various points within the treated area (blue curves). A reference spectrum of red lead is also reported (red curve). c) the same areas measured with the SWIR hyperspectral imaging system.

6.3.3 The Pb speciation

XAS with detail in the near structure (XANES) was performed for the Pb speciation at the L_{III}–edge of Pb (~13035 eV). A combination of transmission, fluorescence yield and Total Electron Yield (TEY) was performed at BM08 beamline at ESRF (see section 3.2.5.1 for details on the set-up), to indirectly obtain depth information of the laser-transformed layer. TEY detection mode has been proved to be a suitable alternative to fluorescence mode thanks to shorter electron escape depth (of the order of tens of nm) compared to fluorescence mode [221]. The average beam used was 100 x 70 μm^2 with a photon flux of 10^9ph/s. The XANES spectra at the Pb L_{III} edge of all the relevant lead oxide phases present very broad spectral features and quite similar with one another (Fig. 6.6a).

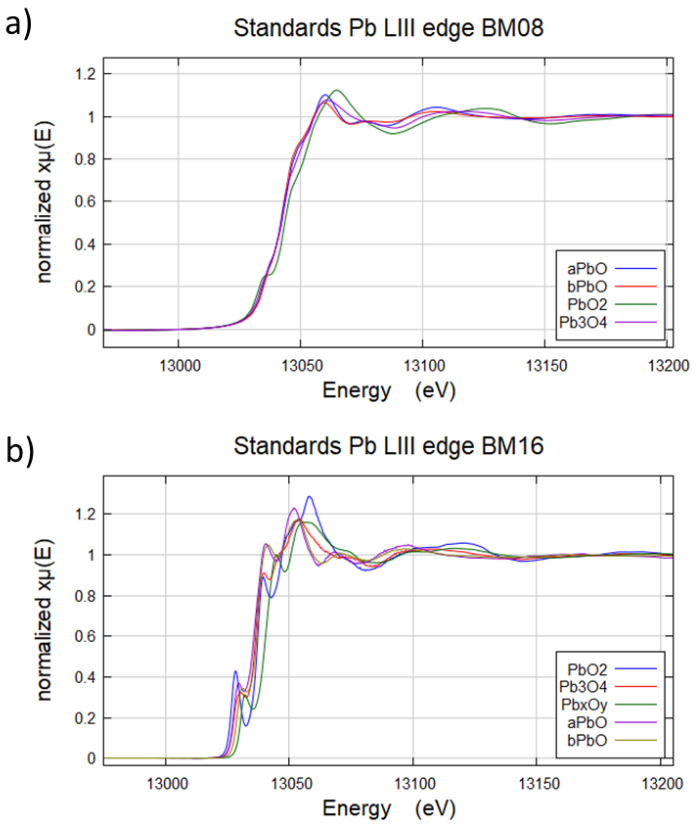

Fig.6. 6 The XANES spectra at the Pb LIII edge of the standard lead compounds (aPbO stands for litharge, bPbO massicot, PbO2 plattnerite, Pb3O4 red lead and PbxOy the intermediate lead oxides obtained at 410°C) used as reference and acquired at a) BM08 beamline and b) reacquired at BM16 beamline at ESRF.

Based on the necessity to gain higher energy resolution to reliably perform a comparison of the XANES features acquired on the laser treated sample with that of the standard compounds, XANES spectra in fluorescence mode were then re-acquired again at the FAME-UHD BM16 at ESRF (Fig. 6.6b). The higher energy resolution of 1 eV allowed to differentiate the spectral features of the different lead oxides and perform a semi-quantitative analysis of the compounds present over an area of 200 x 1500 μm^2 based on linear combination fit (LCF) of the standard compounds (see specification on LCF in section 3.2.5.2). The beam used at BM16 is of 200 x 100 μm^2 with a photon flux of 10^{11} ph/s (more details of the set-up in section 3.2.5).

XANES spectra were collected on the pristine surface plattnerite mock-up and on the irradiated fragment. At BM08, the spectra from the transmission and the fluorescence detectors did not reveal significant differences, while the TEY spectra showed a slight shift of the absorption edge of 1.8 eV towards lower energies on the red area compared to plattnerite (Fig. 6.7b). This data indicates that a reduction occurred on a very superficial layer of the mock-up. It can be consider that the TEY signal would result from the first hundreds of nm (detailed calculation is required), while the fluorescence signal result from the penetration depth of X-rays: between 12 and 13.5 keV at 45 degrees in a 200 µm paint layer composed of $^2/_3$ of PbO_2 and $^1/_3$ of animal glue results in a density of 6.45 g/cm^3, that is ca. 30 µm [222].

At BM16 consecutive spectra over a line of 1.5 mm were acquired in order to assess the homogeneity of the laser treatment. The quantitative analysis of the XANES line map (Fig. 6.7c), obtained by linear combination fit of the spectra of the standard lead phases, reveals that within the probed volume a constant 40% is composed of plattnerite, followed by a 35-40% of red lead, 15% of massicot and less than 5% of the non-stochiometric lead oxides Pb_xO_y. These data suggest a quite homogeneous laser treatment.

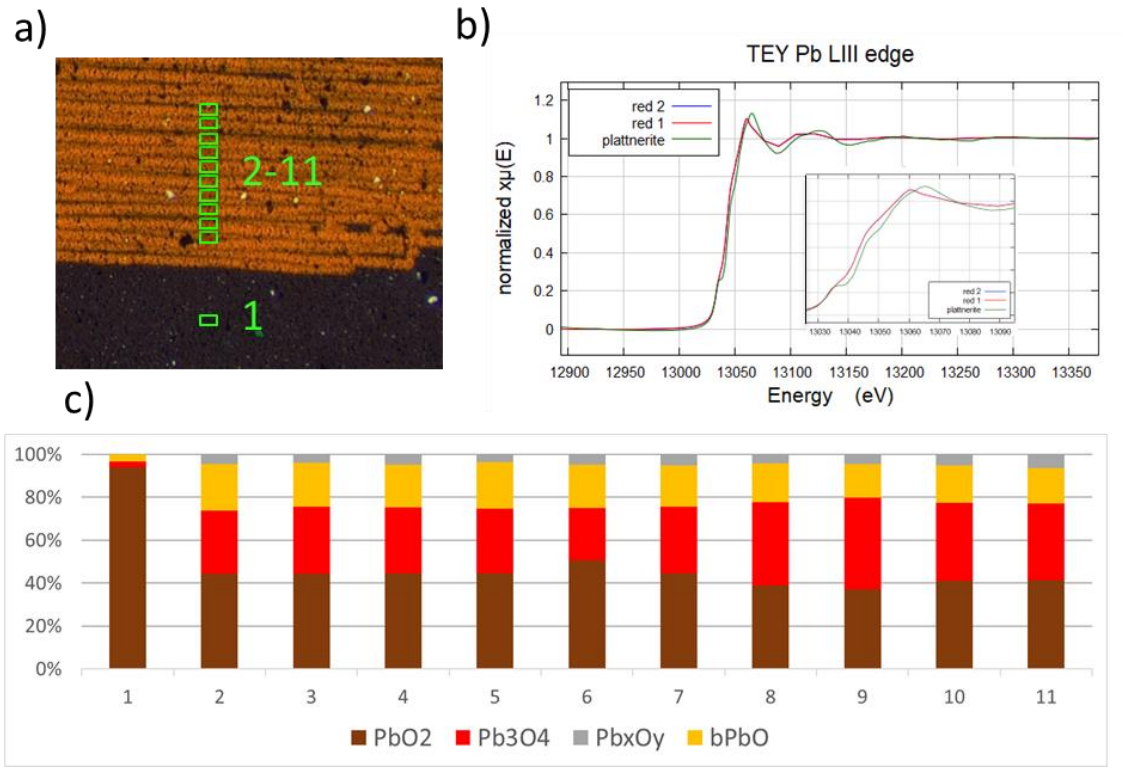

Fig.6. 7 a) the identification of the position from which XANES spectra were acquired on the mock-up. b) TEY spectra, with detail on the edge, on the pristine plattnerite mock-up and 2 spectra obtained on the laser treated area (red 1 and red 2). c) linear combination fit of the XANES spectra obtained from a line scan of 11 points. The first point indicates the composition of the pristine non irradiated mock-up. bPbO stands for massicot, PbO2 plattnerite, Pb3O4 red lead and PbxOy the intermediate lead oxides obtained at 410°C.

5.3.4 The in-depth characterization

The thin section obtained from the irradiated area reveals the presence of a thin superficial red layer of about 20 μm (Fig. 6.8a). From the μ-XRPD mapping, the correspondent main crystalline component of the red layer is indeed red lead with traces of massicot. Interestingly, also an intermediate layer between the red lead and the unreacted plattnerite of the bulk is characterized by the presence of double peaks which are the same as the one identified in the variable temperature XRPD experiment (Fig. 6.1) and ascribed to non-stoichiometric lead oxides (Pb_xO_y) co-present with main

diffraction peaks of plattnerite and red lead (Fig. 6.8 b, d). The same measurement was also performed after 2 years since the laser treatment and the distribution of the crystalline compound did not change. From the micro-Raman in correspondence of this intermediate layer a distinctive Raman spectrum is characterized by a strong broad band at 419 cm^{-1}, a medium band at 122 cm^{-1} and weak bands at 228 cm^{-1} 352 cm^{-1} and 540 cm^{-1} (Fig. 6.8c).

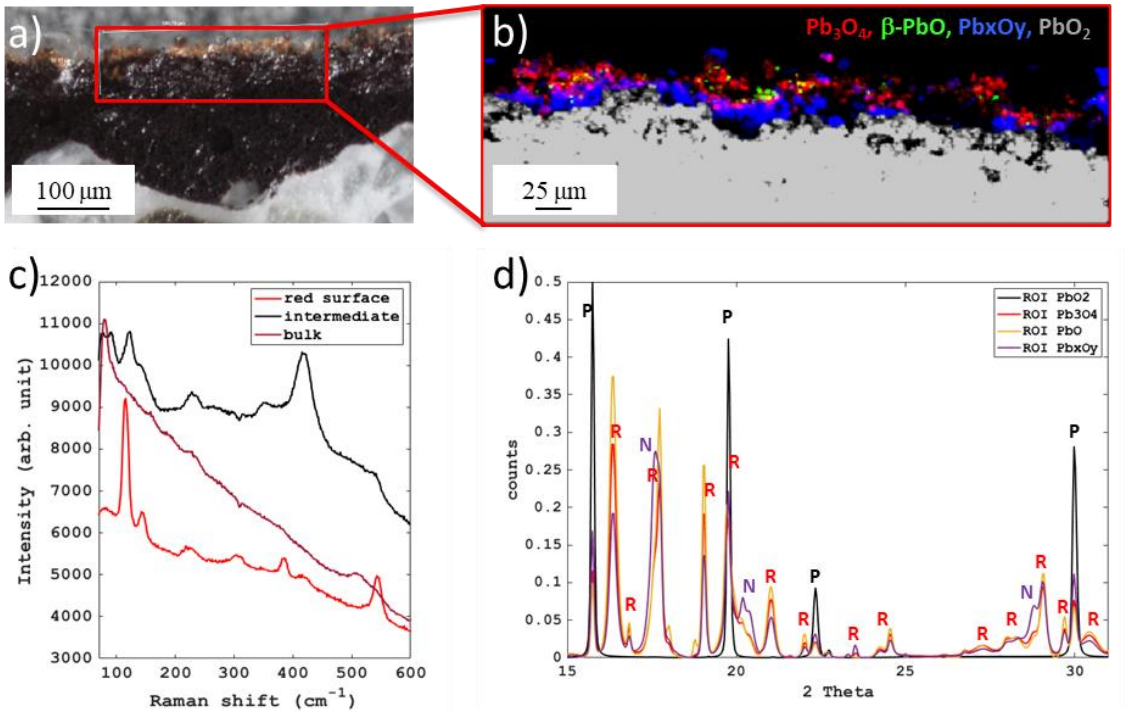

Fig.6. 8 a) Optical microscope image of the stratigraphic thin section of the laser treated plattnerite mock-up. b) the false colour RGB combination map (for details on how it is obtained see section 3.2.4) of red lead (Pb_3O_4), massicot (β-PbO), and intermediate lead oxides (Pb_xO_y). The ROI of plattnerite (PbO_2) is also superimposed in grey scale. c) Raman spectra from the surface (red line, corresponding to red lead), from the intermediate layer (black line, corresponding to non-stoichiometric lead oxides), and from the bulk (brown line, corresponding to the weak signal of plattnerite). d) the average diffractograms obtained from ROI imaging of the different compounds. The main diffraction peaks of plattnerite (P) and red lead (R) are reported, as well as the non-stoichiometric lead oxides (N).

6.4 Discussion

6.4.1 The laser-induced transformation of plattnerite into red lead

An in-depth characterization of the effects of a CW 1064 nm laser irradiation on a plattnerite wall painting mock-up was performed with various spectroscopic and diffraction techniques. Irradiations tests were performed varying laser intensity, spot size and duration to identify the best operative conditions. The duration of the irradiation was found to be a negligible parameter, as after few seconds the temperature reached a plateau (330°C max temperature reached within the laser spot), and no further effects were obtained. With a spot size of 200 µm, first signs of a visible effect (darker irradiated area and small sporadic red grains) appeared at 115 W/cm^2. The optimum intensity at which only red lead was detected from the surface with micro-Raman is 250 W/cm^2. Above this intensity, damage started to appear in forms of craters and yellow edges composed of massicot, indicating an excessive reduction of the lead oxides.

In a recent work, the effective intensity range found to treat plattnerite powder with a similar gaussian beam of a diode 1080 nm laser was 15 W/cm^2 [217]. This intensity is a factor 16 smaller compared to our treatment, but it is extremely important to consider that in their work the experiment was performed using a 2.9 mm (FWHM) spot size vs a 200 µm spot size in our experiment. The heat dissipation of smaller volumes is more efficient, therefore higher intensity is required for smaller spots to achieve similar effects. Moreover, the comparison is made difficult as the experiment was conducted on a pressed pellet pigment powder while in our case an animal glue wall painting mock-up was irradiated. The effective intensity range can significantly change due to several parameters such as the laser profile [74], the laser spot size, the specific material composition [61], the particle size of the pigment [59,167], and the optical properties of the material (such as roughness). Therefore, the intensity range found in our experiment has to be intended as an indication only.

Thanks to μ-XRPD mapping it was possible to estimate the penetration depth of the laser treatment. With the selected laser settings, red lead was formed only within the first 15-20 μm of the overall 200 μm plattnerite paint layer of the mock-up. This finding is also confirmed by the results of XANES investigation, which reports information localised mainly in the first 30 μm of material (estimated based on the X-ray attenuation depth). Apart from red lead, a subsurface layer of ca. 10-15 μm rich in non-stoichiometric lead oxides was also detected both with μ-XRPD and Raman spectroscopy. It is important to note that in these two layers produced by the laser treatment, the contribution of plattnerite is still relevant: both in the ROI of red lead and in the one of the non-stoichiometric lead oxides, the diffraction peaks of PbO_2 are still strong (Fig. 6.8d). This is consistent with the quantification obtained by the linear combination fit of the XANES spectra, from which a 40% of PbO_2 was estimated from the probed volume, corresponding more or less to the reacted depth.

6.4.2 Identification of spectroscopic techniques for monitoring the laser treatment

6.4.2.1 The VIS-NIR and SWIR spectral features of plattnerite

The first reported VIS-NIR absorption spectrum of plattnerite disclose a strong absorption band at 1290.32 nm (0.94 eV) and at 1257.86 nm (0.98 eV) for scrutinyite [223]. Based on the linear correlation obtained between band edge calculated from the optical spectra of solid lead oxides and the average oxidation state, the authors suggested that this NIR feature arises from small amounts of Pb^{2+} present in both polymorphs and has been used by [224] to monitor the dissolved lead in drinking water. In cultural heritage field only in very few recent papers it is reported the VIS-NIR reflectance spectra of plattnerite, highlighting the characteristic spectral feature of plattnerite at 750-800 nm both from mural paintings [225], and synthetic reference

powders [201,217]. The SWIR absorption band was instead never detected, either because the probed spectral range did not cover this region or, even if recorded like in the case of [225], the signal might have been masked by the contribution of some other compounds in the wall painting. In fact, we observed that the presence of already small amount of red lead could totally mask this feature.

In the present work, the VIS-NIR-SWIR reflectance spectral imaging on the laser-treated wall painting mock-up allowed a clear distinction of plattnerite and red lead: the reflection peak at 750-800 nm characteristic of plattnerite gradually shifts towards longer wavelength with the transformation to red lead, via the non-stoichiometric lead oxides. In addition, the plattnerite absorption peak at around 1250 nm disappears during the laser treatment. Therefore, this technique seems very suitable for the assessment of the presence of plattnerite in darkened red lead wall paintings and a valuable tool to monitor the laser treatment efficacy *in situ* for a possible restoration intervention of darkened red lead wall paintings.

6.4.2.2 The vibrational Raman bands of the non-stoichiometric lead oxides

Previous studies assigned the Raman band of synthetic plattnerite at 424, 515, and 653 cm^{-1} to Eg (i.e. symmetric stretching vibration of O-Pb-O), A1g (i.e. anti-symmetric bending vibration of O-Pb-O), and B1g (symmetric bending vibration) modes, respectively, by analogy with the corresponding modes of the isostructural SnO_2 [163]. When detected, the features referred to plattnerite are always very broad and often the identification relies on the only detection of the main band at 515 cm^{-1}. The broad bands indicate that different configurations or many electric or mass defects may exist in the crystal. Indeed, some works report that a pure ideal structure of PbO_2 has never been observed [226] and in the lead-batteries fields is well known that this compound is prone to oxygen deficiencies [227]. The fact that the diffraction pattern of plattnerite reveals often very sharp diffraction peaks white in Raman spectroscopy the bands are very broad, suggests that quite random disorder is present in the molecular short range. The local disorder is highlighted especially in the broadening of bending modes that are

more sensitive to neighbouring entities, as in the case of the main characteristic band of plattnerite at 515 cm^{-1}. Therefore, it is difficult to rely on this main Raman feature but at the same time it can be indicative of the specific structural characteristics of the analysed plattnerite.

From the same region of the cross section where non-stoichiometric lead oxides were detected with μ-XRPD, the Raman spectrum is characterized by a strong broad band at 419 cm^{-1}, a medium band at 122 cm^{-1} and weak bands at 228 cm^{-1}, 352 cm^{-1} and 540 cm^{-1}. The same features were detected in the non-stoichiometric lead oxide powder obtained with the plattnerite thermal treatment at 410°C with the VT-XRPD.

Comparing with the literature, a band between 410 and 426 cm^{-1} has been detected during the transformation of plattnerite. The former is detected during the laser-induced transformation with multiple laser wavelengths [228,229], while the latter upon thermal treatment up to 400-450°C, although in one case the Raman reported is at room temperature and they attributed it to $PbO_{1.55}$ with XRPD [163], while in the other work the Raman spectrum is collected at 400°C and after cooling analysing with XRPD they ascribe it to $PbO_{1.57}$ [228], therefore the peak position is not necessarily comparable and the XRPD attribution is vague.

One of the possible known intermediate lead oxides is the lead sesquioxide (Pb_2O_3) [230]. The Raman spectra of several sesquioxides for the lanthanide elements is characterized by the main band between 380 and 400 cm^{-1} and for higher f electrons and higher atomic number, like in the case of lead, the band shift at higher wavenumbers. So, it could be plausible the assignment the band at 419 cm^{-1} found in our experiments to the Pb_2O_3. But the lead sesquioxide has a clear different crystalline structure (monoclinic) [219] and is bright orange in colour.

Hence, although with the present experimental evidence is not possible to put forward an assignment, this band at 419 cm^{-1} is clearly a marker of the intermediate non-stoichiometric lead oxides formed during the reduction of plattnerite into red lead. Consequently, Raman spectroscopy can be useful to monitor the formation of the precursor of red lead, helping in the identification of the suitable operative conditions for a laser treatment in *situ*.

6.4.2.3 The laser-induced mechanisms and the possible risks

Comparing the products obtained by laser-induced transformation of plattnerite and the ones produced via thermal treatment, it is clear that very similar behaviour was encountered: the same non-stoichiometric intermediate lead oxides were formed, and the detected average surface temperature at which the nucleation of the reaction was observed is 330°C. Due to the gaussian nature of the laser spot and the average surface temperature value, it is very luckily that in the centre of the irradiated area, where red dots appeared, the temperature reached higher values, in agreement with the temperature range of reaction identified: the minimum temperature required to obtain red lead is around 400°C and to obtain the best conversion rate the temperature should be increased up to ca. 500/550°C. This temperature range may be potentially causing several drawbacks to the wall paintings. For instance, if red lead is applied in mixture with lead white or vermilion (very common mixtures), these pigments will be considerably damaged due to their decomposition temperature: vermilion can convert to the black phase metacinnabar from ca. 360°C [75] and lead white decomposes above ca. 250°C and become litharge or massicot [231]. But another common mixture of red lead with red ochre should not be affected due to the higher thermal stability of red ochre [232]. In any case, highly controlled laser treatment is required for an efficient conversion of PbO_2 to Pb_3O_4 as the temperature range is very limited (400-500°C). Considering the spot size effect, the smaller the beam, the more confined the heated area remains as better heat dissipation occurs within a small volume. In fact, with a very small spot size of just 200 µm we obtained only 20 µm of red lead layer. More experiments are ongoing to better identify the most suitable and safer operative conditions to avoid/minimize possible drawbacks.

6.5 Conclusions

This work aimed at shedding light on the efficiency and mechanism behind the recently proposed method to restore darkened red lead wall paintings via CW laser irradiation to convert plattnerite into red lead. Several irradiations' tests of plattnerite wall painting mock-up irradiated with a CW 1064 nm laser have been analysed with various spectroscopic and diffraction techniques. The combination of μ-XRPD mapping, XANES and micro-Raman allowed a clear characterization of the laser-induced products. Apart from red lead, in a subsurface layer of reaction non-stoichiometric lead oxides were identified and they present an un-expected long term (up to 2 years) stability. These intermediate lead oxides show a characteristic Raman band at 419 cm^{-1}. Thus, Raman spectroscopy can be used to monitor at the micro scale the laser treatment *operando* by detecting these precursors of red lead. Moreover, thanks to the characteristic spectral features of plattnerite between 700 and 1300 nm, hyperspectral imaging could also be considered a suitable technique for the assessment at the macro-scale of such alteration *in situ* and a good candidate to check the homogeneity of the laser intervention. The crystalline phases obtained with the laser-induced transformation and the temperature required for such conversion, give strong evidence of the purely thermal nature of the laser treatment. More work needs to be done to identify improving conditions to obtain efficient conversion while minimizing the risks associated with the laser irradiation.

This work contributes to a better understanding of the laser-pigment interaction and represents a valuable base to open the discussion with conservators and the heritage science community regarding the suitability of such restoration interventions in real wall paintings.

7. Conclusions and possible developments

In this work a new online method for monitoring of radiation damage on paintings was developed. The method, described in Chapter 3.1, employs time and spatially resolved VIS-NIR reflectance spectroscopy using an in-house built grating based hyperspectral imaging (HSI) system, previously developed at the ISAAC lab at NTU. This time-resolved imaging method represents a new application of spectral imaging in the Cultural Heritage field, aimed at designing new operative protocols for safe analysis and treatment of paintings.

Any change in reflectance is the result of changes in absorption and/or scattering of the material surface under investigation, hence it provides an indirect indication of chemical and/or physical changes of the surface. These changes can be monitored by recording the reflectance before, during and after irradiation, providing a complete record of the evolution of any perturbation of the system over time caused by irradiation. The method is extremely sensitive to small, subtle changes (~0.5-1% change in reflectance) which are not necessarily perceivable by visual inspection alone. In the assessment of laser-induced damage the method has been shown to be more sensitive to damage detection compared to Raman spectroscopy and SR micro-XRPD mapping. Similarly, it resulted to be much more sensitive in detecting damage than XAS upon X-ray irradiation.
Thanks to the lateral spatial resolution, it is possible to monitor the diffusion of damage along the painting surface, but most importantly, the simultaneous acquisition of the reflectance from areas far from the irradiation spot provides an internal control that makes the method robust. With this internal control, it is possible to assess the quality of the dataset and, case by case, identify the sensitivity of the acquisition on a specific material. Finally, the control of the possible reflectance change outside the irradiated area provides some indication on the type of damage. In fact, some specific spectral changes occurred only within the irradiated surface, while other spectral changes temporarily propagated further away for the irradiate spot due to heat dissipation.

7.1 VIS-NIR reflectance changes as a new metric for radiation damage

The identification of radiation-induced damage thresholds on mock-ups is an intrinsically unreliable method, owing to the highly heterogeneous nature of artists' materials, and its accuracy highly depends on the inspection technique used to define it. In fact, damage is generally defined by visual observation or by changes in the signal collected from the primary beam. For most of the techniques investigated, namely XAS, Raman spectroscopy and XRPD, the sensitivity to damage is limited to local speciation changes of one single atomic species, molecular alteration, and crystallinity and microstructure, respectively. Therefore, these methods are not exhaustive in detecting every type of damage. Hence, an independent and reliable damage metric reflecting both, physical and chemical damage at long and short range, is needed, and may be identified in the change of VIS-NIR reflectance (ΔR).

Moreover, damage threshold is generally defined as intensity for optical lasers and absorbed dose for X-rays, but these parameters are not necessarily sufficient to identify the safe limits, as spot size and dwell time also impact the damage threshold. Therefore, said additional parameters must be taken into account when studying radiation damage for the development of data collection strategies in order to mitigate damage risk. More investigation is needed to ascertain the effect of intensity and fluence on the occurrence of damage, as it is not yet fully established in which cases it might be safer to reduce the intensity and accumulate for longer time. In addition, the spot size effect should be investigated more in-depth as it has potential for reduction of radiation damage (both for X-rays and optical lasers). For SR micro-XRPD further experiments to better understand the effect of a specific X-ray photon energy would benefit the acquisition strategy of XRPD mapping of specific historical materials.

7.2 The hyperspectral imaging monitoring method explored in telescopic and microscopic modalities

In the presented work of Chapter 4, the remote configuration was employed to monitor laser-induced damage just after laser irradiation with common CW lasers used to perform Raman spectroscopy for the characterization of paintings' materials (532, 785 and 1064 nm). On the tested painting mock-ups, which contain some of the most laser sensitive pigments, the HSI monitoring over time enabled to detect a specific transient reflectance change that appears within the first few second post irradiation, and at laser intensities lower than those that induce permanent damage. This reversible change was associated with thermal effect contribution, which was confirmed by thermal imaging. Hence, under circumstances of predominant thermal effects, which is often the case with CW lasers, this independent monitoring method enables avoiding permanent damage thanks to the detection of a prediction damage marker. Therefore, the method can be suitable to use during the analysis of real historical paintings.

The HSI monitoring method enabled assessing the occurrence of any perturbation of the system. To ascertain the radiation-matter mechanisms and characterize the surface damage, several complementary techniques were used. A multimodal imaging set-up was used to help distinguishing predominant thermal and photochemical effects of lasers. Alteration in the optical properties and roughness were assessed with OCT, molecular modifications were investigated using spectroscopic analysis, and crystal structural phase change with diffraction. This characterization highlighted the physical-chemical specificity of this monitoring method, as a particular damage corresponded to a specific reflectance change.

Owing to a thorough study of laser-material interaction it was possible to ascertain the mechanisms of the CW laser treatment as a means to recover darkened wall paintings containing red lead. The crystalline phases obtained during the irradiation of plattnerite to transform it into red lead, and the temperature reached for such conversion, provided strong evidence of the purely thermal nature of the laser treatment. The combination of

SR μ-XRPD mapping, XANES and micro-Raman allowed a clear characterization of the laser-induced products. Apart from red lead, non-stoichiometric lead oxides were identified in a subsurface layer of reaction, and they showed unexpected long term (up to 2 years) stability. These intermediate lead oxides show a specific Raman band that can be used to monitor the laser treatment. Moreover, distinctive spectral features of plattnerite between 700 and 1300 nm range were identified, making VIS-NIR and SWIR hyperspectral imaging a suitable technique to assess the efficacy of the laser intervention at a macro-scale. The study of the mechanism and the identification of the advantages and limitations of the method could contribute to addressing possible improvements in terms of reconversion efficiency and safety of the possible laser treatment. The temperature range required for an effective thermal conversion has been identified (400-500°C) and may be detrimental for pigments often mixed with red lead, such as vermilion or orpiment, but may be harmless when mixed with red ochre. The narrow high temperature range necessary for conversion requires a fine adjustment of laser parameters to confine the thermal treatment by using a small spot size, a top hat profile and a laser wavelength that minimizes damage to the newly formed red lead, using NIR lasers. This work contributed to a better understanding of the laser-pigment interaction and aimed at providing the basis of decision making to open the discussion with conservators and the Heritage Science community about the suitability of such restoration interventions for real wall paintings.

The developed microscopic HSI set-up was used to monitor synchrotron X-ray radiation damage in real time during acquisition of XAS spectra and during fast irradiation conditions to simulate an XRPD measurement of painting materials in a common energy range used to analyse artists' materials (7-13 keV). During the X-ray irradiation some reflectance changes occurred instantaneously, while others appeared later during the irradiation, such as in the case of Prussian Blue paint in animal glue. In some tests, the reflectance changes remained permanent after X-ray irradiation (especially the ones upon prolonged exposure), while in other tests, the changes partially or almost completely reverted in the post monitoring (from 5 min to few hours and days), showing a slow kinetic evolution of X-ray induced damage. Therefore, the HSI monitoring method could be useful for the long-term monitoring of X-ray damage. Further characterization

of the damaged areas is currently investigated to clearly associate them to a particular damage mechanism. With this independent monitoring technique, it was possible to capture early-warning signs of damage not detectable by visual inspection, nor by any XAS spectral changes. Therefore, the method is useful to monitor radiation damage and assess the reliability of the data collected. Thus, it could be implemented at a synchrotron beamline to minimize the impact of an X-ray measurement as much as possible.

This work contributes to the improvement of analytical protocols that are necessary to reassure and support the increasing SR users community from the CH field and it represents a valuable strategy to preserve the integrity of the artworks analysed in large-scale facilities.

7.3 Future perspectives

The online damage detection is not based on *a priori* knowledge of radiation damage; therefore, it represents the most effective strategy to prevent or minimize damage when analysing heterogeneous heritage materials. In the near future, it is desirable that instruments based on intense radiation will incorporate online damage control protocols as part of the advances in data collection strategies.

With respect to Raman spectroscopy, it would be interesting to improve the safety operation by implementing the reflectance monitoring method in a portable or bench-top Raman system. To do so, the use of fibre optics may be more appropriate for a compact set-up suitable also for in situ measurements. With the use of fibre optics, the monitoring would be a point measurement only, but an internal control may still be possible using a Y fibre. Additionally, real-time damage detection would be beneficial. However, as the spectrometer is in the same wavelength range as the optical lasers used, it would require a notch filter.

Before its implementation in instruments, the method needs further validation in order to better define its capabilities and limitations, both in terms of materials and signal

acquisition. A possible improvement concerning signal acquisition could be the exploration of collection geometry to assess whether the contribution of specular reflection would enhance the detection sensitivity of surface changes, without reducing the sensitivity of detection of chemical changes provided mainly by the diffused reflectance. With respect to materials, experiments using different pigments, mixtures and other artists' materials could be helpful to further explore the specificity of damage detection.

For X-ray monitoring it would be beneficial to implement the microscopic HSI method at a beamline, especially as the HSI during the set-up at the beamtime resulted in useful aid in the sample alignment with the X-ray beam. Therefore, the method could potentially prove useful in other steps of a routine beamline operation. To implement the method, a dedicated interface should be developed to trigger the fast X-ray shutter once a specific ΔR change is reached, stopping the acquisition immediately whereby avoiding further damage. To do so, it is necessary to perform more analysis to characterize the types of damage associated to a specific ΔR change and discuss with the Heritage Science community whether a specific ΔR change corresponding to a certain type of surface alteration can be considered acceptable and safe.

Ion beam analysis is generally considered too risky to be applied for the analysis of paintings, hence exploring the reflectance method for the monitoring of damage during ion beam analysis, such as Particle-Induced Xray Emission (PIXE), may result beneficial for its use on paintings.

To conclude, in recent occasions of dissemination, the method raised interest from EXAFS beamline scientists and environmental scientists working with ion beam analysis. Therefore, this work represents one of the few cases where a methodological advancement developed in Heritage Science field is potentially of interest for other fields of research. Another interesting application to test would be the monitoring of *operando* photochemical XAS experiments, as the X-ray radiation can significantly interfere with the reaction under study.

References

[1] Romani A, Miliani C, Clementi C, Grazia C, Colao F, Fantoni R, et al. Portable Instrumentation. Springer Series on Fluorescence, Cham: Springer International Publishing; 2023, p. 1–34. https://doi.org/10.1007/4243_2023_45.

[2] Brunetti B, Miliani C, Rosi F, Doherty B, Monico L, Romani A, et al. Non-invasive Investigations of Paintings by Portable Instrumentation: The MOLAB Experience. Top Curr Chem 2016;374:10. https://doi.org/10.1007/s41061-015-0008-9.

[3] Janssens K, Alfeld M, Van Der Snickt G, De Nolf W, Vanmeert F, Radepont M, et al. The use of synchrotron radiation for the characterization of artists' pigments and paintings. Annual Review of Analytical Chemistry 2013;6:399–425. https://doi.org/10.1146/annurev-anchem-062012-092702.

[4] Cotte M, Dollman K, Fernandez V, Gonzalez V, Vanmeert F, Monico L, et al. New Opportunities Offered by the ESRF to the Cultural and Natural Heritage Communities. Synchrotron Radiat News 2022;35:3–9. https://doi.org/10.1080/08940886.2022.2135958.

[5] Gianoncelli A, Schöder S, Plaisier JR, Fugazzotto M, Barone G, Russo A, et al. X-ray Synchrotron Radiation to Look at Pigments in Antiquities: Overview and Examples. Heritage 2024;7:2118–37. https://doi.org/10.3390/heritage7040100.

[6] Delaney JK, Dooley KA. Visible and Infrared Reflectance Imaging Spectroscopy of Paintings and Works on Paper. In: Colombini MP, Degano I, Nevin A, editors. Analytical Chemistry for the Study of Paintings and the Detection of Forgeries, Cham: Springer International Publishing; 2022, p. 115–32. https://doi.org/10.1007/978-3-030-86865-9_4.

[7] Vanmeert F, De Meyer S, Gestels A, Clerici EA, Deleu N, Legrand S, et al. Non-invasive and Non-destructive Examination of Artists' Pigments, Paints and Paintings by Means of X-Ray Imaging Methods. In: Colombini MP, Degano I, Nevin A, editors. Analytical Chemistry for the Study of Paintings and the Detection of Forgeries, Cham: Springer International Publishing; 2022, p. 317–57. https://doi.org/10.1007/978-3-030-86865-9_11.

[8] Nevin A. Fluorescence for the Analysis of Paintings. In: Colombini MP, Degano I, Nevin A, editors. Analytical Chemistry for the Study of Paintings

and the Detection of Forgeries, Cham: Springer International Publishing; 2022, p. 221–45. https://doi.org/10.1007/978-3-030-86865-9_8.

[9] Bai X, Oujja M, Sanz M, Lopez M, Koch Dandolo CL, Castillejo M, et al. Integrating LIBS LIF Raman into a single multi-spectroscopic mobile device for in situ cultural heritage analysis, SPIE-Intl Soc Optical Eng; 2019, p. 43. https://doi.org/10.1117/12.2527272.

[10] Lutterotti L, Dell'Amore F, Angelucci DE, Carrer F, Gialanella S. Combined X-ray diffraction and fluorescence analysis in the cultural heritage field. Microchemical Journal 2016;126:423–30. https://doi.org/https://doi.org/10.1016/j.microc.2015.12.031.

[11] Bertrand L, Schöder S, Joosten I, Webb SM, Thoury M, Calligaro T, et al. Practical advances towards safer analysis of heritage samples and objects. TrAC - Trends in Analytical Chemistry 2023;164. https://doi.org/10.1016/j.trac.2023.117078.

[12] Bertrand L, Schöeder S, Anglos D, Breese MBH, Janssens K, Moini M, et al. Mitigation strategies for radiation damage in the analysis of ancient materials. TrAC - Trends in Analytical Chemistry 2015;66:128–45. https://doi.org/10.1016/j.trac.2014.10.005.

[13] ISO 21254-1:2011(en) - International Organization for Standardization. https://www.iso.org/obp/ui/#iso:std:iso:21254:-1:ed-1:v1:en n.d.

[14] De Santis A, Mattei E, Pelosi C. Micro-Raman and stratigraphic studies of the paintings on the "Cembalo" model musical instrument (A.D. 1650) and laser-induced degradation of the detected pigments. Journal of Raman Spectroscopy 2007;38:1368–78. https://doi.org/10.1002/jrs.1777.

[15] Gervais C, Thoury M, Réguer S, Gueriau P, Mass J. Radiation damages during synchrotron X-ray micro-analyses of Prussian blue and zinc white historic paintings: detection, mitigation and integration. Appl Phys A Mater Sci Process 2015;121:949–55. https://doi.org/10.1007/s00339-015-9462-z.

[16] Cato E, Borca C, Huthwelker T, Ferreira ESB. Aluminium X-ray absorption near-edge spectroscopy analysis of discoloured ultramarine blue in 20th century oil paintings. Microchemical Journal 2016;126:18–24. https://doi.org/10.1016/j.microc.2015.11.021.

[17] Suzuki A, Cheung CS, Li Y, Hogg A, Atkinson PS, Riminesi C, et al. Time and spatially resolved VIS-NIR hyperspectral imaging as a novel monitoring tool for laser-based spectroscopy to mitigate radiation damage on paintings. Analyst 2024;149:2338–50. https://doi.org/10.1039/D3AN02041J.

[18] IPERION HS, Integrating Platform for the European Research Infrastructure on Heritage Science, H2020-INFRAIA-2019-1, under GA 871034. www.iperionhs.eu n.d.

[19] Targowski P, Iwanicka M. Optical coherence tomography: Its role in the non-invasive structural examination and conservation of cultural heritage objects-A review. Appl Phys A Mater Sci Process 2012;106:265–77. https://doi.org/10.1007/s00339-011-6687-3.

[20] Siano S, Agresti J, Cacciari I, Ciofini D, Mascalchi M, Osticioli I, et al. Laser cleaning in conservation of stone, metal, and painted artifacts: State of the art and new insights on the use of the Nd:YAG lasers. Appl Phys A Mater Sci Process 2012;106:419–46. https://doi.org/10.1007/s00339-011-6690-8.

[21] Nevin A, Spoto G, Anglos D. Laser spectroscopies for elemental and molecular analysis in art and archaeology. Appl Phys A Mater Sci Process 2012;106:339–61. https://doi.org/10.1007/s00339-011-6699-z.

[22] Ziemann MA, Madariaga JM. Applications of Raman spectroscopy in art and archaeology. Journal of Raman Spectroscopy 2021;52:8–14. https://doi.org/https://doi.org/10.1002/jrs.6054.

[23] Vandenabeele P, Castro K, Hargreaves M, Moens L, Madariaga JM, Edwards HGM. Comparative study of mobile Raman instrumentation for art analysis. Anal Chim Acta 2007;588:108–16. https://doi.org/10.1016/j.aca.2007.01.082.

[24] Li Y, Cheung CS, Kogou S, Liggins F, Liang H. Standoff Raman spectroscopy for architectural interiors from 3-15 m distances. Opt Express 2019;27:31338. https://doi.org/10.1364/oe.27.031338.

[25] Bai X, Detalle V. Time-Gated Pulsed Raman Spectroscopy with NS Laser for Cultural Heritage. Heritage 2023;6:1531–40. https://doi.org/10.3390/heritage6020082.

[26] Madonini F, Maurina AA, Villa F. SPAD Sensors for Time-Gated Raman Spectroscopy. Biophotonics Congress: Biomedical Optics 2022 (Translational, Microscopy, OCT, OTS, BRAIN), Washington, D.C.: Optica Publishing Group; 2022, p. JM3A.13. https://doi.org/10.1364/TRANSLATIONAL.2022.JM3A.13.

[27] Mosca S, Conti C, Stone N, Matousek P. Spatially offset Raman spectroscopy. Nature Reviews Methods Primers 2021;1:21. https://doi.org/10.1038/s43586-021-00019-0.

[28] Conti C, Colombo C, Realini M, Zerbi G, Matousek P. Subsurface Raman Analysis of Thin Painted Layers. Appl Spectrosc 2014;68:686–91. https://doi.org/10.1366/13-07376.

[29] Conti C, Realini M, Colombo C, Matousek P. Comparison of key modalities of micro-scale spatially offset Raman spectroscopy. Analyst 2015;140:8127–33. https://doi.org/10.1039/C5AN01900A.

[30] Li Y, Cheung CS, Kogou S, Hogg A, Liang H, Evans S. ICOM-CC 19th Triennial Conference Standoff laser spectroscopy for wall paintings, monuments and architectural interiors. 2021.

[31] Vandenabeele P, Rousaki A. Developing Macro-Raman Mapping as a Tool for Studying the Pigment Distribution of Art Objects. Anal Chem 2021;93:15390–400. https://doi.org/10.1021/acs.analchem.1c03197.

[32] Liang H, Mari M, Cheung CS, Kogou S, Johnson P, Filippidis G. Optical coherence tomography and non-linear microscopy for paintings – a study of the complementary capabilities and laser degradation effects. Opt Express 2017;25:19640. https://doi.org/10.1364/oe.25.019640.

[33] Dal Fovo A, Fontana R, Striova J, Pampaloni E, Barucci M, Raffaelli M, et al. Nonlinear optical imaging techniques (NLO) for painting investigation. Proceedings of the International Conference LACONA XI, Nicolaus Copernicus University Press; 2017, p. 141–53. https://doi.org/10.12775/3875-4.10.

[34] Filippidis G, Gualda EJ, Melessanaki K, Fotakis C. Nonlinear imaging microscopy techniques as diagnostic tools for art conservation studies. Opt Lett 2008;33:240. https://doi.org/10.1364/OL.33.000240.

[35] Nevin A, Comelli D, Osticioli I, Filippidis G, Melessanaki K, Valentini G, et al. Multi-photon excitation fluorescence and third-harmonic generation microscopy measurements combined with confocal Raman microscopy for the analysis of layered samples of varnished oil films. Applied Physics A 2010;100:599–606. https://doi.org/10.1007/s00339-010-5644-x.

[36] Samineni P, deCruz A, Villafaña TE, Warren WS, Fischer MC. Pump-probe imaging of historical pigments used in paintings. Opt Lett 2012;37:1310–2. https://doi.org/10.1364/OL.37.001310.

[37] Fischer MC, Wilson JW, Robles FE, Warren WS. Invited Review Article: Pump-probe microscopy. Review of Scientific Instruments 2016;87. https://doi.org/10.1063/1.4943211.

[38] Pisu FA, Ricci PC, Carbonaro CM, Chiriu D. Degradation study of pigments through transient absorption and colorimetry. 2022.

[39] Pisu FA, Marceddu M, Ricci PC, Melis C, Porcu S, Carbonaro CM, et al. Transient absorption study on Red Vermilion darkening in presence of chlorine ions and after UV exposure. J Photochem Photobiol A Chem 2023;435:114291. https://doi.org/https://doi.org/10.1016/j.jphotochem.2022.114291.

[40] Anglos D. Laser-induced breakdown spectroscopy in heritage science 2019;4. https://doi.org/doi:10.1515/psr-2018-0005.

[41] Salimbeni R, Pini R, Siano S. A variable pulse width Nd:YAG laser for conservation. J Cult Herit 2003;4:72–6. https://doi.org/https://doi.org/10.1016/S1296-2074(02)01149-4.

[42] Vergès-Belmin V, Rolland O, Jourd'heuil I, Guiavarc'h M, Zanini A. Nd:YAG long Q-switched versus short free-running laser cleaning trials at Chartres cathedral, France. Studies in Conservation 2015;60:S12–8. https://doi.org/10.1179/0039363015Z.000000000202.

[43] Bartoli L, Pouli P, Fotakis C, Siano S, Salimbeni R. Characterization of Stone Cleaning by Nd:YAG Lasers with Different Pulse Duration. Laser Chemistry 2006;2006:081750. https://doi.org/https://doi.org/10.1155/2006/81750.

[44] Suzuki A, Riminesi C, Ricci M, Vettori S, Salvadori B. Testing of a new Yb:YAG fiber laser system for the removal of graphic vandalism from marble. Herit Sci 2023;11:132. https://doi.org/10.1186/s40494-023-00966-9.

[45] Dajnowski A, Dajnowski BA. Using the new G.C. Laser Cleaning System for cleaning and surface preparation for re-gilding of a large outdoor bronze monument of Alexander Hamilton. Proceedings of the International Conference LACONA XI, Nicolaus Copernicus University Press; 2017, p. 217–28. https://doi.org/10.12775/3875-4.15.

[46] Smith GD, Burgio L, Firth S, Clark RJH. Laser-induced degradation of lead pigments with reference to Botticelli's Trionfo d'Amore. vol. 440. 2001.

[47] Coccato A, Moens L, Vandenabeele P. On the stability of mediaeval inorganic pigments: A literature review of the effect of climate, material selection, biological activity, analysis and conservation treatments. Herit Sci 2017;5. https://doi.org/10.1186/s40494-017-0125-6.

[48] Pouli P, Oujja M, Castillejo M. Practical issues in laser cleaning of stone and painted artefacts: Optimisation procedures and side effects. Appl Phys A

Mater Sci Process 2012;106:447–64. https://doi.org/10.1007/s00339-011-6696-2.

[49] Ristau D. Laser-Induced Damage in Optical Materials. vol. 568. 1st edition. United States: CRC Press; 2014. https://doi.org/10.1201/b17722.

[50] Yu J, Xiang X, He S, Yuan X, Zheng W, Lü H, et al. Laser-Induced Damage Initiation and Growth of Optical Materials. Advances in Condensed Matter Physics 2014;2014:364627. https://doi.org/https://doi.org/10.1155/2014/364627.

[51] Burgio L, Clark RJH, Firth S. Raman spectroscopy as a means for the identification of plattnerite (PbO2), of lead pigments and of their degradation products. Analyst 2001;126:222–7. https://doi.org/10.1039/b008302j.

[52] Moretti G, Gervais C. Raman spectroscopy of the photosensitive pigment Prussian blue. Journal of Raman Spectroscopy 2018;49:1198–204. https://doi.org/10.1002/jrs.5366.

[53] Wood RM. Laser-Induced Damage of Optical Materials. CRC Press; 2003.

[54] Ciofini D, Martínez-Weinbaum M, Castillejo M, Oujja M, Chillé C, Siano S, et al. Quantitative spectroscopic characterization of laser-induced effects on oil paint films using 213, 266, or 2940 nm. J Cult Herit 2024;66:155–65. https://doi.org/10.1016/j.culher.2023.11.015.

[55] Ciofini D, Oujja M, Cañamares MV, Siano S, Castillejo M. Spectroscopic assessment of the UV laser removal of varnishes from painted surfaces. Microchemical Journal 2016;124:792–803. https://doi.org/https://doi.org/10.1016/j.microc.2015.10.031.

[56] Marucci G, Beeby A, Parker AW, Nicholson CE. Raman spectroscopic library of medieval pigments collected with five different wavelengths for investigation of illuminated manuscripts. Anal Methods 2018;10:1219–36. https://doi.org/10.1039/C8AY00016F.

[57] Siano S, Salimbeni R. Advances in Laser Cleaning of Artwork and Objects of Historical Interest: The Optimized Pulse Duration Approach. Acc Chem Res 2010;43:739–50. https://doi.org/10.1021/ar900190f.

[58] Oujja M, Sanz M, Rebollar E, Marco JF, Domingo C, Pouli P, et al. Wavelength and pulse duration effects on laser induced changes on raw pigments used in paintings. Spectrochim Acta A Mol Biomol Spectrosc 2013;102:7–14. https://doi.org/10.1016/j.saa.2012.10.001.

[59] Mattei E, De Vivo G, De Santis A, Gaetani C, Pelosi C, Santamaria U. Raman spectroscopic analysis of azurite blackening. Journal of Raman Spectroscopy 2008;39:302–6. https://doi.org/10.1002/jrs.1845.

[60] Ciofini D, Cacciari I, Siano S. Multi-pulse laser irradiation of cadmium yellow paint films: The influence of binding medium and particle aggregates. Measurement (Lond) 2018;118:311–9. https://doi.org/10.1016/j.measurement.2017.07.046.

[61] Ciofini D, Agresti J, Mencaglia AA, Siano S, Osticioli I. Temperature sensing during Raman spectroscopy of lead white films in different purity grades and boundary conditions. Sens Actuators B Chem 2020;325. https://doi.org/10.1016/j.snb.2020.128958.

[62] Douglass DL, Shing C, Wang G. The light-induced alteration of realgar to pararealgar. American Mineralogist 1992;77:1266–74.

[63] Pouli P, Selimis A, Georgiou S, Fotakis C. Recent studies of laser science in paintings conservation and research. Acc Chem Res 2010;43:771–81. https://doi.org/10.1021/ar900224n.

[64] Pouli P, Emmony DC. The effect of Nd:YAG laser radiation on medieval pigments. vol. 1. 2000.

[65] Sansonetti A, Realini M. Nd:YAG laser effects on inorganic pigments. vol. 1. 2000.

[66] Chappé M, Hildenhagen J, Dickmann K, Bredol M. Laser irradiation of medieval pigments at IR, VIS and UV wavelengths. 2003.

[67] Castillejo M, Martín M, Oujja M, Silva D, Torres R, Manousaki A, et al. Analytical study of the chemical and physical changes induced by KrF laser cleaning of tempera paints. Anal Chem 2002;74:4662–71. https://doi.org/10.1021/ac025778c.

[68] Pouli P, Emmony DC, Madden CE, Sutherland I. Studies towards a thorough understanding of the laser-induced discoloration mechanisms of medieval pigments. 2003.

[69] Cooper MI, Fowles PS, Tang CC. Analysis of the laser-induced discoloration of lead white pigment. Appl Surf Sci 2002;201:75–84. https://doi.org/https://doi.org/10.1016/S0169-4332(02)00499-3.

[70] Bruder R, L'Hermite D, Semerok A, Salmon L, Detalle V. Near-crater discoloration of white lead in wall paintings during laser induced breakdown spectroscopy analysis. Spectrochim Acta Part B At Spectrosc 2007;62:1590–6. https://doi.org/10.1016/j.sab.2007.10.031.

[71] Shebanova ON, Lazor P. Raman study of magnetite (Fe3O4): Laser-induced thermal effects and oxidation. Journal of Raman Spectroscopy 2003;34:845–52. https://doi.org/10.1002/jrs.1056.

[72] Acquaviva S, Baraldi P, D'Anna E, de Giorgi ML, Della Patria A, Giotta L, et al. Yellow pigments in painting: Characterisation and UV laser-induced modifications. Journal of Raman Spectroscopy 2009;40:1664–7. https://doi.org/10.1002/jrs.2316.

[73] El Mendili Y, Bardeau JF, Randrianantoandro N, Gourbil A, Greneche JM, Mercier AM, et al. New evidences of in situ laser irradiation effects on γ-Fe 2O3 nanoparticles: A Raman spectroscopic study. Journal of Raman Spectroscopy 2011;42:239–42. https://doi.org/10.1002/jrs.2762.

[74] Aze S, Vallet J-M, Grauby O, Detalle V, Delaporte P. Restauration des peintures au plomb par irradiation laser. TECHNIQUES DE L'INGÉNIEUR 2013:RE 224 1-11.

[75] Pérez-Diez S, Larrañaga A, Madariaga JM, Maguregui M. Unraveling the role of the thermal and laser impacts on the blackening of cinnabar in the mural paintings of Pompeii. Eur Phys J Plus 2022;137. https://doi.org/10.1140/epjp/s13360-022-03392-1.

[76] Gaspard S, Oujja M, Moreno P, Méndez C, García A, Domingo C, et al. Interaction of femtosecond laser pulses with tempera paints. Appl Surf Sci 2008;255:2675–81. https://doi.org/https://doi.org/10.1016/j.apsusc.2008.07.205.

[77] Zafiropulos V, Balas C, Manousaki A, Marakis Y, Maravelaki-Kalaitzaki P, Melesanaki K, et al. Yellowing effect and discoloration of pigments: experimental and theoretical studies. J Cult Herit 2003;4:249–56. https://doi.org/https://doi.org/10.1016/S1296-2074(02)01205-0.

[78] Zafiropulos V, Stratoudaki T, Manousaki A, Melesanaki K, Orial G. Discoloration of pigments induced by laser irradiation. Surface Engineering 2001;17:249–53. https://doi.org/10.1179/026708401101517773.

[79] Yu J, Warren WS, Fischer MC. Visualization of vermilion degradation using pump-probe microscopy. vol. 5. 2019.

[80] Li Z, Wang S, Zheng W, Wang Y, Pan Y. A review of dynamic monitoring technology and application research of laser cleaning interface. Measurement 2024;238:115311. https://doi.org/https://doi.org/10.1016/j.measurement.2024.115311.

[81] Marczak J, Koss A, Targowski P, Góra M, Strzelec M, Sarzyński A, et al. Characterization of Laser Cleaning of Artworks. Sensors 2008;8:6507–48. https://doi.org/10.3390/s8106507.

[82] Klein S, Stratoudaki T, Zafiropulos V, Hildenhagen J, Dickmann K, Lehmkuhl Th. Laser-induced breakdown spectroscopy for on-line control of laser cleaning of sandstone and stained glass. Applied Physics A 1999;69:441–4. https://doi.org/10.1007/s003390051029.

[83] Colao F, Fantoni R, Lazic V, Morone A, Santagata A, Giardini A. LIBS used as a diagnostic tool during the laser cleaning of ancient marble from Mediterranean areas. Applied Physics A 2004;79:213–9. https://doi.org/10.1007/s00339-004-2649-3.

[84] Fortes FJ, Cabalín LM, Laserna JJ. The potential of laser-induced breakdown spectrometry for real time monitoring the laser cleaning of archaeometallurgical objects. Spectrochim Acta Part B At Spectrosc 2008;63:1191–7. https://doi.org/10.1016/j.sab.2008.06.009.

[85] Choi S, Park C. Convolution Neural Network with Laser-Induced Breakdown Spectroscopy as a Monitoring Tool for Laser Cleaning Process. Sensors 2023;23. https://doi.org/10.3390/s23010083.

[86] Conesa S, Palanco S, Laserna JJ. Acoustic and optical emission during laser-induced plasma formation. Spectrochim Acta Part B At Spectrosc 2004;59:1395–401. https://doi.org/https://doi.org/10.1016/j.sab.2004.06.004.

[87] Cooper MI, Emmony DC, Larson J. Characterization of laser cleaning of limestone. Opt Laser Technol 1995;27:69–73. https://doi.org/https://doi.org/10.1016/0030-3992(95)93962-Q.

[88] Jankowska M, Śliwiński G. Acoustic monitoring for the laser cleaning of sandstone. J Cult Herit 2003;4:65–71. https://doi.org/https://doi.org/10.1016/S1296-2074(02)01230-X.

[89] Tserevelakis GJ, Pozo-Antonio JS, Siozos P, Rivas T, Pouli P, Zacharakis G. On-line photoacoustic monitoring of laser cleaning on stone: Evaluation of cleaning effectiveness and detection of potential damage to the substrate. J Cult Herit 2019;35:108–15. https://doi.org/https://doi.org/10.1016/j.culher.2018.05.014.

[90] Dimitroulaki E, Tserevelakis GJ, Melessanaki K, Zacharakis G, Pouli P. Photoacoustic real-time monitoring of UV laser ablation of aged varnish coatings on heritage objects. J Cult Herit 2023;63:230–9. https://doi.org/https://doi.org/10.1016/j.culher.2023.08.006.

[91] Chen Y, Deng G, Zhou Q, Feng G. Acoustic signal monitoring in laser paint cleaning. Laser Phys 2020;30:066001. https://doi.org/10.1088/1555-6611/ab85c7.

[92] Papanikolaou A, Tserevelakis GJ, Melessanaki K, Fotakis C, Zacharakis G, Pouli P. Development of a hybrid photoacoustic and optical monitoring system for the study of laser ablation processes upon the removal of encrustation from stonework. Opto-Electronic Advances 2020;3:1–11. https://doi.org/10.29026/oea.2020.190037.

[93] Vounisiou P, Selimis A, Tserevelakis GJ, Melessanaki K, Pouli P, Filippidis G, et al. The use of model probes for assessing in depth modifications induced during laser cleaning of modern paintings. Applied Physics A 2010;100:647–52. https://doi.org/10.1007/s00339-010-5647-7.

[94] Oujja M, Rebollar E, Castillejo M. Spectroscopic studies of laser ablation plumes of artwork materials. Appl Surf Sci 2003;211:128–35. https://doi.org/https://doi.org/10.1016/S0169-4332(03)00245-9.

[95] Kokkinaki O, Dimitroulaki E, Melessanaki K, Anglos D, Pouli P. Laser-induced fluorescence as a non-invasive tool to monitor laser-assisted thinning of aged varnish layers on paintings: fundamental issues and critical thresholds. Eur Phys J Plus 2021;136. https://doi.org/10.1140/epjp/s13360-021-01929-4.

[96] Targowski P. MJ, KEA, SM, SA. Optical coherence tomography for high resolution real-time varnish ablation monitoring. In: Saunders D., Strlič M., Korenberg C., Luxford N., Birkhölzer K., editors., London: Archetype Publications Ltd; 2013, p. 26–31.

[97] Góra M. TP, KA, MJ, RA. Fast spectral optical coherence tomography for monitoring of varnish ablation process. In: Castillejo Marta, Moreno Pablo, Oujja Mohamed, Radvan Roxana, Ruiz Javier, editors., CRC Press, Taylor & Francis Group; 2008, p. 2327.

[98] Moretti P, Iwanicka M, Melessanaki K, Dimitroulaki E, Kokkinaki O, Daugherty M, et al. Laser cleaning of paintings: in situ optimization of operative parameters through non-invasive assessment by optical coherence tomography (OCT), reflection FT-IR spectroscopy and laser induced fluorescence spectroscopy (LIF). Herit Sci 2019;7. https://doi.org/10.1186/s40494-019-0284-8.

[99] Papadakis V, Loukaiti A, Pouli P. A spectral imaging methodology for determining on-line the optimum cleaning level of stonework. J Cult Herit 2010;11:325–8. https://doi.org/10.1016/j.culher.2009.10.007.

[100] Dal Fovo A, Sanz M, Mattana S, Oujja M, Marchetti M, Pavone FS, et al. Safe limits for the application of nonlinear optical microscopies to cultural heritage: A new method for in-situ assessment. Microchemical Journal 2020;154. https://doi.org/10.1016/j.microc.2019.104568.

[101] Philippidis A, Mikallou A, Anglos D. Determining optimum irradiation conditions for the analysis of vermilion by Raman spectroscopy. Eur Phys J Plus 2021;136. https://doi.org/10.1140/epjp/s13360-021-02186-1.

[102] Lucazeau G. Effect of pressure and temperature on Raman spectra of solids: anharmonicity. Journal of Raman Spectroscopy 2003;34:478–96. https://doi.org/https://doi.org/10.1002/jrs.1027.

[103] Hanesch M. Raman spectroscopy of iron oxides and (oxy)hydroxides at low laser power and possible applications in environmental magnetic studies. Geophys J Int 2009;177:941–8. https://doi.org/10.1111/j.1365-246X.2009.04122.x.

[104] Oujja M, Pouli P, Concepcio´ C, Domingo C, Fotakis C, Castillejo M. Analytical Spectroscopic Investigation of Wavelength and Pulse Duration Effects on Laser-Induced Changes of Egg-Yolk-Based Tempera Paints. 2010.

[105] Mencaglia AA, Osticioli I, Siano S. Development of an efficient and thermally controlled Raman system for fast and safe molecular characterization of paint layers. Measurement (Lond) 2018;118:372–8. https://doi.org/10.1016/j.measurement.2017.11.056.

[106] Osticioli I, Mencaglia AA, Siano S. Temperature-controlled portable Raman spectroscopy of photothermally sensitive pigments. Sens Actuators B Chem 2017;238:772–8. https://doi.org/10.1016/j.snb.2016.07.104.

[107] Calvagna C, Mencaglia AA, Osticioli I, Ciofini D, Siano S. Novel Probe for Thermally Controlled Raman Spectroscopy Using Online IR Sensing and Emissivity Measurements. Sensors 2022;22. https://doi.org/10.3390/s22072680.

[108] Ruvalcaba-Sil JL, Casanova-González E, Pérez-Castellanos NA, García-Bucio MA. HERAS: A helium jet to prevent damage on works of art in Raman experiments. Journal of Raman Spectroscopy 2013;44:1711–7. https://doi.org/10.1002/jrs.4402.

[109] Lux A, Realini M, Botteon A, Maiwald M, Müller A, Sumpf B, et al. Advanced portable micro-SORS prototype coupled with SERDS for heritage science. Analyst 2024;149:2317–27. https://doi.org/10.1039/D3AN02215C.

[110] Harth A. X-ray fluorescence (XRF) on painted heritage objects: a review using topic modeling. Herit Sci 2024;12:17. https://doi.org/10.1186/s40494-024-01135-2.

[111] Alfeld M. MA-XRF for Historical Paintings: State of the Art and Perspective. Microscopy and Microanalysis 2020;26:72–5. https://doi.org/DOI: 10.1017/S1431927620013288.

[112] Malzer W, Schlesiger C, Kanngießer B. A century of laboratory X-ray absorption spectroscopy – A review and an optimistic outlook. Spectrochim Acta Part B At Spectrosc 2021;177:106101. https://doi.org/https://doi.org/10.1016/j.sab.2021.106101.

[113] https://www.tudelft.nl/en/me/about/departments/materials-science-and-engineering/research/research-programmes/smartlight n.d.

[114] Raimondi P, Benabderrahmane C, Berkvens P, Biasci JC, Borowiec P, Bouteille J-F, et al. The Extremely Brilliant Source storage ring of the European Synchrotron Radiation Facility. Commun Phys 2023;6:82. https://doi.org/10.1038/s42005-023-01195-z.

[115] Artioli G. Science for the cultural heritage: the contribution of X-ray diffraction. Rendiconti Lincei 2013;24:55–62. https://doi.org/10.1007/s12210-012-0207-z.

[116] Cotte M, Gonzalez V, Vanmeert F, Monico L, Dejoie C, Burghammer M, et al. The “Historical Materials BAG”: A New Facilitated Access to Synchrotron X-ray Diffraction Analyses for Cultural Heritage Materials at the European Synchrotron Radiation Facility. Molecules 2022;27. https://doi.org/10.3390/molecules27061997.

[117] Gonzalez V, Cotte M, Vanmeert F, de Nolf W, Janssens K. X-ray Diffraction Mapping for Cultural Heritage Science: a Review of Experimental Configurations and Applications. Chemistry – A European Journal 2020;26:1703–19. https://doi.org/https://doi.org/10.1002/chem.201903284.

[118] https://www.nicas-research.nl/projects/irradiation-passport-for-art/ n.d.

[119] Huntley J, Westaway KE, Gore DB, Aubert M, Ross J, Morwood MJ. Non-Destructive or Noninvasive? The Potential Effect of X-Ray Fluorescence Spectrometers on Luminescence Age Estimates of Archaeological Samples. Geoarchaeology 2016;31:592–602. https://doi.org/10.1002/gea.21574.

[120] Immel A, Le Cabec A, Bonazzi M, Herbig A, Temming H, Schuenemann VJ, et al. Effect of X-ray irradiation on ancient DNA in sub-fossil bones – Guidelines

for safe X-ray imaging. Sci Rep 2016;6:32969. https://doi.org/10.1038/srep32969.

[121] Gimat A, Schöder S, Thoury M, Dupont A-L. Degradation of historical paper induced by synchrotron X-ray technical examination. Cellulose 2022;29:4347–64. https://doi.org/10.1007/s10570-022-04552-3.

[122] Monico L, Cotte M, Vanmeert F, Amidani L, Janssens K, Nuyts G, et al. Damages Induced by Synchrotron Radiation-Based X-ray Microanalysis in Chrome Yellow Paints and Related Cr-Compounds: Assessment, Quantification, and Mitigation Strategies. Anal Chem 2020;92:14164–73. https://doi.org/10.1021/acs.analchem.0c03251.

[123] Gervais C, Languille MA, Reguer S, Gillet M, Vicenzi EP, Chagnot S, et al. “Live” Prussian blue fading by time-resolved X-ray absorption spectroscopy. Appl Phys A Mater Sci Process 2013;111:15–22. https://doi.org/10.1007/s00339-013-7581-y.

[124] Godet M, Binet L, Schöder S, Brunel-Duverger L, Thoury M, Bertrand L, et al. X-ray irradiation effects on Egyptian blue and green pigments X-ray irradiation eects on Egyptian blue and green pigments †. J Anal At Spectrom 2022;2022. https://doi.org/10.1039/D2JA00020Bï.

[125] Garman EF, Weik M. Radiation damage to biological samples: still a pertinent issue. J Synchrotron Radiat 2021;28:1278–83. https://doi.org/10.1107/S1600577521008845.

[126] Wlodawer A, Dauter Z, Jaskolski M. Protein Crystallography Methods and Protocols Methods in Molecular Biology. 2017.

[127] Ganio M, Pouyet ES, Webb SM, Schmidt Patterson CM, Walton MS. From lapis lazuli to ultramarine blue: Investigating Cennino Cennini’s recipe using sulfur K-edge XANES. Pure and Applied Chemistry 2018;90:463–75. https://doi.org/10.1515/pac-2017-0502.

[128] Webb SM, Pouyet E, Ganio M, Patterson CS, Walton MS. Characterization of the radiation damage of ultramarine pigments by microscale x-ray spectroscopy. 2017.

[129] Holton JM. A beginner’s guide to radiation damage. J Synchrotron Radiat 2009;16:133–42. https://doi.org/10.1107/S0909049509004361.

[130] McGeehan J, Ravelli RBG, Murray JW, Owen RL, Cipriani F, McSweeney S, et al. Colouring cryo-cooled crystals: Online microspectrophotometry. J Synchrotron Radiat 2009;16:163–72. https://doi.org/10.1107/S0909049509001629.

[131] Shimizu N, Shimizu T, Baba S, Hasegawa K, Yamamoto M, Kumasaka T. Development of an online UV-visible microspectrophotometer for a macromolecular crystallography beamline. J Synchrotron Radiat 2013;20:948–52. https://doi.org/10.1107/S0909049513022887.

[132] Garman EF. Radiation damage in macromolecular crystallography: What is it and why should we care? Acta Crystallogr D Biol Crystallogr 2010;66:339–51. https://doi.org/10.1107/S0907444910008656.

[133] Sutton KA, Black PJ, Mercer KR, Garman EF, Owen RL, Snell EH, et al. Insights into the mechanism of X-ray-induced disulfide-bond cleavage in lysozyme crystals based on EPR, optical absorption and X-ray diffraction studies. Acta Crystallogr D Biol Crystallogr 2013;69:2381–94. https://doi.org/10.1107/S0907444913022117.

[134] Owen RL, Yorke BA, Pearson AR. X-ray-excited optical luminescence of protein crystals: A new tool for studying radiation damage during diffraction data collection. Acta Crystallogr D Biol Crystallogr 2012;68:505–10. https://doi.org/10.1107/S0907444912002946.

[135] Tranchant L, Gueriau P, Schöder S, Cohen SX, Bertrand L, Thoury M. Detecting visual and chemical modifications induced by the high-flux synchrotron X-ray analysis of ancient teeth . TECHNART 2023 LISBON, 2023, p. 410.

[136] Zhang Z, Liu Z, Jiang Y, Zhu H, Ji T, Wang J, et al. In situ investigation of synchrotron radiation damage effect of ancient paintings by time-resolved ED-XAS and IR combined techniques. X-Ray Spectrometry 2022;51:394–402. https://doi.org/10.1002/xrs.3289.

[137] Godet M, Binet L, Schöder S, Brunel-Duverger L, Thoury M, Bertrand ıc. “X-ray irradiation effects on Egyptian blue and green pigments.” 2022.

[138] Snell EH, Bellamy HD, Rosenbaum G, Van Der Woerd MJ. Non-invasive measurement of X-ray beam heating on a surrogate crystal sample. J Synchrotron Radiat, vol. 14, 2007, p. 109–15. https://doi.org/10.1107/S090904950604605X.

[139] Moini M, Rollman CM, Bertrand L. Assessing the impact of synchrotron X-ray irradiation on proteinaceous specimens at macro and molecular levels. Anal Chem 2014;86:9417–22. https://doi.org/10.1021/ac502854d.

[140] Shimizu N, Hirata K, Hasegawa K, Ueno G, Yamamoto M. Dose dependence of radiation damage for protein crystals studied at various X-ray energies. J Synchrotron Radiat 2007;14:4–10. https://doi.org/10.1107/S0909049506049296.

[141] Sanishvili R, Yoder DW, Pothineni SB, Rosenbaum G, Xu S, Vogt S, et al. Radiation damage in protein crystals is reduced with a micron-sized X-ray beam. PNAS 2011;108:6127–32. https://doi.org/10.1073/pnas.1017701108/-/DCSupplemental.

[142] Zeldin OB, Gerstel M, Garman EF. RADDOSE-3D: time- and space-resolved modelling of dose in macromolecular crystallography. J Appl Crystallogr 2013;46:1225–30. https://doi.org/10.1107/S0021889813011461.

[143] Dalecky L, Sottile F, Hung L, Cazals L, Desolneux A, Chevalier A, et al. Non-resonant inelastic X-ray scattering for discrimination of pigments. Phys Chem Chem Phys 2024;26:4363–71. https://doi.org/10.1039/D3CP04753A.

[144] Garman EF, Owen RL. Cryocooling and radiation damage in macromolecular crystallography. Acta Crystallographica Section D 2006;62:32–47. https://doi.org/10.1107/S0907444905034207.

[145] Liang H. Advances in multispectral and hyperspectral imaging for archaeology and art conservation. Appl Phys A Mater Sci Process 2012;106:309–23. https://doi.org/10.1007/s00339-011-6689-1.

[146] Cucci C, Casini A. Chapter 3.8 - Hyperspectral imaging for artworks investigation. In: Amigo JM, editor. Hyperspectral Imaging, vol. 32, Elsevier; 2019, p. 583–604. https://doi.org/https://doi.org/10.1016/B978-0-444-63977-6.00023-7.

[147] Rosi F, Miliani C, Braun R, Harig R, Sali D, Brunetti BG, et al. Noninvasive Analysis of Paintings by Mid-infrared Hyperspectral Imaging. Angewandte Chemie International Edition 2013;52:5258–61. https://doi.org/https://doi.org/10.1002/anie.201209929.

[148] Liang H, Lucian A, Lange R, Cheung CS, Su B. Remote spectral imaging with simultaneous extraction of 3D topography for historical wall paintings. ISPRS Journal of Photogrammetry and Remote Sensing 2014;95:13–22. https://doi.org/https://doi.org/10.1016/j.isprsjprs.2014.05.011.

[149] Li Y, Suzuki A, Cheung CS, Gu Y, Kogou S, Liang H. A study of potential laser-induced degradation in remote standoff Raman spectroscopy for wall paintings. The European Physical Journal Plus 2022;137:1102. https://doi.org/10.1140/epjp/s13360-022-03305-2.

[150] Kirby J, Saunders D, National Gallery T. Fading and Colour Change of Prussian Blue: Methods of Manufacture and the Influence of Extenders. 2004.

[151] Moore DS, McGrane SD. Raman temperature measurement. J Phys Conf Ser, vol. 500, Institute of Physics Publishing; 2014. https://doi.org/10.1088/1742-6596/500/19/192011.

[152] McGrane SD, Moore DS, Goodwin PM, Dattelbaum DM. Quantitative tradeoffs between spatial, temporal, and thermometric resolution of nonresonant Raman thermometry for dynamic experiments. Appl Spectrosc 2014;68:1279–88. https://doi.org/10.1366/14-07503.

[153] Cheung CS, Spring M, Liang H. Ultra-high resolution Fourier domain optical coherence tomography for old master paintings. Opt Express 2015;23:10145. https://doi.org/10.1364/oe.23.010145.

[154] Lawman S, Liang H. Fourier domain optical coherence tomography for high-precision profilometry. Proc.SPIE, vol. 7391, 2009, p. 73910H. https://doi.org/10.1117/12.827518.

[155] Historical Materials BAG data DOI 10.15151/ESRF-ES-750948257; DOI 10.15151/ESRF-ES-1371497379 n.d.

[156] Kieffer J, Valls V, Blanc N, Hennig C. New tools for calibrating diffraction setups. J Synchrotron Radiat 2020;27:558–66. https://doi.org/10.1107/S1600577520000776.

[157] Solé VA, Papillon E, Cotte M, Walter Ph, Susini J. A multiplatform code for the analysis of energy-dispersive X-ray fluorescence spectra. Spectrochim Acta Part B At Spectrosc 2007;62:63–8. https://doi.org/https://doi.org/10.1016/j.sab.2006.12.002.

[158] d'Acapito F, Lepore GO, Puri A, Laloni A, La Manna F, Dettona E, et al. The LISA beamline at ESRF. J Synchrotron Radiat 2019;26:551–8. https://doi.org/10.1107/S160057751801843X.

[159] d'Acapito F, Puri A, Lepore G, de Donatis G, Cicconi MR, Ali SE, et al. Activity report of the Italian CRG beamline at the European Synchrotron Radiation Facility (ESRF) - Year 2018. Zenodo 2022.

[160] Perry DL, Wilkinson TJ. Synthesis of high-purity α- and β-PbO and possible applications to synthesis and processing of other lead oxide materials. Applied Physics A 2007;89:77–80. https://doi.org/10.1007/s00339-007-4073-y.

[161] Ravel B, Newville M. ATHENA, ARTEMIS, HEPHAESTUS: data analysis for X-ray absorption spectroscopy using IFEFFIT. J Synchrotron Radiat 2005;12:537–41. https://doi.org/10.1107/S0909049505012719.

[162] Bersani D, Madariaga JM. Applications of Raman spectroscopy in art and archaeology. Journal of Raman Spectroscopy 2012;43:1523–8. https://doi.org/https://doi.org/10.1002/jrs.4219.

[163] Burgio L, Clark RJH, Firth S. Raman spectroscopy as a means for the identification of plattnerite (PbO2), of lead pigments and of their degradation products. Analyst 2001;126:222–7. https://doi.org/10.1039/b008302j.

[164] Sherrer NC. Laser dependent shifting of Raman bands with phthalocyanine pigments. 6th international Congress on the Application of Raman Spectroscopy in Art and Archaeology, Parma: 2011, p. 203–4.

[165] Suzuki MA, Li Y, Gu Y, Cheung CS, Riminesi C, Liang H. Investigation of laser-induced damage to historical paint during Raman analysis. Proc.SPIE, vol. 11784, 2021, p. 117840N. https://doi.org/10.1117/12.2593925.

[166] Li Y, Suzuki A, Cheung CS, Gu Y, Kogou S, Liang H. A study of potential laser-induced degradation in remote standoff Raman spectroscopy for wall paintings. The European Physical Journal Plus 2022;137:1102. https://doi.org/10.1140/epjp/s13360-022-03305-2.

[167] Varadwaj KSK, Panigrahi MK, Ghose J. Effect of capping and particle size on Raman laser-induced degradation of γ-Fe 2O 3 nanoparticles. J Solid State Chem 2004;177:4286–92. https://doi.org/10.1016/j.jssc.2004.08.025.

[168] Macchia A, Campanella L, Gazzoli D, Gravagna E, Maras A, Nunziante S, et al. Realgar and Light. Procedia Chem 2013;8:185–93. https://doi.org/https://doi.org/10.1016/j.proche.2013.03.024.

[169] Čiuladienė A, Luckutė A, Kiuberis J, Kareiva A. Investigation of the chemical composition of red pigments and binding media. Chemija 2018;29. https://doi.org/10.6001/chemija.v29i4.3840.

[170] Chiriu D, Pala M, Pisu FA, Cappellini G, Ricci PC, Carbonaro CM. Time through colors: A kinetic model of red vermilion darkening from Raman spectra. Dyes and Pigments 2021;184:108866. https://doi.org/https://doi.org/10.1016/j.dyepig.2020.108866.

[171] Ballirano P, Botticelli M, Maras A. Thermal behaviour of cinnabar, α-HgS, and the kinetics of the β-HgS (metacinnabar) - α-HgS conversion at room temperature. European Journal of Mineralogy 2014;25:957–65. https://doi.org/10.1127/0935-1221/2013/0025-2341.

[172] Spring M, Grout R. The Blackening of Vermilion: An Analytical Study of the Process in Paintings. National Gallery Technical Bulletin, vol. 23, 2002, p. 50–61.

[173] Cotte M, Susini J, Metrich N, Moscato A, Gratziu C, Bertagnini A, et al. Blackening of Pompeian Cinnabar Paintings: X-ray Microspectroscopy Analysis. Anal Chem 2006;78:7484–92. https://doi.org/10.1021/ac0612224.

[174] Gliozzo E. Pigments — Mercury-based red (cinnabar-vermilion) and white (calomel) and their degradation products. Archaeol Anthropol Sci 2021;13:210. https://doi.org/10.1007/s12520-021-01402-4.

[175] Mohammed N, Dagher H f. Synthesis and Characterization of Mercuric Sulfide Nanoparticles Thin Films by Pulsed Laser Ablation (PLA) in Distilled Water (DW). IUST 2020;17:11–6. https://doi.org/10.22068/ijmse.17.3.11.

[176] Béarat H, Chizmeshya A, Sharma R, Barbet A, Fuchs M. MECHANISTIC AND COMPUTATIONAL STUDY OF CINNABAR PHASE TRANSFORMATION: APPLICATIONS AND IMPLICATIONS TO THE PRESERVATION OF THIS PIGMENT IN HISTORICAL PAINTING. Third International Conference on Science and Technology in Archaeology and Conservation, 2004, p. 53–70.

[177] http://www.crystallography.net/cod/ n.d.

[178] Bonazzi P, Bindi L, Pratesi G, Menchetti S. Light-induced changes in molecular arsenic sulfides: State of the art and new evidence by single-crystal X-ray diffraction 2006;91:1323–30. https://doi.org/doi:10.2138/am.2006.2165.

[179] Kyono A. Experimental study of the effect of light intensity on arsenic sulfide (As4S4) alteration. J Photochem Photobiol A Chem 2007;189:15–22. https://doi.org/https://doi.org/10.1016/j.jphotochem.2006.12.043.

[180] Gliozzo E, Burgio L. Pigments—Arsenic-based yellows and reds. Archaeol Anthropol Sci 2021;14:4. https://doi.org/10.1007/s12520-021-01431-z.

[181] Liang H, Lange R, Lucian A, Hyndes P, Townsend JH, Hackney S. Development of portable microfading spectrometers for measurement of light sensitivity of materials. International Council of Museums, Committee for Conservation (ICOM-CC) Triennial Conference, Lisbon: 2011.

[182] Cao J, Querales-Flores JD, Fahy S, Savić I. Thermally induced band gap increase and high thermoelectric figure of merit of n-type PbTe. Materials Today Physics 2020;12:100172. https://doi.org/https://doi.org/10.1016/j.mtphys.2019.100172.

[183] Garnier P, Berar JF, Calvarin G. Calorimetric study of lead oxide Pb3O4 phase transition. Mater Res Bull 1979;14:1275–9. https://doi.org/https://doi.org/10.1016/0025-5408(79)90004-7.

[184] Madelung O. Semiconductors: Data Handbook. Berlin, Heidelberg: Springer Berlin Heidelberg; 2004. https://doi.org/10.1007/978-3-642-18865-7.

[185] Garman E, Nave C. Radiation damage to crystalline biological molecules: current view. J Synchrotron Radiat 2002;9:327–8. https://doi.org/10.1107/S0909049502014565.

[186] Proposal number: 20231243, PUMA beamline, SOLEIL synchrotron. n.d.

[187] Christensen J, Horton PN, Bury CS, Dickerson JL, Taberman H, Garman EF, et al. Radiation damage in small-molecule crystallography: Fact not fiction. IUCrJ 2019;6:703–13. https://doi.org/10.1107/S2052252519006948.

[188] Schulze-Briese C, Wagner A, Tomizaki T, Oetiker M. Beam-size effects in radiation damage in insulin and thaumatin crystals. J Synchrotron Radiat 2005;12:261–7. https://doi.org/10.1107/S0909049505003298.

[189] Absil J, Garnir H-P, Strivay D, Oger C, Weber G. Study of color centers induced by PIXE irradiation. Nuclear Instruments and Methods in Physics Research B 2002;198:90–7.

[190] Melvin BR. The Color and Electronic Configurations of Prussian Blue. Inorg Chem 1962;1:337–42.

[191] Gervais C, Languille MA, Moretti G, Réguer S. X-ray Photochemistry of Prussian Blue Cellulosic Materials: Evidence for a Substrate-Mediated Redox Process. Langmuir 2015;31:8168–75. https://doi.org/10.1021/acs.langmuir.5b00770.

[192] Bajt S, Sutton SR, Delaney JS. X-ray microprobe analysis of iron oxidation states in silicates and oxides using X-ray absorption near edge structure (XANES). Geochim Cosmochim Acta 1994;58:5209–14. https://doi.org/https://doi.org/10.1016/0016-7037(94)90305-0.

[193] Samain L, Gilbert B, Grandjean F, Long GJ, Strivay D. Redox reactions in Prussian blue containing paint layers as a result of light exposure. J Anal At Spectrom 2013;28:524–35. https://doi.org/10.1039/c3ja30359d.

[194] Lerwill A, Brookes A, Townsend JH, Hackney S, Liang H. Micro-fading spectrometry: investigating the wavelength specificity of fading. Appl Phys A Mater Sci Process 2015;118:457–63. https://doi.org/10.1007/s00339-014-8645-3.

[195] Samain L, Silversmit G, Sanyova J, Vekemans B, Salomon H, Gilbert B, et al. Fading of modern Prussian blue pigments in linseed oil medium. J Anal At Spectrom 2011;26:930–41. https://doi.org/10.1039/c0ja00234h.

[196] West Fitzhugh E. Red lead and Minium. In: Feller RL, editor. Artists' pigments : a handbook of their history and characteristics, vol. 1, Washington: Archetype Publications; 1986, p. 109–40.

[197] Amat A, Rosi F, Miliani C, Sassi P, Paolantoni M, Fantacci S. A combined theoretical and experimental investigation of the electronic and vibrational properties of red lead pigment. J Cult Herit 2020;46:374–81. https://doi.org/10.1016/j.culher.2020.04.014.

[198] Gavrichev K, Bolshakov A, Kondakov D, Khoroshilov A, Denisov S. Thermal transformations of lead oxides. J Therm Anal Calorim 2008;92:857–63. https://doi.org/10.1007/s10973-007-8590-x.

[199] Aze S, Vallet JM, Detalle V, Grauby O, Baronnet A. Chromatic alterations of red lead pigments in artworks: A review. Phase Transitions 2008;81:145–54. https://doi.org/10.1080/01411590701514326.

[200] Saunders D, Kirby J. The Effect of Relative Humidity on Artists' Pigments. National Gallery Technical Bulletin 2004;25:62–72.

[201] Cavallo G, Aceto M, Emmenegger R, Keller AT, Lenz R, Villa L, et al. Preliminary non-invasive study of Carolingian pigments in the churches of St. John at Müstair and St. Benedict at Malles. Archaeol Anthropol Sci 2020;12. https://doi.org/10.1007/s12520-020-01024-2.

[202] Wainwright INM, Moffatt EA, Sirois PJ, Young GS. Analysis of wall painting fragments from the Mogao and Bingling Grottoes. Conservation of Ancient Sites on the Silk Road: Proceedings of an International Conference on the Conservation of Grotto Sites., 1997, p. 334–40.

[203] Aze S, Vallet J-M, Baronnet A, Grauby O. The fading of red lead pigment in wall paintings: tracking the physico-chemical transformations by means of complementary micro-analysis techniques. European Journal of Mineralogy 2006;18:835–43. https://doi.org/10.1127/0935-1221/2006/0018-0835.

[204] Blänsdorf C, Pfeffer S, Melzl E. The Polychromy of the Giant Buddha Statues in Bāmiyān. In: Petzet M, editor. The Giant Buddhas of Bamiyan: Safeguarding the Remains Safeguarding the Remains, Berlin: 2009, p. 237–64.

[205] Sotiropoulou S, Bikiaris D, Salpistis C, Karagiannis G, Chryssoulakis Y, Price BA, et al. Panselinos' Byzantine wall paintings in the Protaton Church, Mount Athos, Greece: a technical examination. vol. 1. 2000.

[206] Costantini I, Lottici PP, Bersani D, Pontiroli D, Casoli A, Castro K, et al. Darkening of lead- and iron-based pigments on late Gothic Italian wall

paintings: Energy dispersive X-ray fluorescence, μ-Raman, and powder X-ray diffraction analyses for diagnosis: Presence of β-PbO2 (plattnerite) and α-PbO2 (scrutinyite). Journal of Raman Spectroscopy 2020;51:680–92. https://doi.org/10.1002/jrs.5817.

[207] Kotulanová E, Bezdička P, Hradil D, Hradilová J, Švarcová S, Grygar T. Degradation of lead-based pigments by salt solutions. J Cult Herit 2009;10:367–78. https://doi.org/https://doi.org/10.1016/j.culher.2008.11.001.

[208] Avranovich Clerici E, de Meyer S, Vanmeert F, Legrand S, Monico L, Miliani C, et al. Multi-Scale X-ray Imaging of the Pigment Discoloration Processes Triggered by Chlorine Compounds in the Upper Basilica of Saint Francis of Assisi. Molecules 2023;28. https://doi.org/10.3390/molecules28166106.

[209] Daniilia S, Minopoulou E. A study of smalt and red lead discolouration in Antiphonitis wall paintings in Cyprus. Appl Phys A Mater Sci Process 2009;96:701–11. https://doi.org/10.1007/s00339-009-5163-9.

[210] Aze SV, Baronnet A, Grauby O. Red lead darkening in wall paintings: natural ageing of experimental wall paintings versus artificial ageing tests. European Journal of Mineralogy 2007;19:883–90. https://doi.org/10.1127/0935-1221/2007/0019-1771.

[211] Gutman M, Lesar-Kikelj M, Mladenovič A, Čobal-Sedmak V, Križnar A, Kramar S. Ramanmicrospectroscopic analysis of pigments of the Gothic wall painting from the Dominican Monastery in Ptuj (Slovenia). Journal of Raman Spectroscopy 2014;45:1103–9. https://doi.org/10.1002/jrs.4628.

[212] Ayalew E, Janssens K, De Wael K. Unraveling the Reactivity of Minium toward Bicarbonate and the Role of Lead Oxides Therein. Anal Chem 2016;88:1564–9. https://doi.org/10.1021/acs.analchem.5b02503.

[213] Gliozzo E, Ionescu C. Pigments—Lead-based whites, reds, yellows and oranges and their alteration phases. Archaeol Anthropol Sci 2022;14. https://doi.org/10.1007/s12520-021-01407-z.

[214] Saunders D, Spring M, Higgitt C. Colour change in red lead-containing paint films. 13th triennial ICOM-CC conference, Rio de Janeiro: 2002, p. 455–63.

[215] Kang ZC, Machesky L, Eick HA, Eyring L. The solvolytic disproportionation of mixed-valence compounds: III. Pb3O4. J Solid State Chem 1988;75:73–89. https://doi.org/https://doi.org/10.1016/0022-4596(88)90304-0.

[216] Bolong C, Zongren Y, Manli S, Zhongwei S, Jinli Z, Biwen S, et al. Virtual reconstruction of the painting process and original colors of a color-changed

Northern Wei Dynasty mural in Cave 254 of the Mogao Grottoes. Herit Sci 2022;10. https://doi.org/10.1186/s40494-022-00785-4.

[217] de Seauve T, Detalle V, Semerok A, Aze S, Grauby O, Bosonnet S, et al. Continuous wave laser thermal restoration of oxidized lead-based pigments in mural paintings. Appl Phys B 2021;127. https://doi.org/10.1007/s00340-021-07702-w.

[218] WHITE WB, ROY R. Phase Relations in the System Lead—Oxygen. Journal of the American Ceramic Society 1964;47:242–9. https://doi.org/10.1111/j.1151-2916.1964.tb14404.x.

[219] Bouvaist J, Weigel D. Sesquioxyde de plomb, Pb2O3. I. Determination de la structure. Acta Crystallographica Section A 1970;26:501–10. https://doi.org/10.1107/S0567739470001316.

[220] Anderson JS, Sterns M. The intermediate oxides of lead. J Inorg Nucl Chem 1959;11:272–85.

[221] Monico L, d'Acapito F, Cotte M, Janssens K, Romani A, Ricci G, et al. Total electron yield (TEY) detection mode Cr K-edge XANES spectroscopy as a direct method to probe the composition of the surface of darkened chrome yellow (PbCr1-xSxO4) and potassium chromate paints. Nucl Instrum Methods Phys Res B 2023;539:141–7. https://doi.org/https://doi.org/10.1016/j.nimb.2023.03.040.

[222] https://henke.lbl.gov/optical_constants/atten2.html n.d.

[223] Keester KL, White WB. ELECTRONIC SPECTRA OF THE OXIDES OF LEAD AND OF SOME TERNARY LEAD OXIDE COMPOUNDS. Mat Res Bull 1969;4:757–64.

[224] Guo D, Robinson C, Herrera JE. Role of Pb(II) defects in the mechanism of dissolution of plattnerite (β-PbO2) in water under depleting chlorine conditions. Environ Sci Technol 2014;48:12525–32. https://doi.org/10.1021/es502133k.

[225] Kogou S, Shahtahmassebi G, Lucian A, Liang H, Shui B, Zhang W, et al. From remote sensing and machine learning to the history of the Silk Road: large scale material identification on wall paintings. Sci Rep 2020;10. https://doi.org/10.1038/s41598-020-76457-9.

[226] Moseley PT, Steele IM. The importance of the non-stoichiometry of lead dioxide and the location of hydrogen in the positive active mass of the lead–acid battery. J Energy Storage 2023;61:106754. https://doi.org/https://doi.org/10.1016/j.est.2023.106754.

[227] Payne DJ, Egdell RG, Law DSL, Glans PA, Learmonth T, Smith KE, et al. Experimental and theoretical study of the electronic structures of α-PbO and β-PbO2. J Mater Chem 2007;17:267–77. https://doi.org/10.1039/b612323f.

[228] Costantini I, Lottici PP, Castro K, Madariaga JM. Use of temperature controlled stage confocal raman microscopy to study phase transition of lead dioxide (Plattnerite). Minerals 2020;10. https://doi.org/10.3390/min10050468.

[229] Vagnini M, Vivani R, Viscuso E, Favazza M, Brunetti BG, Sgamellotti A, et al. Investigation on the process of lead white blackening by Raman spectroscopy, XRD and other methods: Study of Cimabue's paintings in Assisi. Vib Spectrosc 2018;98:41–9. https://doi.org/10.1016/j.vibspec.2018.07.006.

[230] Rahimi S, Jahanbakhsh O, Ahadzadeh I. Effects of Pb2O3 nanoparticles on thermal and mechanical properties of epoxy resin, silicone, and PVC-based nanoshields. Progress in Nuclear Energy 2024;169. https://doi.org/10.1016/j.pnucene.2024.105083.

[231] Ciomartan DA, Clark RJH, McDonald LJ, Odlyha M. Studies on the thermal decomposition of basic lead(II) carbonate by Fourier-transform Raman spectroscopy, X-ray diffraction and thermal analysis. J Chem Soc, Dalton Trans 1996:3639–45. https://doi.org/10.1039/DT9960003639.

[232] Genestar Juliá C, Pons Bonafé C. The use of natural earths in picture: study and differentiation by thermal analysis. Thermochim Acta 2004;413:185–92. https://doi.org/https://doi.org/10.1016/j.tca.2003.10.016.

[233] Larkin PJ. Chapter 2 - Basic Principles. In: Larkin PJ, editor. Infrared and Raman Spectroscopy (Second Edition). Second Edition, Elsevier; 2018, p. 7–28. https://doi.org/https://doi.org/10.1016/B978-0-12-804162-8.00002-1.

[234] Vollmer M. Fundamentals of Thermal Imaging. In: Haglund J, Jeppsson F, Schönborn KJ, editors. Thermal Cameras in Science Education, Cham: Springer International Publishing; 2022, p. 7–25. https://doi.org/10.1007/978-3-030-85288-7_2.

[235] Clearfield A. Introduction to Diffraction. Principles and Applications of Powder Diffraction, 2009, p. 73–122. https://doi.org/https://doi.org/10.1002/9781444305487.ch2.

[236] Tourillon G, Dartyge E, Fontaine A, Lemonnier M, Bartol F. Electron yield X-ray absorption spectroscopy at atmospheric pressure. Phys Lett A 1987;121:251–7. https://doi.org/https://doi.org/10.1016/0375-9601(87)90015-6.

[237] Ouvrard Guy and Jobic S. X-Ray Absorption Spectroscopy (XAS). In: Bahnemann Detlef and Patrocinio AOT, editor. Springer Handbook of Inorganic Photochemistry, Cham: Springer International Publishing; 2022, p. 273–302. https://doi.org/10.1007/978-3-030-63713-2_11.

Appendix A. Alignment and focusing strategy for the remote HSI monitoring of laser damage

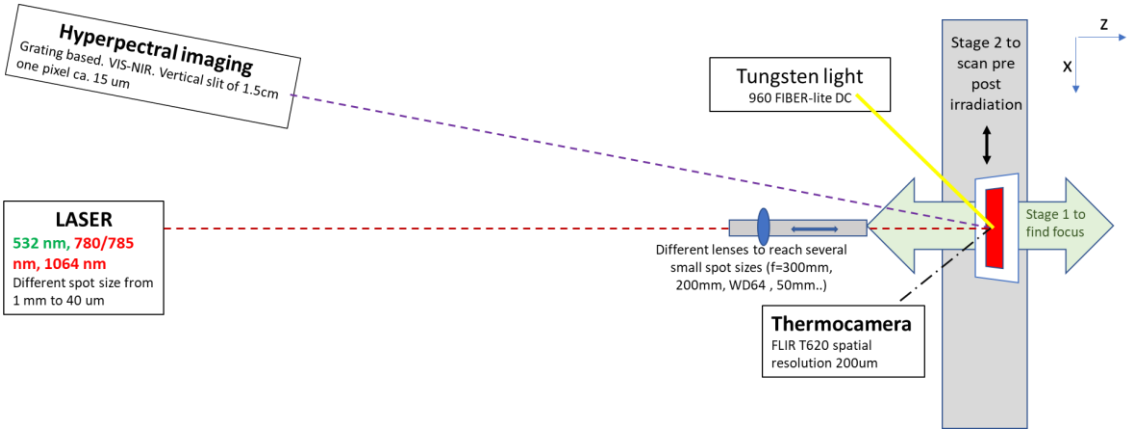

Fig. A1 Schematic of the set-up with details on the sample stage and lens position to obtain small laser beams.

As the HSI system images only a vertical line of the target, it is not possible to guide the positioning. To do so, a small ccd camera (EO-3112C LE) is placed on top of the telescope and by inserting a mirror in the optical path it is possible to visualize a 2D image of the sample. The focusing is first performed by moving the primary mirror of the telescope and looking at the sample surface with the use of the ccd camera. The focus position of the ccd camera and the HSI slit do not match, therefore a second focusing step consists in positioning a dedicated target with horizontal lines (Fig.A2) on the sample surface to focus the HSI slit by observing the sharp edges between black and white stripes. To know the exact location of the irradiated spot on the sample, the right side of the dedicated target was imaged to find the edge between the single line area and the stripy area. The

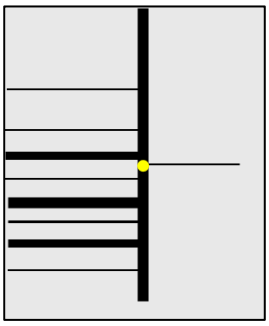

Fig. A2 The schematic of the dedicated target prepared for focusing and alignment. The yellow dot corresponds to the position of the laser beam.

alignment of the sample, laser beam and the HSI slit was performed by shooting the laser on the sample covered with the target to localize the region of interest, then a strongly attenuated laser beam (with neutral density ND filters to avoid saturation of the HSI camera) was imaged by rotating the HSI system until it captures the laser beam on the slit. This procedure also enabled the recording of the exact spatial position of the beam over the slit and the beam spot size for each dataset.

Appendix B. Evaluation of the suitable lens for microscopic HSI

Three different configurations were tested with the aim of identifying the best compromise between minimum working distance, low chromatic aberration and high spatial resolution:

1. a 500 mm Opteka) lens with f 6.3
2. a telecentric lens (melles griot p/n 39480 s/n 072)
3. an apochromatic Mitutoyo objective lens with 0.14 NA.

For each configuration we checked the chromatic aberration and the spatial resolution by scanning a 1951 USAF chart (Table B1).

The best configuration was obtained with the Mitutoyo lens as it has a large bandwidth, long working distance, and is apochromatic, which reduces aberrations.

Telescope ETX90 (min WD 3 m)	400	450	500	550	600	650	700	750	800	850	900	AVG
lp/mm	11.31	17.96	20.16	22.63	22.63	22.63	22.63	22.63	20.16	16.00	11.31	17.26
width of a line in µm	44.19	27.84	24.8	22.10	22.10	22.10	22.10	22.10	24.8	31.25	44.19	27.96
Optika lens (WD 1.75 m)	**400**	**450**	**500**	**550**	**600**	**650**	**700**	**750**	**800**	**850**	**900**	**AVG**
lp/mm	12.70	14.25	16.00	16.00	16.00	10.08	10.08	8	5.04	4.49	3.56	10.56
width of a line in µm	39.37	35.08	31.25	31.25	31.25	49.61	49.61	62.50	99.21	111.36	140.31	61.91
Telecentric lens (WD 0.19 m)	**400**	**450**	**500**	**550**	**600**	**650**	**700**	**750**	**800**	**850**	**900**	**AVG**
lp/mm	28.51	28.51	28.51	28.51	28.51	28.51	25.40	16.00	12.70	8.98	7.13	21.93
width of a line in µm	17.54	17.54	17.54	17.54	17.54	17.54	19.69	31.25	39.37	55.68	70.15	29.22
Mitutoyo lens (WD 0.03 m)	**400**	**450**	**500**	**550**	**600**	**650**	**700**	**750**	**800**	**850**	**900**	**AVG**
lp/mm	181.0	181.0	181.0	181.0	181.0	181.0	181.0	161.3	114.0	101.06	57.0	154.58
width of a line in µm	2.76	2.76	2.76	2.76	2.76	2.76	2.76	3.10	4.38	4.92	8.77	3.68

Table B1 The optical resolution measurements on the 1951 USAF resolution chart at each 50 nm step in the 400-900 nm range for each configuration tested.

Appendix C. Brief general introduction of the complementary techniques used to characterise radiation-damage

C1. Raman spectroscopy

Raman spectroscopy is a vibrational spectroscopic technique that provides the identification of specific molecular structures, enabling for example the distinction of polymorphs (same molecular formula but different crystalline structure). It is well suited to characterize mainly the symmetric vibrations of non-polar bonds and the frequency at which they appear depends on the atomic mass, the bond strength and (partially) the geometrical arrangement of the molecule. This technique is based on the inelastic scattering (Raman effect) produced by the interaction of an absorbed incoming monochromatic beam by a specific molecule. The result of inelastic scattering is the emission of photons with lower frequency (Stokes) or higher frequency (anti-Stokes) with respect to the primary beam (Fig. C1). The intensity ratio of Stokes and anti-Stokes depends on the absolute temperature of the material; thus, it can also be used to measure the materials temperature (Raman thermometry). The inelastic effect is due to the change in polarizability (deformability of the electron cloud of the molecule by an external electric field) of the molecule during a vibration or rotation. The polarizability is characteristic of specific chemical bonds. The Raman effect has lower probability of occurring than the elastic scattering (Rayleigh). For Raman scatterer materials the Raman intensity is ca. 10^{-6} with respect to the one of the incident lights [233]. In cultural heritage field, it is extremely useful for the identification of historical materials, such as pigments and dyes.

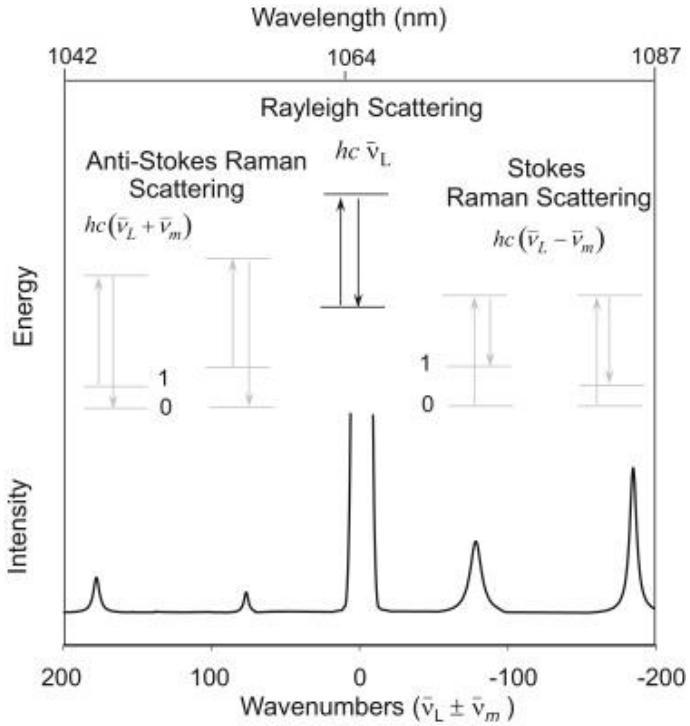

Fig. C1 Schematic representation of the elastic scattering signal (Rayleigh) and the inelastic Raman scattering, both Stokes and anti-Stokes

C2. Infrared thermal imaging

Infrared thermal imaging is based on the main principle that all materials at a temperature above 0 K emit thermal radiation). This can be used to indirectly acquire the temperature in an imaging modality over specific materials. It is commonly used also to identify different materials due to their characteristic radiative response. In fact, the amount of thermal radiation emitted depends on the temperature (to the 4th power) and the material property of emissivity (ε). The ε is the ratio of the effective emission of a specific material and its maximum possible emission if considered as a black body; its value ranges from close to 0 (non-emitting) to 1 (maximum emission like a black body). Spectral range used in thermal imaging is typically 1-14 μm. The optimum range for room temperature applications is 8-14 μm (Fig C2) [234].

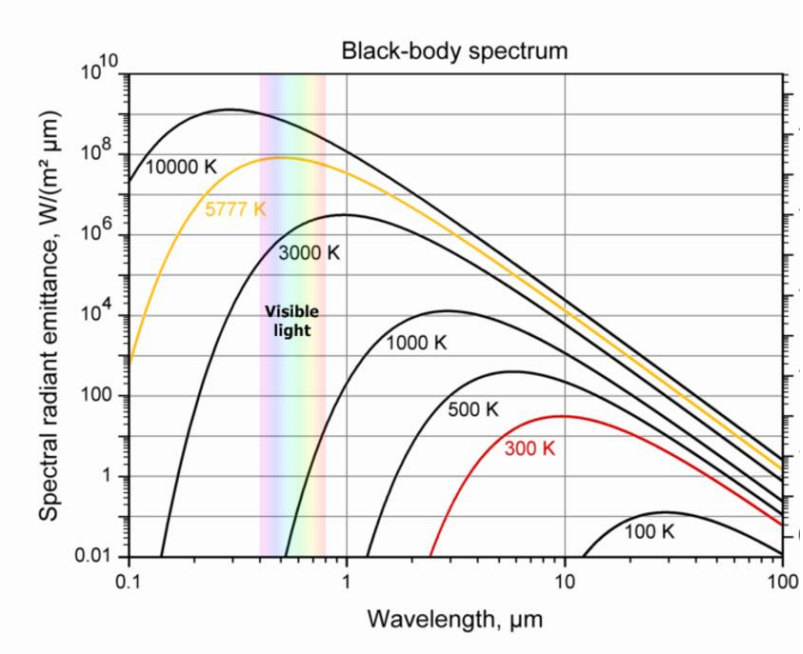

Fig. C2 The relationship between emitted radiation and the temperature of a black body [234]).

C3. Optical Coherence Tomography

OCT is based on a Michelson interferometer and makes use of a broadband light. This technique allows the real-time reconstruction of virtual cross sections of transparent and semi-transparent materials and their subsurface microstructure. The broadband source is divided by a beam splitter into two beams: one reaching the target and the other beam propagating until reaching a reference mirror. Once the beams are reflected back, they are recombined when passing through the beam splitter, and the interference signal is measured at the detector. In the Fourier domain OCT the reference mirror path is fixed, and a spectrometer is used as detector. The reconstruction of the depth profile is obtained from the Fourier Transform of the spectra. Nowadays, this non-contact and non-invasive technique is well-established in the cultural heritage field, and it is applied for the analysis of many types of objects [19].

C4. X-ray powder diffraction

XRPD is a technique based on the scattering of X-rays from electrons that are bound to an atom, giving information regarding the relative position of atoms in space. This powerful technique allows the identification of the specific structure of a crystal, that is an ordered material where the atoms are positioned in a repetitive geometrical form in symmetrically arranged planes. In a polycrystalline material (powder) the crystallites are generally randomly oriented. When a family of planes with interspacing d are in a condition of diffraction (reflection from many semi-transparent layers of atoms with constructive and destructive interference) at a given angle θ, they produce diffracted beams with rotational symmetry with respect to the X-ray incident beam, following the Bragg's law:

$$\sin\theta = \frac{n\lambda}{2d}$$

Usually, the X-ray source used is monochromatic and, as for the Bragg law, the narrower the wavelength dispersion is (also estimated as ΔE/E), the lower the angular dispersion, hence higher angular resolution. Each specific diffracted reflection degenerates into a diffraction cone (Debye ring) and by using a 2D arial detector it is possible to collect many diffraction rings. From the azimuthal integration of these rings, it is possible to extract the typical 1D XRPD pattern, with each peak corresponding to the diffraction peaks coming from a specific family of planes. The geometry of incoming beam-sample-detector can be either in reflection (Bragg-Brentano geometry) or in transmission. With the former geometry, the incident X-ray beam and the detector synchronously rotate in the same circle, forming the same θ angle with respect to the sample surface; therefore, it can be performed on bulk materials only with flattened surface as only the atomic planes parallel to the surface will be measured. The transmission can be performed only for small powders in a capillary or thin samples that allow transmission of X-rays. [235]

C5. X-ray absorption spectroscopy

X-ray absorption spectroscopy is a technique based on the photoelectric effect: X-rays are absorbed by electrons strongly bound in a core level of an atom, and the excess energy of the electronic binding energy is transformed in kinetic energy of the photoelectron ejected from the atom. To induce absorption, the X-ray photons must have energy just above a core-level electron of a specific atom (threshold energy or absorption edge). What is obtained during an XAS measurement is the fine change in the linear absorption coefficient μ(E), based on the attenuation of the incident photon intensity I_0 impinged on a material of thickness t, and the resultant intensity I measured after interaction with the sample, following the Lambert Beer's law:

$$I = I_0 e^{-\mu t}$$

To describe a XAS spectrum, an example is shown in Fig. C3 at vanadium K-edge (5465 eV). The acquisition is usually performed with monochromatic beam performing a scan in energy from below the absorption energy (pre-edge, marked as area 1 and 2 in Fig. C3) up to generally 1000 eV after absorption (post-edge, marked as area 4 in Fig. C3). The overall decrease is due to the higher penetration of X-rays at higher energies. The first small peak (marked as area 2 in Fig. C3) in the pre-edge region is not always present and depends on the electronic structure of the specific atom. It corresponds to the transfer of photoelectron into the first empty discrete electronic states, just above the Fermi level. Then an abrupt increase of absorbance defines the main absorption edge of the element (marked as area 3 in Fig. C3) with few peaks just after the edge. The edges are tabulated for each atom but experimentally they slightly vary based on the electronic population and the arrangement of the atom in a specific molecule. In general, a decrease or increase of energy of the edge corresponds to respectively a reduction or oxidation of the chemical element under study. In the continuum post edge (marked as area 4 in Fig. C3), which correspond to several interatomic distances, some small oscillations are present which are related to the photoelectrons interacting with neighbouring atoms. The technique is commonly divided in two, based on the energy regions just described: the near edge (XANES) from pre-edge to few tens of eV post-

edge, and extended fine structure (EXAFS) from ca. 50 eV to ca. 1000 eV post-edge, depending on the material.

The technique enables to selectively analyse the speciation of a single atom in the analysed compound at close-range, obtaining information on its electronic properties, structural arrangement, or molecular shape if not crystalline. Generally, from the XANES it is possible to obtain information on the atomic structure, like its oxidation state and the electronic configuration, while from EXAFS for example, it is possible to obtain the coordination number of the chemical element in the compound, and the distance and nature of the surrounding atoms. It can be performed in three different modalities: transmission, fluorescence or Total Electron Yield (TEY). With the first modality, the transmitted intensity (*I*) is measured and μ(E) is obtained as:

$$\mu(\mathrm{E}) = \ln \frac{I_0}{I}$$

It is the desirable set-up for highly concentrated samples, to avoid self-absorption (attenuation of the fluorescence signal due to reabsorption of the fluorescence X-rays from the absorber atom in the sample) that affect the florescence modality. The indirect fluorescence modality usually makes use of a geometry of incident beam-sample-detector of 45°/0/ 45° and the samples measured are usually diluted and/or with infinite thickness (not allowing transmission of the incident photons). With TEY, instead of measuring the attenuated X-ray flux, it is measured the sum of the electrons (photoelectron, *Auger* and secondary electrons) produced upon X-ray interaction with the target material, thanks to an anode placed on the sample and using an electron amplifier, such as He gas in the environment if atmospheric measurements are needed [236]. The signal obtained is highly superficial (hundreds of nm, [221] and references therein) and it is possible to measure thick and concentrated samples at low energy, where the yield of fluorescence is relatively much lower [237].

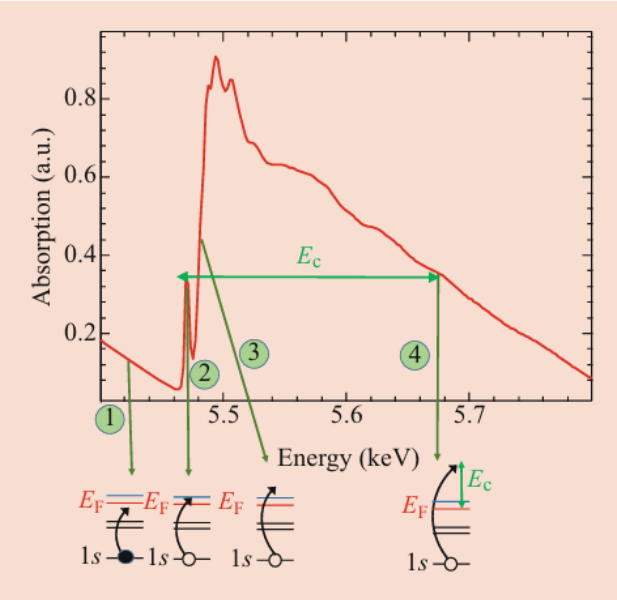

Fig. C3 An example of a raw XAS of V_2O_5 powder at the V K-edge collected in transmission mode (figure from [237]) with green numbers marking different parts of the spectrum: areas 1 and 2 are pre-edge, area 3 is the main absorption edge, and area 4 is the extended region fine structure with small oscillations.